

SCUOLA DI SCIENZE

Dipartimento di Fisica e Astronomia

Corso di Laurea Magistrale in Astrofisica e Cosmologia

**Unveiling the inner morphology and
gas kinematics of NGC 5135 with
ALMA**

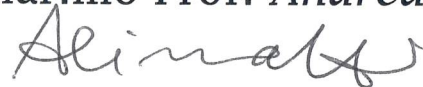
Tesi di laurea Magistrale

Presentata da:

Giovanni Sabatini

Relatore:

Chiar.mo Prof. *Andrea Cimatti*



Correlatori:

Dott.ssa *Carlotta Gruppioni*

Dott.ssa *Marcella Massardi*

Dott.ssa *Francesca Pozzi*

Sessione II

Anno Accademico 2016-2017

*This Thesis work was done as part of the research activity of the
Italian node of the European ALMA Regional Centre
and of the Istituto di Radioastronomia –
Istituto Nazionale di Astrofisica (INAF) in Bologna.*

*“The Road goes ever on and on
Out from the door where it began.
Now far ahead the Road has gone,
Let others follow it who can!
Let them a journey new begin,
But I at last with weary feet
Will turn towards the lighted inn,
My evening-rest and sleep to meet”*

⊗ ⊗ ⊗ ⊗ ⊗ ⊗ ⊗ ⊗ ⊗ ⊗ ⊗ ⊗ ⊗ ⊗ ⊗ ⊗ ⊗ ⊗

*“Still round the corner there may wait
A new road or a secret gate;
And though I oft have passed them by,
A day will come at last when I
Shall take the hidden paths that run
West of the Moon, East of the Sun.”*

J. R. R. Tolkien - *“The Lord of the Ring”*

Contents

Abstract	10
Sommario	12
1 Introduction: The AGN-Galaxy coevolution	14
1.1 A brief overview of the “AGNs families”	15
1.1.1 AGN components and the Unified Model	19
1.2 From high-redshift observations to general properties	23
1.2.1 The SFR history across the Universe	23
1.2.2 The massive Black-Holes accretion History	27
1.3 The Black Holes fueling	29
1.4 Possible SF-AGN phenomena connections	31
2 NGC 5135: a peculiar Galaxy	36
2.1 Luminous Infrared Galaxies	37
2.2 NGC 5135	40
2.2.1 Radio observations	42
2.2.2 Near IR observations	42
2.2.3 Optical and UV observations	44
2.2.4 X-ray observations	47
3 Analysis of ALMA data	50
3.1 <i>The Atacama Large Millimeter/submillimeter Array</i> interferometer	51
3.1.1 ALMA observational-bands	56
3.2 The ALMA data: data retrieval and analysis procedures	58
3.2.1 The ALMA archive:	58
3.2.2 ALMA data of NGC 5135:	60
3.3 Data reduction	64
3.3.1 Software used: CASA	64
3.3.2 Flagging procedure	65
3.3.3 Calibration procedure	69
3.4 Data Imaging	79
3.4.1 Imaging procedure	79
3.4.2 Our results	83

CONTENTS

4	The 3^DBAROLO software: a new way to investigate gas kinematics	94
4.1	Introduction on the Spiral Galaxy dynamics:	95
4.2	3^D BAROLO as a tool for kinematic analysis	98
4.3	The limits and the strengths of 3^D BAROLO	104
5	The complex morphology and kinematics in the inner regions of NGC 5135: <i>Are we witnessing the AGN influence?</i>	108
5.1	Moments analysis	109
5.2	Kinematic model	121
5.2.1	Results from the low resolution model	125
5.2.2	Result from the high-resolution model	130
5.3	Physical interpretations	136
	Conclusions	140
	Appendices	144
A	Script for calibration: ALMA band 9	144

Abstract

Active galactic nuclei (AGN) are thought to play a major role in the formation and evolution of galaxies, providing mechanisms for feedback from the supermassive black hole (SMBH) to its hosting galaxy and the intergalactic medium. In co-evolutionary scenarios, the SMBH properties are strictly connected to those of the host galaxy, in either high redshift quasars and in local Seyfert nuclei. Local Seyfert galaxies hosting both SMBHs and star forming regions, can be considered as the nearest counterparts of high redshift sub-millimetre heavily dust obscured star forming galaxies, where a significant fraction of the optical and UV photons are absorbed by dust and re-emitted in the IR and sub-mm bands. In the absence of major merging events and companions, the mechanisms that link the star formation (SF) and the accretion onto the black hole (BH) lie in the inner galactic regions (within ~ 1 kpc from the BH) and are responsible for the feeding of the BH and the quenching of the SF through feedback mechanisms from the BH itself. On the one hand, high resolution observations in the sub-mm band suggest that feeding might happen through the formation of bars at the inner end of the spiral galactic arms. On the other hand, outflows from the SMBHs have been observed and seem to be responsible for halting the gas infall and the SF in the inner galactic regions.

Fuelling and outflows seem to constitute a self-regulating combination of processes on the small scales that determine the galaxy morphology and dynamics. How the small scales dynamics influences the overall galaxy morphology, what is the timescale on which different processes happen, and if the different evolutionary stages justify the different observed morphologies, are still open questions.

This thesis project develops within the above astrophysical context, with the main goal of studying the morphology, the kinematics and the physical processes at play in the inner regions of the nearby Seyfert 2 galaxy **NGC 5135**. This source was selected from a sample of local IR selected Seyfert galaxies, for the availability of a wide set of data from the literature, both photometric and spectroscopic, covering basically the whole electromagnetic spectrum, including high resolution observations with the Atacama Large Millimeter Array (ALMA).

- The first part of this Master thesis is finalised to the reduction and analysis of all the ALMA data available in the ALMA data archive for **NGC 5135**. Three datasets have been found: the first two – relative to observations in Band 6 (i.e., ~ 250 GHz) – have been combined into a unique dataset, then analysed as a single observation, after separate calibration; the third observation – in Band 9 (e.g., ~ 670 GHz) – required a new manual calibration and flagging of part of

data. From the comparison of our final continuum maps with the results found in the archive, we have improved the signal to noise ratio (SNR) by a factor of 4 for the extended configuration-Band 6 observation, and by a factor of 2 for the other configurations.

Thanks to the large frequency coverage of our data, it has been possible to obtain the CO(2-1) and CS(5-4) line emission cubes from Band 6 (centred at $\nu_{rest-CO} = 230.538$ GHz and $\nu_{rest-CS} = 244.936$ GHz respectively), and the CO(6-5) line emission cube (centred at $\nu_{rest-CO} = 691.473$ GHz).

- In the second part of this project, we have interpreted the complex morphology of NGC 5135 and the physical processes associated to each of the different components identified in the nuclear region. In particular, we have analysed the 0th, 1st and 2nd moments of the entire set of CO line spectral cubes, finding a very complex kinematics. The overall structure, especially that obtained from the analysis of the CO(2-1) moments, resembles that of a spiral galaxy with gas flowing through the arms and a nuclear bar.
- In order to model the kinematics in the innermost regions of NGC 5135, in the third part of the project, we have applied the *3D-Based Analysis of Rotating Object via Line Observations* (^{3D}BAROLO) software to our data cubes.

^{3D}BAROLO is a specific software developed to fit rotational curves of galaxies from emission line data cubes by using a 3D tilted-ring model.

To interpret the physics at play in the innermost regions of NGC 5135, we have considered a rotating disk perturbed by radial motions, finding a best fitting solution that well reproduces the overall structure of the galaxy, but cannot explain in detail the behaviour of a few regions. The gas behaviour in these regions is likely due to AGN or Supernova driven outflows and associated to shock fronts and “super-bubbles”. Higher resolution ALMA observations will be necessary in order to shed a definitive light on the gas dynamics in the innermost regions of this complex galaxy, on the dusty torus around the AGN, on the different molecule tracers, on the role of bars in triggering SF and shocks.

Sommario

E' ormai opinione consolidata che i Nuclei Galattici Attivi (AGN) giochino un ruolo fondamentale nella formazione e nell'evoluzione delle galassie, influenzando sia l'attività dei Buchi Neri Super-massicci (SMBH), sia le galassie che li ospitano ed il mezzo intergalattico. In uno scenario coevolutivo, sia nei quasar ad alto redshift che nei nuclei delle Seyfert locali, le proprietà dei SMBH sono fortemente legate a quelle della galassia ospite. Le galassie di Seyfert locali, ospitando sia SMBH che zone di formazione stellare, possono essere considerate come la controparte più vicina delle galassie sub-millimetriche (sub-mm) ad alto redshift con formazione stellare attiva e fortemente oscurate, in cui una considerevole frazione dei fotoni ottici e ultravioletti (UV) sono assorbiti dalla polvere e riemessi nelle bande infrarossa e sub-mm. In assenza di fenomeni di interazione su grande scala o di galassie compagne, i meccanismi che legano la formazione stellare (SF) ai fenomeni di accrescimento sul Buco Nero (BH) si verificano nelle regioni più interne (entro ~ 1 kpc dal BH) e sono responsabili dell'alimentazione del BH e dello spegnimento della formazione stellare attraverso meccanismi di feedback dipendenti dallo stesso BH. Da un lato, osservazioni ad alta risoluzione in banda sub-mm suggeriscono che l'alimentazione (*fuelling*) possa avvenire attraverso la formazione di barre nelle zone interne dove terminano le braccia delle galassie a spirale. D'altro canto, sono stati osservati fenomeni di fuoriuscita di materiale dai SMBHs (*outflows*) ritenuti potenziali responsabili del rallentamento del gas in caduta e del blocco della SF nelle regioni galattiche più interne.

Fuelling e outflows sembrano costituire una combinazione auto-regolante dei processi che, su piccola scala, determinano la morfologia e la dinamica delle galassie.

Come le dinamiche sulle piccole scale influenzino la morfologia complessiva della galassia, quali siano i tempi in cui i diversi processi si verificano, e se le diverse fasi evolutive giustifichino le diverse morfologie osservate, sono ancora domande aperte.

Questo lavoro di tesi si sviluppa nell'ambito astrofisico suddetto, con l'obiettivo principale di studiare la morfologia, la cinematica ed i processi fisici in gioco nelle regioni interne della galassia di Seyfert locale NGC 5135. Questa sorgente è stata selezionata da un campione di AGN selezionati nell'IR, per la disponibilità di un ampio insieme di dati in letteratura, sia fotometrici che spettroscopici, che coprono l'intero spettro elettromagnetico, incluse osservazioni ad alta risoluzione con l' Atacama Large Millimeter Array (ALMA).

- La prima parte di questa Tesi Magistrale è finalizzata alla riduzione e all'analisi di tutti i dati ALMA relativi a NGC 5135 disponibili nel archivio ALMA. Sono stati trovati tre set di dati: due - nella Banda 6 (i.e., ~ 250 GHz) - sono

stati combinati in un unico insieme di dati e, dopo essere stati opportunamente calibrati in modo separato, sono stati analizzati come una singola osservazione; il terzo set di dati - in Banda 9 (i.e., ~ 670 GHz) - ha richiesto una nuova calibrazione manuale e l'esclusione *flagging* di una parte dei dati. Dal confronto delle mappe da noi ottenute nel continuo con quelle presenti in archivio, risulta che il rapporto segnale-rumore (SNR) è stato migliorato di un fattore 4 per la configurazione estesa in Banda 6, e di un fattore 2, per le altre configurazioni. Grazie alla ampia copertura in frequenza dei dati, è stato possibile ottenere i cubi delle righe di emissione del CO(2-1) e del CS(5-4) dalla Banda 6 (centrate rispettivamente a $\nu_{rest-CO} = 230.538$ GHz e $\nu_{rest-CS} = 244.936$ GHz), ed il cubo del CO(6-5) dalla Banda 9 (centrato a $\nu_{rest-CO} = 691.473$ GHz).

- Nella seconda parte di questo progetto, abbiamo interpretato la complessa morfologia di NGC 5135 ed i processi fisici associati ad ognuna delle componenti identificate nella regione centrale. In particolare, abbiamo analizzato i momenti 0, 1 e 2 dell'insieme completo di cubi delle emissioni in riga del CO, trovando una dinamica particolarmente complessa. La struttura nel suo complesso, in particolare quella ottenuta dall'analisi dei momenti del CO(2-1), assomiglia a quella delle galassie a spirale, con il gas che sta fluendo attraverso le braccia e la barra nucleare.

- Al fine di descrivere la cinematica nelle regioni più interne di NGC 5135, nella terza parte del progetto, abbiamo applicato il software *3D-Based Analysis of Rotating Object via Line Observations* (^{3D}BAROLO) ai nostri dati. Per interpretare la fisica in gioco nelle regioni più interne di NGC 5135 abbiamo considerato un modello a disco di rotazione perturbato da moti radiali, trovando una soluzione che ben riproduce la struttura complessiva della galassia, ma che tuttavia non riesce a descrivere in dettaglio il comportamento di alcune regioni.

Il comportamento del gas in queste zone è probabilmente dovuto agli *outflows* generati dall'AGN o da un resto di Supernova, associati a fronti di shock ed alla presenza di una "super-bubble". Saranno necessarie osservazioni ALMA a più alte risoluzioni per far luce definitivamente sulle dinamiche del gas nelle regioni più interne di questa complessa galassia, sul toro di polvere attorno all'AGN, sui differenti traccianti molecolari, sul ruolo che le barre hanno nell'innesco della SF e nella formazione degli shock.

Chapter 1

Introduction: The AGN-Galaxy coevolution

Abstract

The origins and evolution of galaxies are among the most intriguing and complex chapter in the formation of the cosmic structures. Astrophysical observations in this field of research have accumulated at a surprising pace. Ideally, a deep understanding of the evolution of the galaxy structures will include the complete sequence of events that led to the formation of the first stars after the end of cosmic dark ages at today's diversity of shapes, sizes, masses, colors, brightness, metallicities and galaxy clustering. In the last two decades, many works have been tried to shed light on the complex connection between the star formation phenomena and the consequences that BH nuclear activity may have on the galactic environment.

The purpose of this chapter is to present a general picture on these topics, trying to highlight the state of the art explaining the mutual influence between star formation and nuclear activity phenomena. In the first part of this chapter the main observed classes of active galactic nuclei are presented, with particular emphasis on what is called Unified Model. The the central paragraphs are focused on the phenomena of star formation and BH accretion activity, with the aim of summarizing the main discoveries. In the final part, we summarize the most recent results on the literature trying to link the SF and AGN accretion processes and to study how they evolve with time.

1.1 A brief overview of the “AGNs families”

The *Active Galactic Nuclei* (AGNs) are defined as compact objects that occupy the most central regions of galaxies. They are characterized by an emission too intense to be explained by stellar activity; it requires a much more efficient energy source. This source of energy has been associated with the matter accretion mechanisms onto a compact object with high gravitational attraction (a BH), and its conversion into energy.

It’s a common thought that the majority ($\sim 99\%$) of all galaxies host an AGN in their centre, but only $\sim 1\%$ of them are active.

Although, this is a small fraction of the total, AGN show different properties depending on the spectral band in which they are observed. This allowed to create a series of classes for these objects, which characterize them according to their main observed properties.

According to the observed emission in the radio band, AGN can be subdivided into the Radio-Loud (RL) and Radio-Quiet (RQ) categories. Several definitions, either based on the radio power only or on the ratio between, e.g., radio and optical fluxes/luminosities, are considered.

By adopting the criterion which considers the ratios of radio (5 GHz) to optical (B-band) flux $F_{5\text{GHz}}/F_B \gtrsim 10$ (Kellermann et al. [1989]), roughly 15 – 20% of all the AGN are RL, although the RL fraction increases with optical (La Franca et al. [1994], Padovani [1993]) and X-ray (della Ceca et al. [1994]) luminosities. With few exceptions, the optical and ultraviolet emission-line spectra and the infrared to soft X-ray continuum of most RL and RQ AGN are very similar (Sanders et al. [1989]) and so must be produced in more or less the same way. The characteristic of radio-loudness itself may be related in some way to the host galaxy type (Smith et al. [1986]) or to the black hole spin (Wilson and Colbert [1995]), which might enable the formation of powerful relativistic jets.

RL objects have emission contributions from both the jet(s) and the lobes that the jets inflate. These emission contributions dominate the luminosity of the AGN at radio wavelengths and possibly at some or all other wavelengths.

In RQ objects jets (and any jet-related emission) can be neglected at all wavelengths.

AGN terminology is often confusing, since the distinctions between different types of AGN reflect historical differences in how the objects were discovered or initially classified, rather than real physical differences. Here we list the main observational classes of AGN.

1. Seyfert I and Seyfer II:

Seyfert galaxies are lower-luminosity active galactic nuclei, with $M_B > -21.51 + 5\log h_0$, according to the criterion established by Schmidt and Green [1983] for distinguishing Seyfert galaxies from quasars. A Seyfert galaxy has a quasar-like nucleus, but the host galaxy is clearly detectable. The original definition of the class (due to Seyfert [1943]) was primarily morphological, i.e., these are galax-

ies with high surface brightness nuclei. Subsequently spectroscopy revealed unusual emission-line characteristics. Observed through a large telescope, a Seyfert galaxy looks like a normal distant spiral galaxy with a star superimposed on the center. The definition has evolved so that Seyfert galaxies are now identified spectroscopically by the presence of strong, high-ionization emission lines. Morphological studies indicate that most if not all Seyferts occur in spiral galaxies. [Khachikian and Weedman \[1974\]](#) were the first to realize that there are two distinct subclasses of Seyfert galaxies which are distinguished by the presence or absence of broad bases on the permitted emission lines.

Type I Seyfert galaxies have two sets of emission lines, superposed on one another. One set of lines is characteristic of a low-density (electron density $n_e \approx 10^3 - 10^6 \text{ cm}^{-3}$) ionized gas with widths corresponding to velocities of several hundred kilometers per second (i.e., somewhat broader than emission lines in non-AGNs), and are referred to as the “narrow lines”. A second set of “broad lines” are also seen, but in the permitted lines only: these lines have widths of up to 10^4 km s^{-1} . The absence of broad forbidden-line emission indicates that the broad-line gas is of high density ($n_e \approx 10^9 \text{ cm}^{-3}$ or higher), so the non-electric-dipole transitions are collisionally suppressed.

Type II Seyfert galaxies differ from Seyfert I galaxies in that only the narrow lines are present in type II spectra.

In addition to the strong emission lines, weak absorption lines due the late-type giant stars in the host galaxy are also observed in both type I and type II Seyfert spectra; the absorption lines are relatively weak because the starlight is diluted by the non-stellar “featureless continuum”. Indeed, the AGN continuum is usually so weak in Seyfert II galaxies that it is very difficult to isolate it from the stellar continuum unambiguously.

The narrow-line spectra are clearly distinguishable from the HII-region spectra seen in some normal galaxies, as the Seyfert spectra show a wide range in ionization level, which is typical of a gas ionized by a source where the input continuum spectrum falls off slowly (relative to a *Wien law*) at ionizing wavelengths.

The origin of the differences between Seyferts of type I and type II is not known. One school of thought holds that all Seyferts II are intrinsically Seyferts I where we are unable to see the broad components of the lines from our particular vantage point. It is not clear, however, that this hypothesis can explain all of the observed differences between the two subclasses.

[Osterbrock \[1981\]](#) has introduced the notation Seyfert 1.5, 1.8, and 1.9, where the subclasses are based purely on the appearance of the optical spectrum, with numerically larger subclasses having weaker broad-line components relative to the narrow lines. In Seyfert 1.9 galaxies, for example, the broad component is detected only in the H_α line, and not in the higher-order Balmer lines. In Seyfert 1.8 galaxies, the broad components are very weak, but detectable at H_β as well as H_α . In Seyfert 1.5 galaxies, the strengths of the broad and narrow components in H_β are comparable.

1.1 A brief overview of the “AGNs families”

2. Quasars:

Quasars comprise the most luminous subclass of AGN. The first quasar observed (Hazard et al. [1963]) appeared at radio and optical wavelengths as faint, point-like objects with unusual optical emission spectra: hence the definition of “*Quasi-stellar radio source*” (Quasar).

Their spectra, however, are quite unlike those of stars and the emission lines turn out to be significantly red-shifted.

A few years after their discovery, Schmidt [1969] summarized the Quasar general properties with a study on a large statistical quasar sample. Each quasar shows itself as:

- Very far objects;
- Star-like objects identified with radio sources;
- Extremely luminous in UV continuum;
- With a continuum flux variable in time;
- Broad emission lines.

The optical spectra of quasars are similar to those of Seyfert I galaxies, with prominent broad lines but rather weaker narrow lines. However, the shape of the nonstellar continuum in the Spectral Energy Distribution (hereafter, SED) of quasars and Seyfert 1 galaxies is quite different: quasars show a considerable steepening of the continuum at high frequencies compared to the Seyfert one.

3. Radio Galaxies:

They are the RL analogue of the Seyfert galaxies. In terms of basic phenomenology of the optical spectra, we recognized two many classes, perfectly comparable to the Seyfert one: the *Broad-line radio galaxies* (BLRGs) and the *Narrow-line radio galaxies* (NLRGs).

One important different compared to the Seyfert is that they are strong radio sources identified with giant elliptical galaxies rather than spirals, although some of the brightest one are associated with quasars.

Among the radio AGN, some are characterized by strong extended radio emission even at much larger dimensions than the galaxy itself (> 100 kpc). These sources are associated with the FR I and FR II classification. The name of the class comes from the scientists who first studied and categorized them (Fanaroff and Riley [1974]), who defined the threshold limit between the two object classes with respect to their 178 kHz Luminosity. The FR I have $L_{178\text{kHz}} < 2 \cdot 10^{25} W$ and show twin-jets issued in opposing directions. The FR II have $L_{178\text{kHz}} > 2 \cdot 10^{25} W$ and can show the complete absence or presence of one of the two jets extending far larger than those of FR I. In addition, the FR II show the the presence of two large regions, called *hotspots*, that follow the direction of the jets and identify the “points” in which the ultra-relativistic jets transferred enough energy to interstellar medium to be visible. In Figure 1.1 four examples of FR-galaxies are shown.

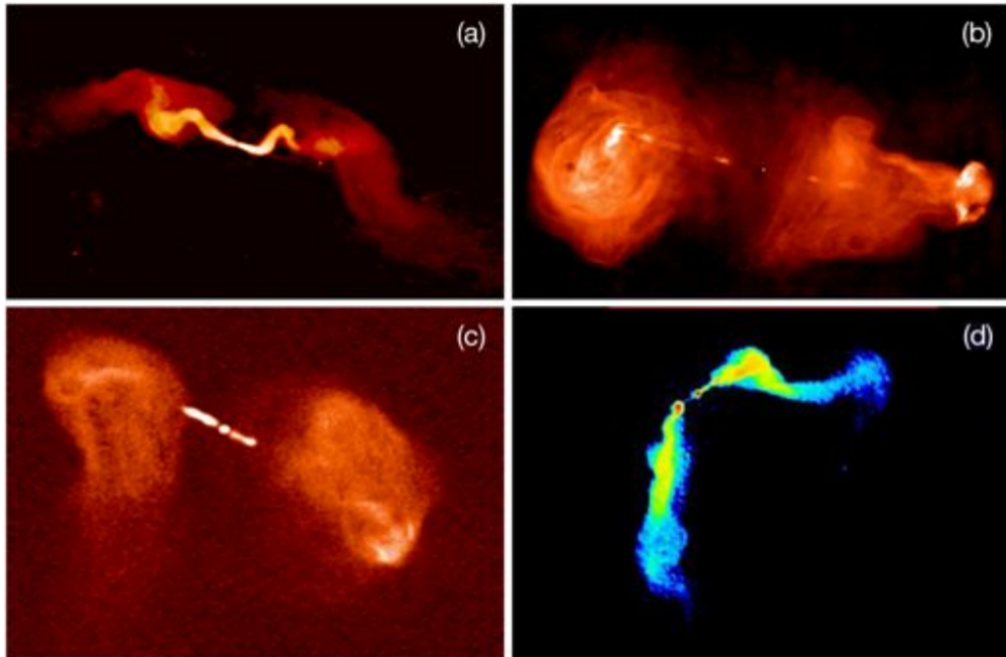


Figure 1.1: Four examples of various radio loud galaxy morphologies taken by (Banfield *et al.* [2015]). (a) FR-I radio source 3C31 at 1.4 GHz with the VLA (Laing [1996]). (b) FR-II radio source 3C353 at 8.4 GHz with the VLA (Swain *et al.* [1998]). (c) FR-I radio source 3C288 at 8.4 GHz with the VLA (Bridle *et al.* [1989]). (d) FR-I radio source 3C465, in Abell 2634 at 1.4 GHz with the VLA (Eilek *et al.* [1984]).

4. **Blazars:** Generally, AGNs show a variability in the continuum emission at all wavelengths: from radio to X-rays. However, some of these objects show more intense variability on shorter time scales. These objects are called Blazars and have a variability over a number of days or less. Blazars can be divided into two subclasses:

- *BL Lac*: They are characterised by spectra in which emission lines are either absent or extremely weak. They lie at relatively low redshifts. At first, they were mistaken for variable stars until their spectra were studied. Their name derives from *BL Lacertae* (BL Lac) which is the variable-star designation originally given to the first object of this type to be studied.
- *OVV*: They are very similar to BL Lacs but have stronger, broad emission lines in the optical spectra and tend to have a more intensive variability on shorter scale times. From this fact, the name of *Optically Violent Variables* (OVVs).

1.1.1 AGN components and the Unified Model

In this section we will give a rapid description of the various components that, now a days, are thought to constitute the innermost regions of an AGN.

We exploit Figure 1.2 with two goals: to understand the various components of an AGN and to explain, with a single model, all the “AGN families” described in the previous paragraph.

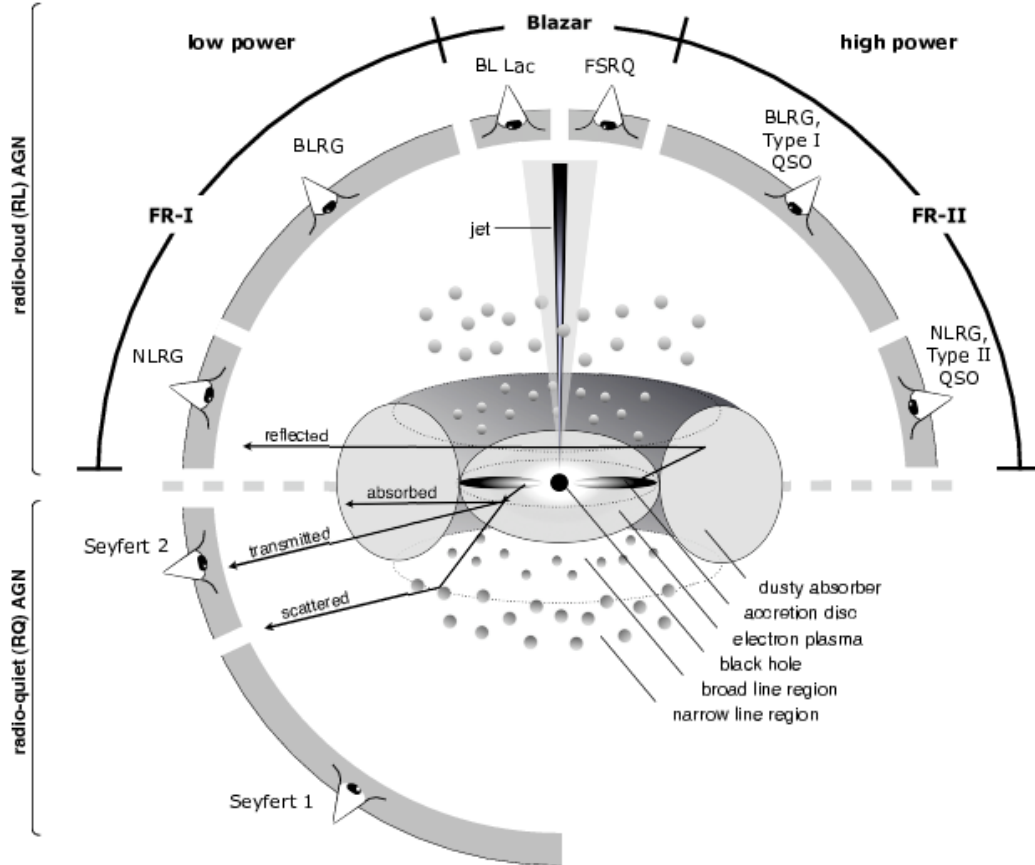


Figure 1.2: *Schematic representation of our understanding of the AGN phenomenon in the unified scheme reproduced from Singh [2014]. The type of object we see depends on the viewing angle, the presence or the absence of the jet, and the power of the central engine in AGN. Note that RL objects are generally thought to display symmetric jet emission.*

At the center of the models we find the BH. Its dimensions are defined by the spherically symmetric *Schwarzschild's solution* of the *Einstein's field equations* in the vacuum (Schwarzschild [1916]), which define the well known *Schwarzschild's Radius*, directly proportional to the BH mass (M_{BH})¹: $r_s = 2GM_{BH}/c^2$.

Under the assumption that gas around the BH is already provided with its own angular momentum, and with the caveat of *sub-Eddington regimes*, in the nearest regions

¹where G is the *Gravitational constant* and c is the speed of light.

of the BH a thin disk of material rotates around the central engine under its gravitational influence at distances of $10^{-6} pc \lesssim r \lesssim 10^{-3} pc$. Exhaustive models of accretion disks are very complex (e.g., [Abramowicz and Fragile \[2013\]](#)) but as the simplest model, we can assume the disk as a series of concentric rings with their density and at temperatures rising from the outer to the inner regions. Each ring emits according to the *Planck's law* and participates in the AGN SED with a series of black body radiation functions, each at its own temperature.

Gravitational and frictional forces compress and raise the temperature of the material by approaching the AGN, and the gas infalling participates in BH mass accretion.

Around the accretion disk, a very hot and highly ionized gas region occurs, with temperatures around $\sim 10^8 - 10^9 K$, called *Hot Corona* (“electron plasma” in [Figure 1.2](#)). This zone participates in the SED with an intense X-ray emission due to *Inverse Compton* interactions.

It is thought that this temperature and the amount of re-emitted radiation in the surrounding of the accretion disk and the hot corona, play an important role in the creation of a series of partially ionized gas structures that are formed at different distances of the central engine: the regions that emits the broad-lines (called BLR) and the narrow-lines (called NLR) defined above (e.g., [Czerny et al. \[2016\]](#) (BLR) and [Richardson et al. \[2014\]](#) (NLR)).

In regions immediately outside the accretion disk, between 1 and 10 *pc*, it is thought that dense and optically thick molecular gas rings are formed, the so called *Dusty Molecular Torus*. From the earliest theorization of the molecular torus (e.g., [Krolik and Begelman \[1988\]](#) analyzing NGC1086) and the more recent models in the literature (e.g., [García-González et al. \[2017\]](#)) it is thought that the presence of the torus just described could be reasonable, as it should have the suitable properties to reproduce the intense IR radiation that is detected in almost all the AGN.

In [Table 1.1](#) we summarized the spatial and density characteristics of the various regions we have described.

Component	Location [<i>pc</i>]	Density [cm^{-3}]
Accretion disk	$10^{-6} - 10^{-3}$	$\sim 10^{13}$
BLR	$10^{-2} - 10^{-1}$	$\sim 10^9$
Dusty Torus	1 – 10	$10^3 - 10^6$
NLR	$10^2 - 10^3$	$10^3 - 10^6$
Jets	$10^{-3} - 10^6$	– – –

Table 1.1: *Summary of the distances and the average densities of the various components of an AGN, that provides on explanation of the obsevational differences between the AGN classes based on the viewing angle.*

[Figure 1.2](#) represents what is called *Unified Model of AGN*. From the first unification models [[Antonucci, 1993](#), [Urry and Padovani, 1995](#)] the free parameters on which the models were based could be simplified to four main ones: the mass of BH and its

1.1 A brief overview of the “AGNs families”

spin, the inclination of the torus plane with respect to the line of sight and accretion efficiency on BH.

The first two parameters influence the size of the different AGN components, that decrease as both parameters increase (with important effects on the third parameter). The third parameter is the one on which the unification of the various classes of the “AGN family” is based. Assuming a inclination angle of 0° for totally edge-on galaxies, the observational characteristics of the various AGN classes are supposed to occur by changing the angle.

By considering the case of RQ-AGN, in Figure 1.2 we can see that type II Seyfert galaxies are associated to objects with edge-on tori, or to a very small angles, so that the dusty torus can obscure the BLR emission, while Seyfert I galaxies are associated to almost face-on tori.

In the case of RL-AGN, to small angles correspond NRLG, while BLRG are associated to intermediate angles, and Quasars to face-on tori.

Finally, the presence or absence of the jets allows to formulate hypotheses on the mechanisms underlying the matter accretion on the AGN, that is the fourth parameter from which we have seen that the unified model depends.

In the local Universe, AGN can be divided in others two major categories by changing the accretion efficiency on the BH (Antonucci [2012]). These categories are summarized in Figure 1.3.

The first category (Figure 1.3 (a)) consists of objects with a high efficiency of converting the potential energy of the gas accreted onto the Super Massive Black Hole (SMBH). In this model, the central BH is surrounded by a thin optically thick gas disk in which the gas rotates rapidly on Keplerian orbits. The disk shows a radial temperature gradient, which can be simplified with a series of concentric rings - at different temperatures - that emit following the black body radiation law. As a result, in the SED of these objects, a thermal continuum emission is present, called Big Blue Bump (BBB), which emerges from the extreme UV to the visible portion of the electromagnetic spectrum. As defined by in Heckman and Best [2014], we refer to this class of objects as *Radiative-mode AGN*.

The second category consists of objects that produce smaller luminosity. According to this model, reported in Figure 1.3 (b), the optically thick accretion disk does not reach the closest regions around the AGN, but it ends on larger spatial scales. An highly-ionized, optically thin gas region is created between the disk and the AGN. This region makes ineffective the accretion mechanisms on the central body and limits its luminosity. The primary energy production takes the form of two collimated cones and emitted in two opposite directions from the growth-plane. These structures are called *jets*. The mechanisms behind the jet-theory are complex and characterize their shape, intensity and orientation. We limit ourselves to note that jets can include an important source of matter that is reintroduced into the galactic environment and their presence can lead to positive and negative feedbacks in the surrounding environment (e.g., Gaibler et al. [2012], Lanz et al. [2015], Russell et al. [2017]). As we did for the previous category, we assume the same nomenclature (of Heckman and Best [2014]) and we associate to these objects the model called *Jet-mode AGN*.

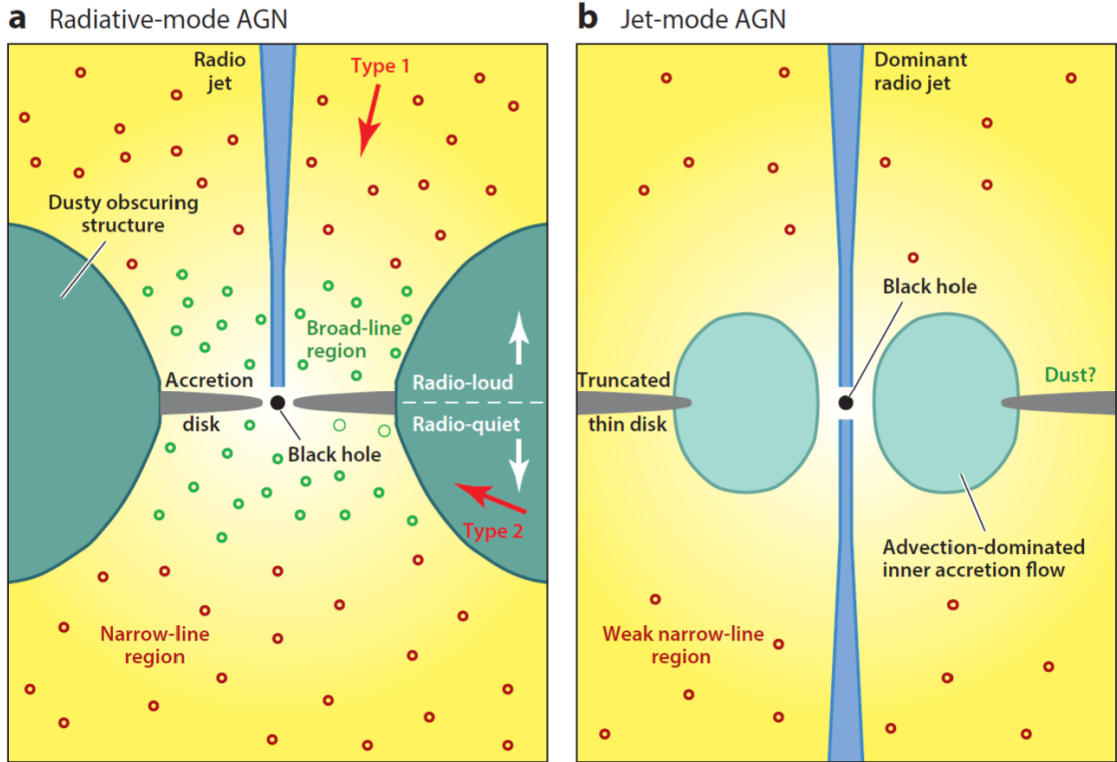


Figure 1.3: *The two main categories of AGNs model based on the accretion efficiency: (a) the Radiative-mode AGN; (b) the Jet-mode AGN. This picture is taken from Heckman and Best [2014]*

The dominance of one or the other accretion mechanism determines the presence or absence of the jet structures and allows to explain the difference between FRI and FRII galaxies.

Assuming this model exemplified in Figure 1.2, the different classification of AGN is not due to an intrinsic difference in the inner structures of these objects, but it is based on the combination of the four parameters just described.

Although the unified model is now strongly endorsed by the scientific community, it is important to emphasize that, for some of the components we have described, it has not yet been possible to obtain real detection due to angular resolution limitations.

Among the current facilities, ALMA (§3.2) is one of the most suitable instruments to undertake a morphological study of the innermost regions of the galactic nuclei, with the resolution needed to resolve the dusty and molecular tours expected to surround the BH and to be responsible for the different classes of observables.

1.2 From high-redshift observations to general properties

AGN are thought to play a major role in the formation and evolution of galaxies, providing mechanisms for feedback from the SMBH to its hosting galaxy and the intergalactic medium (see, e.g., [Fabian \[2012\]](#), [Somerville and Davé \[2015\]](#) and references therein). In co-evolutionary scenarios (e.g., [Hopkins et al. \[2007\]](#), [Lapi et al. \[2014\]](#)) SFR and SMBH properties are strictly connected, both in high redshift quasars and in local Seyfert nuclei, which are fuelled by accretion of material onto the SMBH. In the absence of major merging events and companions, as it is the case for the vast majority of local galaxies, the mechanisms that link star formation and SMBH lie in the inner galactic regions (within ~ 1 kpc from the BH) and are thought to be responsible for the feeding of the BH and the halting of the star formation through feedback mechanisms from the BH itself. The association of the BH growth with star formation is supported by the fact that most of the BH growth occurs in type 2 AGN and is obscured by dust. However, the picture is complicated by the fact that the processes that drive inflows of gas towards the center are not univocally identified and seem to depend strongly on the scale considered. At kiloparsec scale, stellar bars are the most robust and efficient instabilities, constituting preferential directions of infall of the material towards the centre, possibly triggered by galaxy interactions. At the edges of the bars, shock fronts and dense dusty star forming regions are not unusual as result of the sudden change of direction of the spiralling infalling material. Similarly, it is not uncommon to identify dynamically decoupled bars on different angular scales with overlapping dynamical resonances ([Combes et al. \[2013\]](#) and reference therein). In fact, on smaller scales, secondary nuclear bars seem to proceed from the primary bars, and on ~ 10 - 100 pc scales, nuclear disks become unstable. On even smaller scales the clumpiness of the interstellar medium (e.g., dynamical friction and viscous torques due to turbulence) starts to play a major role.

1.2.1 The SFR history across the Universe

The origins and evolution of galaxies are among the most intriguing and complex chapters in the formation of the cosmic structure. The astrophysical observations in this field of research have accumulated at a surprising pace.

Ideally, an in-depth understanding of the evolution of galaxies will include the full sequence of events that led to the formation of the first stars after the end of cosmic dark ages at today's diversity of shapes, sizes, masses, colors, brightness, metallicity and clustering of galaxies.

In order to answer these questions and solve the problem, new and interesting methodologies have been taken into account in recent years: one method focuses on the output properties of the galactic population as a whole, traces the evolution with cosmic time of the galaxy density from the far-UV (FUV) to the far-infrared (FIR), and offers the prospect of empirical determination of the global history of the formation of stars and

the production of heavy elements of the Universe, regardless of the complex evolutionary phases of the individual sub-populations of galaxies.

The modern version of this technique is based on some fundamental properties of stellar populations and dusty star forming galaxies (by [Madau and Dickinson \[2014\]](#)):

- The UV continuum emission in all the oldest galaxies is dominated by short-lived massive stars. Therefore, for a given initial mass function (IMF) and dust content, it is a direct measure of the instantaneous star formation rate density (SFRD).
- The rest-frame near-infrared (NIR) light is dominated by quasi-solar-mass evolved stars that constitute the majority of the mass of a starburst galaxy and can therefore be used as total Stellar Mass Density (SMD) tracers.
- Interstellar dust preferentially absorbs UV-radiation and re-emits it in thermal IR, so that the FIR emission of dusty starburst galaxies can be a sensitive trace of young star populations and SFRD.

Understanding how SFR evolves over time, how the galaxies could influence the mechanisms and the speed at which the stars are formed and reveal how galactic environment has an influence in solving this problem, are still open questions for modern astrophysics. To shed light on this issue, a large number of direct observations are needed on how SFR changes over time in the statistically complete samples that we are detected in the Universe.

Unfortunately, to study the evolution of SFR, it is necessary to use other observable properties of the galaxy as the luminosity in a generic band (which to simplify we will call “Y”), as SFR is not directly detectable. It is therefore possible to obtain the SFR using the general form in which the two quantities are bound:

$$SFR_Y [M_\odot yr^{-1}] = c L_Y [erg s^{-1}] \quad (1.2.1)$$

Numerous results can be found in the literature that define the value of the constants c (e.g., [Kennicutt \[1998a,b\]](#)), connecting the SFR to the galaxy luminosity in a given band.

Once we understand how to obtain the SFR from the direct study of a galaxy observable quantity, we need to understand how the observable value changes with time, in order to have an idea of how the luminosity associated with it changes and, consequently, how the corresponding SFR is changing as well. To do this, the *Luminosity Functions* (LF) are used.

Given a sample (S), the LF ($\phi_S(L)$) defines the number of galaxies per unit of luminosity per volume unit. If for the same type of objects, we could construct complete samples at different redshifts, we can reconstruct the LF of each sample and then describe how the number of objects per unit of luminosity and unit of volume changes with changing redshift (see [Figure 1.4 \(left\)](#)).

1.2 From high-redshift observations to general properties

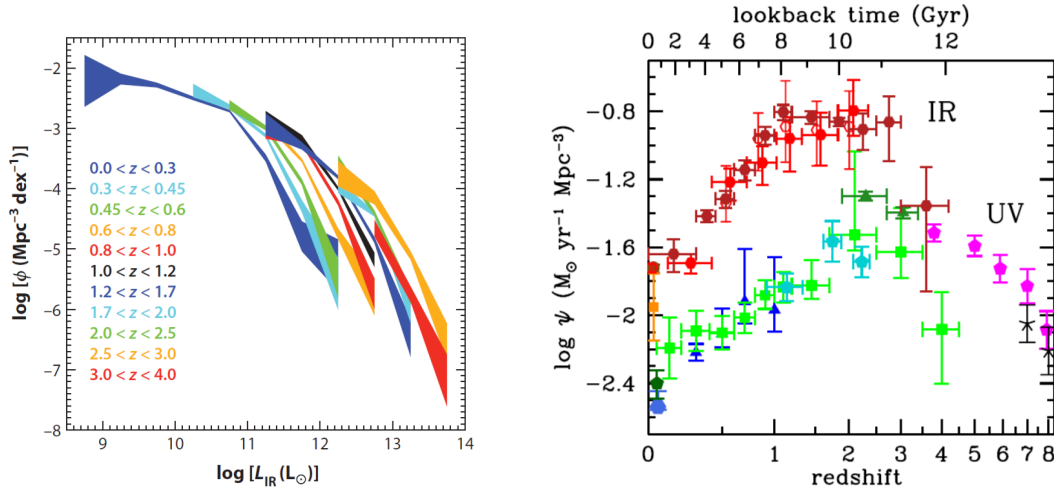


Figure 1.4: (**left:**) Evolution of the total infrared (8-1000 μm) LF. Image is from [Lutz \[2014\]](#), in which the results obtained from [Gruppioni et al. \[2013\]](#) are reported. The width of the band indicates the $\pm 1\sigma$ Poissonian error; (**right:**) SFR densities in the FUV (uncorrected for dust attenuation) and in the FIR. All UV and IR luminosities have been converted to instantaneous SFR densities using the factors $c_{\text{FUV}} = 1.15 \times 10^{-28} [M_{\odot} \text{ yr}^{-1} \text{ erg}^{-1} \text{ s Hz}]$ and $c_{\text{IR}} = 4.5 \times 10^{-44} [M_{\odot} \text{ yr}^{-1} L_{\odot}^{-1}]$ valid for a Salpeter IMF.

The data points with symbols correspond to the different surveys used in [Madau and Dickinson \[2014\]](#). FUV points: [Wyder et al. \[2005\]](#) (blue-gray hexagon); [Schiminovich et al. \[2005\]](#) (blue triangles); [Robotham and Driver \[2011\]](#) (dark green pentagon); [Cucciati et al. \[2012\]](#) (green squares); [Dahlen et al. \[2007\]](#) (turquoise pentagons); [Reddy and Steidel \[2009\]](#) (dark green triangles); [Bouwens et al. \[2012a,b\]](#) (magenta pentagons) and [Schenker et al. \[2013\]](#) (black crosses). IR points: [Sanders et al. \[2003\]](#) (brown circle); [Takeuchi et al. \[2003\]](#) (dark orange square); [Magnelli et al. \[2011\]](#) (red open hexagons); [Magnelli et al. \[2013\]](#) (red filled hexagons) and [Gruppioni et al. \[2013\]](#) (dark red filled hexagons).

For each redshift, the integral:

$$L_{tot>(> L) = \int_L^\infty \phi_z(L') L' dL' \quad (1.2.2)$$

provides the averaged luminosity density of the sample. Finally, by using the correct (or the most suitable) form for eq. 1.2.1, we could obtain the SFRD for each redshift bins.

In the recent decades, many works have followed this process to estimate the trend of SFRD through the universe. An example can be found in the work by [Madau et al. \[1998\]](#), who collected from the literature the SFRD from a large number of samples at different redshifts, obtained from UV to IR surveys.

As we have already emphasized, IR and UV radiations are generated by two different physical processes: UV emission allows direct SFR detection as it is generated by the spectral contribution of massive young stars to the total galaxies spectra. ON the contrary, IR emission does not directly trace the radiation generated by the young stars, but is produced by the reprocessing of that radiation by the dust, absorbing the UV light and re-emiting it at IR wavelengths.

Figure 1.4 (*right*) shows the different results obtained by deriving the SFRD from UV or IR surveys: the UV results are clearly depressed, due to significant dust extinction. In the contrary, IR results are not affected by obscuration and show the amount of the correction one needs to consider when using optical/UV data to derive the SFRD. At $z > 3$ poor IR coverage exist and our knowledge of the SFRD must rely on UV data only.

Although galaxies with lower SFR may have reduced by extinction, purely UV-selected samples at high redshift may also be biased against dusty star-forming galaxies. Unfortunately, a robust census of star-forming galaxies at $z \gg 2$ selected on the basis of dust emission alone does not exist, due to the sensitivity limits of past and present FIR and submillimeter observatories. Therefore, the total amount of star formation that is missed from UV surveys at such high redshifts remains uncertain.

1.2.2 The massive Black-Holes accretion History

In recent years, the close link between AGN and host galaxies has been the subject of numerous studies. Numerous relationships have been found connecting the BH-mass (M_{BH}) to different galactic physical parameters.

Most famous examples of these relationships can be the Ferrarese and Merritt [2000] [$M_{BH}-\sigma_c$] and Häring and Rix [2004] [$M_{BH}-M_{bulge}$] relations, showing the connection between M_{BH} and the star velocity dispersion in the central galaxy regions (σ_c) and between M_{BH} and the galactic bulge mass (M_{bulge}).

At the same time, it is not yet entirely clear whether these relationships can be applied indiscriminately at any redshifts, how tight they were at the time of the formation of galactic structures and whether/how they evolved over time.

The study of how these relationships change through the Universe is still an open question. For our purposes, we are interested in understanding how the evolution of AGN can be related to the evolution of their host galaxies.

In this regard, in a recent work Mullaney et al. [2012] try to obtain the *BH accretion rate* ($\dot{M}_{BH}(M_*, z)$) from the observed bolometric luminosity (L_{bol}). The authors takes L_{bol} of the AGN as an indicator of they BH accretion rate ($L = \epsilon c^2 \dot{M}_{BH}$). The bolometric luminosity is obtained from the X-ray luminosity (2-10 keV).

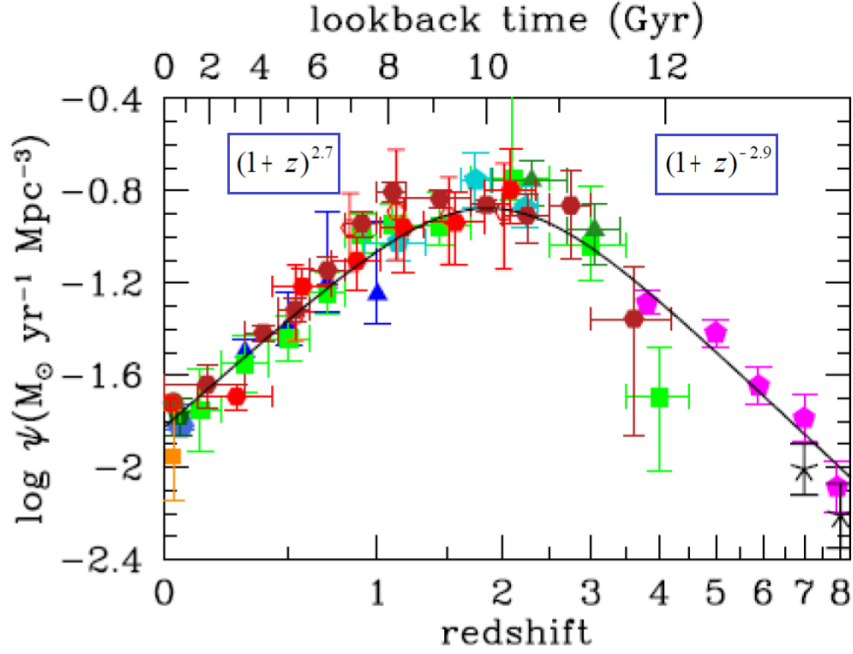
Under these assumptions, the relationship they find is:

$$\dot{M}_{BH}(M_*, z) = \frac{1 - \epsilon}{\epsilon c^2} L_{bol}(M_*, z) \quad (1.2.3)$$

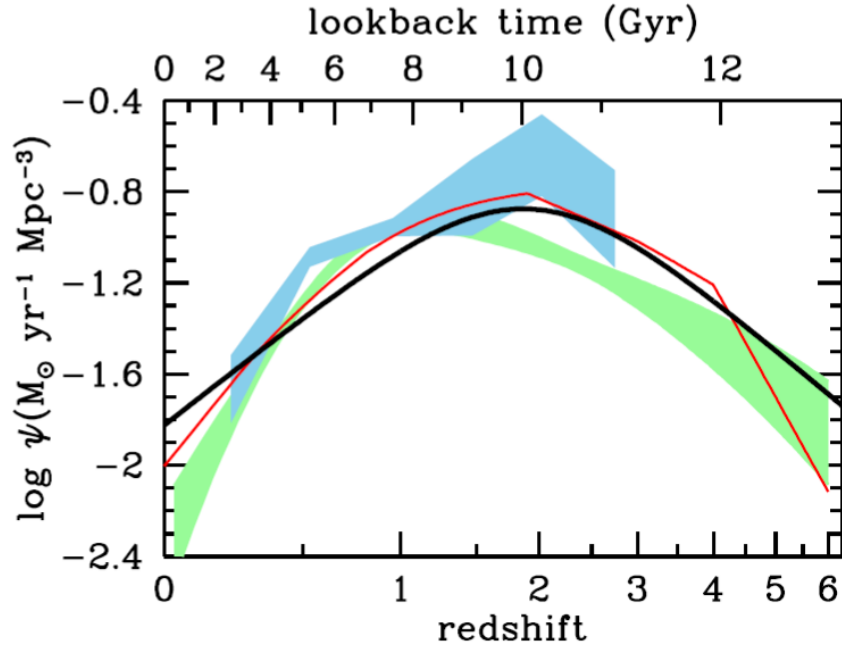
where ϵ is the *conversion efficiency* by which mass is converted into radiated energy via the accretion process (here assumed as $\epsilon = 0.1$) and c is the speed of light. This approach has been applied to many works, whose results are shown in Figure 1.5 (b). Delvecchio et al. [2014] derived for the first time the BHARD from the IR (i.e. *Herschel*, see blue coloured area in Figure 1.5 (b)), finding a very good agreement with optical/X-ray results, though with much smaller bolometric corrections and no assumptions about the obscured AGN fraction.

The Figure 1.5 may be exploited to understand the bond between SFRD and BHARD over time. Both functions show an intensity peak around $z \sim 2$ and a similar pattern by increasing z . Viewed in parallel, the two quantities seem to follow the same evolution, as if they were closely connected to each other.

However, the mechanisms with which BHs accrete matter and influence star formation are still open questions. The following paragraph summarizes the state of the art on this specific topic.



(a) Cosmic history of SFRD from both FUV (corrected for extinction) and IR data, as collected by *Madau and Dickinson [2014]* (this plot combines the data shown in the right panel of Figure 1.4).



(b) BHAR density as a function of redshift from different wavelength data: the best-fit function by *Madau and Dickinson [2014]* (solid black line) and the BHARD from different works (*Shankar [2009]*, solid red line; *Aird et al. [2010]*, light green shading; *Delvecchio et al. [2014]*, light blue shading).

Figure 1.5: Plots are taken from *Madau and Dickinson [2014]*: see captions for more details.

1.3 The Black Holes fueling

To understand the reason of the similar behaviour of the SFRD and the BHARD, it is necessary to study the mutual influence of the SF and the accretion processes in objects containing both phenomena. In order to do this and to understand the physics at play, we need to study the innermost parts of galaxies, where we could observe the effects of the BH on the surrounding material.

The study of the mechanisms with which BHs accretes matter is a very active field of research. Unfortunately, this aspect of research is strongly conditioned by the angular resolution limits of our telescopes. The impossibility of spatially resolving the internal regions of the dusty torus prevent any direct tests of the theoretical models.

Gültekin et al. [2009] recently found a relation between the radio luminosity (L_R), the X-rays luminosity (L_X) and the black hole mass (M_{BH}) in AGN:

$$\log\left(\frac{L_R}{\text{erg s}^{-1}}\right) = (4.80 \pm 0.24) + (0.78 \pm 0.27) \log\left(\frac{M_{BH}}{M_\odot}\right) + (0.67 \pm 0.12) \log\left(\frac{L_X}{\text{erg s}^{-1}}\right) \quad (1.3.1)$$

referred to as the *Fundamental Plane of black hole activity* (BHFP).

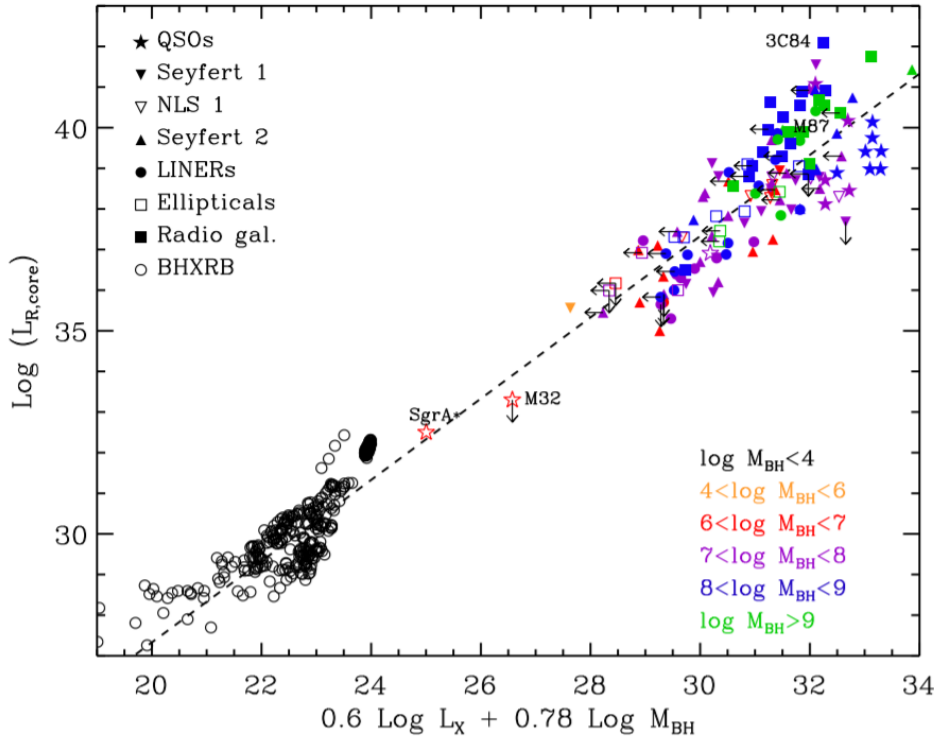


Figure 1.6: **Fundamental Plane of black hole activity:** the correlation extends over many decades of BH mass and accretion luminosity, and includes many different source types: X-ray binaries (empty black circles) and various classes of AGNs (colored points). The plot is taken from Yuan and Narayan [2014].

Figure 1.6 shows the expected results from equation (1.3.1).

The close relationship, valid for both X-ray binaries and AGN, suggests that the growth mechanisms of X-binaries and AGN may be very similar. In particular, for X-ray binaries two principal cases are recognized:

- **A low-hard state:** dominated by low luminosity and hard X-ray emission with the presence of low-power radio jets.
- **A High-soft state:** characterized by high-luminosity thermal X-ray component with the features of a standard geometrically thin, optically thick accretion disk.

The main difference between these two states is observed to be the accretion rate on the BH relative to the *Eddington rate*. To the low-hard state is associated an accretion rate below a few percent of the boundary imposed by Eddington's limit, whereas to the high-soft state arises when the accretion rate exceeds that value.

In the first part of this chapter, we presented the two main categories of AGNs (the radiative-mode AGN and the jet-mode AGNs); we explained how the two models differ because of the different growth efficiency due to the different processes that made up the nearest regions of AGN.

The mechanisms responsible for the relationship between AGN and host galaxy and the fuelling of AGN can be summarized in the following two points:

1. **Mergers and interactions:**

This idea has long been the basis of theoretical modelling (e.g.; [Kauffmann and Haehnelt \[2000\]](#); [Hopkins et al. \[2008\]](#)). Moreover, the difficulty of succeeding in observing these phenomena is the most difficult step for this hypothesis.

Two major observational tests can be done: the first involves the measure of the incidence of close companion galaxies, the second being based on the determination of the morphological structure of their host galaxies.

[Li et al. \[2008a\]](#) used the amplitude of the cross-correlation function in order to study the merging hypothesis through the first test. They found that on scales less than 100 kpc, there is a strong dependence of the cross-correlation function to the *Specific Star Formation Rate*² (here after, sSFR): their conclusion is that merging triggers SF-phenomena but this does not involve the ignition of nuclear activity [[Li et al., 2008b](#)].

The other test is to consider the morphology of galaxies (through the analysis of the light brightness distribution) in order to evaluate a sort of connection between nuclear activity and the asymmetry of nuclear zones. This kind of approach was dealt with by [Reichard et al. \[2009\]](#): they say that, although galaxies with intense nuclear activity show a remarkable asymmetry in the distribution of brilliance, this is also demonstrated by galaxies with inactive nuclear activity. This suggests that the presence of cold gas in the central region of a kpc scale (seen as a result of a recent fusion) is a necessary but not sufficient condition

²Define as the ratio between the Star formation rate and the total galaxy stellar mass: $sSFR = SFR/M_*$.

1.4 Possible SF-AGN phenomena connections

to further boost the growth of BHs. Although many jobs support a direct link between merging phenomena and triggering AGN activity. [Reichard et al. \[2009\]](#) conclude that other processes are subsequently required to deliver the gas from scales of a few kpc all the way to the black hole accretion disk and these would not be directly related to the process(es) that produced asymmetry in the distribution of brilliance.

We can conclude that although the phenomenon of merging is certainly important to triggering the AGN activity, many of the AGN analysed in the local universe do not present the need for major-mergers or strong interactions with companions. in the absence of these interactions, other mechanisms are needed to facilitate the AGN activity.

2. Secular evolution:

The loss of gas angular momentum can guide the slow secular evolution from the outer regions to the galactic nuclei and influence the fuelling of BH. In [Kormendy and Kennicutt \[2004\]](#), the authors discuss how secular evolution can be considered as the basis for the formation of the pseudo-bulges. Following this path, we should expect to find the fastest AGN growing within pseudo-bulges or in strongly barred galaxies (this because the presence of the bars and the study of the gas dynamics within them are one of the mechanisms for the development of radial motions and for their guidance; [Shlosman et al. \[1990\]](#)).

Unfortunately, the level of knowledge we have today does not allow us to come to a safe view of these mechanisms. The conclusions on this are contradictory: recent studies do not show obvious connections between the selected samples and the dominance of secular evolution as the main fueling mechanism for AGN. This evolution is still a mystery to be revealed.

1.4 Possible SF-AGN phenomena connections

The mechanisms described in the previous paragraph, besides providing the material for the BH accretion and driving the AGN activity, have other important feedbacks on the galactic environment. Both processes are seen as means for triggering star-formation. Indeed, [Kormendy and Kennicutt \[2004\]](#) show that in the innermost regions of the galactic bulge, where the gas is slowly accumulated due to secular evolution, the density grows to the point of favouring star-formation.

At the same time, hydrostatic simulations (e.g. [Bischko et al. \[2015\]](#), [Renaud et al. \[2015\]](#), [Steinhauser et al. \[2016\]](#)) show that mergers and interactions can favour the triggering of star formation phenomena by dissipative processes and ram pressures.

What is the dominant mechanism between the two, if they alternate over time to guide the global evolution of galaxies, and if there are preferential spacial scales on which a mechanism is dominated by the other, are still open questions. In any case, an appearance is now clear: the connection of star formation to the same processes that drive the fuelling of AGNs implies a possible connection between these two phenomena.

Rosario et al. [2012] studied the link between the SFR and AGN accretion luminosity by connecting the far-infrared (FIR) luminosity and the X-ray luminosity (linked to the AGN activity) for a sample obtained from three survey fields (GOODS-South, GOODS-North and COSMOS). The study covers nearly 4.5 orders of magnitude in AGN luminosity, in a range of redshift between of $z = 0$ and $z = 2.5$ (see Figure 1.7).

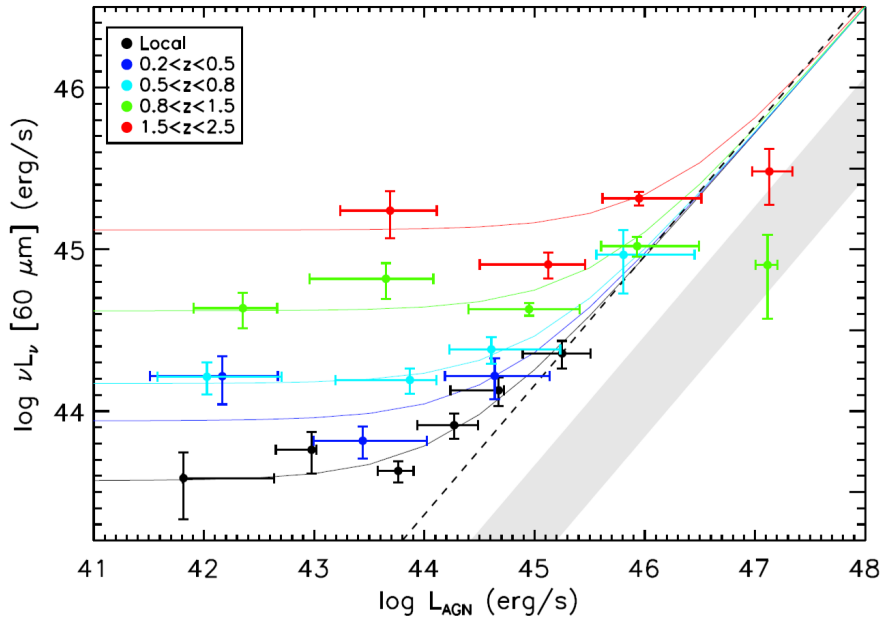


Figure 1.7: *SF luminosity (L_{60}) versus AGN luminosity ($\sim L_X$) for an X-ray selected AGN in 5 different redshift bins, from the local Universe to $z = 2.5$. The coloured data points are a combinations of measurements in 3 fields of the PACS Evolutionary Probe (PEP) program: GOODS-North, GOODS-South and COSMOS, while the black data points are from the Rosario et al. [2012] analysis of the SWIFT BAT sample. The solid coloured lines are the best-fit functions. The dashed line is the correlation line shown by AGN-dominated systems in Netzer (2009). The shaded region corresponds to the approximate 1σ range exhibited by empirical pure-AGN SEDs. The image is taken from Rosario et al. [2012].*

As result, this study shows that the link between SFR and AGN activity depends essentially on the AGN luminosity (at fixed redshift), with a slope that changes from low to high AGN luminosity, announcing a sort of dichotomy between the mechanisms that guide this relationship. This dichotomy is slowly flattened as the redshift grows. For $z < 1$ two distinct behaviours are recognized:

- **For $L_X \gtrsim 10^{44} \text{ erg s}^{-1}$:** the nuclear activity closely tracks the bulk of star formation. The authors interpret this behaviour as evidence for the importance of gas-rich major mergers in fueling high accretion phases in AGNs at these redshifts, consistent with the results of modern hydrodynamic simulations.
- **For $L_X \lesssim 10^{44} \text{ erg s}^{-1}$:** this connection slowly fades and until the complete independence of the two processes. Black hole fuelling in these systems is probably

1.4 Possible SF-AGN phenomena connections

dominated by secular processes related to gas inflow and momentum transfer in galaxy disks and is unrelated to the overall growth of the host.

This double behaviour decreases with increasing redshift (for $z > 1$): this implies that BH accretion and galaxy evolution could be increasingly disconnected from each other and that at higher redshift would be other processes that connect nuclear activity to SF. Recently, [Lanzuisi et al. \[2017\]](#) analyses the same problem from another perspective. The results of [Rosario et al. \[2012\]](#), in fact, seek a functional relationship between SFR and AGN activity starting from a redshift-binned sample and obtaining each point of Figure 1.7 in L_X bins.

Therefore, we might ask if the same results would be obtained by getting the points in L_{IR} bins. This is exactly the approach followed in [Lanzuisi et al. \[2017\]](#), in which the authors selected a sample of 692 X-ray and FIR detected sources selected from *Chandra*, *XMM-Newton* and *Herschel* observations. Tanks to the large sample collected, they could divide it in five redshift bins, from $z = 0.1$ to $z = 4.0$, with a large number of sources per bin ($\sim 60 - 180$). The results of their studies is reported in Figure 1.8.

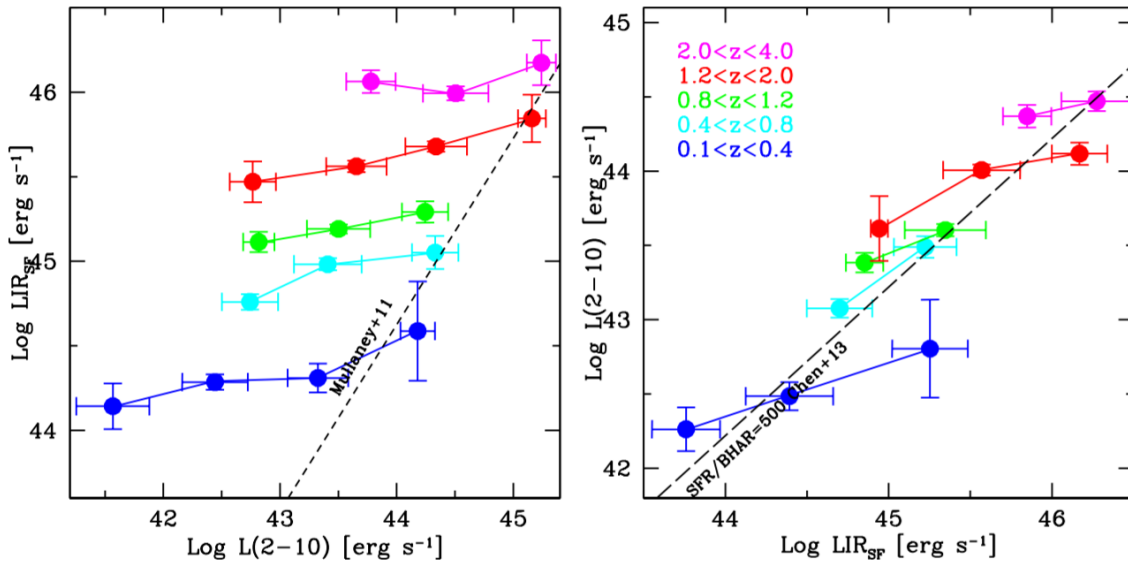


Figure 1.8: **left panel:** averaged IR luminosity computed only for the SF ($\text{Log}(L_{IR}^{SF})$) in bins of $\text{Log}(L_X)$ both in logarithmic scale. The L_{IR}^{SF} was calculated by subtracting the AGN contribution calculated with a SED decomposition template by [Fritz et al. \[2006\]](#). The short dashed line is the correlation derived in [Mullaney et al. \[2011\]](#) for the pure AGN SED; **right panel:** averaged $\text{Log}(L_X)$ in bins of $\text{Log}(L_{IR}^{SF})$. The long dashed line represents a constant SFR/BHAR of 500, from [Chen et al. \[2013\]](#). Redshift bins are shown on the top left. In both panels the vertical error bars are computed through a bootstrap resampling procedure, while the horizontal error bars show the 1σ dispersion of those bins.

Focusing on the left panel of Figure 1.8, we can recognise the same trend found by Rosario et al. [2012]. The points with $L_X \lesssim 10^{44} \text{ erg s}^{-1}$ do not show a correlation, indicating a sort of independence between the SF and the AGN processes. On the other hand, computing average $\text{Log}(L_X)$ in $\text{Log}(L_{IR}^{SF})$ bins, from the same distribution, gives different results (see right panel in Figure 1.8). At all redshifts, the average L_X correlates with the L_{IR}^{SF} and the binned points are close to the SFR/BHAR ~ 500 ratio found in Chen et al. [2013], suggesting a close connection between the two processes to which the luminosities are linked. The exact value of the ratio SFR/BHAR in terms of L_X and L_{IR}^{SF} depends strongly on the assumptions made to scale between these quantities, i.e. the accretion efficiency and bolometric correction in the first case, and the SF law and IMF in the second.

A possible physical explanation for the behaviour shown in Lanzuisi et al. [2017] is that, when looking at left panel of Figure 1.8, we are averaging a slowly changing quantity, such as the host SFR, grouped on the basis of the rapidly changing AGN L_X . In the right panel, instead, the average L_X of a large sample of sources grouped on the basis of the slowly changing SFR, allows us to recover the underlying, long term correlation between AGN activity and SFR.

The described scenario, therefore, is very complex and intriguing because it requires the ability to analyse large galaxy samples (to minimize fluctuations in AGN activity due to spurious accretion events) and increasing redshifts (to obtain a more general picture of the evolution of this report). The importance of studying this link by analysing a large sample of local galaxies is therefore crucial, as supported by the possibility to directly resolve the central regions of the galaxy, where these phenomena are likely to be linked.

In recent years, outflows of either ionised or molecular gas from the SMBHs have been observed and considered responsible for halting the gas infall and the SF in the inner galactic regions (e.g., Cicone et al. [2014], Feruglio et al. [2010], Harrison et al. [2016]). Fuelling of the SMBH and outflows from it seem to constitute the self-regulating combination of processes on the small angular scales responsible of the morphology and dynamics of the whole galaxy.

The co-existence of such different processes, how the small scales dynamics influences the overall galaxy morphology, the time-scale on which different processes happen, and if different evolutionary stages justify the different observed morphologies are still open questions. These processes can now be investigated thanks to the unprecedented sensitivity and resolution of the *Atacama Large Millimetre Array* (ALMA), with the observation of CO molecule transitions in local Seyfert galaxies offering the possibility of directly witnessing the molecular gas fuelling towards the nucleus, thus allowing for the first time a thorough knowledge of the accretion process in the innermost regions of AGN (i.e., on pc scales from the nucleus; see, e.g., García-Burillo et al. [2016]).

In this thesis, we perform a pilot study on a single object, to provide the guidelines for a future study to be applied to a complete sample of local galaxies. This kind of investigation could help to highlight the mechanisms that guide the interconnection

1.4 Possible SF-AGN phenomena connections

between SF and AGN-related phenomena, by exploring unprecedented small scales around the AGN.

This approach would clarify (with the constraint of a complete sample) the scenario for objects with $L_X \lesssim 10^{44} \text{ erg s}^{-1}$.

In the hypothesis of having complete samples at higher redshifts, the natural evolution of this work would be to investigate this relationship when the connection between SF and AGN activity is getting less stringent (i.e., a high z and low luminosities).

Chapter 2

NGC 5135: a peculiar Galaxy

Abstract

Luminous IR galaxies are found in the local Universe, but are responsible for the bulk of the SFRD at higher redshifts, with their importance rapidly increasing from $z \sim 0$ to $z \sim 2$. In the local Universe they are strongly star-forming galaxies, often hosting an AGN at their centres.

High resolution observations of this class of objects therefore allow to study the regions where AGN and SF influence each other.

In the first paragraphs of this chapter we present a summary description of the Luminous Infrared Galaxies, while in the final part we concentrate on one of them, NGC 5135, on which this thesis work is based. We also summarize the principal observations of this object found in the literature.

2.1 Luminous Infrared Galaxies

The opacity of the Earth’s atmosphere prevents observation of the dust rich galaxies from the ground, as most of the IR-component of their spectra are strongly absorbed by the atmospheric gas. This limitation forces us to find an alternative way to directly investigate these objects, by using external satellites that do not suffer from this atmospheric absorption.

The first survey at mid-IR (MIR) and far-IR (FIR) wavelengths was performed by the *Infrared Astronomical Satellite* (IRAS) at the beginning of ’80s (Pouw [1983]). The survey was able to scan almost 95% of the whole projected sky at wavelengths from 10 to 100 μm , with a sensitivity close to the limitation set by the zodiacal background fluctuations (Neugebauer et al. [1984]). The project allowed the detection of tens of thousands of galaxies, the vast majority of which were too faint to have been included in previous optical catalogues.

These new objects were subsequently grouped based on their integrated luminosity in IR-band, from 8 to 1000 μm ($L_{IR(8-1000\mu m)}$):

- *Luminous Infrared Galaxies* (**LIGs**)
 $10^{11} L_{\odot} < L_{IR(8-1000\mu m)} < 10^{12} L_{\odot}$
- *Ultra-Luminous Infrared Galaxies* (**ULIGs**)
 $10^{12} L_{\odot} < L_{IR(8-1000\mu m)} < 10^{13} L_{\odot}$ (Houck et al. [1985])
- *Hyper-Luminous Infrared Galaxies* (**HyLIGs**)
 $10^{13} L_{\odot} < L_{IR(8-1000\mu m)} < 10^{14} L_{\odot}$ (Cutri et al. [1994])
- *Extreme-Luminous Infrared Galaxies* (**ELIRs**)
 $L_{IR(8-1000\mu m)} > 10^{14} L_{\odot}$ (Tsai et al. [2015])

In the Local Universe, the trigger for the intense infrared emission appears to be the strong interaction/merger of molecular gas-rich spirals, whose probability increases with the increase in IR-luminosity, up to 90% in the more luminous samples (e.g., Clements et al. [1996], Lawrence et al. [1989], Veilleux et al. [2002])

The morphological classification varies according to IR luminosity: most of the galaxies with $L_{IR(8-1000\mu m)} < 10^9 L_{\odot}$ appear to be Early-type and S0 galaxies (Rieke and Lebofsky [1986]), while for higher luminosities ($L_{IR(8-1000\mu m)} > 10^{10} - 10^{11} L_{\odot}$), nearly all the sources were Sb or Sc galaxies (Sanders and Ishida [2004]).

These objects reaching the highest infrared luminosities (over LIRGs) show an extraordinary amount of molecular gas in their central regions (Daddi et al. [2010]).

Single-dish observations of CO and 21-cm line of HI molecular transitions are now present for most of objects of the IRAS *Bright Galaxy Survey* (BGS). The most IR luminous sources showed very broad H I absorption lines, indicating rotation plus large amounts of unusually turbulent neutral gas (Mirabel [1982]). Measurements of CO emission have demonstrated that nearly half of the CO mass in LIGs is contained within the central regions, $r < 0.5 - 1$ kpc, after as much as $10^{10} M_{\odot}$, and reaching mean surface densities of $10^4 M_{\odot} pc^{-2}$ in the central regions (Downes and Solomon [1998], Bryant and Scoville [1999]).

The results of the spectral classification of a complete sample of LIGs/ULIGs, obtained through optical spectroscopy (using several emission-line ratio diagnostic) is shown in Figure 2.1 (Sanders and Ishida [2004], Veilleux et al. [1999]).

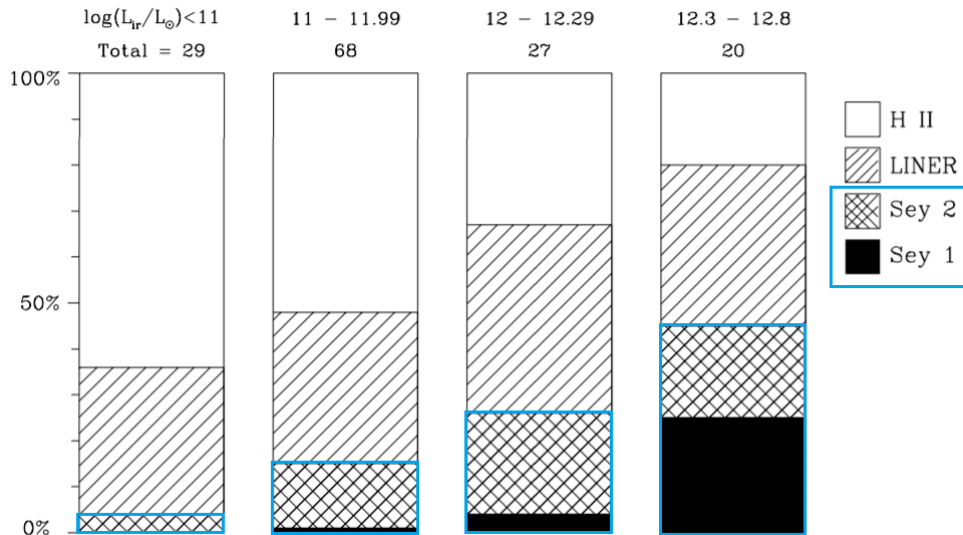


Figure 2.1: *Optical spectral classification of LIGs as a function of IR luminosity (top panel) from the IRAS-BGSs and 1 Jy sample of ULIGs (Veilleux et al. [1999]). The fraction of Seyfert galaxies grows from $\sim 4\%$, for IR fainter objects ($\log(L_{IR}/L_{\odot}) < 11$), to $\sim 50\%$ for objects with $\log(L_{IR}/L_{\odot}) > 12.3$.*

The total mass of molecular gas seems to play a key role in the genesis of LIGs (Gao and Solomon [2004]). Because of heavy dust obscuration, it is hard to distinguish the relative roles of starburst and AGN activity. Nonetheless, these conditions seem to be clearly optimal to fuel the enormous nuclear starbursts (Elbaz et al. [2011], Lutz et al. [1999]) as well as to build and/or fuel a central AGN; this makes them perfect candidates for the separate study of these phenomena and their hypothetical mutual influence.

A $12\text{-}\mu\text{m}$ flux-limited sample of 893 galaxies was selected from the IRAS *Faint Source Catalogue Version-2* (FSC-2), by Rush et al. [1993], considering all FSC-2 objects with $12\text{-}\mu\text{m}$ fluxes >0.22 Jy (hereafter 12MGS). Part of this sample had already been optically selected by Hewitt and Burbidge [1991], Spinoglio and Malkan [1989], Veron-Cetty and Veron [1991], thus forming a sample of 116 IR-selected AGN (51 Seyfert 1s or quasars, 63 Seyfert 2s and 2 blazars).

Recently, Gruppioni et al. [2016] have collected the multi-wavelength photometric data for a sub-sample of 76 Seyfert galaxies from the 12MGS galaxy sample, selected for having available Spitzer-IRS and literature mid- and far-IR spectroscopic data. The sample, incomplete for statistical studies, can be considered as representative of the parent survey catalogue. The photometric data available in the literature – from the radio to the X-ray band – allowed for this sample a detailed SED decomposition (see §2.2). Including the contribution of stars, re-emission from dust in star forming

2.1 Luminous Infrared Galaxies

regions and from a AGN dusty torus, the SED analysis provided precise measurement of the main properties of the AGN and its host galaxy, like, e.g., the AGN bolometric luminosity, the SFR, the total IR luminosity (L_{IR}), and the stellar mass (M_*).

For a few of these nearby Seyfert galaxies sub-mm/mm continuum and spectroscopic observations with ALMA are starting to become available.

For one of them, NGC 5135, ALMA data were available in the archive in two bands (either continuum and CO lines): band 6 (~ 1.2 mm) and band 9 (~ 0.46 mm). In this thesis work, we present the ALMA data, and discuss possible interpretation of the resulting complex morphology and dynamical structure of this galaxy. To this purpose, we considered the available ~ 100 pc resolution ALMA band 6 (B6) and band 9 (B9) observations of the dust continuum emission, the spectroscopic maps of two CO transitions (tracers of molecular mass in star forming and nuclear regions) and of a CS transition (tracer of the densest star forming regions) combined with the outcome of the SED decomposition (see § 5).

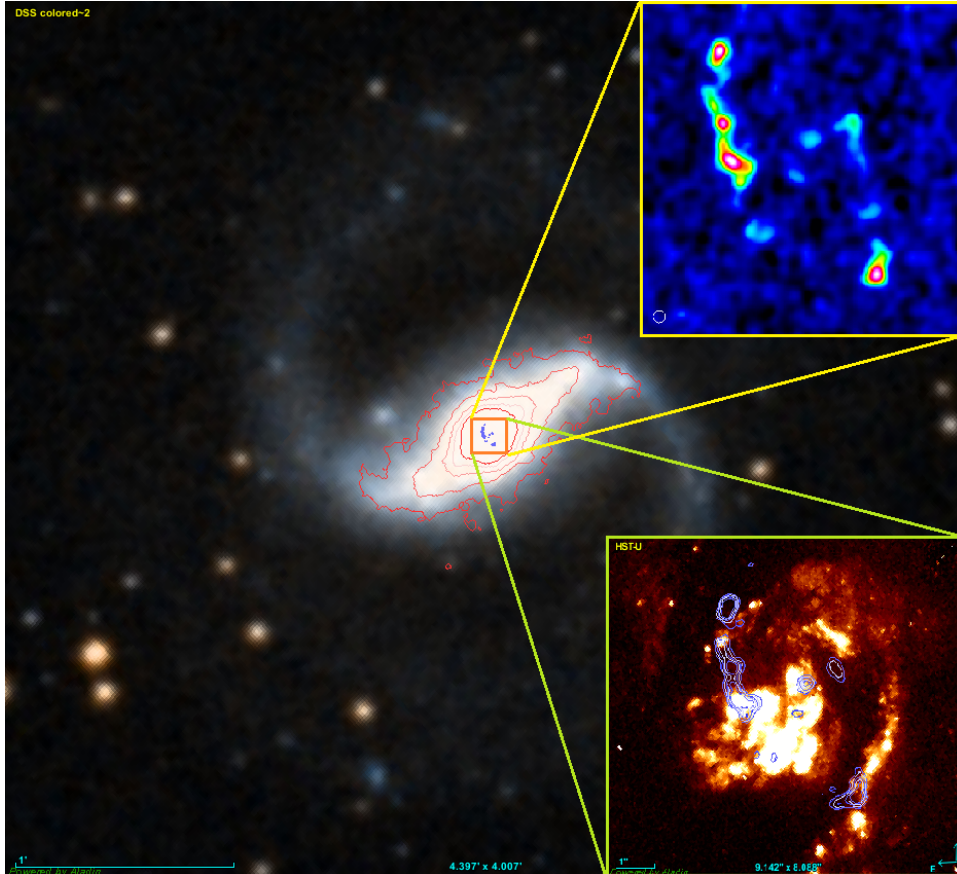


Figure 2.2: *Optical DSS image, with overlaid contours from 2MASS (red) and ALMA B9 (blue, center). The top right insert shows a zoom of the ALMA B9 continuum image, while the bottom right one shows the ALMA contours overlaid to the HST (F606W filter) image by González Delgado et al. [1998].*

2.2 NGC 5135

NGC 5135, a nearby galaxy at $z=0.013693$, was first selected by Phillips et al. [1983] as part of a sample of 23 nearby high-excitation emission-line galaxies, from the original catalogue of 719 bright galaxies by Sandage [1978]. It was then classified as a Seyfert 2 by Véron-Cetty and Véron [2006] based on the $[\text{O III}]\lambda 5007/\text{H}\beta$ and $[\text{N II}]\lambda 6584/\text{H}\alpha$ line ratios (*BPT diagram* from Baldwin et al. [1981]; see § 2.2.3). From its L_{IR} ($\log(L_{\text{IR}}/L_{\odot})=11.17$), NGC 5135 was then classified as a LIG by Sanders et al. [2003].

Its *Digitized Sky Survey* (DSS) image is shown in Figure 2.2, with overplotted our ALMA B9 continuum contours: the ALMA map is zoomed in the top right corner of the figure, while the zoom at the bottom right corner shows the same ALMA B9 contours on top of the HST (F606W) image (González Delgado et al. [1998]). The broad-band (from UV to mm) SED of NGC 5135, and the result of the decomposition performed by Gruppioni et al. [2016] are shown in Figure 2.3.

From the broad-band SED-fitting and decomposition, Gruppioni et al. [2016] have estimated the main physical parameters of NGC 5135 as:

- **Stellar mass:** $M_* = 5.16 \times 10^{10} M_{\odot}$;
- **Total IR luminosity:** $L_{\text{IR}} = 10^{11.23 \pm 0.03} L_{\odot}$;
- **Star formation rate:** $SFR = 15.61 \pm 1.87 M_{\odot} \text{ yr}^{-1}$;
- **AGN bolometric luminosity:** $L_{\text{BOL}}^{\text{AGN}} = 10^{44.3 \pm 0.1} \text{ erg/s}$;

These values correlate well with the luminosities of mid-IR lines tracing star formation and AGN activity, as measured by Tommasin et al. [2008, 2010] from high resolution *Spitzer*-IRS spectra.

Nuclear studies of this object showed a complex morphology and the presence of numerous coexisting structures in the region within 0.7 kpc from the AGN, including a nuclear bar (e.g., Mulchaey and Regan [1997]) and several knots of SF, as derived from HST UV and optical observations of the nuclear regions performed by González Delgado et al. [1998] and Alonso-Herrero et al. [2006] (see § 2.2.3). In Bedregal et al. [2009], NGC 5135 was observed with VLT SINFONI in $[\text{Si VI}] \lambda 1.96 \mu\text{m}$ line, in H-band ($1.45 - 1.85 \mu\text{m}$) and K-band ($1.95 - 2.45 \mu\text{m}$) continuum in order to identify the AGN position (see also Bedregal et al. [2011] in § 2.2.2).

Our target was also observed by Levenson et al. [2004] in the X-rays with Chandra (0.4-8 keV), and the AGN emission component was separated from the stellar one in order to characterize the high emission component of this object (see 2.2.4). Also, radio-VLA observations are available from Ulvestad and Wilson [1989], who defined NGC 5135 as an “ambiguous” radio source due to the particular morphology obtained from the VLA maps (see 2.2.1).

Following we report a brief description of the main works that can be found in the literature about our source. Because of the particular structure of this galactic nucleus,

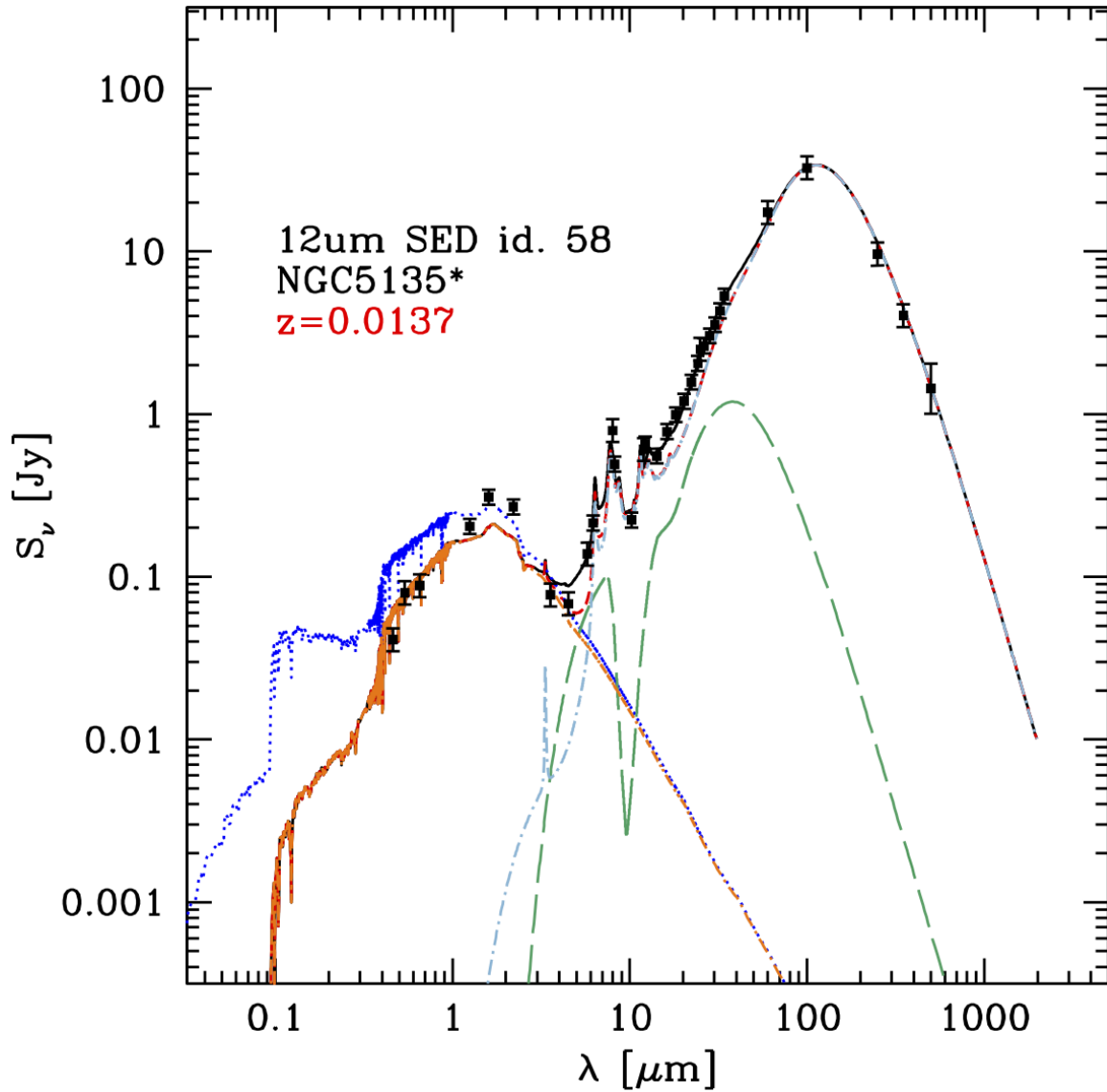


Figure 2.3: *Broad-band SED of NGC 5135 (data from the literature), as fitted by Gruppioni et al. [2016] with a three component model – extinguished stars (red), AGN (green) and dust re-emission (pale blue) – using the SED decomposition method described in Berta et al. [2013]. It is also reported the dust-unabsorbed star component (in electric-blue).*

we will see that every work is an important element for the global understanding of what is happening inside NGC 5135. The results of this Master Thesis work add a further piece to the puzzle, completing the framework with the analysis of high resolution millimeter and sub-millimeter ALMA data.

2.2.1 Radio observations

NGC 5135 is included in the analysis of a sample of 27 Seyfert galaxies observed with the VLA, performed by [Ulvestad and Wilson \[1989\]](#).

The authors selected a sample of objects with recession velocities $< 4600 \text{ km s}^{-1}$.

VLA maps of NGC 5135 show an asymmetric structure at both 6 cm and 20 cm (Figure 2.4), with faint emission extending to the northeast of a bright core source, with total fluxes of 163.2 mJy and 58.8 mJy and a total power of $\sim 1.4 \times 10^{23} \text{ W Hz}^{-1}$ and $\sim 8 \times 10^{22} \text{ W Hz}^{-1}$ in the diffuse emission respectively.

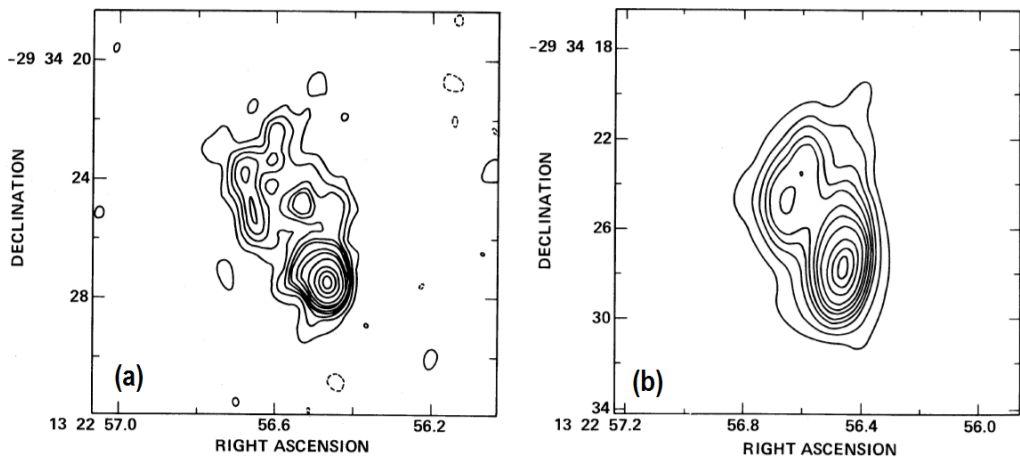


Figure 2.4: Maps of NGC 5135 at 6 cm (left) and 20 cm (on right) from [Ulvestad and Wilson \[1989\]](#): the beam sizes are $\theta_{6 \text{ cm}} = 0.91'' \times 0.60''$ and $\theta_{20 \text{ cm}} = 2.29'' \times 1.18''$ respectively; contour levels are set at -2, 2, 4, 6, 8, 10, 15, 20, 30, 50, 70 and 90% of the peak for the 6 cm map, and -1.5, 1.5, 3, 5, 7.5, 10, 15, 20, 30, 50, 70 and 90% for 20 cm map.

The core source position reported by the authors is RA(J2000):+13 : 25 : 43.94, DEC(J2000):-29 : 50 : 02.78.

The complexity of the radio emission, that presented a diffuse faint North emission with a bright source in the Southern region in both bands, allowed the authors to classify NGC 5135 as an “ambiguous” radio source.

2.2.2 Near IR observations

In order to describe the central engine, [Bedregal et al. \[2009\]](#) observed NGC 5135 by using the *Spectrograph for INtegral Field Observations in the Near Infrared* (SINFONI). The SINFONI camera is a near-infrared (NIR: from $1.1 - 2.45 \mu\text{m}$) integral field spectrograph fed by an adaptive optics module, currently installed at the

2.2 NGC 5135

Cassegrain focus of one of the four telescopes of the ESO *Very Large Telescope* (VLT) in Chile.

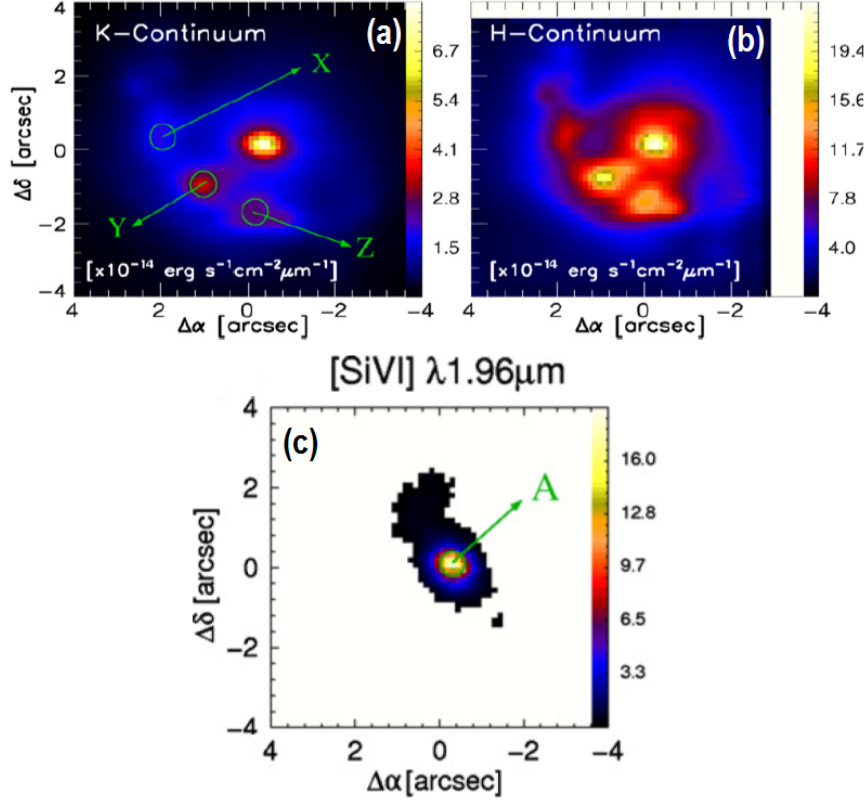


Figure 2.5: **Top panels:** continuous maps with SINFONI in the K and H-bands, from which the authors selected three strongly emitting regions marked as X, Y and Z. In these regions they estimated an upper limit for the last starburst phenomena as 7-8 Myr ago. **Bottom panel:** [Si VI] flux emission line maps in units of $10^{-17} \text{ erg s}^{-1} \text{ cm}^{-2}$, uncorrected for internal extinction. The $8'' \times 8''$ FoV corresponds to the central $2.3 \text{ kpc} \times 2.3 \text{ kpc}$. In all panels, north is up and east is left. Image from [Bedregal et al. \[2009\]](#).

With the VLT SINFONI camera, [Bedregal et al. \[2009\]](#) studied the central 2.3 kpc of NGC 5135 in [Si VI] $\lambda 1.96 \mu\text{m}$ line, and H-band ($1.45 - 1.85 \mu\text{m}$) and K-band ($1.95 - 2.45 \mu\text{m}$) continuum. They found that the region named “A” (marked in Figure 2.5 (c)) corresponds to the nuclear peak in the K-band continuum. This region includes the AGN nucleus. All the emission lines measured and the continuum show a peak at this location, suggesting a strong source of radiation.

The [Si VI] emission, that requires an ionisation energy of 166.7eV, is considered a good tracer of the AGN activity in the areas surrounding the nucleus and it is mainly produced by gas excited just outside the broad line regions ([Bedregal et al. \[2011\]](#)).

The source also presents a [Si VI] weaker “plume” to the North-Est direction, which turns out to be, in term of spatial scales, at least $4 \times$ larger ($\sim 600 \text{ pc}$ in this case) than previous reports on different Seyfert galaxy samples (e.g., [Prieto et al. \[2005\]](#), [Rodríguez-Ardila and Mazzalay \[2006\]](#)), where [Si VI] structures are at most ~ 150

pc across. The authors conclude that, for the first time, the presence of ionizing cones are detected in NGC 5135 are detected.

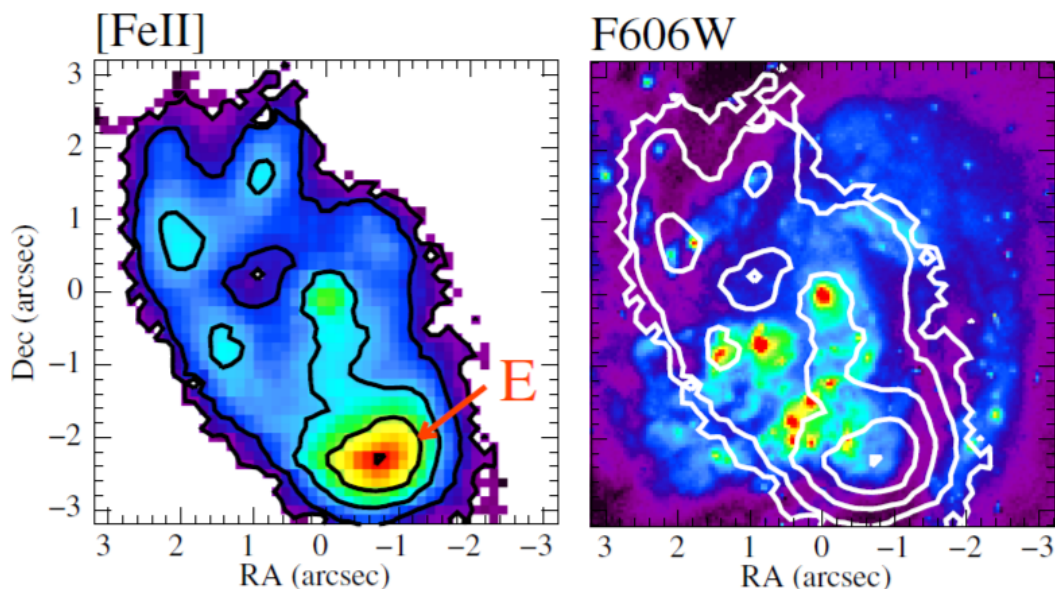


Figure 2.6: **Left panel:** Structures mapped with $[\text{Fe II}]$ line emission in NGC 5135 by Colina et al. [2012]. **Right panel:** optical map obtained with HST F606W by Alonso-Herrero et al. [2006]. The contours are the $[\text{Fe II}]$ ones shown in the left panel.

In Colina et al. [2012], SINFONI observations allowed to detect the signatures of strong outflows in the $[\text{Fe II}] \lambda 1.64 \mu\text{m}$ emission line, in a compact region at 0.9 kpc from the nucleus, spatially coincident with the peak emission at radio wavelengths found by Ulvestad and Wilson [1989] (Figure 2.4).

The velocity field of the $[\text{Fe II}]$ emission around the region that they called “E” (left panel of Figure 2.6) shows a velocity gradient along the east–west direction, characterized by a projected peak-to-peak velocity of 90 km s^{-1} and an overall projected size of 300 pc. This signatures are interpreted as a starburst driven outflow due to the combined effect of several Supernovae in region “E”, in accordance with the previous hypothesis of Bedregal et al. [2009].

2.2.3 Optical and UV observations

Spettroscopic observations

Understanding the basis of the main physical mechanisms that occur within galaxies is crucial for the complete understanding of their evolution. The analysis of galactic optical spectra and the lines therein, are an useful tool for these purposes, as they are directly generated by processes occurring within galaxies.

Baldwin et al. [1981] first proposed a diagnostic diagram considering the optical line

2.2 NGC 5135

ratio, such as $O[III](\lambda 5007)/H_\beta(\lambda 4861)$ vs $N[II](\lambda 6583)/H_\alpha(\lambda 6563)$, as an empirical instrument to separate sources according to the principal excitation mechanism: normal H II regions, planetary nebulae, objects photoionized by a power-law continuum, and objects excited by shock-wave heating.

Over time, these diagrams were called *BPT-diagrams* (from the names of the authors proposing this analysis, Baldwin J. A., Phillips M. M. & Terlevich T.) and implemented with other useful indicators to better characterize the observed sources. For instance, Veilleux and Osterbrock [1987] define a diagnostic diagram to provide the separation between Star Forming and AGN galaxies adding other two line ratios: $[SII](\lambda 6716 + \lambda 6731)/H_\alpha(\lambda 6563)$ and $[OI](\lambda 6300)/H_\alpha(\lambda 6563)$.

lines (λ)	$O[III]$	$N[II]$	$S[II]$	$O[I]$	H_α
$F(\lambda)/H_\beta$	4.83	5.45	0.92 + 0.87	0.31	6.12

Table 2.1: Line ratios between the integrated fluxes of the atomic transition (highlighted in blue) for NGC 5135. The fluxes are taken from Phillips et al. [1983].

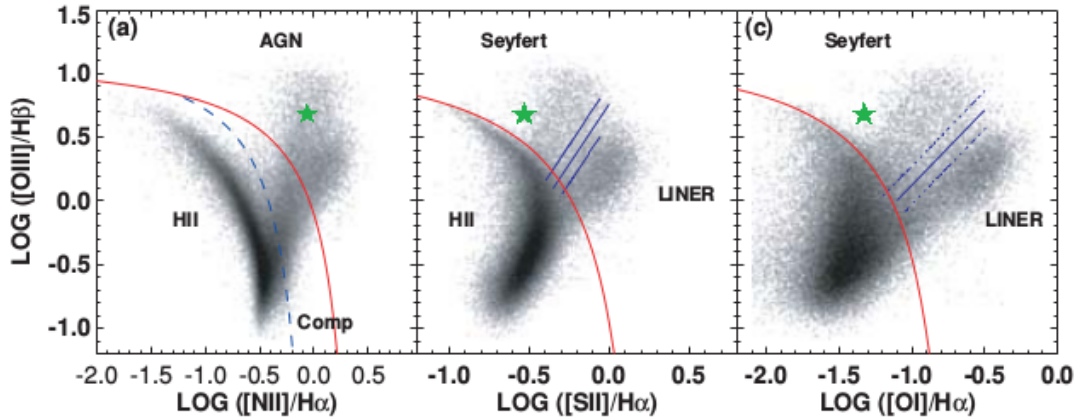


Figure 2.7: The three BPT diagrams from Kewley et al. [2006]. **Left panel (a):** $[OIII]/H_\beta$ vs $[NII]/H_\alpha$ diagnostic diagram; the blue dashed line the Kauffmann et al. [2003] separation, while the red solid line represents the Kewley et al. [2001] classification line. **Middle panel (b):** $[OIII]/H_\beta$ vs $[SII]/H_\alpha$. **Right panel (c):** $[OIII]/H_\beta$ vs $[OI]/H_\alpha$. All plots are in logarithmic scales. Green stars identify the position NGC 5135.

Subsequent works have continued to implement different conditions to BPT-diagrams, to increasingly characterize the internal phenomena of galaxies: in Kewley et al. [2001] the theoretical “maximum starburst line” was introduced, in order to differentiate starburst galaxies from those dominated by nuclear activity; Kauffmann et al. [2003] added an empirical line dividing pure star-forming galaxies from Seyfert-HII composite objects, whose spectra contain significant contributions from both AGN and star formation.

From the Phillips et al. [1983] observations (summarized in [Table 2.1]), we derived the line fluxes and line ratios for NGC 5135 in order to determine the dominant ionizing source through the BPT diagrams. Figure 2.7 illustrates the diagnostic diagrams used in the scheme introduced by Kewley et al. [2006].

From these results, it is confirmed the *Seyfert* nature of NGC 5135, whose emission is driven by AGN activity, and thus confirming the original Véron-Cetty and Véron [2006] classification.

Photometric observations

The Star Forming regions detected in near-IR by Bedregal et al. [2009] were observed in the surrounding of the central engine by using HST-F606W photometry (e.g., Alonso-Herrero et al. [2006], González Delgado et al. [1998])

The optical inner structure of NGC 5135 detected by HST (in Figure 2.8) is sprinkled with about a dozen prominent knots associated with intense SF. The detected emission, globally forms a spiral-like structure with two arms, from the inner to the outer region of the nucleus. In Alonso-Herrero et al. [2006], the authors proposed different models of stellar population concluding that in any case for the last starburst phenomenon could have taken place no later than ~ 6 Myr ago.

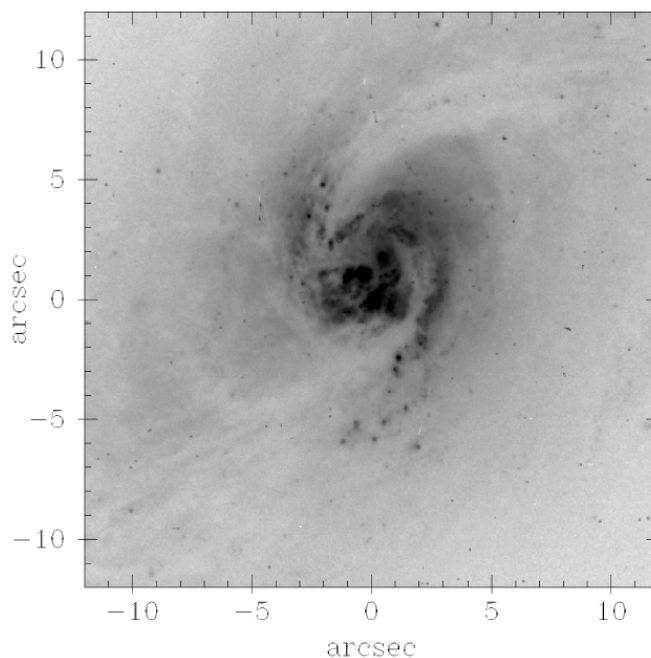


Figure 2.8: *HST F606W* image of NGC 5135. The inner structure (field $\sim 6.5 \times 6.5$ kpc) shows arclike segments spiraling to the center of the galaxy. Image from Alonso-Herrero et al. [2006]

2.2 NGC 5135

2.2.4 X-ray observations

The *Chandra* data for NGC 5135 were analysed by [Levenson et al. \[2004\]](#) (see Figure 2.9), who identified two different components in the central X-ray source: a Northern one associated to the AGN, and a Southern one associated to a star forming region. A starburst emission hiding the direct view of the AGN was also detected, requiring large reservoirs of gas at the center of the galaxy. The dynamic conditions that concentrate this material also serve to further obscure the AGN, producing an hydrogen column density $N_H > 10^{24} \text{ cm}^{-2}$. The starburst may also be related to the activity of the central engine, with the instabilities that lead to star formation aiding accretion and contributing to $\sim 50\%$ of the total bolometric luminosity of the galaxy, $L_{bol} \approx 7 \times 10^{44} \text{ erg s}^{-1}$.

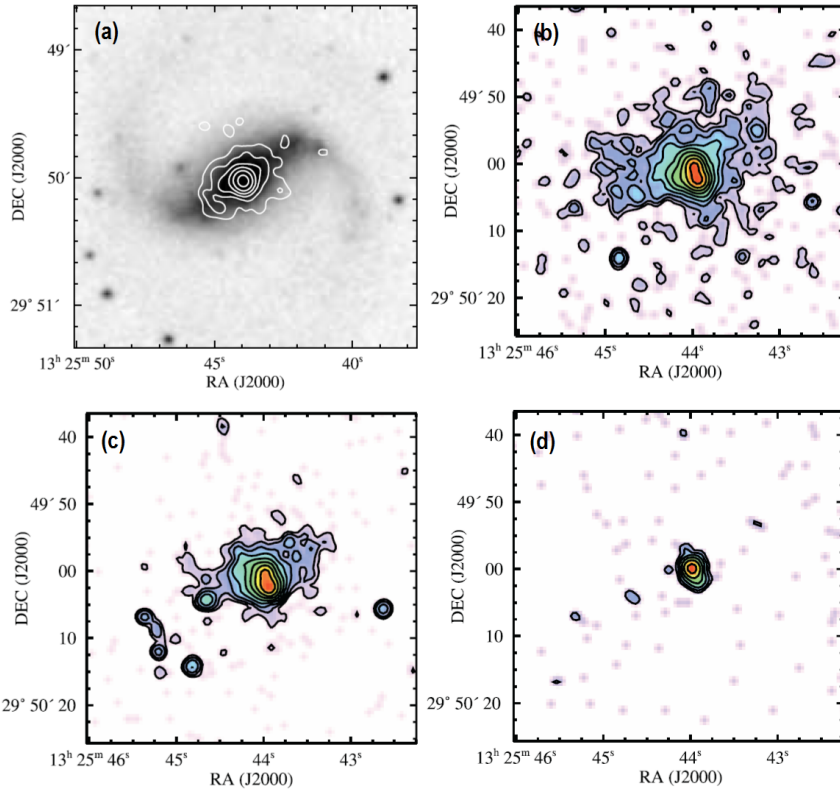


Figure 2.9: **Panel (a):** DSS image of NGC 5135 with overlaid 0.4–8.0 keV X-ray contours. **Panel (b):** Chandra soft X-ray (0.4–1 keV) image. The overlaid intensity contours begin at 8σ above the background level. **Panel (c):** Chandra medium X-ray (1–4 keV) image. The overlaid intensity contours begin at 6σ above the background level. **Panel (d):** Chandra hard X-ray (4–8 keV) image. The overlaid intensity contours begin at 8σ above the background level. The AGN is the strongest source, although resolved emission due to the southern starburst concentration is also evident. All contours increase by factors of 2. All images are smoothed by a Gaussian of $FWHM = 1.5''$ logarithmically scaled. Images taken from [Levenson et al. \[2004\]](#).

In order to complete this scenario, we have analysed the ALMA archival data, adding

the cold dust and molecular gas view to the already available information about NGC 5135.

NGC 5135, thanks to its almost face-on appearance, the presence of a large scale bar, the bulge overdensity of stars, the past evidences of the presence of a Supernova Remnant (SNR) and a central AGN, is an excellent target to investigate the dynamics of inflows and outflows and the star formation and nuclear activity relative feedbacks. These processes can now be investigated thanks to the unprecedented sensitivity and resolution of *ALMA* data, with the observation of CO molecule transitions in local Seyfert galaxies offering the possibility of directly witnessing the molecular gas fuelling towards the nucleus, thus allowing for the first time a thorough knowledge of the accretion process in the innermost regions of AGN.

Chapter 3

Analysis of ALMA data

Abstract

The purpose of this chapter is to provide the basics of interferometric theory and to illustrate the calibration and reduction procedures that we have applied to the ALMA observations of NGC 5135.

In the first paragraph, we briefly summarize the basic concepts of interferometry, describing the parameters that define the properties of an interferometer and of the Atacama Large Millimeter/submillimeter Array (ALMA) in particular. Subsequently, the datasets analyzed during the first phase of the thesis work are described.

In the central paragraphs we describe the calibration procedure, with specific references to the script for the manual calibration of the band 9 dataset, inserted in Appendix A. The last paragraph is dedicated to the imaging procedure.

3.1 *The Atacama Large Millimeter/submillimeter Array* interferometer

The *Atacama Large Millimeter/submillimeter Array* (ALMA) is the interferometer born by the cooperation of four scientific agencies: the *European Southern Observatory* (ESO), the *National Radio Astronomy Observatory* (NRAO), the *Associated Universities, Inc.* (AUI) and the *National Astronomical Observatory of Japan* (NAOJ).

The union of these four agents composes the *Joint ALMA Observatory* JAO, a unique international agency based in Santiago de Chile, that drives the entire observatory. The telescope operates on the Chajnantor Plateau at ~ 5000 m altitude in the Chilean Andes.

A radio interferometer exploits the combination of the electromagnetic signals received from the sky by two or more physically separated antennas.

Two antennas separated by a distance “ b ”, called *baseline*, detect the signal coming from a source at an infinite distance as a plane wavefront. The wavefront reaches the two antennas at different times, with a time delay $\tau = \vec{b} \cos\theta/c$, where θ is a function of telescope latitude and source position (see Figure 3.1).

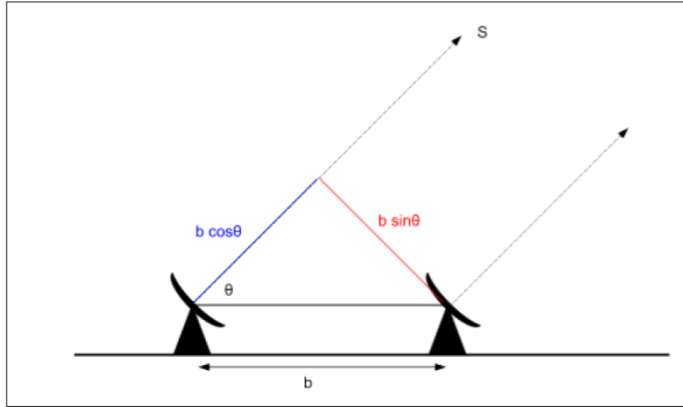


Figure 3.1: *Diagram of an interferometer, consisting of a pair of antennas separated by a distance “ b ” pointing at the same source direction \vec{S} .*

The electromagnetic field detected by the antennas is detected as a potential difference (U) by the diode with $U \propto E e^{i\omega t}$, with E equal to the amplitude of the signal and ωt the signal phase.

The interferometer measures the interference pattern produced by the difference in the radiation path length by combining the signal from each antenna with that from every other through a correlator. This operation can be written as

$$\langle U \cdot U^* \rangle = \mathcal{V}(\tau) \propto \frac{E^2}{T} \int_0^T e^{i\omega t} e^{-i\omega(t-\tau)} dt \quad (3.1.1)$$

where T is the time on which the integral acts. If $T \gg \frac{2\pi}{\omega}$, then we can write:

$$\mathcal{V}(\tau) \propto \frac{\omega}{2\pi} E^2 \int_0^{\frac{2\pi}{\omega}} e^{i\omega\tau} dt \propto \frac{1}{2} E^2 e^{i\omega\tau} \quad (3.1.2)$$

The power induced by the source in terms of *intensity of radiation* (I_ν) and *effective area* (A) in the direction of the source (\vec{s}) can be written as $P \propto E^2$, according to the principles of radiative transport, defining $I_\nu(\vec{s}) = I_\nu \cos\beta$:

$$dP = I_\nu \cos\theta d\Omega d\sigma d\nu \sim A(\vec{s}) I_\nu(\vec{s}) d\Omega d\nu \quad (3.1.3)$$

$d\sigma$ is the infinitesimal element of antenna's effective area, $d\Omega$ is the solid angle covered by the source and $d\nu$ is the range of frequency of the observation. Hence, the output of the correlator, integrated over the source, is the so called *visibility function* $\mathcal{V}(\vec{b})$:

$$\mathcal{V}(\vec{b}) = \int \int_{\Omega} A(\vec{s}) I_\nu(\vec{s}) \exp\left[i2\pi\nu \left(\frac{\vec{b} \cos\theta}{c}\right)\right] d\Omega d\nu \quad (3.1.4)$$

The visibility function contains three important pieces of information. Firstly, the interferometer observes the combination of the same signal detected by two separate antennas with a temporal delay (τ) proportional to the projection of their baseline along the line of sight. The resulting signal contains information about the source flux in the *amplitude* ($A(\vec{s}) I_\nu(\vec{s})$) and its position in the sky (relative to the telescope) in the *phase* ($e^{i\omega\phi}$) of the equation (3.1.4).

Secondly, the term ($A(\vec{s})$) is called *power response function* (PRF) of the antenna and represent the effective area on which almost all of the observed signal is collected. The main lobe of the PRF can be represented in good approximation with a Gaussian function for parabolic antennas. Its *Full-Width Half Maximum* (FWHM) is a measures of the *Field of View* (θ_{FoV}) size of the antenna, also known as *primary beam*. This is one of the quantities that characterize the interferometer. As for diffraction patterns in multiple apertures, the primary beams can be calculated as:

$$\theta_{FoV} = \frac{\lambda}{D} \quad (3.1.5)$$

where λ is the observed wavelength and D is the aperture size, corresponding to the diameter of the antenna in our analysis.

Finally, the functional form of the visibility function (3.1.4), is the *Fourier Transform* (FT) of the observed sky brightness distribution on the sky plane (I_ν , *van Cittern-Zernike Theorem*).

Therefore, the Fourier plane - also called *UV-plane* Figure 3.2 - is the plane orthogonal to the telescope *line of sight* (LoS) - parallel to the incident wavefronts - in which the interferometer baselines are ideally projected. Every baseline defines two points in the UV-plane, one at (u,v) and its complex conjugate at (-u,-v), since visibilities are *Hermitian complex numbers*.

The angular scale of fixed observational wavelength depends on the extension of the baselines of the interferometer. In order to reconstruct the real brightness distribution of the source, we have to sample as many angular scales as possible on the UV-plane. At a given frequency, there are two practical ways to obtain it: on the one hand we can

3.1 The Atacama Large Millimeter/submillimeter Array interferometer

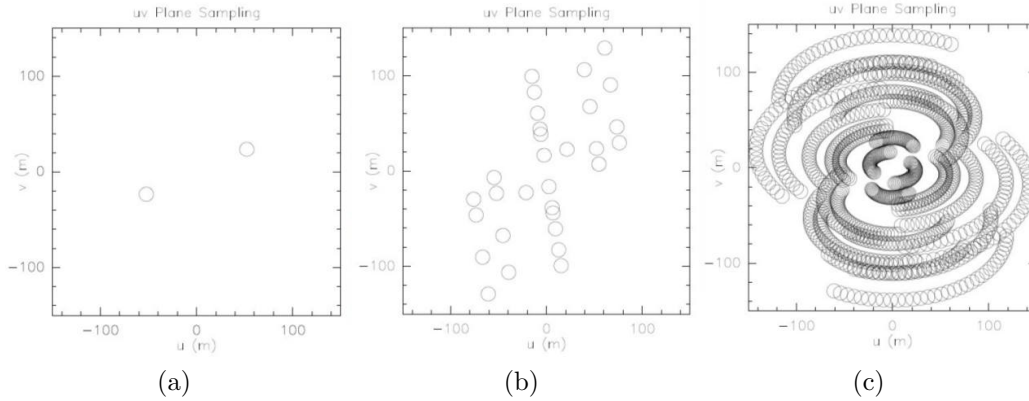


Figure 3.2: *UV-plane of an interferometer composed of six antennas: (a) Single baseline; (b) UV-plane covering whit zero instantaneously; (c) Coverage given by using the Earth rotation*

increase the number of antennas in the real plane, which means considerably increasing the number of baselines on the complex plane ((b) panel of Figure 3.2). On the other hand, we can take advantage of the Earth rotation. Increasing the exposure time of the observation thus the coverage of the UV-plane increases as can be seen in the panel (c) of Figure 3.2. Correlating the signals detected by each couple of antennas, at a given time, it is possible to map every angular scale defined by the baselines, in the range between the *largest angular scale* (θ_{LAS}) and the *angular resolution* (θ_{RIS}). These quantities, which are formally defined by the baseline projections on the UV-plane, can be approximated to:

$$\theta_{RIS} = \frac{\lambda}{b_{max}} \quad (3.1.6)$$

$$\theta_{LAS} = \frac{\lambda}{b_{min}} \quad (3.1.7)$$

where b_{max} is the bigger distance between two antennas in the array and b_{min} is the smallest one. θ_{ris} is often referred as *synthesized beam*. The larger than angular scales θ_{LAS} will not be observable, while the scales smaller than θ_{RIS} will be smooth on the size of the beam. This is the reason why ALMA Figure 3.3 is made up of sixty-six antennas divided into two different arrays: the *main array* is composed by fifty 12-m antennas, distributed up to a maximum baseline of 16 km.

The 12-m array configurations have been designed so that in the most extended configurations the spatial angular resolution will be as small as $\theta_{RIS} = 0.005 \text{ arcsec}$ at 950 GHz (Asayama et al. [2017]), for a complete description see Table 3.1).

However, any array has an angular resolution limit imposed by the physical impossibility of locating the antennas at a distance smaller than their diameter: this problem is called *zero-spacing problem* and it results in the impossibility to sample the center of the UV-plane and all the spacing around it, that correspond to the largest scales. Therefore we are limited in choosing the angular scales used to investigate the source

with the main array. In order to minimize the zero-spacing problem effects, the compact array - *Atacama Compact Array (ACA)* - was built.

It is composed by twelve 7-m antennas joined with four 12-m antennas. On the one hand, the use of antennas with a diameter smaller than 12-m allows to increase the limit of the maximum observable angular scales; passing from a minimum baseline of 15 m to 9 m. For example, in the case of Bands 6 and 9, used in our observations, an hypothetical extension to include of ACA might allow the largest angular scale (LAS) to pass from $\theta_{LAS,ma6} \sim 17''$ to $\theta_{LAS,aca6} \sim 29''$ and from $\theta_{LAS,ma9} \sim 6''$ to $\theta_{LAS,aca9} \sim 10''$ respectively.

On the other hand, the four 12-m antennas solve the zero-spacing problem with single-dish total-power observations, that allow to sample in the center of the UV-plane and collect the total power but losing the info on the structure on the largest scales.



Figure 3.3: *A suggestive image of a restrict numerous of ALMA antennas. In the image (at the center on top) the Large Magellanic Cloud and the Small Magellanic Cloud are clearly visible - Credit: ESO/C. Malin .*

Furthermore, another advantage of an interferometer with respect to a single dish is a higher *Sensitivity* (σ) as more receivers collect the signals simultaneously.

We can define as the noise associated with the instrumentation. It is defined by the conditions of the observation and for a set of *coherent receivers*¹, the theoretical noise takes the mathematical form:

¹the term “coherent receivers” identifies receivers that preserve the phase of the detected signal

3.1 The Atacama Large Millimeter/submillimeter Array interferometer

$$\sigma = \frac{2k_B T_{sys}}{A_{eff} \sqrt{(N(N-1)n_p \Delta\nu \Delta t_{int})}} \quad (3.1.8)$$

where:

- $k_B = 1.38 \times 10^{-16} \text{ erg } K^{-1}$ is the *Boltzmann constant*;
- T_{sys} is the *System Temperature* that corresponds to the brightness temperature equivalent to the flux received by the antenna, including source, atmosphere and instrumental noise;
- A_{eff} is the *effective area* of the antenna, equal to its *geometrical area* (πr^2) multiplied by a numerical term which takes into account the *aperture efficiency* (η_{eff})² and the *instrumental efficiency*, that for ALMA is equal to 0.845 (Asayama et al. [2017]);
- N is the number of the antennas constituting the interferometer;
- n_p is the number of detected polarization, and depends on the used observation mode³;
- $\Delta\nu$ is the bandwidth/*spectral resolution element width*;
- Δt_{int} is the *total on-source integration time*.

The sensitivity is directly proportional to the T_{sys} and inversely proportional to the spectral channel resolution ($\Delta\nu$), to the exposure time (Δt_{int}) and to the number of the antennas that compose the array (N).

Generally, the *Principal Investigator* of the observation (PI), during the proposal writing phase, sets the above described parameters, so to provide the observations with an optimum noise level for the pursued scientific goals.

The *ALMA sensitivity calculator*⁴ helps to predict the noise level of an observation, given the free parameters of the equation (3.1.8) and the set up of the observing array and frequency bands.

²define by the *Ruze equation* and equal to:

$$\eta_{eff} = R_0 e^{-\frac{16\pi^2\sigma^2}{\lambda^2}} \quad (3.1.9)$$

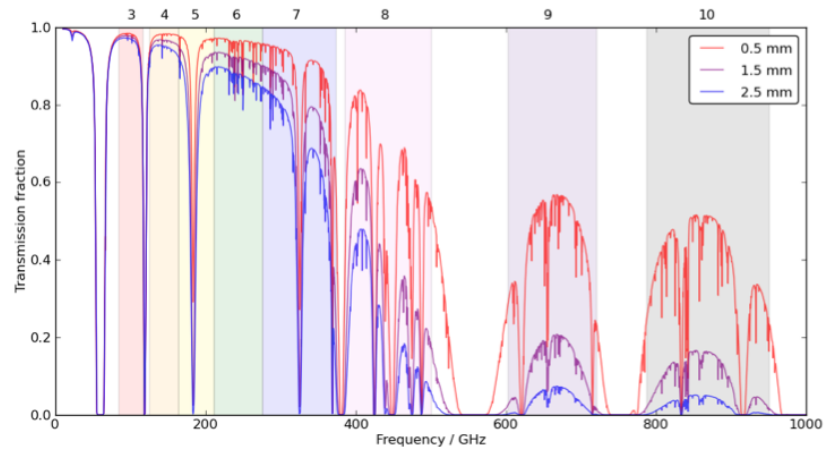
where $R_0 = 0.72$, σ is the *rms surface accuracy* of the antenna and λ is the observed wavelength (Asayama et al. [2017])

³ALMA is able to detect both orthogonal linear polarization (X and Y) so that 3 polarization observing modes are possible three types of correlation mode: the *single polarization* (XX or YY) to which $n_p = 1$ is associated, the *double polarization* (XX , YY) and finally the *full polarization* (XX , YY , XY , YX) that allows the definition and calibration of all the Stokes parameter. Both the letters correspond to $n_p = 2$, as in our case

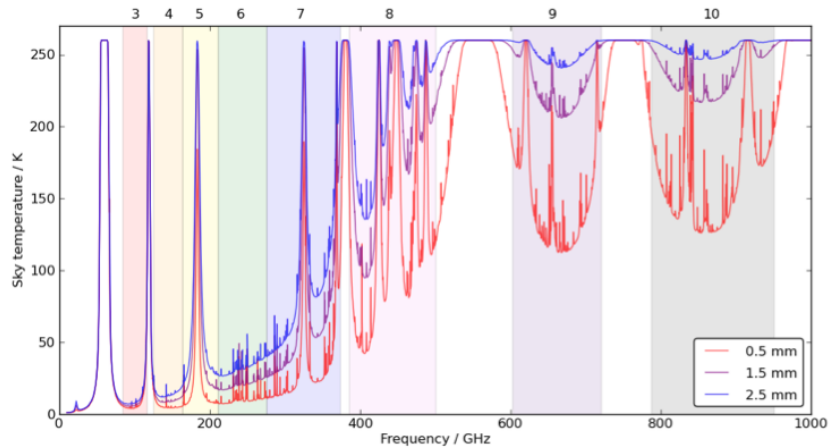
⁴ Available at: <https://almascience.eso.org/proposing/sensitivity-calculator>

3.1.1 ALMA observational-bands

Earth's atmosphere is not totally transparent to electromagnetic radiation: the interaction between photons coming from sources outside the atmosphere and the particles (electrons, ions and molecules) that constitute it generate a mixture of absorption, emission and reflection phenomena producing bands opaque to the electromagnetic radiation. The radio-submm window is one of the bands of the electromagnetic spectrum that allows astronomical observation using telescopes equipped with coherent receivers and covers a range of wavelength in the $\lambda \sim 0.3 \text{ mm}$ to $\lambda \sim 10 \text{ m}$ range.



(a)



(b)

Figure 3.4: Atmospheric transmission (a) and relative sky-temperature (b), between 1 to 1000 GHz for three different concentration of p_{wv} equal to 0.5 mm, 1.5 mm and 2.5 mm (in red, violet and blue respectively). Only the to date available ALMA bands are overlapped and its IDs are reported on top of the plot.

3.1 The Atacama Large Millimeter/submillimeter Array interferometer

ALMA covers only a part of the total radio-submm window, included between ~ 30 GHz to ~ 950 GHz (~ 9.6 mm to ~ 0.3 mm). To do this, the ALMA window is divided into ten observational bands covering the frequency intervals where the transmission of the atmosphere is higher, as it is shown in Figure 3.4 (a). The transmission of the atmosphere drastically drops down upon the rising of the *precipitable water vapour* (PWV) that is defined as the depth of the water vapour converted to the liquid phase.

Band Number	Frequency Range[GHz]	Wavelength [mm]	θ_{LAS}	θ_{RIS}
1	31.3 - 45.0	6.7 - 9.6	112''	0.10''
2	67 - 90	3.3 - 4.5	67''	0.05''
3	84 - 116	2.6 - 3.6	43''	0.04''
4	125 - 163	1.8 - 2.4	29''	0.03''
5	163 - 211	1.4 - 1.8	22''	0.02''
6	211 - 275	1.1 - 1.4	17''	0.016''
7	275 - 373	0.8 - 1.1	13''	0.012''
8	385 - 500	0.6 - 0.8	10''	0.009''
9	602 - 720	0.4 - 0.5	6''	0.006''
10	787 - 950	0.3 - 0.4	5''	0.005''

Table 3.1: Summary of all the ten ALMA bands, with their frequency and wavelength range in GHz and mm. Bands-1 and Bands-2 are not available yet. For each band, central wavelength were used to obtain the values of θ_{LAS} and θ_{RIS} considering the equations (3.1.6) and (3.1.7) with the shorter possible baseline $b_{min} = 15$ m and the longer one $b_{max} = 16000$ m.

Focusing on Band 6 and Band 9, centred at about ~ 250 and ~ 650 GHz respectively and both used to investigate our target (see, §2), it is easy to see how the transmission of the atmosphere changes from ~ 0.98 to ~ 0.8 and from ~ 0.6 to $\gtrsim 0.1$ respectively (Asayama et al. [2017]), with an increase of fivefold of the pwv. This explains also why the plateau of *Puna de Atacama* was chosen to host the entire technical equipment of ALMA: the extreme dryness of the *Puna de Atacama* ensures high transmission of the atmosphere and consequently an acquisition of a large amount of radiation coming from the astrophysical objects.

In Table 3.1 we summarized all ALMA-bands with their frequency ranges. In the ALMA-Cycle 5, only bands from 3 to 10 are available. The last two columns summarize the angular resolution and the largest angular scale for each band calculated using the central wavelength of bands in the limit of the minimum (15 m) and maximum (16000 m) baseline of the main array.

It should be noted how each band changes both the covered angular scales range. The instrumental features of ALMA receivers are therefore different for each band. To make the processing of the observations easier, the frequencies observed are then con-

verted to the operational frequency range set between 2 and 4 GHz in a process called *downconversion*. This allows to avoid to change all the electronics dedicated to the observed signal analysis when the observed frequency range change. The downconversion is performed by a device connected to the receiver, called *mixer* that convolves an artificial signal to the observed one and converts it to the predetermined frequencies. This mechanism is responsible of the structure of the observable bands, that are constituted by two separated sidebands. The size of the sidebands depends on the receiver properties, as well as the rule to set observing spectral windows within them. The spectral resolution instead depends on the properties of the correlator.

3.2 The ALMA data: data retrieval and analysis procedures

3.2.1 The ALMA archive:

The ALMA observations are organized in *Cycles*. In the early science cycles observations are performed on a best effort and product formats, data reduction pipeline availability or version of the software used to run calibration scripts might differ. In Table 3.2 time slots and available bands are summarized divided by Cycle.

ID Cycle	Start Date	End Date	Available Bands
<i>Cycle 0</i>	30 September 2011	31 August 2012	3, 6, 7, 9
<i>Cycle 1</i>	01 January 2013	31 May 2014	3, 6, 7, 9
<i>Cycle 2</i>	03 June 2014	30 September 2015	3, 4, 6, 7, 8, 9
<i>Cycle 3</i>	01 October 2015	30 September 2016	3, 4, 6, 7, 8, 9, 10
<i>Cycle 4</i>	01 October 2016	30 September 2017	3, 4, 6, 7, 8, 9, 10
<i>Cycle 5</i>	01 October 2017	30 September 2018	3, 4, 5, 6, 7, 8, 9, 10

Table 3.2: Summary of the periods covered by ALMA-Cycles, and each available bands.

An observing project in the ALMA archive⁵ has an associated structure divided into several hierarchical steps.

Generally, projects are divided into:

- **Science Goals (SG):** the minimum proposed observational unit, including targets in the same sky regions that roughly share the same calibration, aimed at reaching a requested sensitivity in a given angular resolution, largest angular scale and spectral setup.
- **Scheduling Blocks (SBs):** each SG is converted into scheduling blocks, that are the minimum set of command parameters, given to the telescope for ob-

⁵with the only exception of Cycle 0 data

3.2 The ALMA data: data retrieval and analysis procedures

ervation. Generally, each SB lasts ~ 30 min, in order to allow flexibility of scheduling and better calibration.

- **Execution Block (EB):** each repetition of a SB is called Execution Block, that is the minimum observative and data reduction unit (including all the calibrators for an observative session). Typically, an observation is composed by several EBs. More EBs can be grouped into a *Member* observing unit (MOUs). More MOUs can be grouped in a Group to fulfill the purposes of a SG.

The data stored in and downloadable from the ALMA science archive, preserve this structure. An example of the data structure is shown in Figure 3.5.

Project / OUSet / Executionblock	File	Size	Accessible
Request 1948844809			
Project 2013.1.00243.S			
readme	2013.1.00243.S.readme.txt		
Science Goal OUS uid://A001/X122/X48a			
Group OUS uid://A001/X122/X48b			
Member OUS uid://A001/X122/X48c			
SB NGC_5135_a_06_TE			
product	2013.1.00243.S_uid_A001_X122_X48c_001_of_001.tar	977.9MB	✓
raw	2013.1.00243.S_uid_A002_Xa68906_X1bd.asdm.sdm.tar	28.3GB	✓
Member OUS uid://A001/X122/X48e			
SB NGC_5135_a_06_TC			
product	2013.1.00243.S_uid_A001_X122_X48e_001_of_001.tar	243.5MB	✓
raw	2013.1.00243.S_uid_A002_X9652ea_Xbf8.asdm.sdm.tar	12.5GB	✓
		Total: 41.9GB	

Figure 3.5: Hierarchical structure in which an observing project and its data are divided. This configuration generally takes the name of ALMA data-tree .

Finally, for every EB, ALMA data are imported in the CASA (*Common Astronomy Software Application*) software in several dataset structured as *measurement sets* (MS), a collection of tables that contain all the pieces of information about visibilities, that can be reduced and/or displayed.

In order to ensure high-quality data, the ALMA-team provides the *Quality Assurance* (QA), which is a procedure that ensures that a reliable final data product is delivered to the Principal Investigator (PI), that is, the product has reached the desired control parameters outlined in the science goals, within a tolerance ranges, it is calibrated to the desired accuracy, and calibration and imaging artefacts are mitigated as much as possible.

To be more efficient in detecting problems, ALMA QA has been divided into several stages that mimic the main steps of the data flow. The broad classification of this multi-layered QA approach is:

- **QA0:** Monitoring of calibrations and overall performance during observations;

- **QA1:** Measurement of performance parameters and telescope properties by the observatory;
- **QA2:** Full Calibration and generation of science products;
- **QA3:** The PI may request re-reduction if the performance parameter of the proposal were not satisfied.

Once the source/es has been selected, it is possible to download from the ALMA-archive any kind of available data: the *raw data*, the *products* (if the QA2 has been passed) and the *calibration script* that must be run using the same CASA-version used by the ALMA-team in calibration QA2 steps. A text file is also available containing all the useful information about the CASA-version and how to process the data.

3.2.2 ALMA data of NGC 5135:

In this Master Thesis, we analyzed the observations of the local Seyfert galaxy NGC5165 available in the ALMA data archive. The data are all publicly available in the ALMA Science Archive.

The observations are divided into three datasets: two in Band 6 (one in a compact configuration and the other in extended configuration) and one in Band 9.

The real distribution of antennas for each observation are reported in Figure 3.6.

Samples of the UV plane are shown in Figure 3.7. The pattern of the two band 6 covers is summarized in a single UV plane in Figure 3.7 (d).

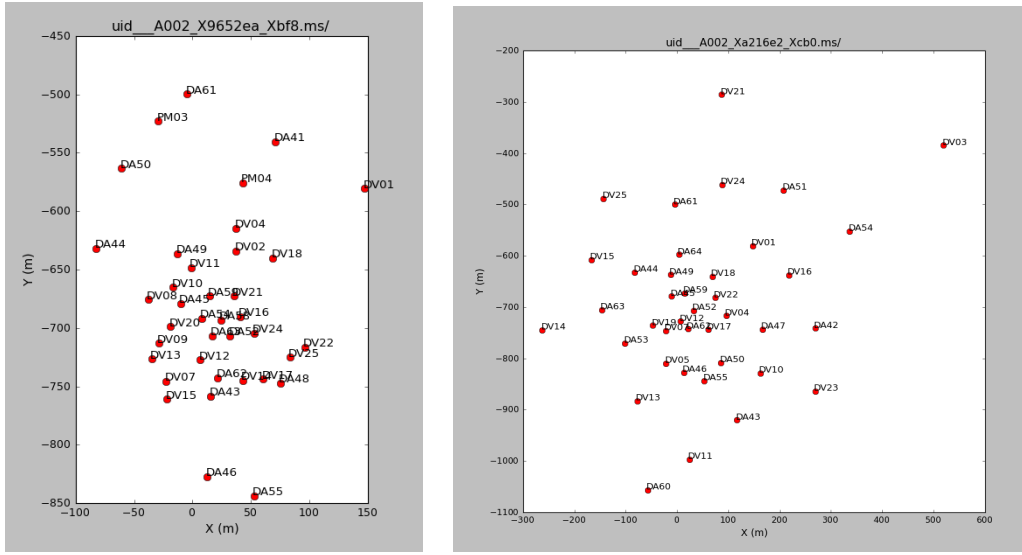
The applied calibration procedure (see §3.3.2) changes with the datasets. For the imaging procedure (after calibrating them separately) we combined the two bands 6 datasets and treat them as a single observation.

Below there is a description of the analyzed datasets.

BAND 6 datasets:

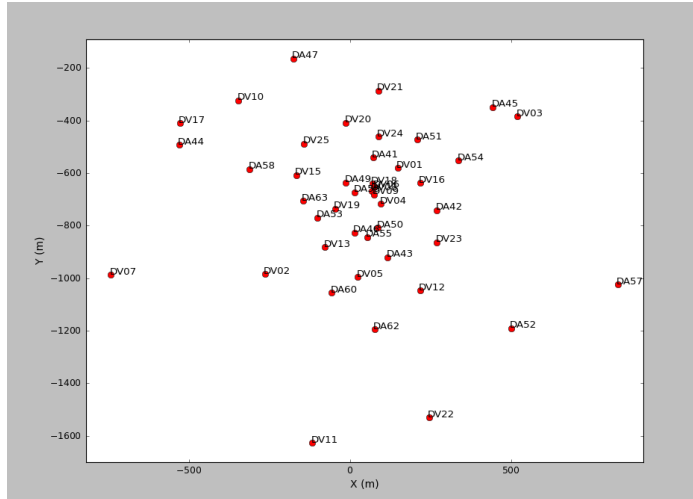
Band 6 dataset is composed of two different SB of the project 2013.1.00243.S (PI: Luis Colina), observed with two different configurations. Each SB was executed in a single EB. The first one was observed on December 10th 2014 in Cycle 2, with a compact array composed of 38 12-m antennas using a range of baseline included between 15.0 m and 348.5 m. The three spectral windows (spw) used to observe the galaxy are respectively set at the sky frequencies of 227.426 GHz, 241.629 GHz and 228.868 GHz. The spectral set up allowed us to detect the CO(2-1) and CS(5-4) molecular transition at 230.5 and 244.9 GHz. For our object (see § 2) the lines rest frequencies (ν_{rest}) are shifted to the observed frequencies (ν_{obs}) 227.4 GHz and 241.6 GHz respectively. The second observation was taken on July 23rd 2015 in Cycle 3, with an extended array configuration formed by 44 12-m antennas. In this case, the range of baselines is between a minimum baseline of 15.0 m and a maximum baseline of 1600 m. The spectral set-up is roughly the same in the two band 6 observations. These values are summarized for convenience in Table 3.3.

3.2 The ALMA data: data retrieval and analysis procedures



(a) Banda 6 - Compact configuration.

(b) Banda 9 - Extended configuration.



(c) Banda 6 - Extended configuration.

Figure 3.6: The real plane antenna disposition.

The two data sets were concatenated in a unique band 6 observation with a total duration of approximately two hours of which 50min and 11s were spent on source. The observations were centred on the coordinates at RA: 11:25:44:06 DEC:-29:50:01.2 (J2000.0)⁶ in the proximity of the galaxy nucleus, with a single pointing expected Field of View $\theta_{FoV} \sim 26.86''$ and an expected beam of $0.25'' \times 0.20''$ and $PA = 57.25^\circ$. For the two datasets concatenation we have calculated a $\theta_{ris} = 0.1''$, corresponding

⁶From *NASA/IPAC Extragalactic Database* (NED): https://ned.ipac.caltech.edu/cgi-bin/objsearch?objname=ngc5135&extend=no&hconst=73&omegam=0.27&omegav=0.73&corr_z=1&out_csyst=Equatorial&out_equinox=J2000.0&obj_sort=RA+or+Longitude&of=pre_text&zv_breaker=30000.0&list_limit=5&img_stamp=YES

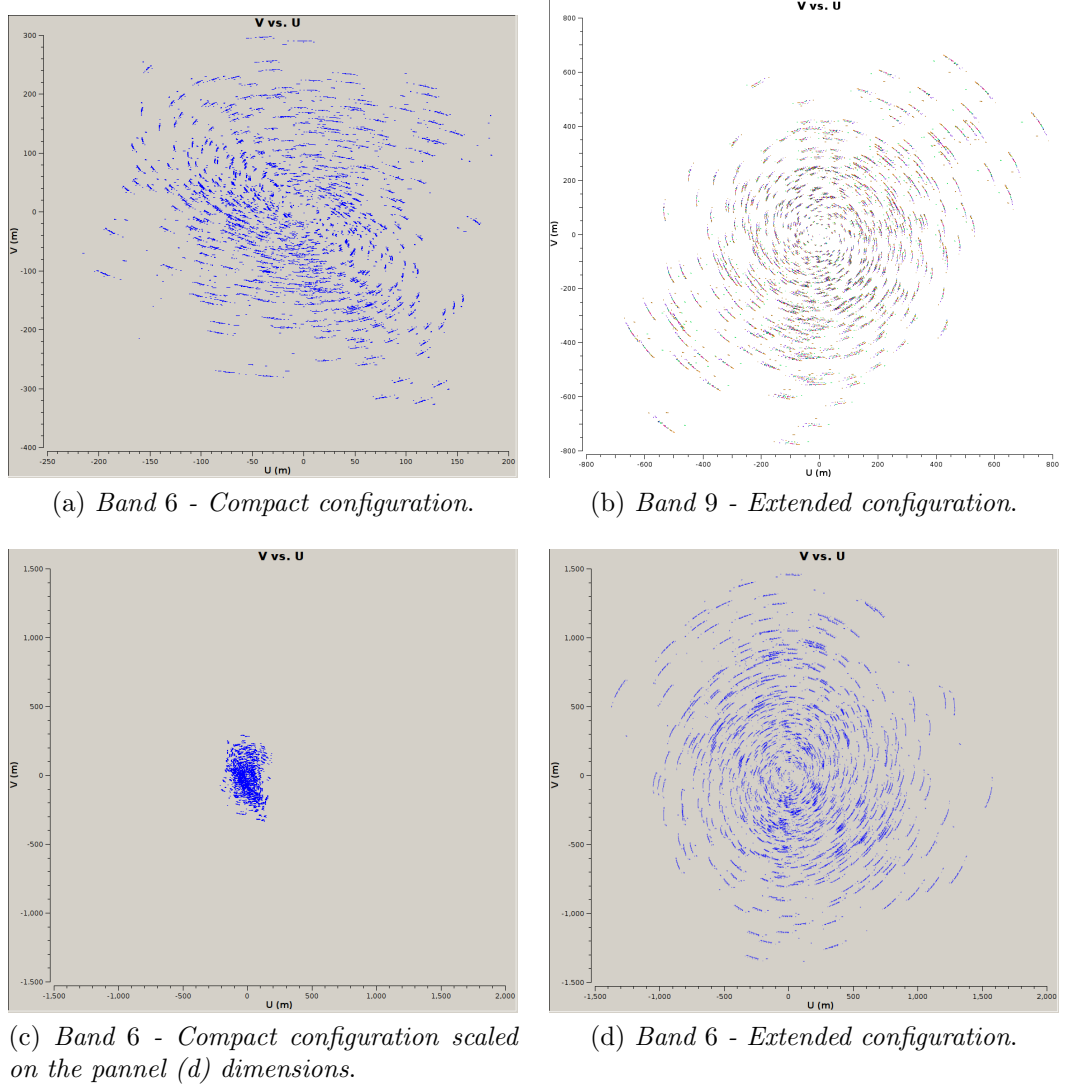


Figure 3.7: Baselines pattern on the UV-Plane for each configuration. Panel (c) and (d) are scaled at the same spatial dimensions in order to ease the comparison of the baselines of the two B6 configurations .

	Band 6		Band 9	
	<i>Spectral set up</i>		<i>Spectral set up</i>	
Spectral windows 1	230.538 GHz	<i>CO(2-1)</i>	687.700 GHz	<i>continuum</i>
Spectral windows 2	232.400 GHz	<i>continuum</i>	689.670 GHz	<i>continuum</i>
Spectral windows 3	244.936 GHz	<i>CS(5-4)</i>	691.473 GHz	<i>CO(6-5)</i>
Spectral windows 4	246.900 GHz	<i>continuum</i>	693.270 GHz	<i>continuum</i>

Table 3.3: Summary of the spectral set up in the two bands.

3.2 The ALMA data: data retrieval and analysis procedures

to the angular resolution of the extended configuration, and a $\theta_{LAS} = 12.32''$, corresponding to the largest angular scale of the compact configuration.

This angular scales correspond to 28.9 pc – 3.56 kpc at the galaxy redshift.

The galaxy was observed in dual polarization mode with 1.875 GHz total bandwidth per baseband for the spectral windows dedicated to the molecular lines, divided in 3840 channels and a velocity resolution of 0.488MHz ($\sim 0.42 \text{ km s}^{-1}$). The continuum spectral window has 2.00GHz total bandwidth per baseband with a velocity resolution of 15.625MHz ($\sim 20.470 \text{ km s}^{-1}$). The median system temperatures (T_{sys}) of the compact-array configuration is $T_{sys} = 90 \text{ K}$, that corresponds to a sensitivity $\sigma \sim 0.038 \text{ mJy/beam}$ for the spectral windows linked to the line molecular transitions and to $\sigma \sim 6.3 \times 10^{-5} \text{ mJy/beam}$ for the continuum one.

For the extended configuration, $T_{sys} = 75 \text{ K}$ corresponding to theoretical sensitivity $\sigma \sim 0.0028 \text{ mJy/beam}$ for spectral line band resolution and $\sigma \sim 1.9 \times 10^{-5} \text{ mJy/beam}$ for the continuum one.

Data were calibrated using the PIPELINE version “31667 (Pipeline-Cycle2-R1-B)” and the version 4.2.2 of CASA.

The calibrated data set of the two configurations were concatenated and imaged with CASA 4.7.1.

Details about the calibration procedure, with the explanation of each phase and our particular choices will be discussed in the § 3.3.2.

BAND 9 dataset:

Band 9 data are composed by a single observation in an extended configuration as part of the project 2013.1.00524.S (PI: Nanyao Lu). The EB was observed obtained on June 2nd 2015 – Cycle 3 with an array composed of 39 12-m antennas included in a range of baselines between 20.5 m and 886. This range of baselines corresponds respectively to a largest angular scale $\theta_{LAS} = 9.56''$ and an angular resolution of $\theta_{ris} = 0.1''$ comparable with the angular parameters of the band 6 concatenated observation and corresponding to 2.76 kpc and 28.9 pc at the galaxy redshift respectively. In order to make the comparison between the two arrays easier, we summarized in Table 3.4 the main properties of the three configuration observations.

Type of configuration	b_{max}	b_{min}	θ_{RIS}	θ_{LAS}	Δt_{int}	σ
Band 6 - compact	348.5 m	15.0 m	0.77''	17.86''	1013 s	0.038 mJy
Band 6 - extended	1600.0 m	15.1 m	0.16''	17.75''	1994 s	0.0028 mJy
Band 9 - extended	20.5 m	886.0 m	0.10''	9.52''	1232 s	0.53 mJy

Table 3.4: Summary of the observation parameters of the datasets including array configuration properties, the time on source (Δt_{int}) and the theoretical noise (σ).

The four spectral windows that compose this measurement set are centred on the sky frequency of 678.243GHz, 680.183GHz, 683.736GHz and 681.975GHz. The last one includes the emission of CO(6-5) molecular transition at the rest frame frequency

of $\nu_{rest} = 691.5$ GHz, for our object (see § 2) shifted to the observed frequencies $\nu_{obs} = 682.1$ GHz (Table 3.3).

The median temperature of antennas that can be associated to all the spectral windows is close to $T_{sys} = 950$ K that corresponds to a sensitivity like $\sigma \sim 0.53$ mJy/beam associated to a total integration time on source $\Delta t_{source} = 1232$ s as a part of the total time of the observation $\Delta t_{int} = 3216$ s. The observation was centred at RA: 11:25:43:99 DEC:-29:50:01.1 (J2000.0) very closely to the coordinates assumed as center for band 6 concatenation data, with a single pointing covering a FoV $\theta_{FoV} = 9.25''$ and with an expected synthesized beam of $0.30'' \times 0.29''$, corresponding to 86.7 pc \times 83.8 pc at source redshift.

Manual calibration was performed for the archival data (see § Appendix A for the script). The phase calibrator (J1316 – 3338) is faint at these observing frequencies (~ 0.4 Jy).

With respect to the script available in the archive, we improved the calibration by flagging four misbehaving antennas and updated the flux density model for the flux density calibrator by a factor 0.84, exploiting an observation of the calibrator coeval to those of the target (not yet available in the calibrator manual at the time of the quality assessment analysis). Further details about this calibration procedure in the § 3.3.2.

3.3 Data reduction

3.3.1 Software used: CASA

The software usually used for ALMA data analysis is **CASA** (*Common Astronomy Software Applications*), specifically developed to respond to data reduction needs of large modern radio submm telescopes.

Operations are performed through tasks well suited to extract scientifically usable information from *raw* data.

In the following we will specify the tasks that have been used, indicating also some of the most relevant parameters they require.

The ALMA data originally has the ASDM format, and are then converted and organized in collection of tables called *measurement set* (MS), that can be directly investigated with the **BROWSETABLE** task. Data are articulated into columns, including: **DATA**, which contains raw data and is never overwritten; **CORRECTED**, containing data processed after calibration; **MODEL**, which contains reference models; **FLAGS**, where the information on applied flags resides.

To make the calibration procedure clearer, henceforth we will explicitly refer to the various calibration steps of the script we wrote for the band 9 data (which we reported in full in Appendix A).

3.3.2 Flagging procedure

“A priori” editing:

It can happen that a portion of the data in the measurement set is useless for our purposes. In order to maintain the integrity of the original observation, it is preferable not to completely delete such data.

An ideal flag (represented by a “1” in the FLAGS column in the main table) is assigned to these data, that notifies the software not to use them with the valid data, unless explicitly required. This procedure is called Flagging or Editing, and in *CASA* it is executed through the FLAGDATA task.

Flags are divided into two categories: the “a priori” editing that edits data needed to verify the instrumentation conditions and the “a posteriori” editing, that verifies the quality of the observed source data. In band 9 script the former is addressed in mystep 3.

Let’s see in detail the various types of flagging in this category:

- **Data for atmosphere calibration:**

Data used for the T_{sys} calculation, with a atmospheric intent are flagged, in order to reduce the data size during the calibration procedure.

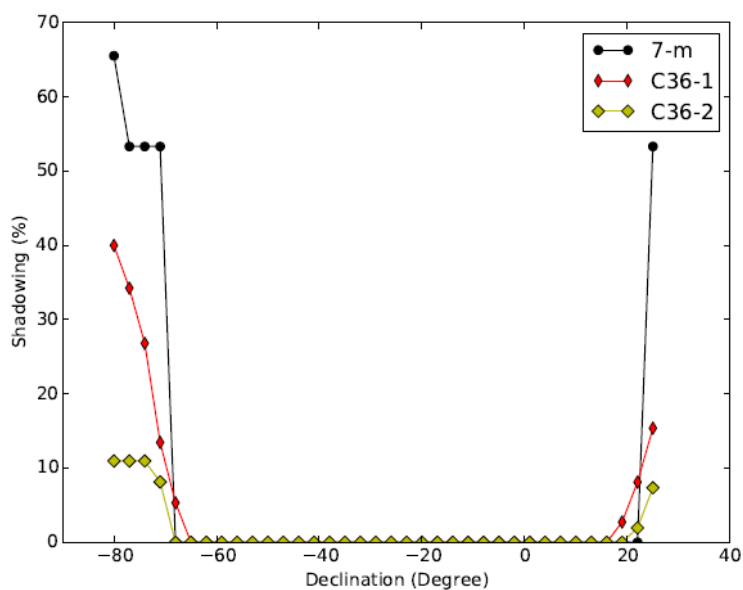


Figure 3.8: *Shadowing fraction vs. declination in three different ALMA array during ALMA-Cycle 3 [from Asayama et al. [2017]].*

- **Shadowing:**

Shadowing is the partial or, in the extreme case, the total occultation of an antenna by another one. This problem may arise in compact configurations (often in ACA), or with sources with low elevation.

It is appropriate to exclude the data with antennas that exceed a 5% of shadowed fraction (Asayama et al. [2017]). Figure 3.8 shows the shadowing fractions for three different arrays: C36-1 is the more compact configuration of 12 m antennas, while C36-2 is slightly less compact (7-m stay for ACA). In our case, $\sim 1\%$ of the data was flagged as affected by shadowing during the compact band 6 calibration procedure.

- **Pointing correction:**

From time to time, it is necessary to check the antennas pointing in order to obtain a correct orientation for each antennas.

This procedure is performed with observations that are stored within the measurement set and used to correct the subsequent pointing at the same time as the observations. Such data are then useless afterwards and therefore have to be flagged.

- **Auto-correlations:**

The correlated signals received from two distinct antennas from the same source are in phase once corrected for the delay; however, the associated noise, as produced by the various electronic components of each antenna, is not in phase and is thus cancelled by the correlation itself.

For auto-correlation this is not valid: the noises are in phase because they are generated by the same instrumental components.

Autocorrelations are important for some specific calibration tests and could be flagged for most of the scientific purposes. In our case, $\sim 5\%$ of the data was flagged as a result of self-correlation in the compact band 6 calibration procedure.

“A posteriori” editing

The “a posteriori” editing requires a detailed analysis of the data before it can be applied. Every single observation of the data set must be examined. The result can depend on the analyst sensibility. A completely heuristic flagging process is still in its way to come because many conditions have to be considered in different cases.

In band 9 script, this passage is done within a part of `mystep10`.

The list below summarizes the set of flagging that we applied to our data:

- **Edge channels:**

In this case, it is necessary to evaluate the correctness of channel measurements at the edges of the spectral windows set where the spectral response function is no longer a flat top-hat function (see Figure 3.9); usually 10-15% of the data is excluded for this reason.

In the case of manual calibration (band 9 data set), the channels contained in each continuum spectral windows are 128. We deleted the selections 0-3 and 124-128 (this corresponds to $\sim 8\%$ of our data).

3.3 Data reduction

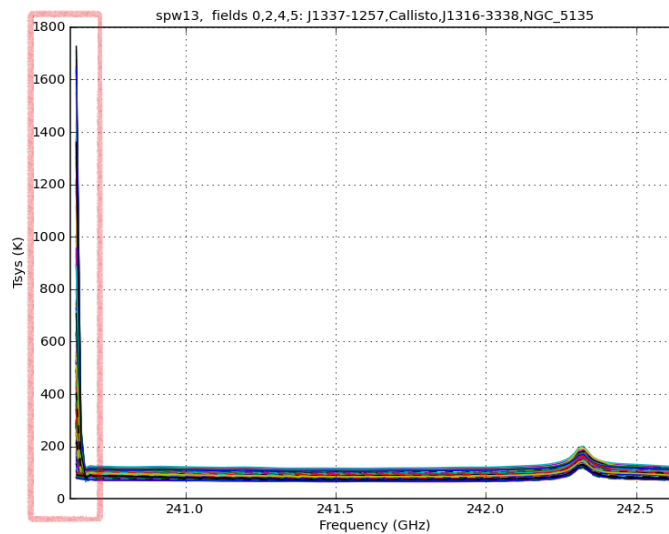
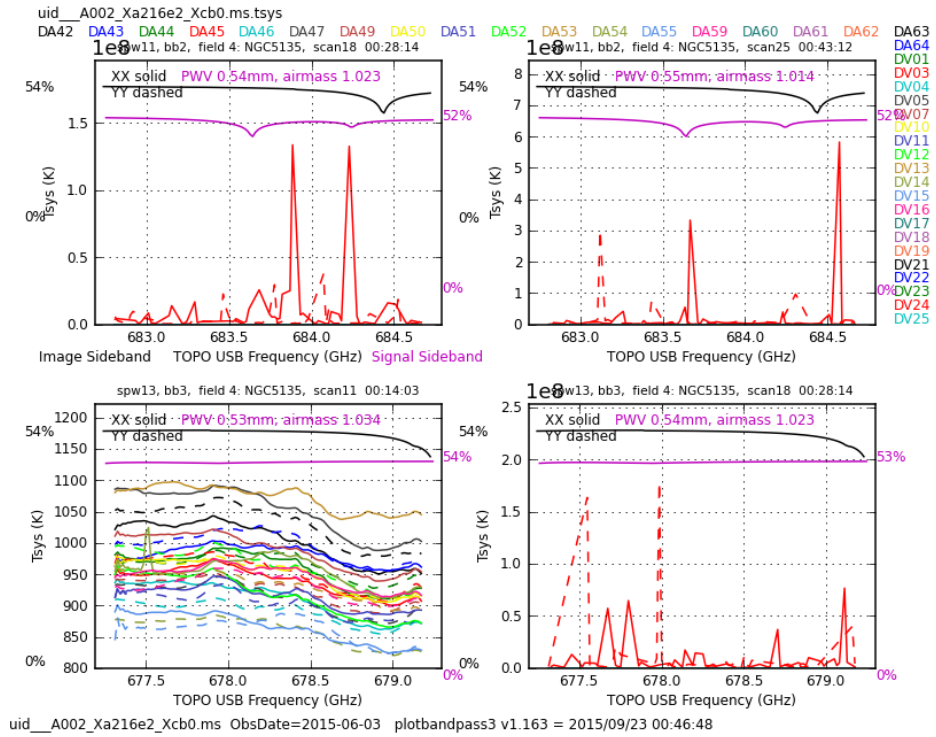


Figure 3.9: Plot T_{sys} vs. ν : an example of the edgchannels problem is shown to the left of the image (red-rectangle): The channels close to the edges of the spw show higher noise.

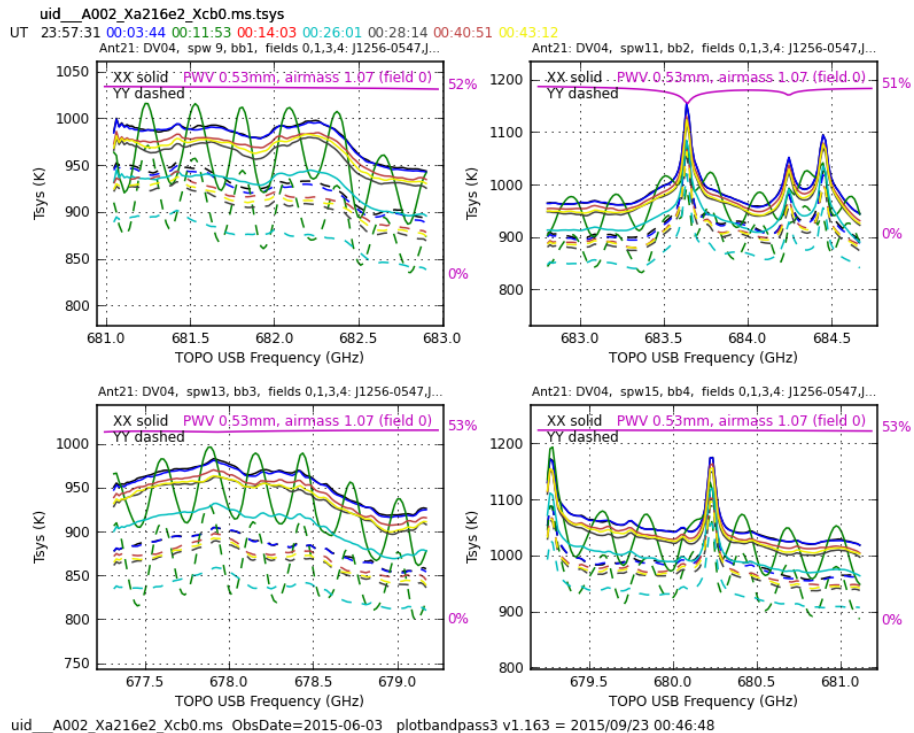
- **Electronics related issues:**

Since T_{sys} amplitude should be a continuous slowly changing function, with similar behaviour for all the well behaving antennas that share the same atmospheric pattern towards the same source, spikes, discontinuities or periodic patterns suggest malfunctioning, typically due to antennas or correlator electronic misbehaves. Hence, the correct functioning of the antennas can be evaluated by displaying the T_{sys} vs frequency channels for each antenna.

Figure 3.10 shows an example of this problem: in (a) an apparently malfunctioning antenna is displayed. We can easily see how the antenna DV03 shows an abnormal behaviour in spw11 (scan 18 and 25) and in spw13 (scan 18) that it is completely absent in spw13 (scan 11 - bottom left in the figure). This type of error is easily identifiable. An antenna's missing flag showing a similar behaviour could seriously undermine the ultimate quality of the images. In (b) another special case is shown to which we applied a flag. T_{sys} vs. plot for the DV04 that reports a periodic sinusoidal behaviour (green line) in scan 6. The effects of this type of interference are easily found in the final image (which would show a periodic "strange" pattern).



(a) Malfunction of DV03 Antenna: Easy to see too high T_{sys} ..



(b) Periodic sinusoidal behaviour (green line) of the antenna DV03 in scan6.

Figure 3.10: Two instructive examples of possible errors due to antenna electronics founded during the manual calibration procedure of band 9.

3.3 Data reduction

3.3.3 Calibration procedure

The results of an interferometric measure, for the generic baseline between antennas i and j , are the observed visibility defined by the eq. (3.1.4). They are complex numbers with a *real component* (A) and an *imaginary* (ϕ) one: $\mathcal{V} = Ae^{i\phi}$.

An interferometer observes the $\mathcal{V}_{ij}^{obs} = A_{obs}e^{i\phi_{obs}}$ which differs from the true one $\mathcal{V}_{ij}^{true} = A_{true}e^{i\phi_{true}}$ by values due to the presence of numerous degradation factors of the received signal. These values can be collected in the calibration or gain matrices G_{ij} :

$$V_{ij}^{obs} = G_{ij} \cdot V_{ij}^{true} \quad (3.3.1)$$

The calibration procedure consists in the reconstruction of the V_{true} from the available V_{obs} data. A crucial step for achieving this is the observation of V_{obs} for calibrators sources, for which the expected V_{true} visibility is known - thanks to reconstructed model based on previous observations and obtain the G^{ij} matrices from the equation (3.3.1).

One fundamental assumption to proceed is that the elements that corrupt the observations are independent of each other: hence the total gain table can then be factorized into multiple $G_{ij}^{(N)}$ matrices separately calculated:

$$V_{ij}^{obs} = G_{ij} \cdot V_{ij}^{true} = \prod_N G_{ij}^{(N)} \cdot V_{ij}^{true} \quad (3.3.2)$$

With this premise, calibration can take several steps, each of which deals with a single defect correction.

A second fundamental hypothesis is that all corruption factors are baseline independent (i.e. they depend solely by the single antenna). This allows further gain factorization, according to:

$$G_{ij} = g_i \cdot g_j \quad (3.3.3)$$

To find these g_i , we need at least three antennas that observe an ideal pointing source, with known flux F , at the centre of the phases:

$$\begin{cases} V_{12}^{obs} &= g_1 g_2 \cdot F \\ V_{13}^{obs} &= g_1 g_3 \cdot F \\ V_{23}^{obs} &= g_2 g_3 \cdot F \end{cases} \quad g_1^2 = \frac{V_{12}^{obs} \cdot V_{13}^{obs}}{V_{23}^{obs} \cdot F} \quad (3.3.4)$$

In a telescope such as ALMA, equipped with a much larger number of antennas, the system for resolving gains is over-defined. The solution provided by CASA software is a least squares interpolation of all the found solutions. Below we provide a theoretical description of the calibration procedure, by concentrating on the millimetric and submillimetric band and on the outcomes of this procedure performed on our data set.

In these bands the main factors that degrade the data are the instrument electronics and the atmosphere.

“A priori” calibration

The “a priori” calibration is based on the known instrumental response. It is aimed at correcting data for the impact of the atmosphere in opacity (which affects the system temperatures) and phase.

For this procedure we must assume an atmosphere pattern to correct the atmospheric lines and find their respective gains.

The T_{sys} are determined both by electronics and, to a greater extent, by the atmosphere. On the one hand, in all radio bands, the atmosphere results in a long-time phase-shift of data varying on time scale shorter as the frequency increases. On the other hand, due to its opacity, absorbs part of the signal and emits spectral lines due to the transitions of its components.

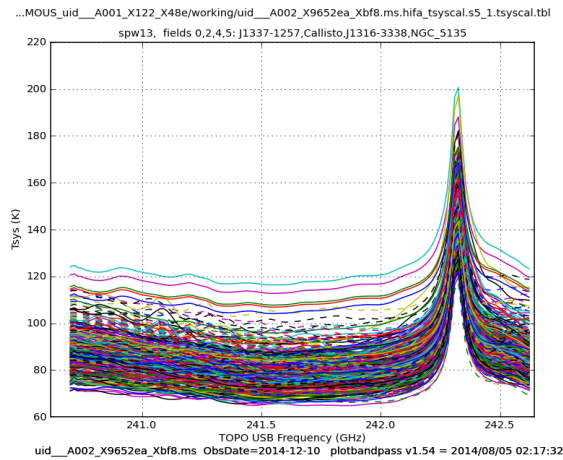


Figure 3.11: **Example:** Plot of time-averaged T_{sys} for spectral window 19, coloured by antenna. Note the intense line of T_{sys} at ~ 242.4 GHz which let’s presume an atmospheric absorption line at the same frequency (from calibration procedure of band 6 (compact), spw 13).

In Figure 3.11 and Figure 3.12 it is possible to appreciate the T_{sys} calibration results: where the latter has an emission peak (this is an atmospheric line as it is present in the same channels for all antennas) the data have an absorption feature, due to the greater opacity of the atmosphere; this disappears in the corrected data, which also changes the scale of the amplitudes that increase precisely for correction of the absorption.

The atmosphere’s absorption lines and the PWV cooperate with the creation of a signal phase-shift, called *phase-noise*. It has multiple repercussions on the data because it does not allow to reconstruct the exact position of the object in the sky. In the same time, it causes an underestimation of the average value of the calculated amplitude by integrating on the time duration of the scan:

$$\langle V \rangle = V_0 \exp \left\{ -\sigma_\phi^2 / 2 \right\} \quad (3.3.5)$$

The impact of the troposphere is peculiar to the millimetre bands as it is responsible for very fast phase displacement as a function of time (≈ 1 s). To fix it a radiometer

3.3 Data reduction

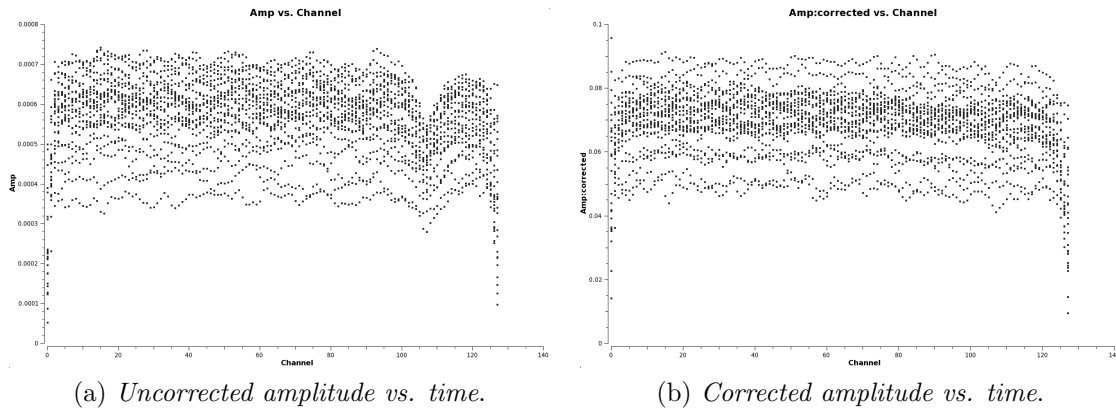


Figure 3.12: **Example:** A noticeable line of absorption is noted before correction. It disappears once the a priori calibration has been made. Plots have Amplitude vs Channel axis.

is mounted on each antenna of the main array which constantly monitors the water transition to 182.5 GHz⁷ in order to evaluate the amount of *Precipitable Water Vapor* (PWV), from which phase noise depends linearly⁸.

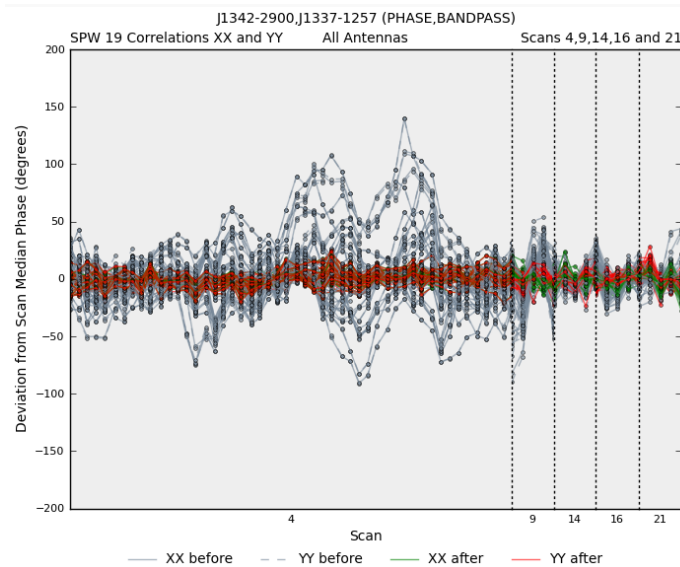


Figure 3.13: **Example:** Deviation from scan median phase before and after WVR application for band 6 (compact) - spw 19, all antennas.

The radiometer calibration results are shown in Figure 3.13: the plot shows the deviation from the scan median phase before and after PWV correction application. Points

⁷In other places, where high humidity makes saturate this water line transition, it is still possible to monitor the amount of water vapour by yielding other transitions and H_2O .

⁸The *phase noise* depends linearly on the length of the baseline: the closer two antennas are, the more similar the atmosphere they 'see' is.

are plotted per integration and per correlation.

This calibration step is contained in the `mystep 4` to `7` of the script for calibration in Appendix A.

Bandpass calibration

The purpose of the bandpass calibration is the correction of the frequency response across each spectral windows and polarization due to a different instrumental response to the channel variation for each baselines. To do this, it is necessary to observe a bright flat-spectrum point source and then calculate the frequency-dependent gain factors that make the spectrum observed agree with the true spectrum.

From the CASA task BANDPASS the amplitude and phase gains for each antenna, spectral windows and polarization as a function of frequency is determined and then applied to the source. Typically flat-spectrum quasars have all the spectral features needed to be used for this purpose. If the observation of a flat-spectrum object is impossible, it is sufficient to know beforehand the spectral index of the observed source to achieve the same result. In our cases the *bandpass calibrators* are the quasars J1337-1257 in band 6 observations, and J1256-0547 in the band 9 one. The calibrator is normally observed a single observation at the beginning of the execution block (EB) and it is assumed that the electronic instrumental response may be the same (for each single antenna) for the entire observation time. A further key assumption for calibration is that the time axis and the frequencies axis are independent of each other: the calculation of the Gain B_{ij} table requires in fact a time averaging to minimize the errors associated with gains. If this was done with the raw data, the temporal average would underestimate the amplitude of the signal, because raw data are not in phase to avoid this. It is enough to apply an “*on the fly*” calibration of phases in time.

This part of calibration is contained in the `mystep 13` band 9 script for calibration.

Phase calibration

This second step allows us to calibrate the amplitudes and phases for atmospheric variations in time for each antenna. For this purpose, the calibrator must be a point source at the center of the phases and close to the scientific target, so that the atmosphere seen by the instrument when pointing the target and the calibrator is the same. The phase calibrator should be observed periodically during the observation. The time span between two consecutive observations increases with observing frequency. Then, since the calibrator must be observed several times during the EB, the telescope’s re-pointing time is also reduced if it is close to the target.

Phase gains for each antennas should be evaluated assuming a reference antenna, which gain phase are set to 0. It is advisable to choose it at the center of the array so that the reference antenna shares part of the atmosphere with the other antennas⁹.

⁹This is mainly valid for antennae in extended configuration in Main Array. In the case of very compact configurations (and especially of ACA antennas) it is preferable to select the reference antenna externally in the array. This is because being very close the antennas share the atmosphere almost completely but the outer antennas are less likely to exhibit a high shadowing-factor.

3.3 Data reduction

An incorrect selection of the reference antenna (which presents errors during the observation) results in an erratic data calibration: for this reason the analyst will first check the antenna's validity by looking at the diagnostic plots in T_{sys} .

This part of the calibration is contained in the `mystep 15` of the band 9 script for calibration.

In this work, the phase calibrators are: J1342-2900 in the compact band 6 observation, J1321-2636 in the extended band 6, and J1316-3338 in the band 9 one.

Flux density calibration

Calibrating in flux density means converting the relative scale of the amplitudes in degrees Kelvin to the absolute one in Jy and scaling the gains to the same power. To do this, a calibrator whose flux is known and as constant as possible over the time is required, which is observed only once for every observation.

Normally, in the radio bandwidth bright flat-spectrum quasar are used, but in millimetric bands they are usually highly variable.

Alternatives are thermal objects such as planets, moons and asteroids. These sources however are all solar system objects and are not point-like sources. Their spectrum is not constant in frequency and time and may have emission lines that need to be suitably modelled.

In this work, the flux calibrators are: Callisto in the compact band 6 observation, Titan in the extended band 6 and J1337-129 in the band 9 one.

This part of the calibration is contained in the `mystep 11` in Appendix A script for calibration.

During the band 9 calibration step, we have updated the flux density model for the flux density calibrator multiplying it by a factor 0.84 (at the value of 1.39 Jy) compared to the value associated with it in the archived script.

The reference value of the flux density of the flux calibrator can be obtained in two ways: using the task CALFLUX, which returns the flux (in Jy) of a calibrator source at a given frequency (in GHz) getting it from the *ALMA Calibrator Source Catalogue*¹⁰. The second is by consulting the online catalogue directly.

After calibrating the data and reducing the calibrator images for the first time, we noticed that the flux density value that we found from the flux density calibrator was different from that given by the catalogue.

The issue was due to the fact that CALFLUX associated a wrong value to the calibrators. As shown in the Figure 3.14, these are two band 9 observations for J1337-129 on 2014-03-12 and 2015-05-31 (two days before the date of our observations).

The task associated the first observation value of 1.631 Jy as the flux density that is 0.84 times bigger than the real one (1.396 Jy) closer in time to our observation. We then changed the value associated with the flux density of the calibrator and again applied a calibration to the data.

¹⁰Available at <https://almascience.eso.org/alma-data/calibrator-catalogue> .

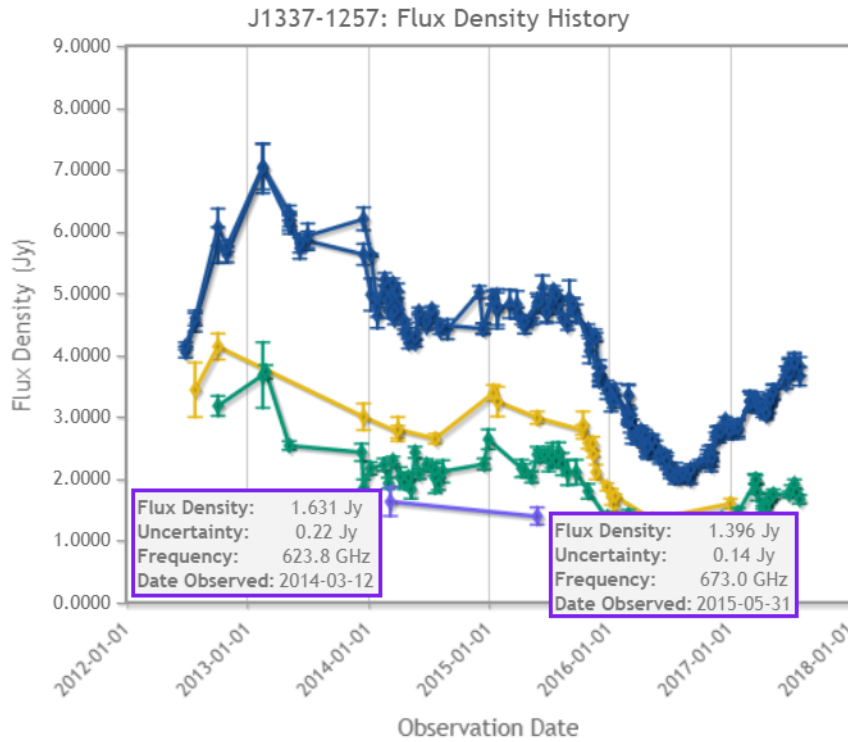


Figure 3.14: Record of phase calibrator observations accessible by the “ALMA Calibrator Source Catalogue”. The different colors highlight the observational band available: band 3 (in blue), band 6 (yellow), band 7 (in green) and band 9 (in violet) for J1337-129. The boxes show the specifications of the two band observations 9.

Data Calibration: CASA task’s specifications

CASA tasks require the specification of several parameters, some of which are of importance to understand how the calibration works: we list here the meaning of some of them.

- “*vis*” parameter that sets the dataset for which the corrections apply;
- “*caltable*” is the name of the correction table that is created;
- “*spw*” specifies the spectral windows for which corrections are calculated;
- “*field*” specifies the astrophysical object for which corrections are calculated (i.e. bandpass calibrator, phase calibrator) specifying field id(s) or field name(s);
- “*refant*” specifies the reference antenna we want to use in the phase calibration procedure (in band 9 calibration we have set it on the DV16 antenna).
- “*solint*” which specifies the time interval in which to find a solution.

Are possible two options for *solint*: if set equal to ‘int’, a solution for every scan is found or, if set equal to ‘inf’ only one solution for all the scans is found (see

3.3 Data reduction

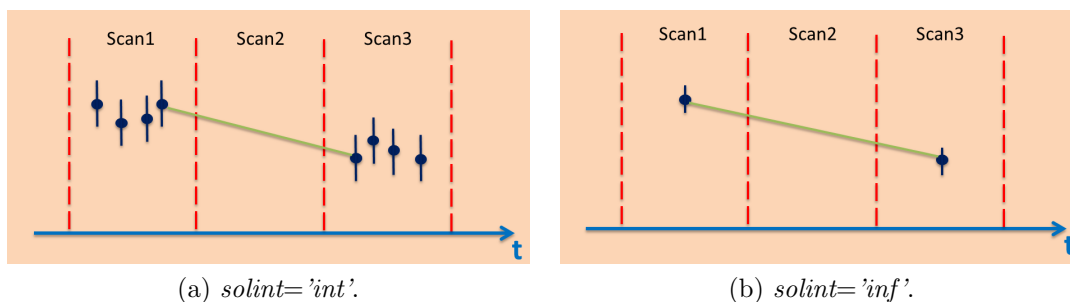


Figure 3.15: Graphic representation of how solutions are found when changing the $solint$ parameter. Notice how to the right, set $solint='inf'$, the error bar associated with the solution is smaller than the left one. This because the solution is mediated throughout the entire scan.

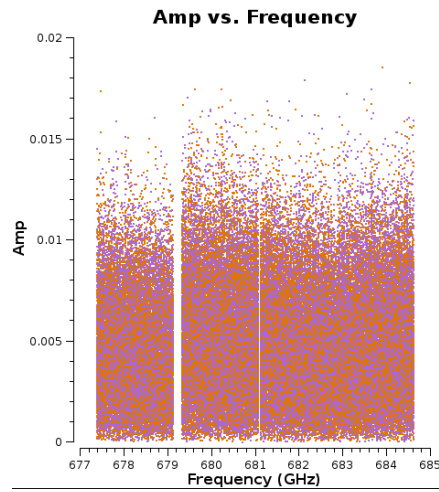
Figure 3.15).

For GAINCAL preliminary application, its value was set to int , specifying the time interval in which we wanted a solution ($int = 15.5 s$). It is interesting to note that this task, by operating an averaging on a scan, would need a preliminary phase correction. This is one of the reasons why the bandpass calibrator must be a bright source: in this case, the relative phase shift is smaller and the calculated averages are more significant. For BANDPASS, we have chosen $solint = 'inf'$ with $combine = 'scan'$, which finds a single solution across the time axis. This is in line with the assumption that electronic behaviour is constant all through the observing time.

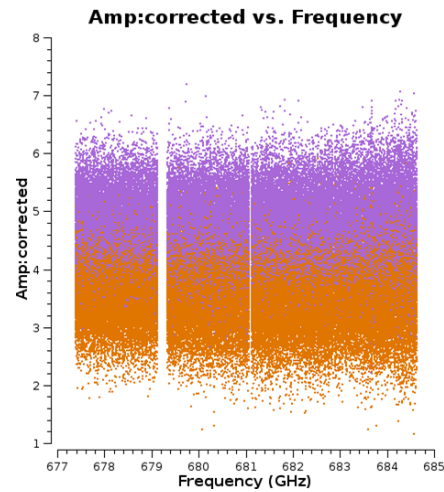
The task “ $solnorm$ ”, which if placed on the $True$ normalizes to one the found solutions: so the gain application does not alter the amplitude scale.

For the final application of GAINCAL, which was made on both calibrators, we have placed $solint = 'inf'$, thus finding a solution for each scan: this option is preferred to finding one for each integration as the signal to noise ratio increases by averaging on longer intervals. Referring to Figure 3.15, what we are interested in is not the punctual trend in scans 1 and 3, but the interpolation that will be done on scan 2, which contains the scientific target: then we choose for the scans 1 and 3 a single solution (which does not reflect the real atmosphere trend) in order to obtain a more significant solution for scan 2, since the associated error is smaller. Once also the FLUXSCALE task is applied (at the end of $mystep 15$), which corrects the GAINCAL calculated table for the correct flux values thus bringing the amplitude scale to Jy, it was possible to proceed with the actual application of the calibration of the calibrators and the target.

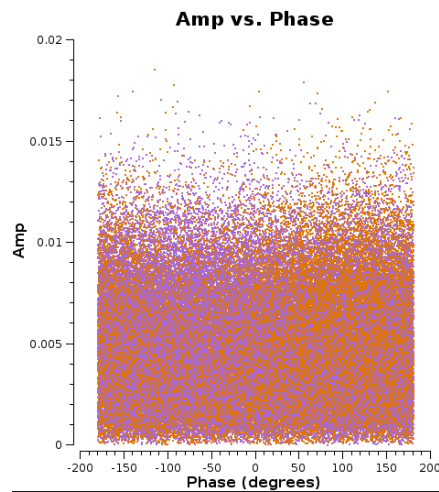
To apply the gain tables, we use the APPLYCAL task that requires to specify the type of time interpolation ($interp$) that we want to apply to each table.



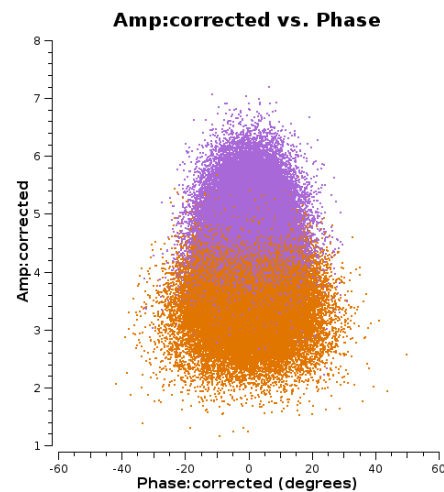
(a) *Amplitude vs. Frequency:* what we expect after calibration is to have the amplitudes around a constant value at the frequency variation, as we have a flat spectrum calibrator.



(b) *Amplitude vs. Frequency:* the positive result of the calibration is clearly visible: the two polarizations are positioned at a different, but constant, value of amplitude, which means that the calibrator is a polarized source.



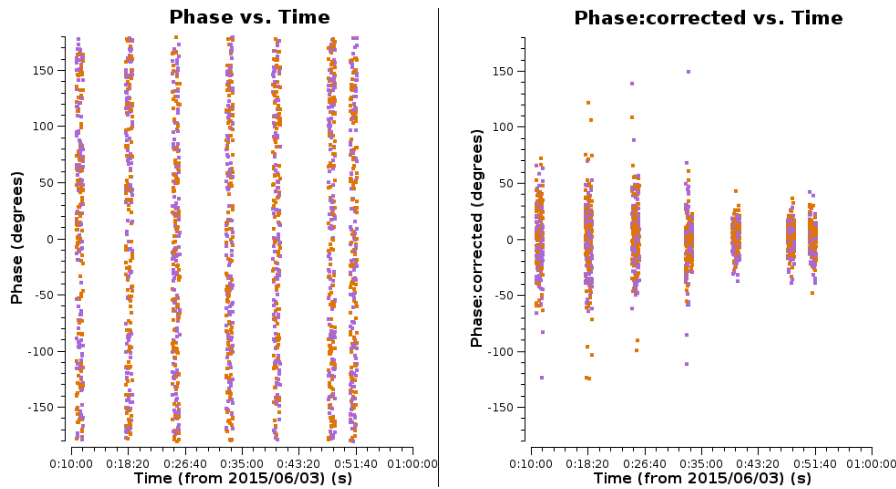
(c) *Amplitude vs. Phase:* what we expect after calibration is the same behavior as (a) and (b) and the phase to zero, as our source is faintlike.



(d) *Amplitude vs. Phase:* the positive result of the calibration is clearly visible as in (b): the polarization of the phase calibrator signal is also shown here.

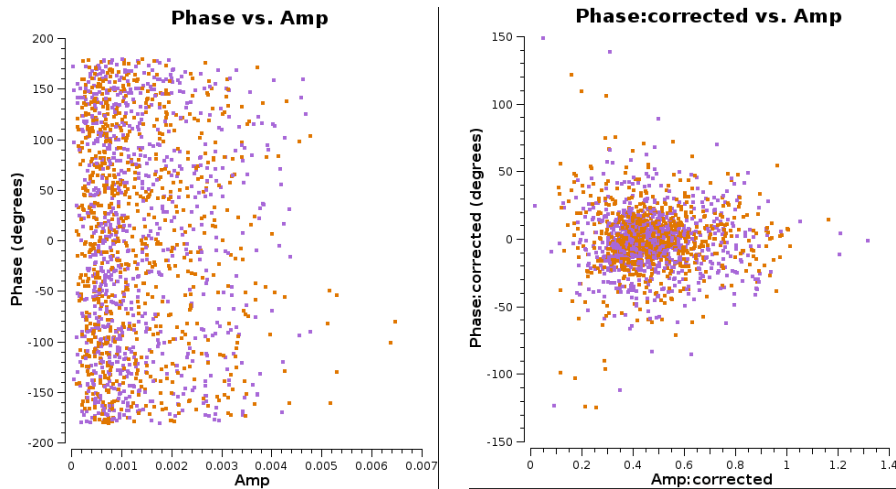
Figure 3.16: Bandpass calibration diagnostic plots for the band 9, pre-calibration (on left) and post-calibration (on right): the plot shows the visibility associated with J1256-0547. Coloured for polarization.

3.3 Data reduction



(a) *Phase vs. Time:* Notice how the phases are totally random and cover from $+180^\circ$ to -180° . The gain table should return the phases of the phase calibrator to the hypothesis of the reference model.

(b) *Phase vs. Time:* The correct phase calibration result is visible from the stretching of the phases around zero. There are some visibilities (around $+100^\circ$ and -100°) that are not corrected to zero, but these are not associated with any antenna in particular.



(c) *Phase vs. Amplitude:* The same graph in [Figure 3.16] (c), with inverted axes.

(d) *Phase vs. Amplitude:* This behaviour is also expected from the results of the [Figure 3.16] (d). The double polarization behaviour, in this case, does not occur because the thickening is around zero and not around the mean flux.

Figure 3.17: Phase calibration diagnostic plots for the band 9, pre-calibration (on left) and post-calibration (on right): the plot shows the visibility associated with J1316-3338. Coloured for polarization and averaged for channels.

We have chosen *linear*, that means that the electronics and atmospheric variation are assumed to have a linear in time¹¹.

In Figure 3.16 and Figure 3.17 we show significant plots used to verify the successful outcome of the calibration procedure.

After applying the gain tables to the band 9 dataset, we have identified other flags to be applied to the data. From the phase calibration results (Figure 3.17 (d)) we notice the presence of some visibilities that did not show the expected close trends (shown in Figure 3.18). We decided to flag such visibility as in part also corresponded with the “misbehaving visibility” in Figure 3.17 (b). After this procedure we recalculated the gain tables for the last time.

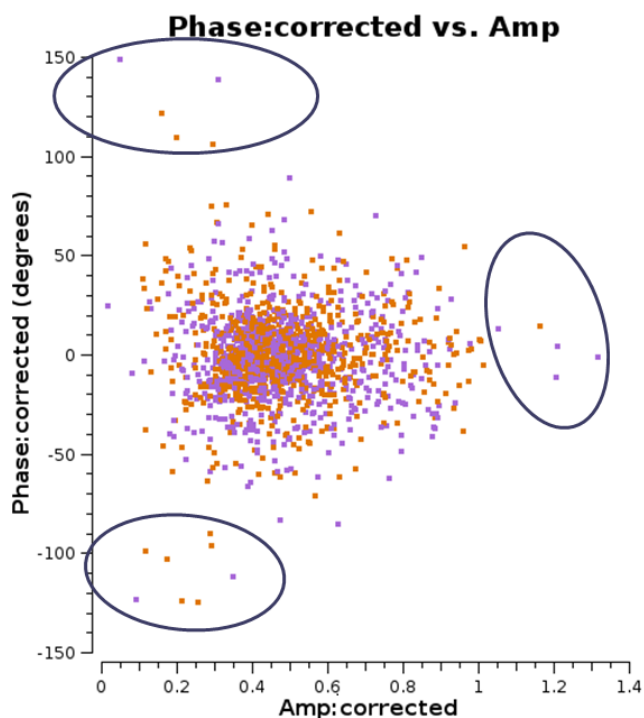


Figure 3.18: Same plot of [Figure 3.17 (d)] in which misleading visibilities are encircled.

Once calibrated the source, immediately showed strong lines already observable in the visibilities at ~ 227.43 GHz, ~ 682.14 GHz and ~ 241.61 GHz : these are the CO J = 2-1, J = 6-5 and CS J = 5-4 rotational transitions respectively. Here after there is an example (Figure 3.19) of one of our lines - CO(2-1) - to give an idea of how easy it is (at best) to recognize a molecular line emission if the calibration is successful in our source.

¹¹There are other options for the *interp* parameter. By setting *interp*='nearest', to each source is applied the nearest in time calibrator's solution. By setting *interp*='spline', the solutions between two consecutive scans of the phase calibrator are interpolated with a *n* degree polynomial and then solutions are applied to the intermediate source scan.

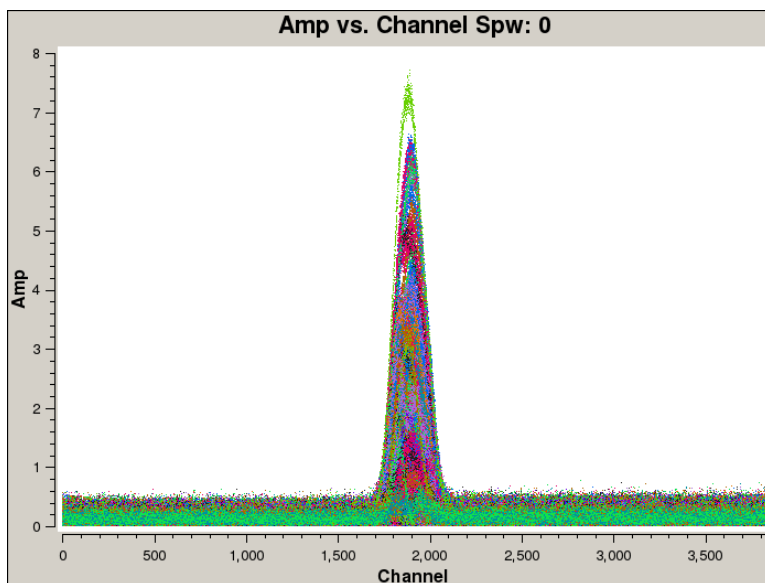


Figure 3.19: *Amplitude vs. channels*: The image represents the intense line of molecular transition of CO $J=2 \rightarrow 1$ in the spw 0 of the two concatenated datasets, time averaged.

3.4 Data Imaging

In these sections, we present the results of the imaging procedure of the data. Initially, the three data sets are reduced separately, producing a continuum image and an emission line data cube for each available molecular transition and each antenna configuration. Finally, once we have checked the quality of the images, we concatenate band 6 observations and imaged it as a single dataset.

3.4.1 Imaging procedure

An interferometric instrument, as we have said, returns data values for visibility only at the points of the UV plane where it was sampled. This means, in other words, that the instrument does not see informations about the entire Fourier transform of the brightness distribution but samples only a parts of it; the observed visibility is thus the product of the ideal one with a function called *Sampling Function* (S), which depends on the parameters of each observation, such as the number of antennas, their configuration, the duration of the exposure, the frequency and the bandwidth:

$$V^{cal} = V^{ideal} \cdot S \quad (3.4.1)$$

where the apex *cal* indicates that the visibility observed has already been calibrated. Knowing that a visibility is the *Fourier Transform* (FT) of the brightness distribution and recalling the *convolution theorem*, one can proceed with anti-transformation and write:¹².

¹²The convolution theorem states that the Fourier Transform of the convolution of two functions

$$FT^{-1}(V^{cal}) = FT^{-1}(V^{ideal}) \cdot FT^{-1}(S) \quad \leftrightarrow \quad I^{dirty} = I^{clean} * B^{dirty} \quad (3.4.2)$$

The right equation indicates that the "dirty" image¹³ is the convolution between the "clean" (true) image and the so-called *dirty beam*, which represents how the tool "sees" a point source at the center of the phases.

The **clean operation** is exactly what allows to rebuild I^{clean} from I^{dirty} . There are several algorithms developed for this purpose. The CASA clean task is based on the *Högbom's algorithm* (Högbom [1974]).

The algorithm is based on a fundamental assumption: *any brightness distribution can be divided in independent point-sources*. That said, it proceeds as follows:

1. We construct the S sampling function, obtained by replacing at each point of the UV plane for which a visibility was measured, an ideal visibility with amplitude 1 and phase 0 (corresponding to a point source in the center of the phases). Our UV-planes are shown in Figure 3.7;
2. By anti-transforming S we find the *dirty beam*;
3. We construct the *dirty image* by using the Fourier's anti-transformation of the observed visibility;
4. In the *dirty image* we find the position of the peaks of intensity, which is reported as a point source (\sim a Dirac Delta) in the so-called *clean components* list;
5. The found peak intensity is multiplied by a *damping factor* (called "gain loop") and by the dirty beam before it is subtracted from the dirty image. At the end of this procedure, we get the *residual map*;
6. This operation is repeated, continuing to subtract the sources identified from the map of the residual, up to a limit that must be a priori fixed. In this regard, we can take advantage of three options: stopping this procedure when we find a peak with intensity equal to a given threshold typically fixed as a multiple of the theoretical noise (defined by the eq. (3.1.8)); completing a given number of cleaning cycles by defining their number using the appropriate parameter *niter*; specifying the minimum flux densities ratio between the residual maps of two consecutive clean cycles. The last choice is usable by specifying the value of that ratio with the parameter *gain*.
7. Once the iterative process is completed, the map of the residuals should appear fairly uniform and with a signal comparable to the expected RMS. It is then added to the point components found convolved with the dirty beam, thus reconstructing the image. This operation is called *restoring*.

is equal to the product of their transformations: $FT(f * g) = FT(f) \cdot FT(g)$

¹³That is obtained directly by an inverse Fourier Transform (FT^{-1}) of the calibrated visibility (V^{cal}).

3.4 Data Imaging

Once the first cycle is completed, the analyst can access the residual map through a viewer. This allows us to evaluate the uniformity of the residual map and stop the procedure if the residual are sufficiently uniform, or to select an extraction mask that forces the algorithm to look for solutions in the selected regions. This latter possibility is a powerful tool in the hands of the analyst because the quality (and the truthfulness) of the final images depends on where and if the masks be set. On the one hand, if an observation has a lot of noise, but the analyst knows a priori the source emission zones, this option greatly improves the quality of the final image because it serves as an aid to the algorithm for selecting the peaks to associate with the astrophysical emission. On the other hand, if the mask is forced on regions with no emission, noise peaks could be integrated as true signal. So exploiting the masks can prove to be very dangerous because it can improve (or worsen) the final results and translate into a correct (or wrong) scientific interpretation.

In our work we have always used this opportunity by applying some caveat. Initially, we reduced every image automatically, setting a large number of clean cycles and a 3σ threshold. Next we repeated the clean procedure interactively, overlapping the contours of the cleaned image above the residual map of the image that we were cleaning. This allowed us to recognize the areas that certainly contained emission and extend the mask to the connection areas between the regions automatically identified.

The practical application of clean procedures requires discretization of FT using the *Fast Fourier Transform* (FFT) algorithm developed by [Cooley and Tukey \[1965\]](#). With FFT, the functions $V(u, v)$ and $I(x, y)$ are expressed as rectangular matrices of sampled values with uniform increments in the variables involved (see [Figure 3.20](#)). This procedure is called *gridding*. Every cell in the UV-plane, define a region in the image plane. The rectangular grid points in which the visibility plane is subdivided are Fourier-transformed one by one and added to the brightness distribution map, by smoothing the flux on the surface of the image-plane cells.

Ideally, there should be at least one visibility, or a small number of them, within each UV-cell. The size of this cells in the visibility plane can not be smaller than the minimum baseline of the array because we might include empty cells in the clean procedure whose would unnecessarily increase the computation time without contributing to the image. We can fix this cell size by setting the value of *grindmode*.

Another limit that must be imposed is the size of the cells of the image plane (the pixels) as it affects the computing time that progressively grows with the number of pixels.

Using the [Cooley and Tukey \[1965\]](#) algorithm it is advised to set the total image size at least equal 2 times of FoV, to include all the transformed signal but preserving an image size as $[2^n \cdot 10, 2^m \cdot 10]$ pixels¹⁴. The dimensions of the cells are instead fixed by the *Nyquist's Theorem*¹⁵ in a value between $\theta_{ris}/3$ and $\theta_{ris}/5$ to ensure good sampling without excessively increasing the computation time.

¹⁴whit n and m natural numbers.

¹⁵Nyquist's theorem states that, in order to correctly reconstruct a signal, the sampling rate must be at least twice the Frequency (maximum) of the signal itself.

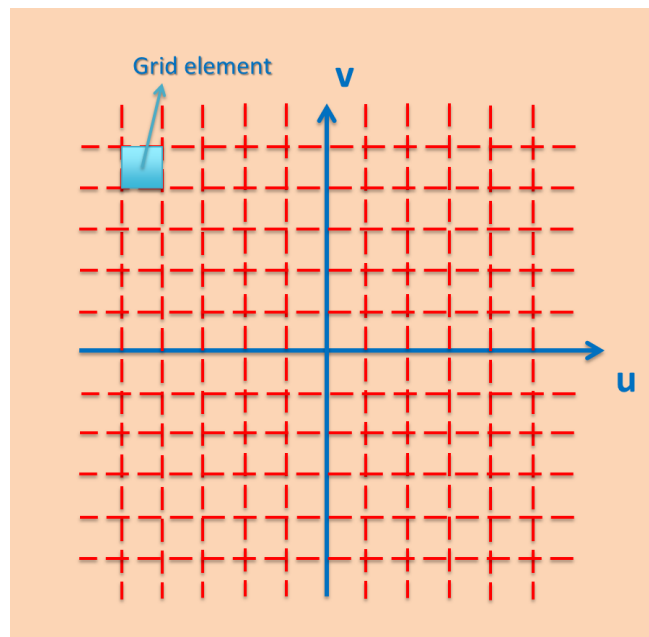


Figure 3.20: Example how the UV-plane is subdivided into cells of the same size for the application of an FFT. The same concept is the basis for the pixel subdivision of the image plane

Furthermore, since the baselines density in the UV-plane is not uniform on all scales, the density of the visibilities will also change at different spatial scales, this is inexorably translated to the image properties as well. Using the *weighting* parameter, we can change the final image characteristics. With this parameter we give more or less weight to certain visibilities in our data set, based on their location in the UV-plane. Emphasizing long-baseline visibilities improves the resolution of the image, while emphasizing shorter baselines improves the surface brightness sensitivity. There are three main weighting schemes that are used in interferometry:

- **Natural weighting:** UV-cells are weighted with values inversely proportional to the noise variance of the visibilities. Data visibility weights are gridded onto a uv-cell and averaged. More visibilities in a cell will thus increase the cell's weight, which will usually emphasize the shorter baselines that are typically the most numerous. Natural weighting therefore results in a better surface brightness sensitivity, but also a larger beam and therefore a degraded resolution.
- **Uniform weighting:** The weights are first gridded as in natural weighting but then each cell is corrected such that the weights are inversely proportional to the sampling density function. Compared to natural weighting, uniform weighting usually emphasizes the longer baselines that are usually less dense. Consequently the beam is smaller, resulting in a better spatial resolution of the image. At the same time, however, the surface brightness sensitivity is reduced compared to natural weighting.

3.4 Data Imaging

- **Briggs weighting:** This scheme was developed in Briggs [1995] and provides a compromise between natural and uniform weighting. It can be controlled with the *robust* parameter where *robust*= -2 is close to uniform and *robust*= 2 is close to natural weighting. Briggs weighting therefore offers a compromise between spatial resolution and surface brightness sensitivity.

If necessary, it is possible to apply additional weight to visibility on the UV-plane. This option can be used by setting the parameter *wtaper*= 'true'. In this case, the weight of visibility is multiplied by a Gaussian function that lowers the visibility weight associated with the longer baselines (this is known as 'outertaper') or the central one (in this case an 'innertaper'). The effect is a smoothing the flux density in the image plane with the consequence of decreasing the rms at the expense of image resolution.

3.4.2 Our results

The first two parameters that are required by the CLEAN task are the name of the dataset (*vis*) and the name of the unscheduled file produced by the clean (*im-name*). To these, we add the target for which we want to create the image (*field*) and the selection of spectral windows, with the channels specification to differentiate the continuum from the emission line images (*spw*).

We have also to specify the pixel dimensions of the image we want (parameter *im-size*) and the size of the single pixel in arcoseconds (*cell*). Subsequently, we set the maximum size of the image based on observation FoV with the parameter *imsize* ($\sim 2 \times \theta_{FoV}$).

For the second, we have first calculated the resolution of the synthetic beam according to eq. (3.1.6); for the calculation of cell-size in band 6, while respecting *Nyquist's Theorem*, we have chosen:

$$cellsize = \frac{\theta_{ris}}{5} \quad (3.4.3)$$

For band 9 in which we used a pixel size equal to $\theta_{ris}/4$.

To constantly monitor the quality of the imaging procedure, we decided to reduce all the images by setting the parameter *interactive* =True. We generally set a high number of cycles by specifying the value of the parameter *niter*. This choice was made to prevent the clean procedure from stopping to reach the maximum number of cycles before the residues were uniform.

The continuum images

As first we produced the continuum image. For both data sets we have selected the channels associated with the continuum: this was done by considering both the continuum and the line spectral windows but being careful to remove from the selection the channels that might contain the line, in order not to risk to contaminate the continuum image.

After the concatenation of band 6 data, the available spws were 8: 4 for the extended

configuration and the same for the compact one. The channels of the two configurations were associated with slightly different frequencies. Once the channels of each spw are selected, CASA automatically associates the correct flux at each frequency in the CLEAN procedure.

For this stage (and also for the production of the line datacubes), an important parameter is the *weighting*, which indicates how the various baselines in the image reconstruction are “ weighed ”. The default value *'natural'* leads to the use of the *'natural'* visibility weights.

In this way, the resolution of the image will be defined by the actual density of the baseline on the UV-plane: a sampled plane at its center (and less externally) will have a worse resolution than a totally opposite configuration.

CONTINUUM	Band 6	Band 9
<i>vis</i>	#CODE.ms.split.cal	#CODE.ms.split.cal
<i>field</i>	0 : 0 ~ 1550; 2250 ~ 3839, 1, 2 : 0 ~ 2300; 3150 ~ 3839 , 3 : 0 ~ 1450; 2400 ~ 3839, 4, 5 : 0 ~ 2350; 3350 ~ 3839 ,	0 : 0 ~ 54; 87 ~ 127, 1 ~ 3
<i>mode</i>	mfs	mfs
<i>niter</i>	100000	100000
<i>gain</i>	0.1	0.1
<i>threshold</i>	0.038 mJy	0.53 mJy
<i>interactive</i>	True	True
<i>imsize</i>	[2048, 2048]	[1500, 1500]
<i>cell</i>	0.032 arcsec	0.02 arcsec
<i>weighting</i>	briggs	briggs
<i>robust</i>	0.5	0.5
<i>wvtaper</i>	False	True
<i>outertaper</i>	—	0.30 arcsec

Table 3.5: *Summary of cleaning parameter for the continuum images.*

Our choice, for band 6 observations, was a compromise between resolution and sensitivity, imposing *weighting = 'briggs'* with the specific *robust = 0.5*: in this way we got a good resolution without worsening the signal-to-noise ratio¹⁶.

In Figure 3.21 is shown the difference between the images cleaned with *natural* and *briggs (robust=0.5)* respectively.

For band 9 we applied a further weight to the visibility by setting the parameter *wvtaper = True*. With this solution the RMS drops considerably but a small part of

¹⁶*robust* can range in the range of [-2,2], where the extremes correspond to *weighting uniform* and *natural* respectively

3.4 Data Imaging

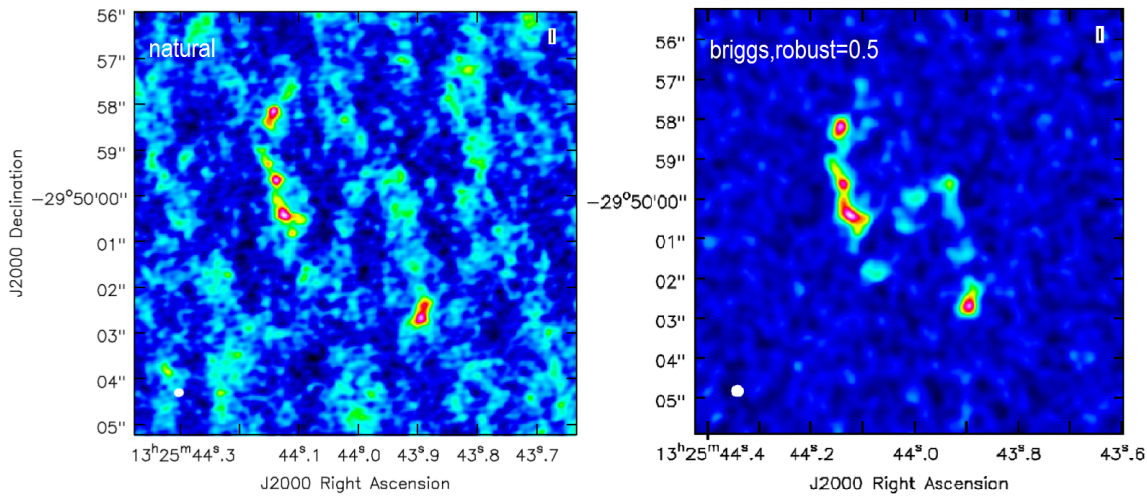


Figure 3.21: *Different calibration results with weighting = 'natural' (left) and weighting = 'briggs' (right): note the far less visible noise in the right image, lower than a factor 0.78 compared to the left image.*

the flux is lost.

However, we kept the longest baselines (setting *outertaper*=0.30 arcsec), so that we did not lose too much in image resolution. It is critical to specify when we want to finish cleaning iterations, as explained above. In this case, we set a large number of iterations¹⁷ by the parameter *niter* = 100000 and we activated the interactive window that allowed us to select a mask where to look for the peaks of the image and stop the procedure when the map of the residuals seemed uniform. In Table 3.5 are shown the parameters set for the continuum image clean procedure are summarized, while Figure 3.22 shows the final results of the clean procedures.

¹⁷To ensure that the algorithm did not block the cleaning process until it was satisfied with the uniformity of the residual map.

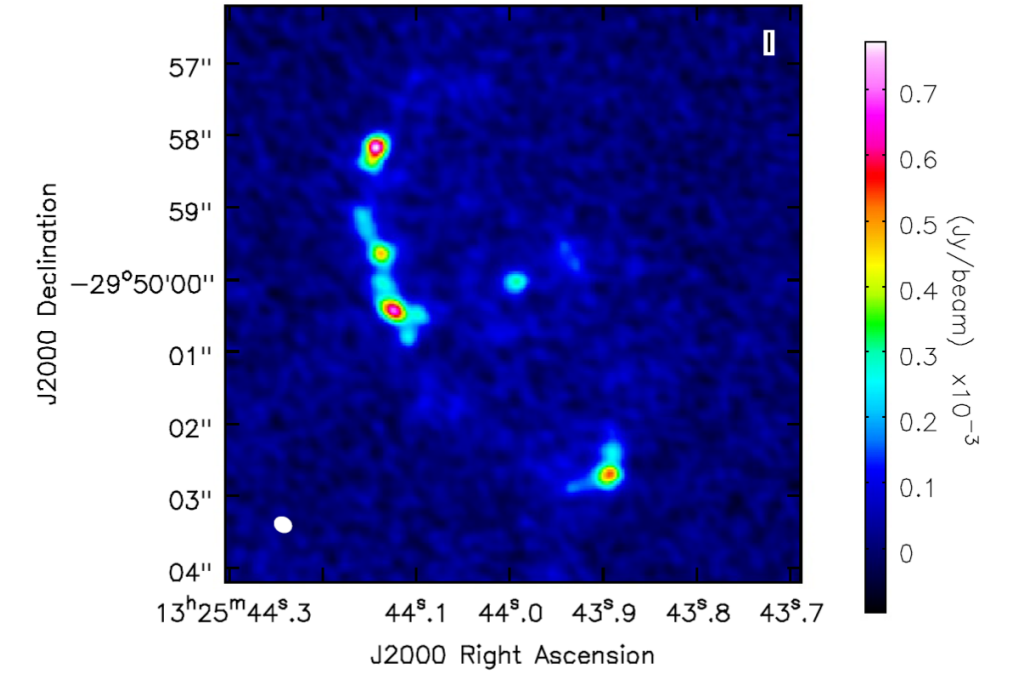
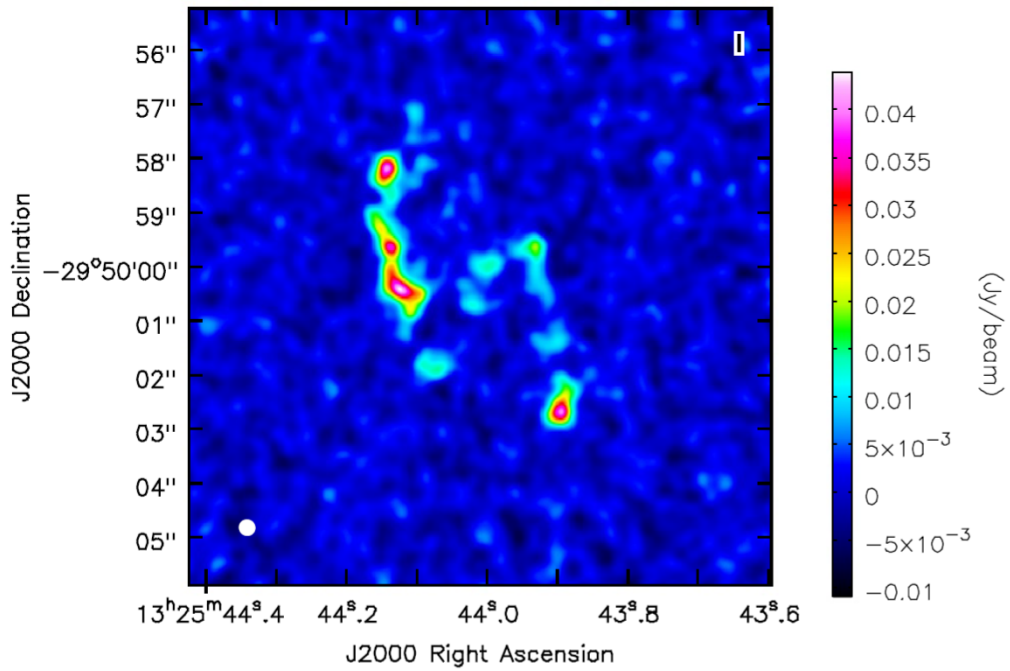

 (a) *Continuum band 6*

 (b) *Continuum band 9*

Figure 3.22: *Continuum images in band 6 (top) and band 9 (bottom). The size of the beams is comparable: $\theta_6 : 0.25'' \times 0.20''$ in band 6 and $\theta_9 : 0.30'' \times 0.29''$ in band 9. However, the noise is strongly different: $\sigma_6 \sim 1.9 \times 10^{-5}$ (band 6) and $\sigma_9 \sim 2.11 \times 10^{-3}$ (band 9); two orders of magnitude of difference.*

3.4 Data Imaging

The line images

The first step to do in order to have a line emission data cube from a complete dataset is the subtraction of the contribution of the continuum. This is done with the appropriate UVCONTSUB task in CASA.

At this point we proceeded with the clean, modifying some parameters: first, we imposed a *threshold* of 0.038 *mJy* for band 6 and 0.53 *mJy* for band 9, corresponding to approximately 1 *sigma*. Though we have set these thresholds, we were interested in stopping the interactive clean procedure when the residual map seemed to be uniform.

LINE CUBEs	CO(2-1) [Figure 3.24] and [Figure 3.25]	CS(5-4) [Figure 3.26]	CO(6-5) [Figure 3.23]
<i>field</i>	0 : 1600 ~ 2200, 3 : 1500 ~ 2350	2 : 2350 ~ 3100, 5 : 2400 ~ 3300	0 : 50 ~ 95
<i>mode</i>	velocity	velocity	velocity
<i>nchan</i>	-1	-1	-1
<i>width</i>	10 km/s	15 km/s	15 km/s
<i>niter</i>	500000	500000	200000
<i>gain</i>	0.1	0.1	0.1
<i>threshold</i>	0.038 mJy	0.038 mJy	0.53 mJy
<i>interactive</i>	True	True	True
<i>imsize</i>	[2048, 2048]	[2048, 2048]	[1024, 1024]
<i>cell</i>	0.032 arcsec	0.032 arcsec	0.02 arcsec
<i>restfreq</i>	227.43 GHz	241.62 GHz	682.14 GHz
<i>weighting</i>	briggs	briggs	briggs
<i>robust</i>	0.5	0.5	0.5
<i>uvtaper</i>	False	False	True
<i>outertaper</i>	—	—	0.30 arcsec

Table 3.6: Summary of cleaning parameter for the line images.

Also to get a data-cube as a result, we used the *mode* parameter: it default to '*mfs*' for continuum and produces only one image for all the available data. Instead, choosing '*channel*' or '*velocity*' we can have an image per channels or velocity-bins respectively. We report the results obtained from this last option since we consider them more relevant for our scientific purposes.

The CLEAN task requires new parameters, including the reference rest frequency *restfreq*.

We could choose to set the line frequency of laboratory, ν_{rest} , or the reshifted one. This last was estimated from the AGN emission line peak for each molecular lines (if

possible) or using the correct laboratory frequency for the cosmological redshift of the source (see § 2 for more information on the AGN position and the redshift).

This latter solution has been considered to be the best because it allows the study of the kinematic of the gas (in § 4) by placing us in the comoving system of the galaxy. Finally, we need to enter a value for *width*, that is, the velocity step we want to establish between an image and the next in the cube.

To do this, we need to convert the frequencies observed to the velocity. This step can be done using the relationship:

$$\boxed{\frac{\Delta\nu}{\nu} = \frac{\Delta v}{c}} \Rightarrow \Delta v = c \cdot \frac{\text{channel width [MHz]}}{\text{line frequency [GHz]}} \quad (3.4.4)$$

Concerning band 9 observations, we chose to maintain a channel width of 15 km/s because the noise was so high that we could not drop below this threshold without losing much of the signal emitted by the source.

For band 6 we produced three different cubes: 7 km/s, 10 km/s and 15 km/s. Though the noise increases by narrowing the channel width, this was so low that we could allow for higher spectral resolutions (and hence to have a more detailed idea of the observed gas behaviour) without losing its flux.

We decided to show in Figure 3.24 and Figure 3.25 the results of the cube at 10 km/s because it seemed the right compromise between RMS and the spectral resolution since the sensitivity, as defined in the equation (3.1.8), is inversely proportional to the square root of the spectral resolution.

The figures below (Figure 3.23, Figure 3.24, Figure 3.25 and Figure 3.26) show the results of the data cubes imaging procedure. In Table 3.6 the clean parameters that produce the following images are summarized.

3.4 Data Imaging

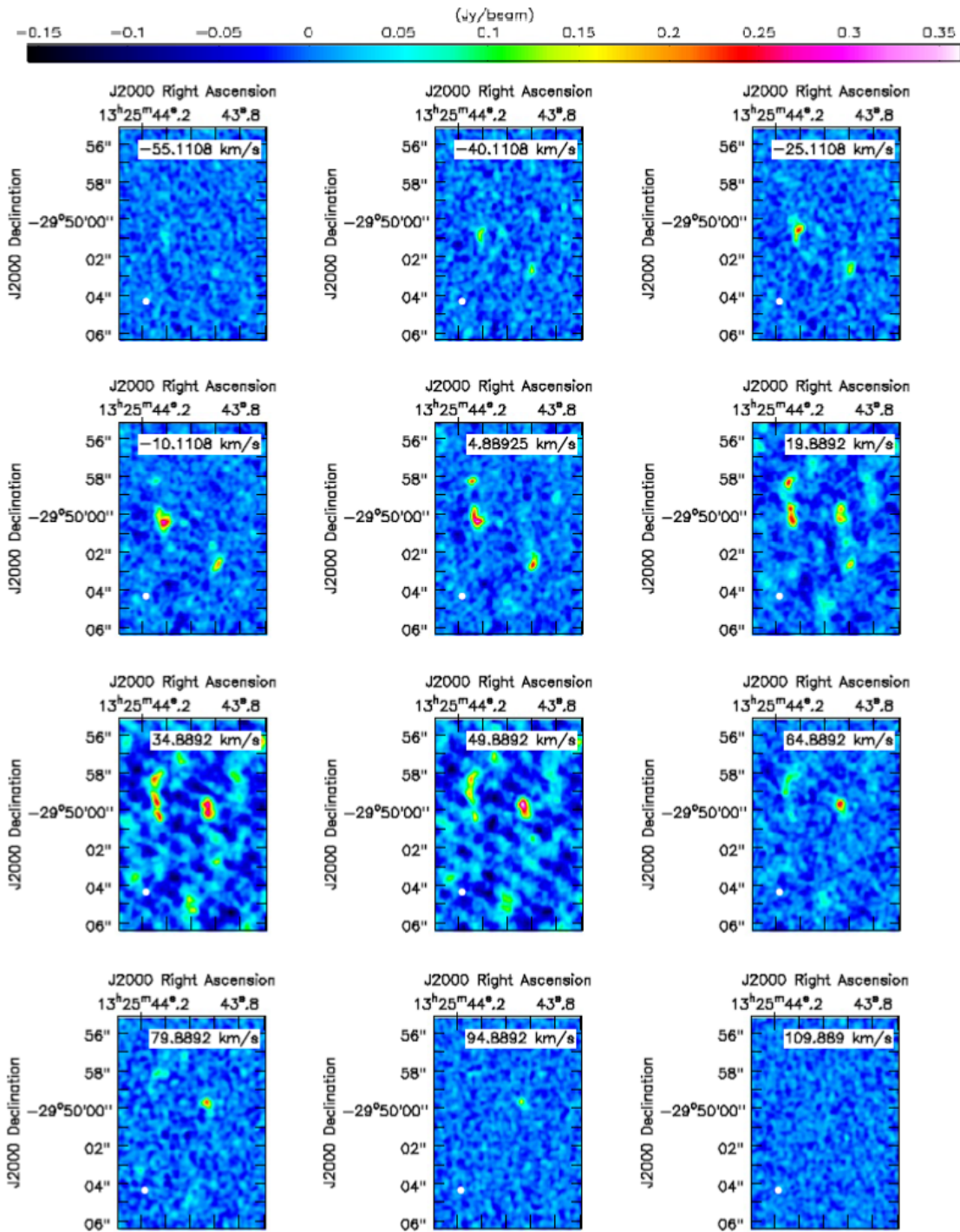
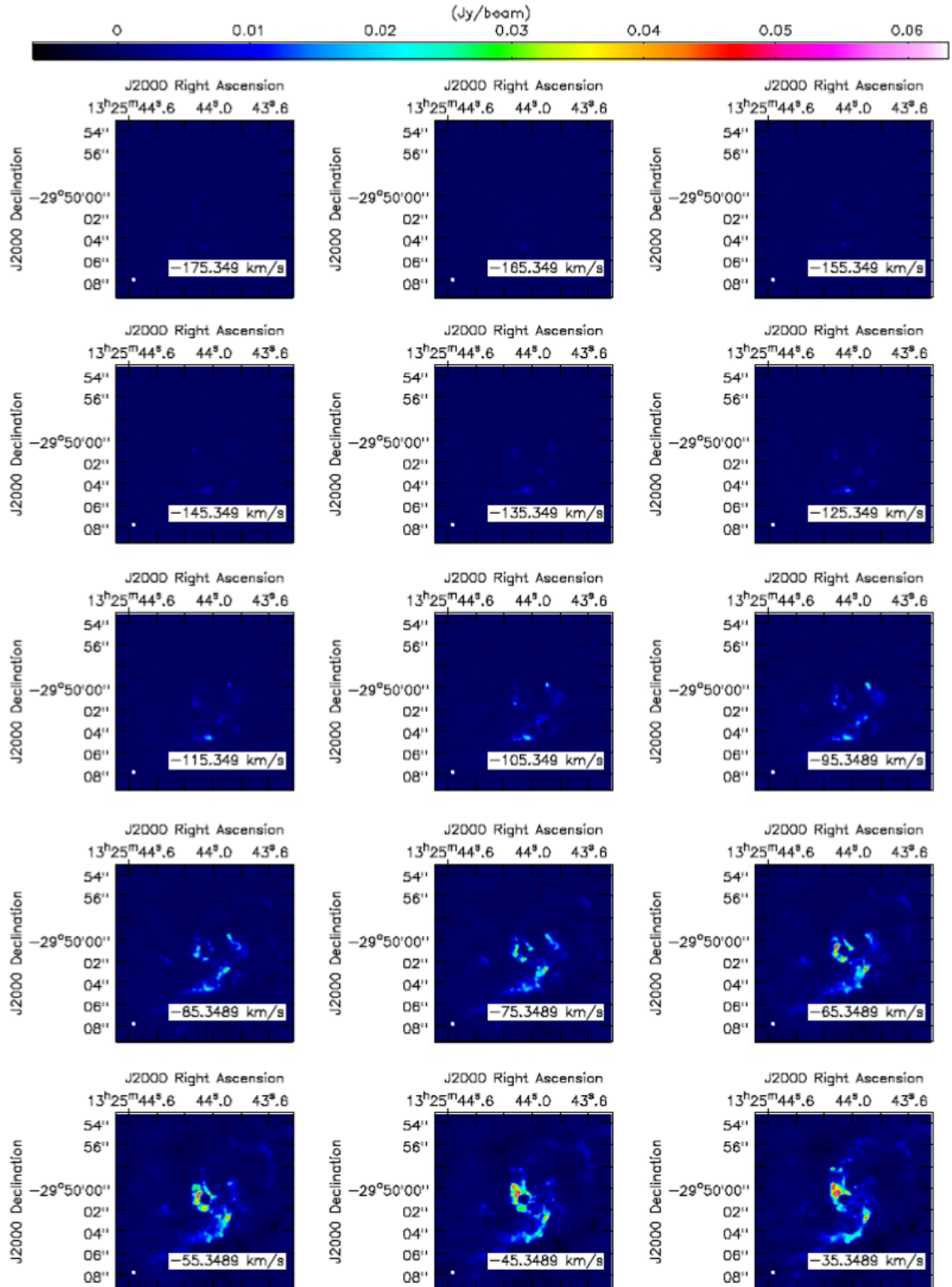


Figure 3.23: *CO(6-5) line emission data cubes.*


 Figure 3.24: $CO(2-1)$ line emission data cubes (continue in [Figure 3.25]).

3.4 Data Imaging

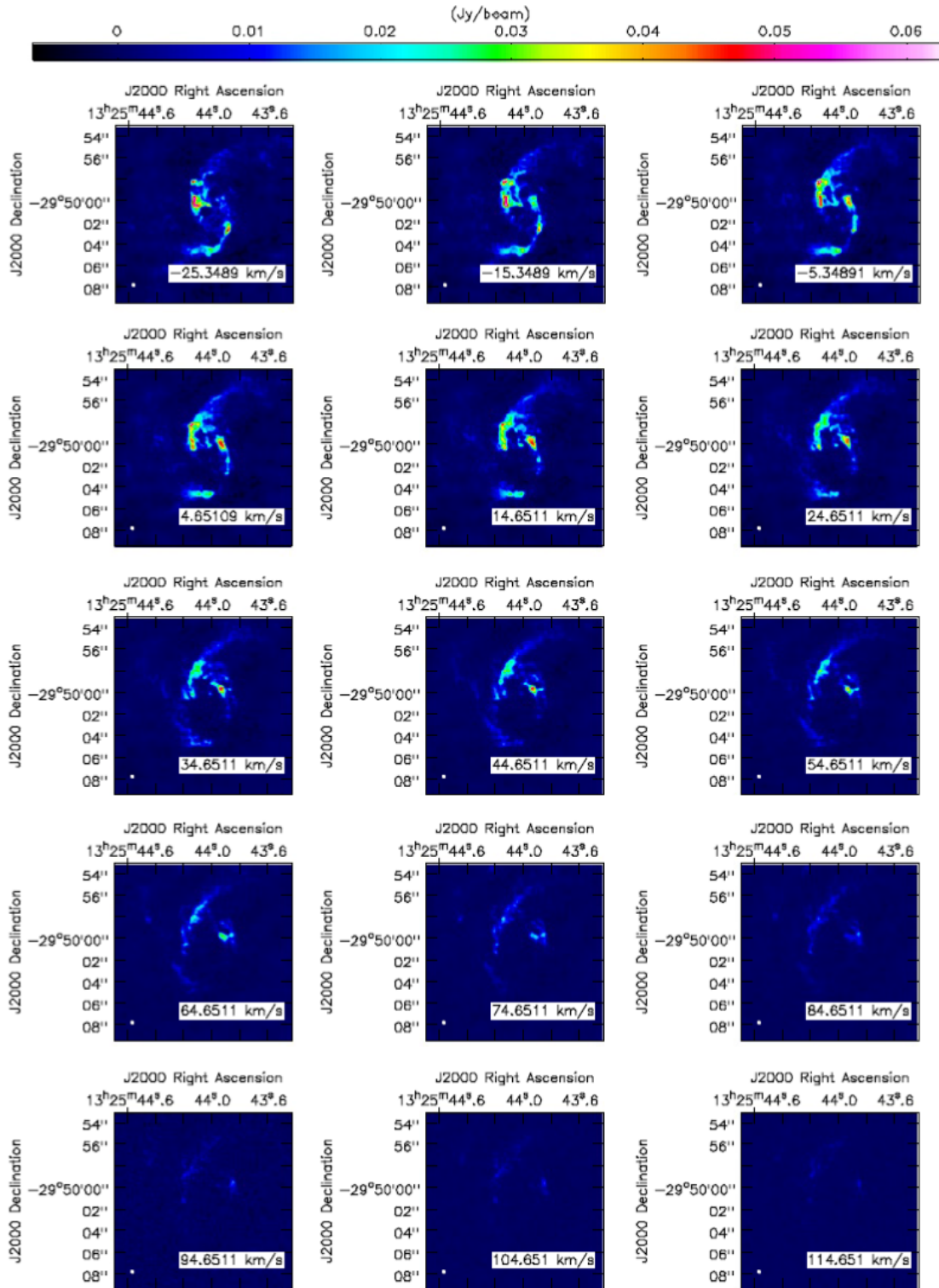


Figure 3.25: (second part) *CO(2-1)* line emission data cubes.

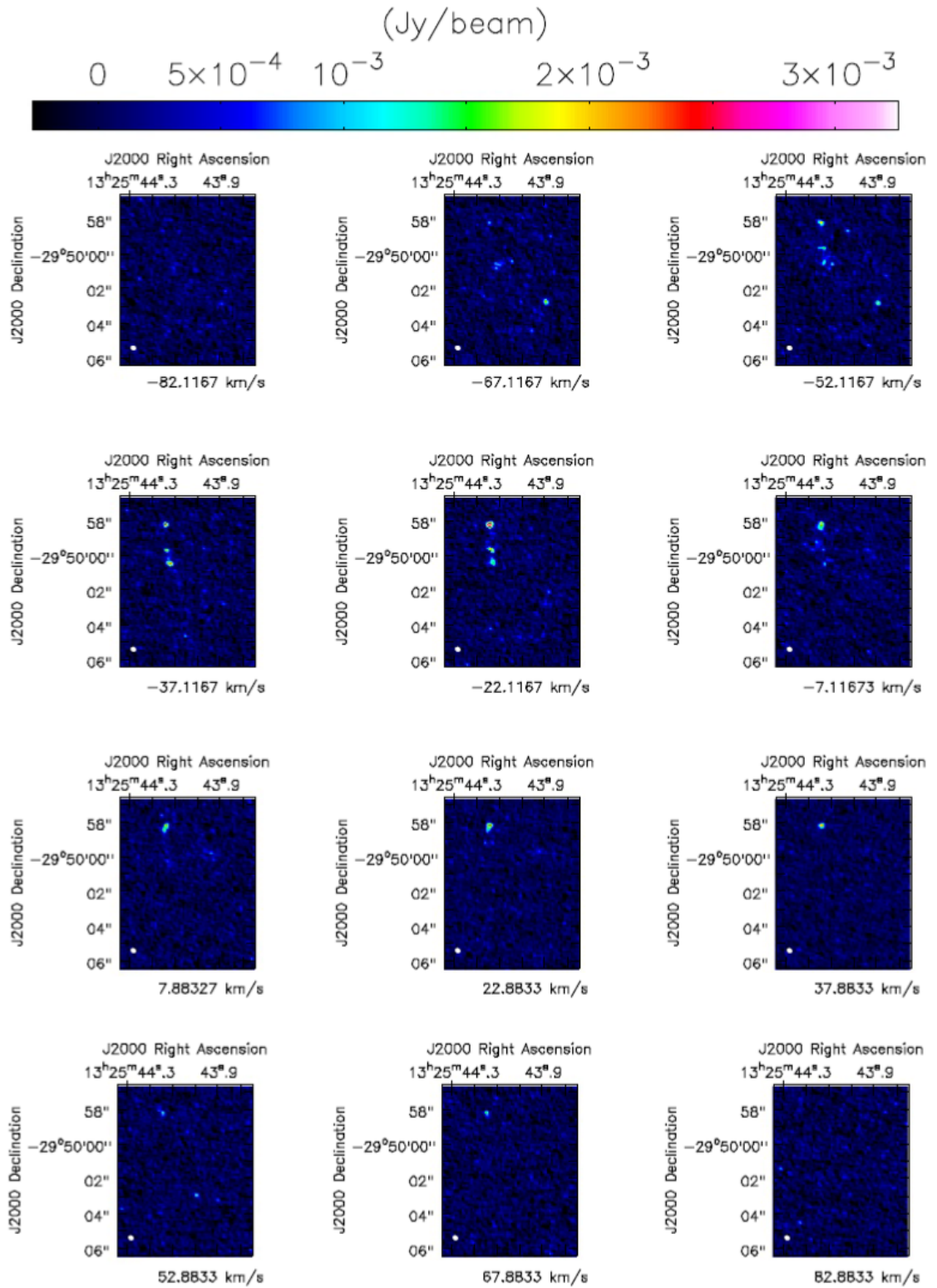


Figure 3.26: *CS(5-4)* line emission data cubes.

Chapter 4

The 3^D BAROLO software: a new way to investigate gas kinematics

Abstract

In order to interpret the physical processes associated to each of the different gas components found by analysing the ALMA data of NGC 5135, we applied the software 3^D BAROLO (described in the chapter) to model the kinematics of the gas motion.

The purpose of this chapter is to illustrate the basis of the software and the way it works applied to data. The first paragraph briefly summarizes the importance of the study of the spiral galaxy rotation curves, which contains the kinematic informations necessary to describe the observed gas motion in the analyzed data.

The central section summarizes the main parameters of 3^D BAROLO, how software sets the initial values of the free parameters and how errors are calculated.

The last paragraph summarizes the strengths and weaknesses of the software.

4.1 Introduction on the Spiral Galaxy dynamics:

In order to understand the gas kinematics within galaxies, we need to briefly introduce what is known of the star and gas motions in spiral galaxies.

In a good approximation, we can consider Spiral Galaxies as thin disks of gas and stars rotating around a common center.

The structure is maintained by the *gravity force*, which drives the stars and gas rotation in approximately circular orbits .

In *Newtonian approximation*, we can expand this concept by claiming that centrifugal acceleration is perfectly balanced by gravity:

$$\frac{m V^2(r)}{r} = \frac{G M(r) m}{r^2} , \quad (4.1.1)$$

where m is the test-star mass, moving with velocity $V(r)$ on a circular orbit of radius r ; G is the *gravitational constant* and $M(r)$ is the enclosed mass inside the stellar orbit.

By measuring the velocity at which stars and gas are moving, we can calculate the amount of mass needed to hold them on circular orbits. This type of study was presented for the first time at the beginning of the 20th century (see Pease [1918]), when the first galaxy *rotational curve* was shown by plotting the value of the velocity as a function of distance from the galactic centre (see Figure 4.1).

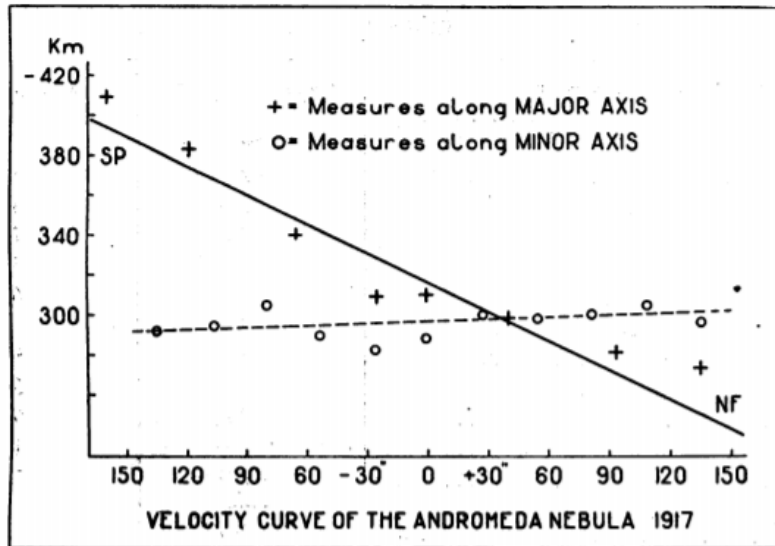


Figure 4.1: The observed radial velocities in Andromeda Galaxy (M31) obtained from the analysis of the absorption-line stellar spectra: the velocities along the major axis (solid line) and along the minor axis (dashed line) show different behaviour. Image is taken from Pease [1918].

By using the *Doppler shifts* of stars moving in the galactic plane, the observation of a velocity variation along the major axis of the galaxy was observed. The same was

not observed along the minor axis, where the velocities were constant with increasing distance from the galactic center.

This behaviour was immediately associated with a rotation around the galaxy axis. In the simplest case of spherical symmetry, it is easily demonstrable that, if the rotation curve of a galaxy is known, it is possible to obtain the radial density profile of matter, $\rho(r)$.

Starting from equation (4.1.1) we can write:

$$\int 4\pi r^2 \rho(r) dr = M(r) = \frac{V^2(r) r}{G} \quad (4.1.2)$$

We can then investigate the radial distribution of matter in galaxies considering the stellar velocity. This kind of study can be applied to various astrophysical topics: the formation of galactic structures, their evolution, the study of internal morphology, etc.

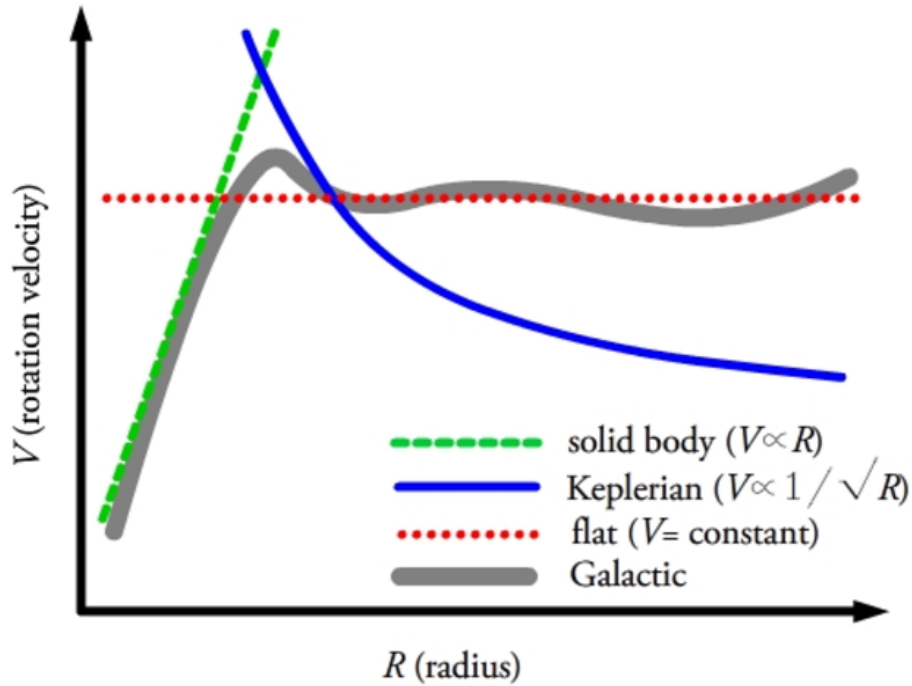


Figure 4.2: Typical rotation curve of a spiral galaxy (thick gray line). The green dashed line shows the solid-body regime, describing the galactic bulge dynamics; the red dotted line is the flat disk component; the blue solid line, the Keplerian regime that one would expect from a disk-limited distribution of matter.

In the assumption that the mass follows the light profile, the majority of the mass in a galaxy is contained in the inner regions. Then we should be able to distinguish three regimes in the circular velocity profile:

1. A first regime in which the disk dynamics is described as a solid-body, with $V/r = const$ ($V \propto r$, green dashed line in Figure 4.2).

4.1 Introduction on the Spiral Galaxy dynamics:

2. A second regime where the mass profile is described by a power law:

$$\rho(r) = \rho_0 \left(\frac{r}{r_0} \right)^{-\alpha}, \quad (4.1.3)$$

where ρ_0 and r_0 are respectively a reference density and a characteristic radius. Equation (4.1.3) combined with equation (4.1.2) produces a velocity profile $V^2(r) \propto r^{2-\alpha}$, constant for $\alpha = 2$ (red dotted line in Figure 4.2).

3. A third region beyond the galaxy luminous disk, where as the distance increases the mass profile remains constant and the rotational curve decreases as $V \propto r^{-1/2}$ (Keplerian regime, solid blue line in Figure 4.2).

When the first radio measurements of the hyperfine transition of HI at 21 cm become available, the first evidence of the complete absence of the Keplerian regime came as well (e.g., [Bosma \[1981a,b\]](#), [Roberts and Rots \[1973\]](#), [Roelfsema and Allen \[1985\]](#)). The rotational curves remained constant even beyond the optical galactic disk. This discovery paved the way for the first postulates of the existence of a non luminous material component that had to fill the outer parts of the galaxies in order to justify the external plateau of the rotational curves. The astrophysical community called this component of matter with the well-known name of *dark matter*.

However, it took a few years before the observers and the theorists (e.g., [Einasto et al. \[1974\]](#), [Ostriker and Peebles \[1973\]](#), [Ostriker et al. \[1974\]](#)) admitted that disk galaxies are immersed in extended dark matter halos.

A few years after the first studies of rotation curves with HI data were presented, where it was shown that the kinematic properties of spiral galaxies were linked to their luminosity (e.g., [Ewen and Purcell \[1951\]](#), [van de Hulst et al. \[1957\]](#)).

From equation (4.1.2), we can see that the mass and kinematics of a spiral galaxy are proportionally connected. Moreover, more massive galaxies contain more stars, resulting in brighter galaxies: the result is a correlation between the galaxy luminosity and its rotational velocity, known as *Tully-Fisher relation* (from [Tully and Fisher \[1977\]](#)). The original relation linked the width of the global HI line profile¹ $W_{20,HI}$ (corrected for the disk inclination and for the gas random motions) and the absolute magnitude of the galaxy (as in Figure 4.3).

The Tully-Fisher relation is a power-law correlation between the rotational velocity and the luminosity of the galaxy, written as:

$$L = C \cdot V^\gamma \quad (4.1.4)$$

where C is the zero-point of the function and $\gamma \sim 4$. C reflects mainly the photometric system in which the relation measurements are done.

If we know the rotation curve of the galaxy, we can derive the distance using the (4.1.4) relation: this makes this method one of the standard-candles to measure astrophysical distances.

¹Where W_{20} is the width calculated at the 20% of the peak intensity of the line flux.

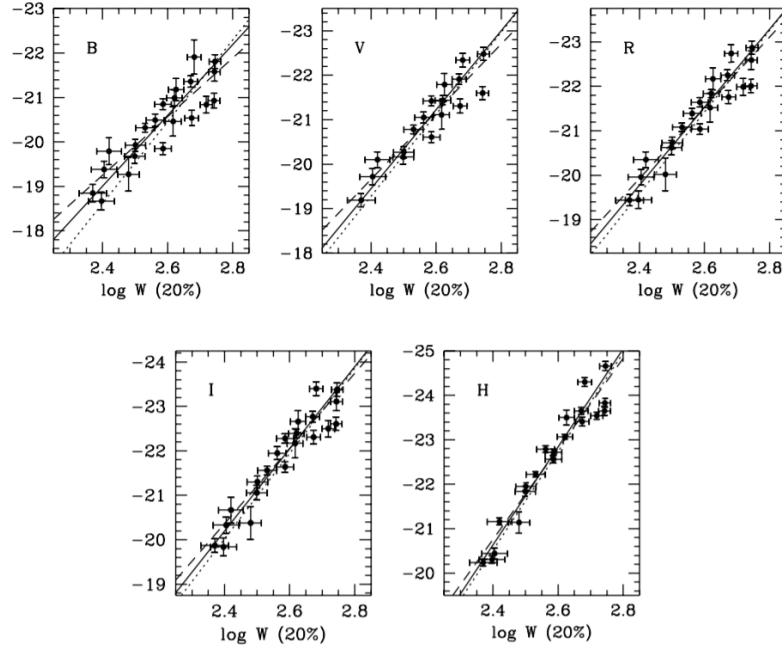


Figure 4.3: **Tully-Fisher Relation:** power-law relation between the line width calculated at the 20% of the peak intensity of the line flux (W 20%) and the magnitude in Jonson Morgan Filters (B, V, R, I, H). Image was taken by Sakai et al. [2000].

The cosmological importance of rotation curves and the practical utility of having a standard candle for estimating distances in the Universe, are two of the most famous examples that clarify the importance of studying the dynamics of spiral galaxies.

NGC 5135 is a spiral galaxy containing an AGN. The ALMA data available in the inner ~ 1 kpc of this galaxy allow us to study the gas morphology and kinematics and if/how the AGN influences them. In order to interpret our data, we have made use of the software “3D-Based Analysis of Rotating Objects from Line Observations” (3^D BAROLO), developed by Di Teodoro and Fraternali [2015].

This software allows us to derive the rotational curves from three-dimensional data cubes including both rotational and radial velocity components in the models.

4.2 3^D BAROLO as a tool for kinematic analysis

As already mentioned, one of the simplest ways to study the rotation of a gas (or a star) distribution is to exploit the Doppler shift of emission lines.

Data produced by integrated field spectroscopy are the perfect way, since provide kinematic informations with three-dimensional data-cubes, with two spatial coordinates and a spectrum along the third coordinated.

The same applies to the ALMA data-cubes that have the same three-dimensional structure (two spatial coordinates and the third axis in frequencies).

A data cube can then be read as a set of mono-dimensional spectra on each pixel of

4.2 ^{3D}BAROLO as a tool for kinematic analysis

the cube, or as a set of two-dimensional *spectral scans*, integrated on a certain range of frequencies that define the data-cube *spectral resolution*. With this in mind, we can define two cube's elements, similar to the definition of a CCD's pixel:

- **The voxel:** as three-dimensional volume element in the coordinates (x, y, v) ;
- **The spaxel:** a two-dimensional surface element in the coordinates (x, y) ;

The integration of the spaxels along all, or part, of the velocity axis returns the moments (for details see § 5.1). A voxel-by-voxel analysis allows us instead to recapture the 3D-kinematics of the gas traced in data-cubes.

With the first method we can study the motion by analysing the integrated moments: the total flux intensity (0th moment), velocity field (1st moment) and the dispersion velocity field (2th moment) of an image.

In the case of voxel analysis, a Gaussian fitting of the emission lines along the frequency axis is used. This allows us to derive the gas recession velocity and the velocity dispersion from the average velocity of each spectrum.

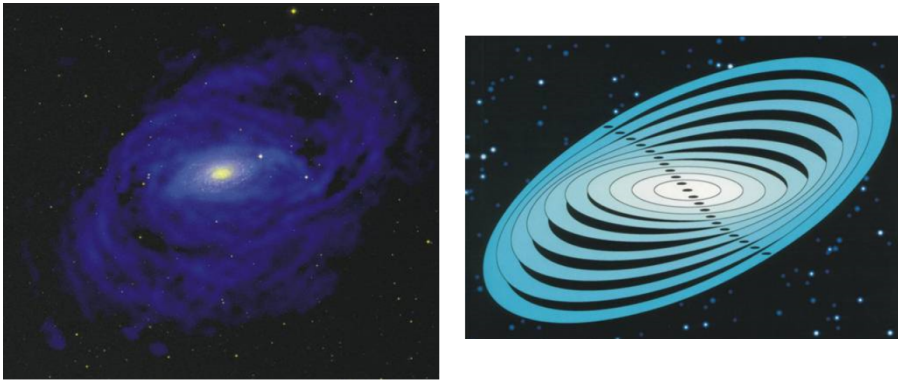


Figure 4.4: *The image illustrates the basic principle of the tilted-ring model: the left panel shows a cartoon reconstruction of the HI gas distribution in the outer regions of the galactic disk, while the right panel shows the reconstruction of the concentric ring pattern assumed by the tilted-ring model.*

^{3D}BAROLO is able to exploit both approaches for the reconstruction of three-dimensional kinematic models of data cubes.

The software was presented in its first version in Di Teodoro and Fraternali [2015] (later discussed in the Ph.D. thesis Di Teodoro [2015]) and it uses the *tilted-ring model* as the basis for the reconstruction of kinematic models of the observed gas.

The tilted-ring model is based on two assumptions: the material which is responsible for the emission lines is contained into a thin disk and the motion is dominated by rotation. In this model, the galaxy disk is divided into a series of concentric rings (in the right panel of Figure 4.4) characterised by seven free parameters (three morphological and four kinematical): the kinematical center (x_0, y_0) , the inclination $(i)^2$, the

²calculated with respect to the observer (90° for edge-on).

position angle (ϕ)³ define the characteristics of the projected rings on the sky plane; while the velocity dispersion (σ)⁴, the rotational velocity (V_{rot}), the systemic velocity (V_{sys}) and the radial velocity (V_{rad}) of the gas define the kinematic characteristics of the model.

In the 3D BAROLO version used in this work (v. 1.3), the three velocity components of the rings are combined to define the observed velocity along the line-of-sight (V_{LoS}), which compose the map of the velocity field extracted with the 1st moment. This version also considers the radial component in the model, which previous versions did not take into account.

The derived velocity map can be written in terms of a generic harmonic expansion (e.g., Schoenmakers [1999], Swaters et al. [1999]), that in a first order approximation can be written as (Roelofs [1995] for details):

$$V_{LoS}(x, y) = V_{sys} - V_{rot}(R)\cos \varphi \sin i - V_{rad}(R)\sin \varphi \sin i \quad (4.2.1)$$

Equation (4.2.1) describes the velocity along the line of sight at a given coordinate (x, y) on the velocity field: φ is the azimuthal angle on the plane of the galaxy between the observed coordinate and the fiducial line defined by the position angle (along the receding semi-major axis).

A further parameter to be specified is the column density of the gas. For this, two different kinds of normalization are implemented in 3D BAROLO: a pixel-by-pixel (i.e., local) normalization and an azimuthally averaged one (i.e., AZIM).

In the former case, the model assumes equal values for the integral of each spatial pixel along the spectral dimension in the model and in the observations. This normalization allows us to consider non-axisymmetric density models and avoids regions with anomalous distribution, like, e.g., clumpy emission or holes, to affect the global fit.

The normalization value of the second model is instead set to the azimuthally averaged flux in each ring. Although the AZIM normalization cannot reproduce the details of the galaxy morphology (which are instead reproduced on a pixel-by-pixel basis by the LOCAL normalization), it is very useful to determine the inclination angle of the outer rings and to understand the global motion of the gas.

The 3D BAROLO algorithm performs a series of computational operations that can be summarized in three main steps. The first is the definition of the disk model.

Once the model normalization is set, the user has two options: choose to fix the ring parameters or to leave them free. In the latter case, 3D BAROLO estimates the initial parameters according to the following conditions (from Di Teodoro [2015]):

- **Kinematical centre:** the coordinates of the center are taken as the flux-weighted average positions (centroids) of the source: this method has limitations

³defines the position of the major axis on the receding half of the galaxy, taken anticlockwise from the North direction in the sky.

⁴define as the intrinsic broadening of the single line profile corrected for the instrumental broadening: $\sigma_{instr} \equiv W_{ch}/\sqrt{2ln2}$ in 3D BAROLO and where W_{ch} is the spectral resolution (channel-width) of the data-cubes. This quantity is linked to the gas turbulence.

4.2 ^{3D}BAROLO as a tool for kinematic analysis

and may not work properly in case the emission does not peak at the center of the gas distribution.

- **Systemic velocity:** this is estimated from the global emission-line profile, by taking the midpoint velocity between the two velocities corresponding to the 20% of peak levels on each side of the spectrum.
- **Position angle:** the position angle is estimated from the velocity field as the straight line that maximizes the gradient in velocity along the line of sight.
- **Inclination:** the inclination is calculated by fitting the theoretical brightness distribution of a beam-convolved disk model. The gas density profile is extracted from the observed map along elliptical rings. A model map is then built from the density profile, smoothed to the same spatial resolution of the data and the inclination is fitted to reproduce the observed map.
- **Rotational velocity:** the initial rotation velocity is calculated as the inclination-corrected half-width of the global line profile at 20% of the peak flux (W_{20}).
- **Velocity dispersion and disk thickness:** these quantities are set by default at 8 km s^{-1} and 150 pc respectively.

The software allows the user to impose the resolution of the model at the size requested, by choosing as lower limit the dimension of a data cube pixel.

This step allows us to solve problems that may arise if the gas distribution is very different from a disk-like one. In this case, by imposing the **AZIM** normalization, the final model appears with strong spikes generated by the non axis-symmetric distribution of the gas clouds in each ring (see panel (a) of Figure 4.5).

This problem is solved by imposing to the model a higher resolution than the data one, convolving successively with the PSF of the observation. The final resolution of the model is always the same of that one of the data cube, and the second step consists in the degradation of the model to the same resolution of the data. In Figure 4.5 (b) the results of this procedure are shown: note that, although still present, the spikes are much less evident than in panel (a) and the gas distribution is more uniform.

As last step, the code finds the best fitting values by minimizing the difference between the data and the kinematic model smoothed to the same resolution of the data.

The residuals are calculated by comparing the data and the model pixel-by-pixel. ^{3D}BAROLO provides three methods for calculating the residuals: we chose the χ^2 . If M is the flux associated with a model-pixel and D is the same for a data-pixel, then ^{3D}BAROLO minimizes the quantity:

$$\Delta r = \frac{(M - D)^2}{\sqrt{D}} \quad (4.2.2)$$

In case D is a blank pixel, we give it the value of the root mean square (rms) of the cube. As a result of this procedure, ^{3D}BAROLO returns a value (F) that defines the congruence of the model with data:

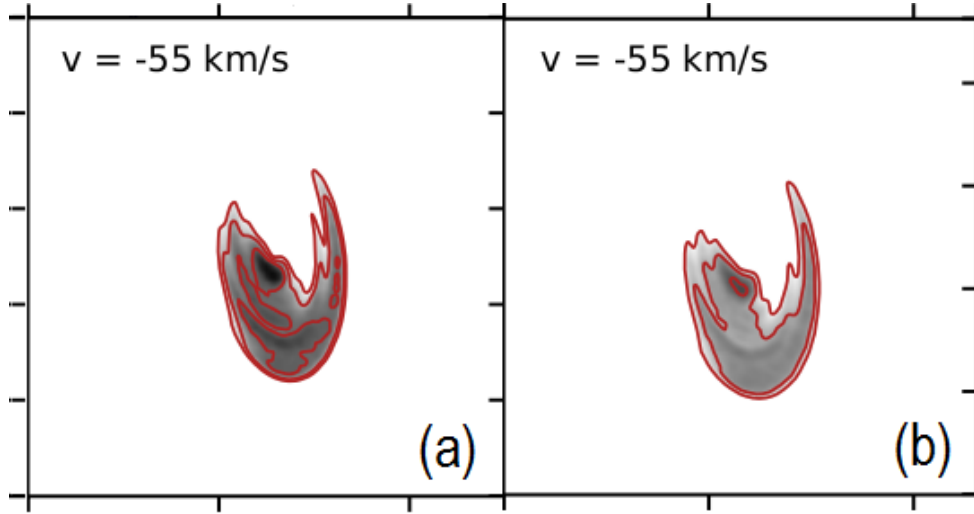


Figure 4.5: *Example of the results obtained by using the convolution in 3D BAROLO: the two panels show two spectral scans of the models obtained using the AZIM normalization (at the velocity of -55 km/s). In the left panel, the model has the same resolution as the data-cubes (in this case ~ 0.26 arcsec); in the right panel, the resolution is halved, then the model is returned to the same resolution of the cube by convolving with the PSF after the fit.*

$$F = \frac{1}{n} \sum_{k=1}^n \Delta r_k \xi(\varphi_k) \quad (4.2.3)$$

equal to the averaged sum of the residuals in each pixel, with n being the pixels number along the v -axis, and k the cyclical variable associated to every pixel.

In Figure 4.6 the results obtained with one of the considered models (the low-resolution one, that will be explained in § 5.2) are shown. This type of output is very time-expensive, but is crucial to ensure that the best fit values found are the absolute minimum of the function. In this case, the software succeeds in finding the absolute minimums in the plane defined by V_{rot} and σ . If at the end of the residual calculation, the software converges in finding a solution, 3D BAROLO passes to the next ring construction, until the condition $R_{ring} < R_{max}$ is valid (with R_{max} equal to the radius of the outer ring, defined a priori).

4.2 $3D$ BAROLO as a tool for kinematic analysis

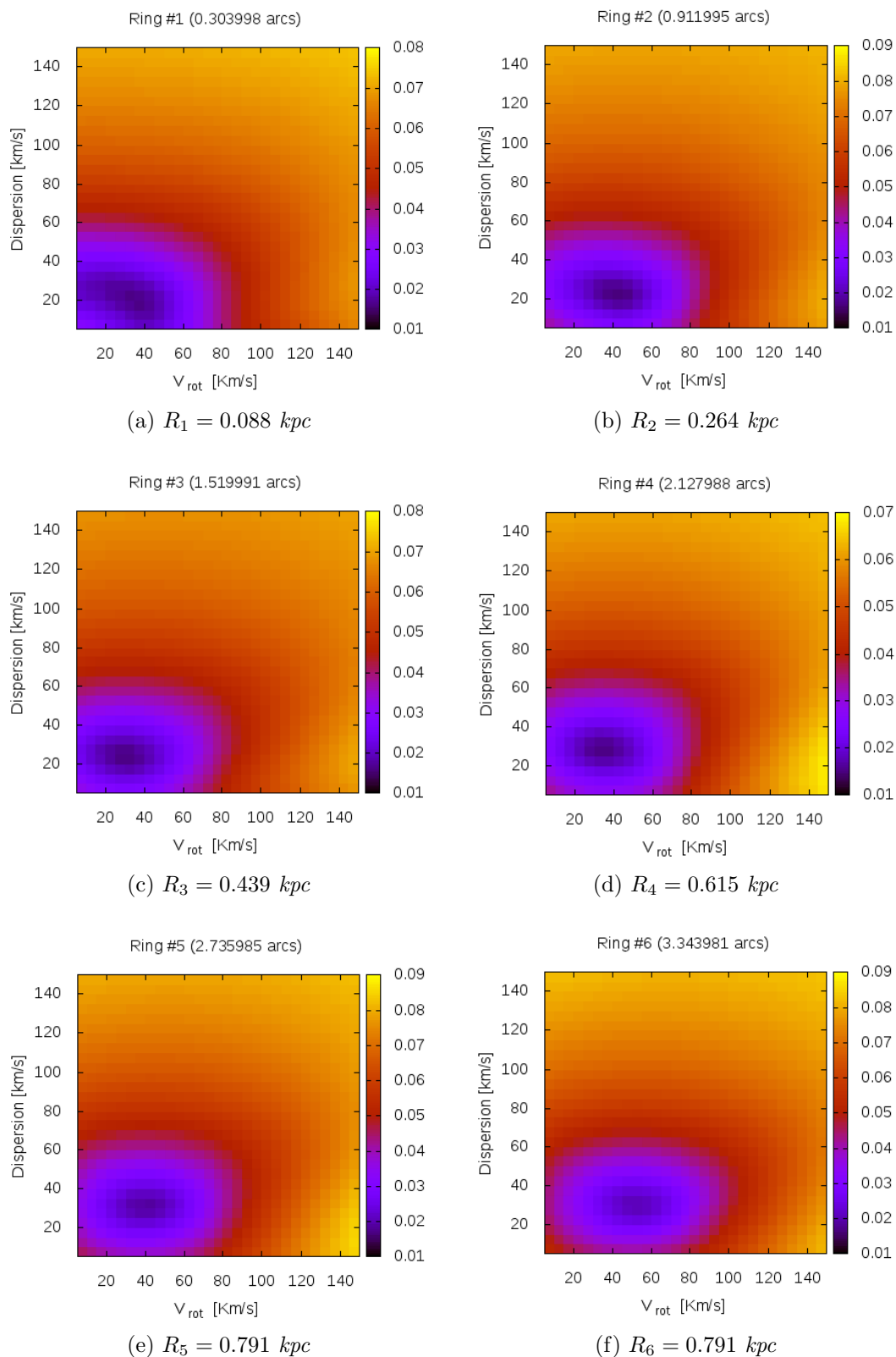


Figure 4.6: Residual of V_{rot} vs σ plane. Each panel shows: the number of the ring and its radius in [arcsec] (on top); the scale of F (on the right); the corresponding radius in [kpc] from the kinematic center (at the bottom).

4.3 The limits and the strengths of 3^D BAROLO

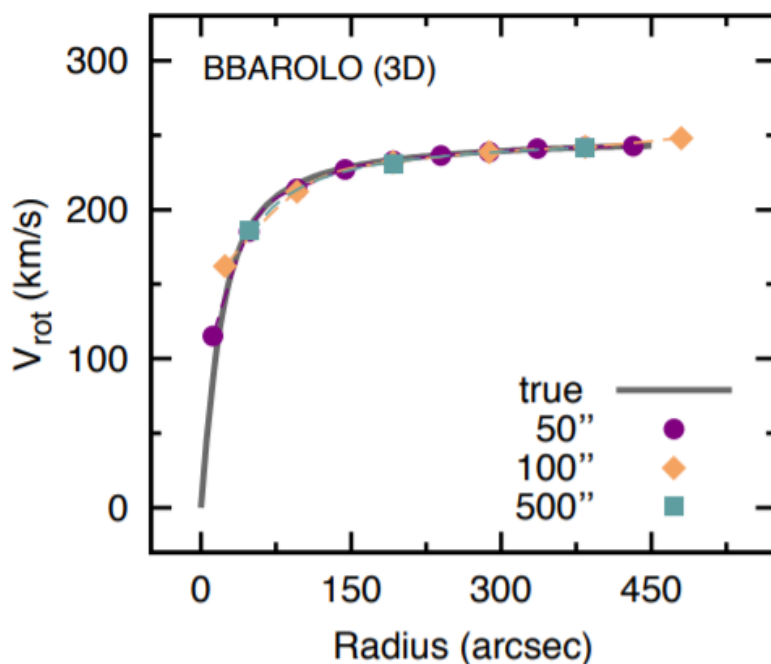
The parameters determining the goodness of a fit obtained with 3^D BAROLO are essentially four: the inclination of the galactic disc, the angular resolution of the data in which the model is calculated, the spectral resolution and the noise associated to each spaxel.

In Di Teodoro [2015], the authors propose a detailed discussion about the limits and the strengths of the code. Here we propose just a short summary of that discussion and tests, to make the reader aware of the limits of the kinematic model that we will present in the following chapter.

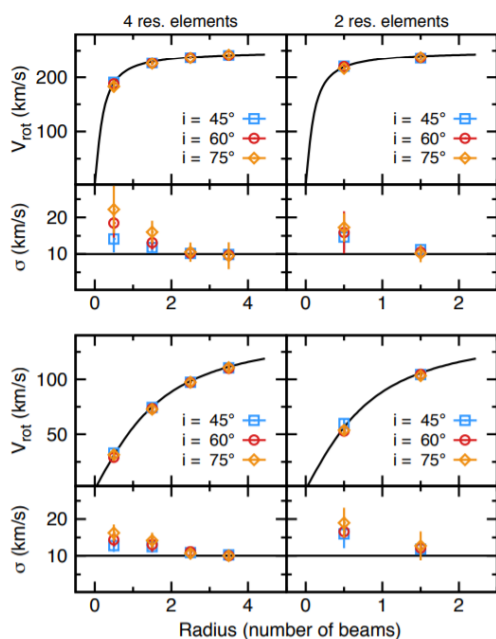
To test the 3^D BAROLO limits, Di Teodoro and Fraternali [2015] used artificial data-cubes with a beam size of 12 arcsec (FWHM), a spectral resolution of 7.5 km s^{-1} and no noise. Every beam covers a total amount of 18 pixels ($3'' \times 3''$ each) and the dimensions of the simulated galaxy have a radius of 400 arcsec. The theoretical cubes were then stressed parameter by parameter to test how far 3^D BAROLO was able to reconstruct a consistent model.

- **Angular resolution:** Keeping all the other parameters as originally set, the authors have reduced the resolution by smoothing the cube up to a limit resolution of $200''$. Although having only two resolving elements, 3^D BAROLO was still able to reconstruct the correct rotational curve (see Figure 4.6 (a)).
- **Inclination:** Figure 4.6 (b) shows the results of the applied tests by varying the inclination value. The simulated galaxy was rotated completely from nearly face-on to almost edge-on, also varying the number of resolution elements (respectively four on the left and two on the right one). The model evaluated V_{rot} and σ as functions of radius. The results show how the rotation velocity is always well traced by 3^D BAROLO. This is not the case of the velocity dispersion, which in the most internal areas of the galaxy is overestimated by a factor of 2. The authors conclude that the inclination parameter is certainly the most delicate one for the modelling: a complete ignorance of its initial value is strongly not advisable for the user, because the software can easily converge to a local-wrong minimum.
- **Noise:** Noise tests were performed by fixing the inclination to a value of 60° and progressively increasing the *signal-to-noise ratio* (SNR) from a minimum of 1 to a maximum of 5. In Figure 4.6 (c), the average errors over the inner disk as a function of the average SNR are shown. From the results, we can see how 3^D BAROLO performances keep below 10% error for $SNR > 2$. Below this SNR, the source is confused with the background signal and the errors grow rapidly up to 100%.

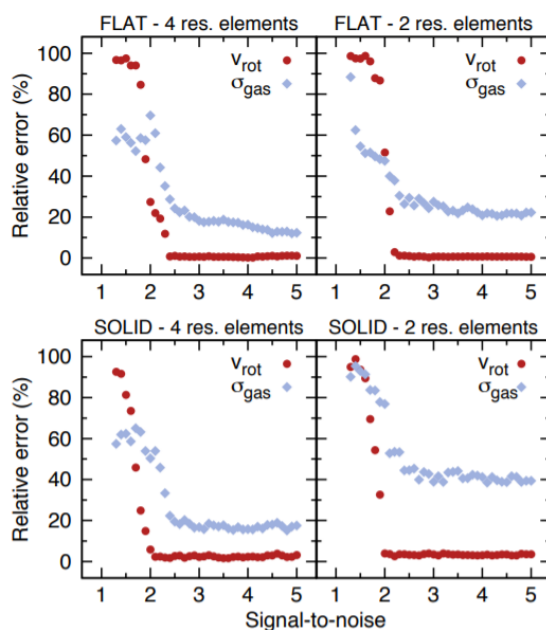
4.3 The limits and the strengths of 3^D BAROLO



(a) Results of the spatial-resolution tests.



(b) Results of the inclination tests.



(c) Results of the noise tests.

Figure 4.7: 3^D BAROLO test results executed by code developers. The plots were taken from [Di Teodoro \[2015\]](#), [Di Teodoro and Fraternali \[2015\]](#).

- **Spectral resolution:** The number of points available to construct a valid model is inversely proportional to the channel width of a data-cube. For this reason, the authors say that as the spectral resolution decreases, the reliability of the models also decreases. To ensure an acceptable result, the minimum number of spectral channels was found to be between 8 and 12, depending on the angular resolution of the cube (all this also with low SNR).

To conclude, the tests presented in Di Teodoro [2015] show that 3^D BAROLO is perfectly capable of working on low resolution (both spectral and spatial) and low SNR data cubes.

However, a combination of these factors with too low quality data makes it impossible for 3^D BAROLO to properly reconstruct the kinematic model.

3^D BAROLO thus proves to be a safe software for this type of analysis, able to process an average observation of today's main telescopes (eg SINFONI-VLT, VLA or ALMA data-cube). The ability of 3^D BAROLO to operate at low resolution; this strongly limits the main problem affecting the study of the kinematics of galactic disks: *beam-smearing*.

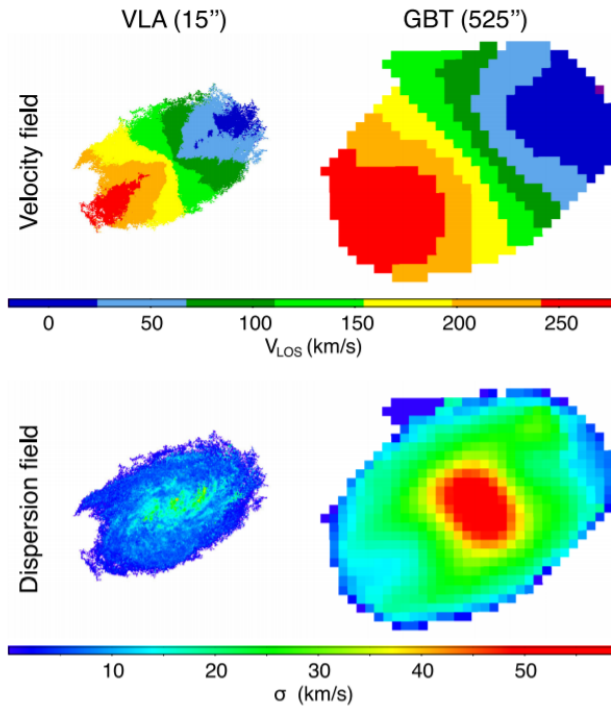


Figure 4.8: **Example of beam-smearing effect:** Velocity fields (top) and velocity dispersion fields (bottom) for NGC 2403 derived from high (left; Fraternali et al. [2002]) and low resolution (right; de Blok et al. [2014]) data-cubes. Images are on the same spatial and velocity scale. The image was taken from Di Teodoro and Fraternali [2015].

This effect is more pronounced with larger PSF. In practice, the finite size of the beam of a telescope causes the line emission to be smeared on the adjacent regions. As a consequence, the observed line profile at a certain spatial position, produced by

4.3 The limits and the strengths of 3D BAROLO

the convolution of the true intensity distribution with the instrumental PSF, revives contributions from adjacent areas and becomes broader and potentially asymmetric. This has a double effect on the moments of an image. In the central regions of the galaxy, the velocity field peak drops down in favour of the outermost regions in which the field however rises (Figure 4.6, top). As a consequence, the 2^{nd} moment gradient increases with the increasing of the PSF size (see Figure 4.6, bottom pannels). All this causes the central region to be associated with a fictitious velocity-gradient, with the consequent difficulty of resolving the areas where the gradient is real.

Chapter 5

The complex morphology and kinematics in the inner regions of NGC 5135: *Are we witnessing the AGN influence?*

Abstract

In this chapter we present the results of the work and our interpretation of the observed gas morphology and kinematics in NGC 5135.

In the first part of this chapter we show, describe and discuss the maps obtained from our ALMA data reduction and calibration, in particular: the continuum images and the CO line distribution, velocity field and velocity dispersion maps.

The central part of the chapter is dedicated to the best-fitting kinematic model obtained by fitting our data with ^{3D}BAROLO.

In the last paragraph, we present an our interpretation of the mechanisms that are occurring in the innermost region of NGC 5135 by considering the morphological and kinematical results described above, with particular emphasis on several zones either studied in previous works or found, for the first time, thanks to analysis performed in this Master Thesis project.

5.1 Moments analysis

The first step performed in the scientific analysis of the ALMA data was the morphological study of the innermost regions of NGC5135. This was done by studying the gas distribution and kinematics from the moments cubes of CO(2-1) molecular transition.

The *moments* are two-dimensional images, obtained from a three-dimensional *data-cube*, that correspond to the map of the distribution moments for each pixel.

We define three moments for an image:

1. *Moment 0* is obtained by integrating the flux along the velocity (or frequency) axis for each pixel. It is mathematically described as:

$$MOM_0 = \int_{chans} S_v(v) dv \quad (5.1.1)$$

The result, in *Jy km/s*, therefore represents the integrated flux over all the available channels.

2. *Moment 1* is useful for kinematical studies, since for each pixel it is obtained by integrating the velocity weighted by the flux along the velocity channels (normalized to MOM_0):

$$MOM_1 = \langle v \rangle = \frac{\int_{chans} S_v(v)v dv}{\int_{chans} S_v(v) dv} \quad (5.1.2)$$

The result, in *km/s*.

3. *Moment 2*, is obtained by integrating the flux weighted velocity dispersion along the velocity axis (also normalised to MOM_0):

$$MOM_2 = \langle \sigma \rangle = \sqrt{\frac{\int_{chans} S_v(v)(v - \langle v \rangle)^2 dv}{\int_{chans} S_v(v) dv}} \quad (5.1.3)$$

In order to obtain significant values of the moments, it is important to limit as much as possible the amount of noise entering into the computed integral, by imposing two different cut-offs.

The first one sets a limit on the flux: if a pixel has a value smaller than a certain threshold (usually set to 3σ) it is not considered in the integral of the moments.

The second cut-off deals with the channels to be considered in order to exclude those in which the source spectral line is not present: this can be selected with the CASA-viewer by selecting the emitting regions of interest and extracting the spectrum. The CASA-viewer offers the possibility not only to change the measurement unit of flux (e.g. *Jy/beam*, *Jy/arcsec²*, *fraction of peak*, *Kelvin*) but also to plot different quantities on the x-axis, including the channels. The Table 5.1 summarizes the parameters we set for extracting the moments of the observed molecular transitions.

**The complex morphology and kinematics in the inner regions of
NGC 5135: *Are we witnessing the AGN influence?***

MOLECULAR TRANSITION	CO(2-1)	CS(5-4)	CO(6-5)
<i>Channels available</i>	51	26	20
<i>Selected channels</i>	10 – 45	6 – 21	4 – 18
<i>threshold [$Jy km s^{-1} beam^{-1}$]</i>	3.2×10^{-3} (3σ)	6×10^{-4} (4σ)	5.87×10^{-2} (4σ)

Table 5.1: *Summary of parameters set to extract moments. The thresholds were calculated directly on the calibrated data-cubes by extracting the average noise from four zones (distant from the source) in all the scans associated with the emission and finally by averaging these values in order to obtain the rms (σ).*

Finally, since the source does not occupy the entire image, but only the central part of it, every moment has been extracted by selecting a box containing the entire emitting region and masking the outer zones that are only filled with noise.

In Figure 5.1, we show the continuum emission in bands 6 and 9.

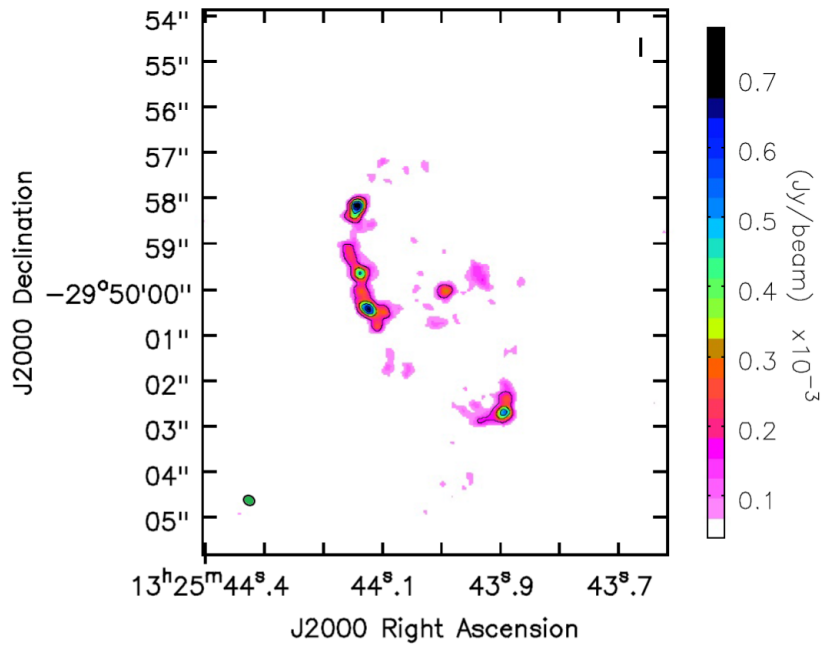
For these images, we imposed a 3σ threshold, masking all the noise smaller than it. The contours, corresponding to the concatenated band 6 continuum flux and are set at 6σ , 12σ , 18σ and 24σ . We chose to overplot the same contours in both continuum images, so as to facilitate the comparison between the different continuum emitting zones. In Figure 5.2, 5.3 and 5.4 we show the moments of the CO molecular transitions: CO $J = 2 - 1$ and CO $J = 6 - 5$ in the top and bottom panels respectively.

To all the moments we have overplot the band 6 continuum. The contour levels are the same shown in the continuum images, while the extraction thresholds are those presented in Table 5.1.

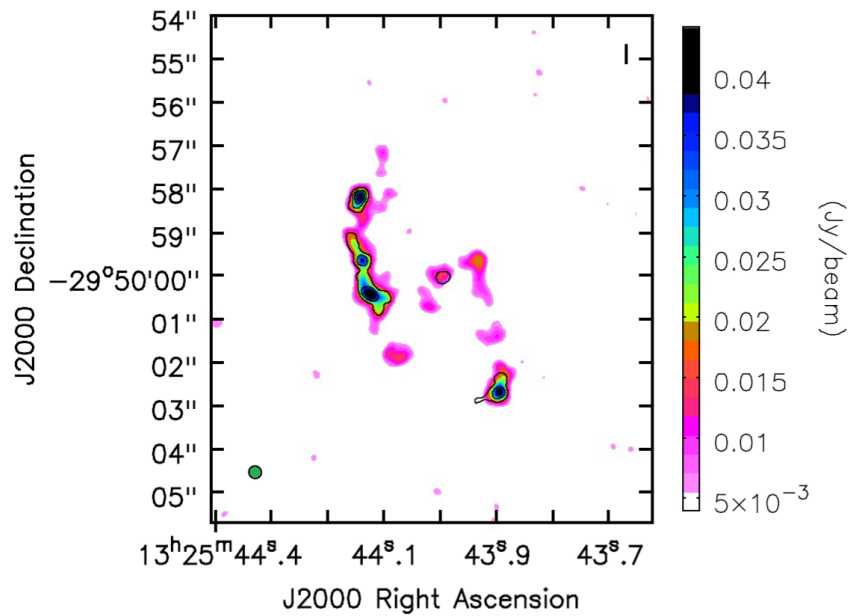
The beam sizes are $\theta_{6-CO} = 0.26'' \times 0.21''$ and $\theta_{9-CO} = 0.30'' \times 0.29''$ respectively for band 6 and band 9. The maximum recoverable scales, in all images, are $\theta_{LAS-6} \sim 5$ arcsec (in band 6) and $\theta_{LAS-9} \sim 1$ arcsec (in band 9).

In Figure 5.2 the integrated brightness distributions are shown, using equation (5.1.1). The integrated velocity field is shown in Figure 5.3, following equation (5.1.2), while Figure 5.4 shows the integrated velocity dispersion field from equation (5.1.3).

5.1 Moments analysis



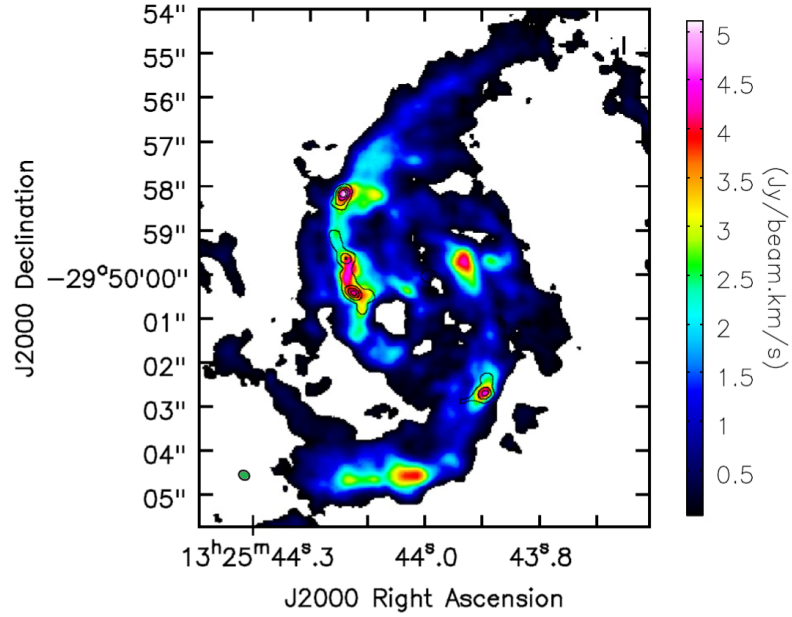
(a) *Continuum band 6*



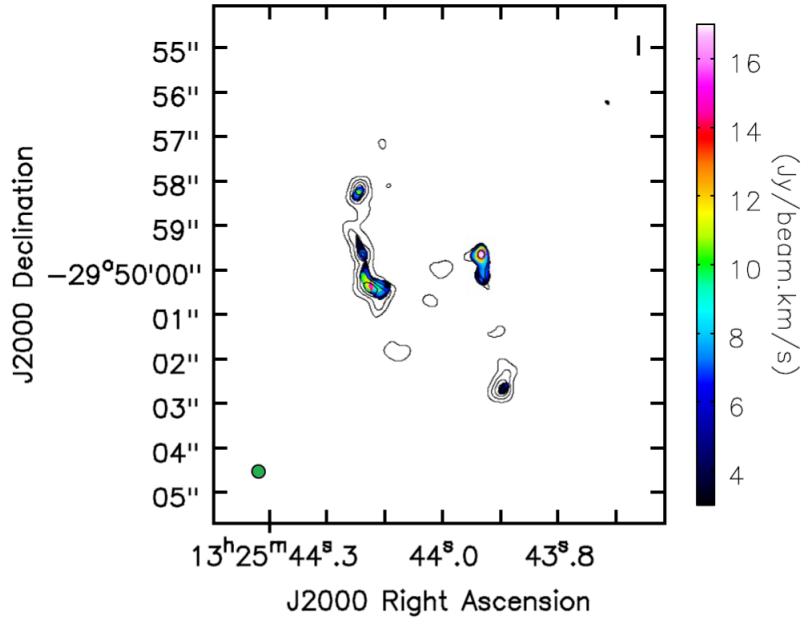
(b) *Continuum band 9*

Figure 5.1: *Continuum emission in band 6 (top) and band 9 (bottom): the beam sizes are $\theta_{6-cont} : 0.25'' \times 0.20''$ and $\theta_{9-cont} : 0.30'' \times 0.29''$ respectively, while the maximum recoverable scales, in all images, are $\theta_{LAS-6} \sim 5$ arcsec - in band 6 - and $\theta_{LAS-9} \sim 1$ arcsec - in band 9. The contours are set at 6σ , 12σ , 18σ , 24σ .*

The complex morphology and kinematics in the inner regions of
 NGC 5135: *Are we witnessing the AGN influence?*



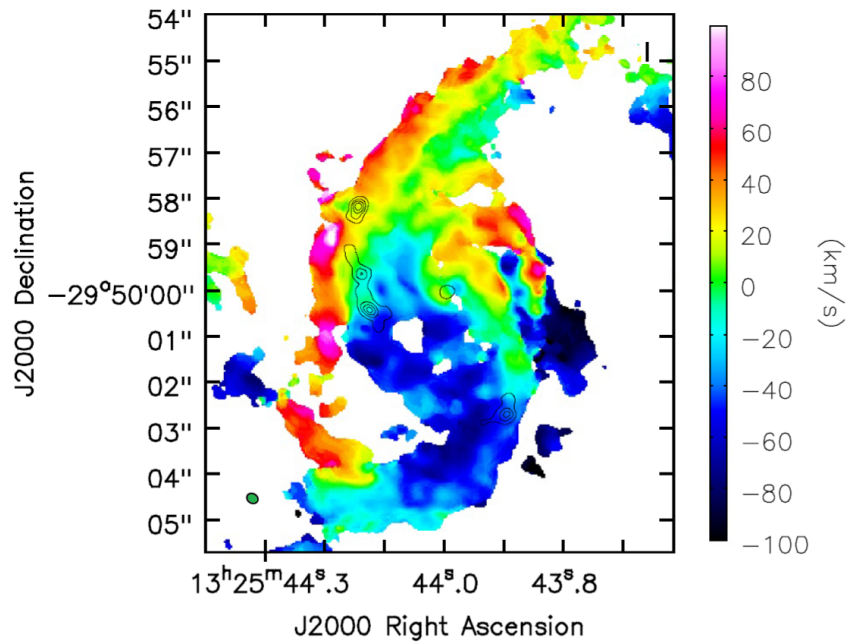
(a) *Integrate brightness distribution - CO J = 2 – 1*



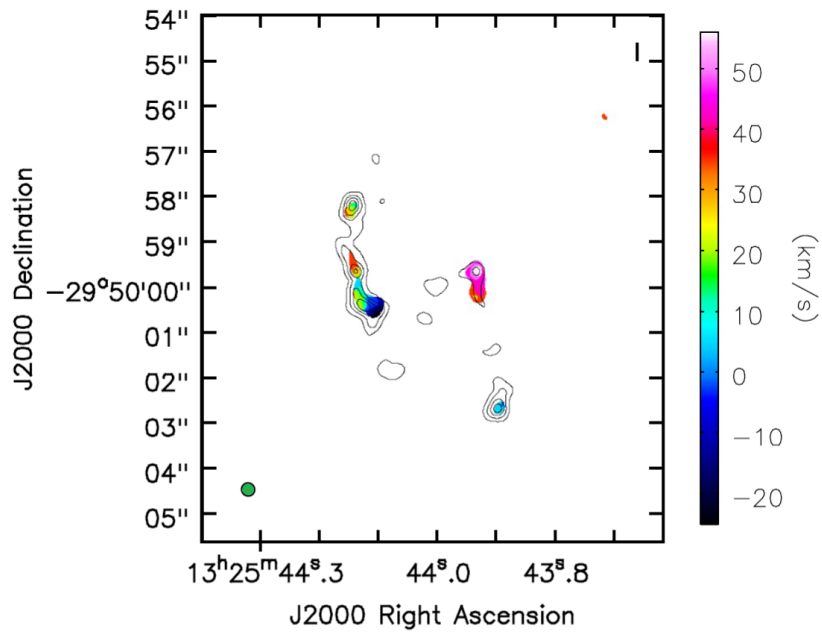
(b) *Integrate brightness distribution - CO J = 6 – 5*

Figure 5.2: *Integrated brightness distributions, extracted at 3σ in band 6 (top) and 4σ in band 9 (bottom): the beam sizes are $\theta_{6-CO} : 0.26'' \times 0.21''$ and $\theta_{9-cont} : 0.30'' \times 0.29''$ respectively, while the maximum recoverable scales are the same of the continuum. The beam size is shown in green on the bottom right corner of each figure. The contours, belonging to the continuum emissions of the same band of molecular transition, correspond to 6σ , 12σ , 18σ , 24σ .*

5.1 Moments analysis



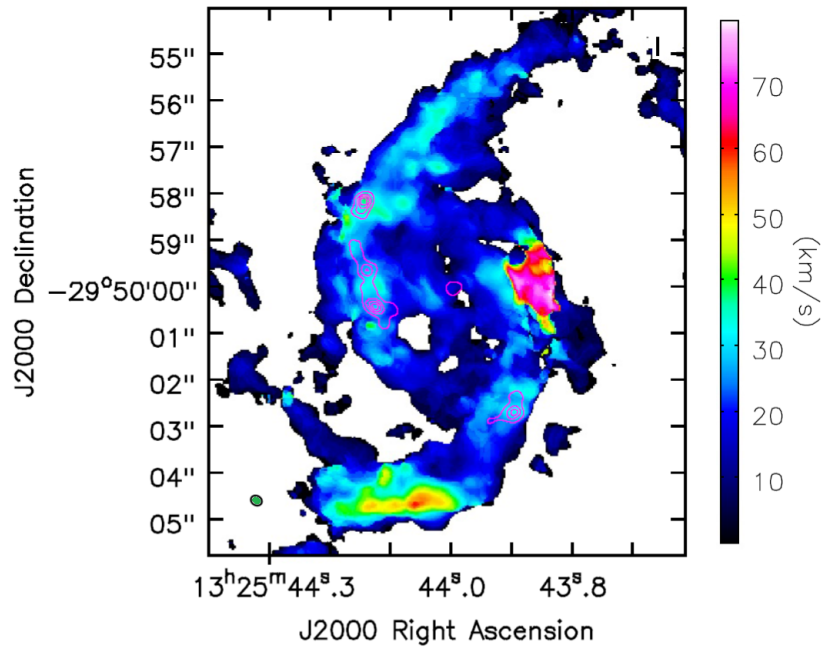
(a) *Velocity field - CO $J = 2 - 1$*



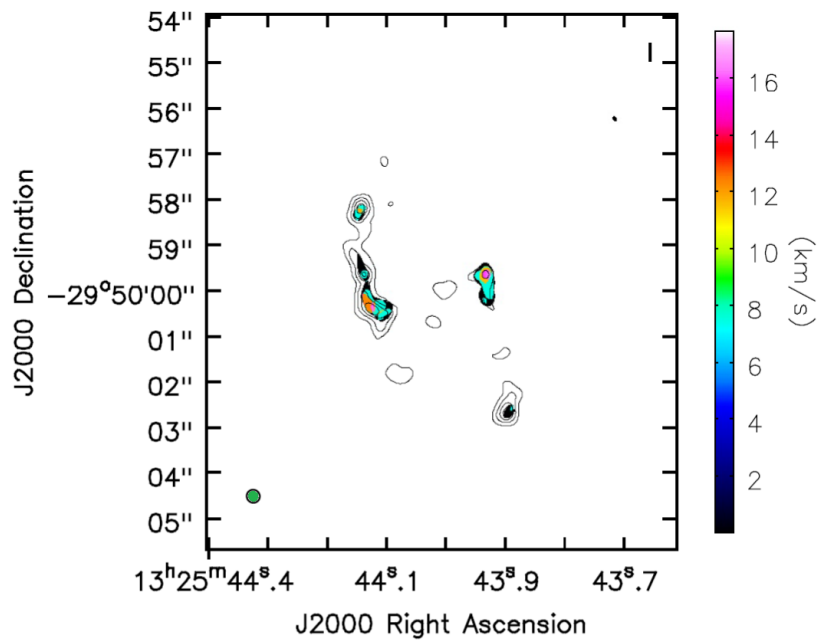
(b) *Velocity field - CO $J = 6 - 5$*

Figure 5.3: *Velocity fields, extracted at 3σ in band 6 (top) and 4σ in band 9 (bottom): the angular scales and the parameters of the contours are the same of Figure 5.1 and 5.2.*

The complex morphology and kinematics in the inner regions of
 NGC 5135: *Are we witnessing the AGN influence?*



(a) *Velocity dispersion field - CO $J = 2 - 1$*



(b) *Velocity dispersion field - CO $J = 6 - 5$*

Figure 5.4: *Velocity dispersion fields, extracted at 3σ in band 6 (top) and 4σ in band 9 (bottom): the angular scales and the parameters of the contours are the same of Figure 5.1 and 5.2.*

5.1 Moments analysis

These images show the complex gas and dust distribution in this source. Overall, the inner gas structure resembles that of a spiral galaxy with a central bar linking two potential arms. Several regions that deserve special attention and interpretation are identified by combining the informations derived from the continuum and the various moments of the CO. For convenience and to facilitate the comparison, in Figure 5.5 and 5.6 the continuum maps and the moments are plotted again with highlighted (labelled with letters and, if needed, encircled by ellipses) the emission regions that we have identified for further investigation.

For each region, we have extracted the observed fluxes with CASA. This operation was done using the same extraction areas in each band, being careful to define an area that would contain the emission at the largest angular scale.

In other words, after we chose an emitting region and once we controlled its angular scales, the resolution is always fixed at the worse one, to be sure to loose the less flux possible.

In Table 5.2 are summarized the integrated flux densities of the various regions:

REGIONS	$(Band\ 6)_{cont}^{(1)}$	$(Band\ 9)_{cont}^{(2)}$	CO(2-1) ⁽³⁾	CS(5-4) ⁽⁴⁾	CO(6-5) ⁽⁵⁾
“A”	2.69	5.51	–	–	–
“B”	3.87	10.7	14.0	56.2	–
“C”	10.7	26.6	13.4	51.3	4.20
“D”	8.27	20.6	11.6	10.5	3.48
“E”	8.36	17.1	12.0	11.3	11.7
“F”	–	–	4.83	–	–
“G”	9.29	22.5	12.6	4.99	1.97
“H”	–	–	45.4	–	–

Table 5.2: *Summary of integrated flux densities each of the regions studied in detail and enlightened in Figure 5.5 and 5.6. Fluxes are reported in units of: (1) $10^1 mJy$; (2) $10^3 mJy$; (3) $10^2 mJy\ km/s$; (4) $10^2 mJy\ km/s$; (5) $mJy\ km/s$.*

In Figure 5.5 and 5.5 we show the continuum images in both band 6 and 9 and the CO(2-1) and CO(6-5) moments with several regions highlighted. Some of the regions detected by ALMA have already been identified and studied in the past. Below is a detailed description of these regions and of previous results from the literature (see § 2):

- **Region “A”:**

The coordinates of this region are centred at RA(J2000) +13:25:43.99 DEC(J2000) -29:50:00.02, as found from the band 6 continuum image (we will discuss the choice of these coordinates in § 5.2). Region “A” includes the AGN position, as identified in VLT-SINFONI [Si IV] and Chandra X-ray maps (as in § 2: RA(J2000) +13:25:44.0 DEC(J2000) -29:50:01.0; Bedregal et al. [2009] and Levenson et al. [2004]).

The complex morphology and kinematics in the inner regions of
 NGC 5135: *Are we witnessing the AGN influence?*

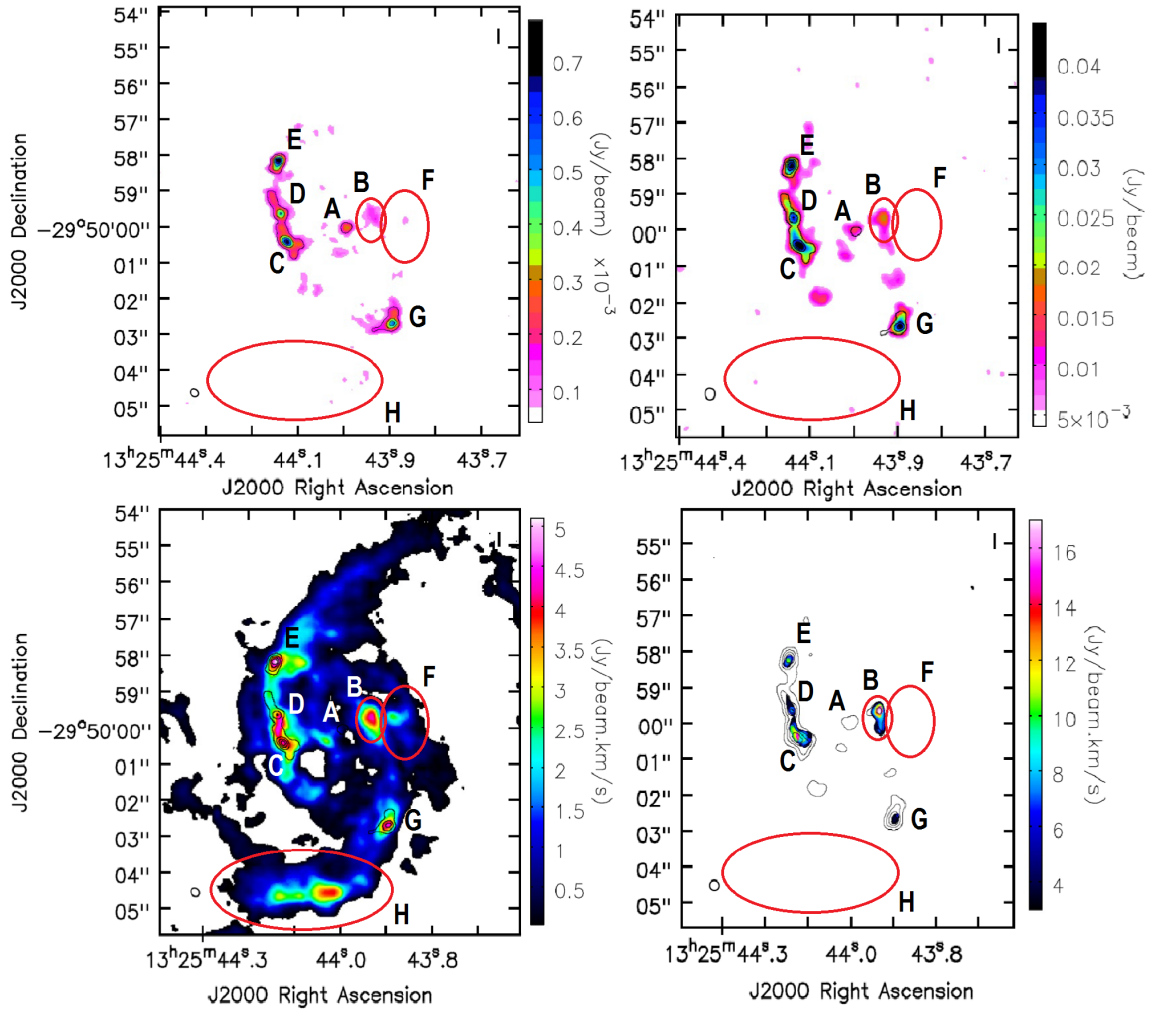


Figure 5.5: ALMA images of NGC 5135 in band 6 (left) and band 9 (right). Continuum emission (top, mJy/beam) and 0th moment (bottom, Jy km s⁻¹ beam⁻¹) of CO(2-1) (left) and CO(6-5) (right). The angular scales and the parameters of the contours are the same as in Figure 5.1 and 5.2.

5.1 Moments analysis

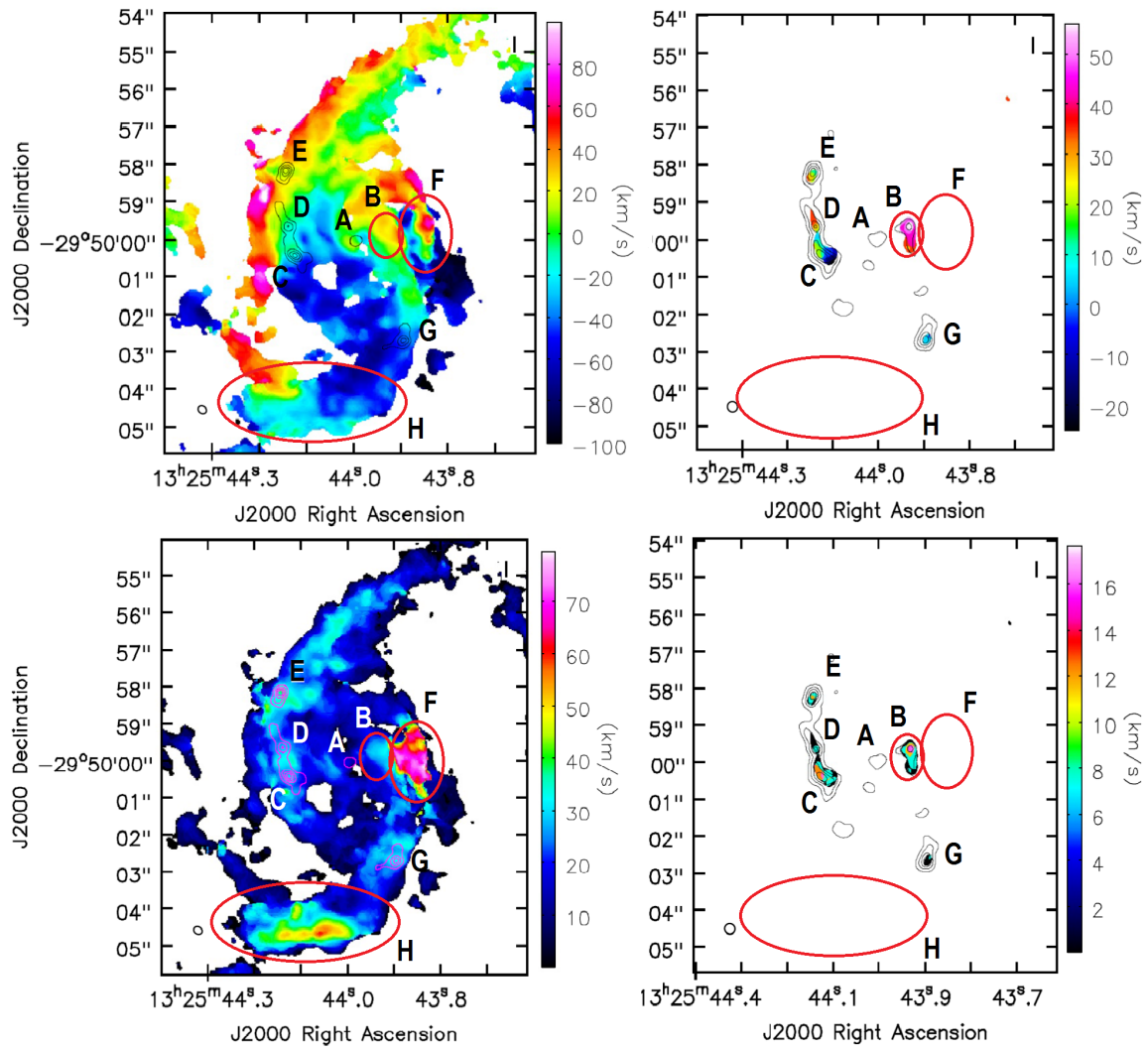


Figure 5.6: *Top: 1st moments (velocity field) of CO(2-1) (left) and CO(6-5) (right); bottom: 2nd moments (velocity dispersion) of the same transitions. The colour scales are in units of $Jy km s^{-1} beam^{-1}$.*

The complex morphology and kinematics in the inner regions of
NGC 5135: Are we witnessing the AGN influence?

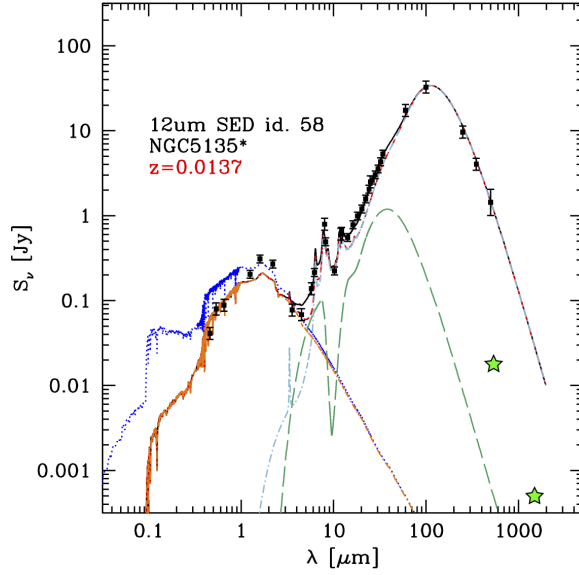


Figure 5.7: *Broad-band SED of NGC 5135 (data from the literature), as fitted by Grupioni et al. [2016] with a three component model – extinguished stars (red), AGN (green) and dust re-emission (pale blue) – using the SED decomposition method described in Berta et al. [2013]. The blue emission at short wavelengths shows the expected unextinguished stellar contribution. The green stars show the ALMA band 6 and band 9 data corresponding to the central region (AGN dusty torus?) obtained from our analysis (see Table 5.2).*

An unresolved emitting region at the AGN radio and X-ray position is clearly visible in both the continuum maps, implying the presence of warm and dense dust in the very central regions, but it is not detected in the observed spectral line transitions. Similarly, Schinnerer et al. [2000] did not detect the nucleus of NGC 1068 in CO, although very recently the NGC 1068 torus and multiple knots of SF have been resolved in CO with ALMA at much higher resolution (7–10 pc; García-Burillo et al. [2016]). In analogy with what happens in NGC 1068, where the AGN is part of a circum-nuclear disk that could be resolved only with very high-resolution observation (García-Burillo et al. [2016]), the flux from region “A” can be contaminated by star-formation and only partially due to the AGN dusty torus. However, at odds with the dust distribution in NGC 1068, the continuum emission from region “A” in NGC 5135 appears unresolved at the resolution of our data, but already isolated (i.e., not embedded in a circum-nuclear ring, which is expected to extend out to larger distance).

In any case, since it is difficult to estimate the continuum emission from AGN torus without SF contribution unless the AGN torus is clearly resolved, we can consider the flux measured from region “A” as an upper limit to the cold dust emission from the torus. The ALMA band 6 and band 9 data corresponding to the central region (e.g., “A”) are shown as green stars in Figure 5.7. Our ALMA measurements seem to show much higher cold dust contribution from the nucleus than expected from only torus models. ALMA higher resolution

5.1 Moments analysis

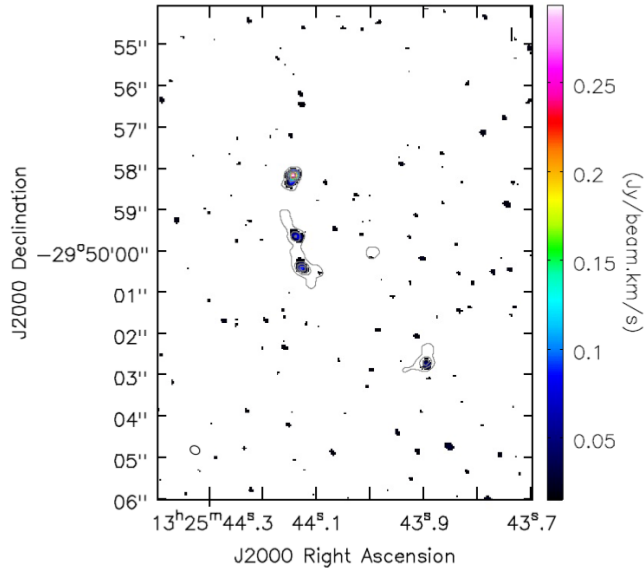


Figure 5.8: *Brightness distribution (0th moment) of the CS(5-4) line. The moment was extracted at $> 4\sigma$, while the colour scale represents the line intensity in units of $\text{Jy km s}^{-1} \text{beam}^{-1}$. The angular scales and the parameters of the contours are the same of the band 6 ones shown in Figure 5.2.*

measurements would be necessary, in order to be sure to properly model and interpret the emission from the AGN (i.e., without any SF contamination), so far totally unconstrained by data in the Rayleigh Jeans tail. Only by resolving the torus emission itself we can derive its real contribution, although if the flux measured in the central region will come out to be mostly due to the AGN, this result will challenge the current torus models, implying the presence of a colder dust component.

- **Regions “B”, “C”, “D” and “E”:**

Regions “B” and “C” correspond to the bar edges. The sudden change of the in-falling direction in this region seems to produce a dense and hot environment where star formation is active.

The CO(2-1) spectrum of region “B” peaks at the galaxy velocity (i.e., 0 km/s in Figure 5.9), but shows a positive velocity tail (possibly a secondary peak at about 40-50 km s⁻¹), while the spectrum of the “C + D” regions peaks at negative velocities (e.g., -30-40 km s⁻¹ in Figure 5.9).

Together with regions “D” and “E”, they were already identified as SF loci by [Bedregal et al. \[2009\]](#): this is confirmed now by the presence of strong CO emission.

Region “E” is also the dominant region in the CS(5-4) brightness distribution (flux density $\sim 0.29 \pm 0.03 \text{ Jy/beam}$, see Figure 5.8), thus likely to be denser than the others (since CS is a tracer of high density regions).

**The complex morphology and kinematics in the inner regions of
NGC 5135: *Are we witnessing the AGN influence?***

- **Region “G”:**

This region corresponds to the SNR identified by HST and VLT SINFONI observations and clearly visible here in all the observed emissions. Observation with VLA at 6 cm (Ulvestad and Wilson [1989]) also shows a strong emission at this location, suggesting strong synchrotron emission from SNR.

- **Region “F” and “H”:**

Two regions of high-velocity dispersion, namely regions ‘F’ and ‘H’, are not detected in any previous observations.

- **Region “F”:** is aligned along the bar, but seems to lie outside its edge. It is characterised by a double peaked spectrum with two opposite velocity components (e.g., $\sim -70/ + 70$ km s⁻¹ in Figure 5.9). It is not detected in the continuum emission.

- **Region “H”:** lies along the Southern arm and it appears only in the CO(2-1) maps (not in the continuum or CO(6-5)), showing a high velocity dispersion and a secondary peak in the spectrum corresponding to high negative velocity (~ -70 -80 km s⁻¹; see Figure 5.9).

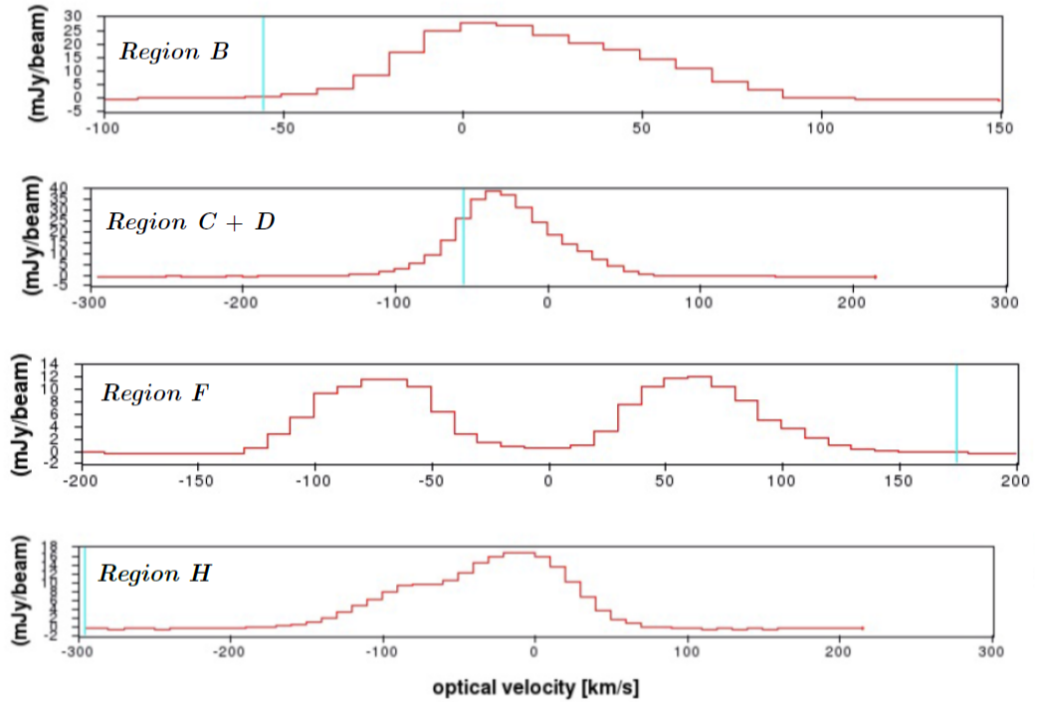


Figure 5.9: Spectra of the regions marked in the CO(2-1) brightness distribution (Figure 5.5, bottom left). The name of the regions is shown in the top left of each spectrum. The extraction regions were selected so that they contained all the radiation $> 4\sigma$, being careful to separate the various regions (if possible).

5.2 Kinematic model

From the analysis of the 1st moment of CO(2-1) (Figure 5.3), the global gas kinematics seems to be well described by a rotating (thin) disk in which material flowing through two arms (the northern and the southern) to the edge of the nuclear bar contributes to the rotating structure.

In order to understand and interpret what is happening in the nuclear regions of NGC 5135, we have reproduced the global motion of the gas detected with ALMA by means of a kinematic model.

This study was possible using the ^{3D}BAROLO software (Di Teodoro and Fraternali [2015]) described in the previous chapter. The software version used allows us to include radial motions in the model. In our case, the gas can be strongly affected by the presence of the central engine. Part of the gas can move spiralling towards the BH, contributing to its massive growth. This kind of behaviour, therefore, involves the presence of a radial velocity component for the gas, which can be accounted for in the ^{3D}BAROLO model.

In order to obtain models capable of describing the gas motion throughout the whole analysed regions, used the cube of the molecular transition of CO (2-1), since it was the clearest data-cube, where most of the regions could be clearly seen. In particular, regions “F” and “H”, described in the previous paragraph, are only identifiable through this transition (as reported also in the Table 5.2).

In order to reduce the computing time of the code, we modified the cube by degrading the angular resolution by a factor of ~ 3 . At the same time, we reduced the cube size from [2048, 2048] pixels to [500, 500] pixels, including all the emitting regions and maintaining the same center (the AGN coordinates). The preliminary results provided by this low-resolution model have allowed us to understand the global gas motion, choosing the parameters to fix in the higher resolution models. Here we list the main parameters describing the model, that we have set before running the fit.

- **The kinematical centre:** (x_0, y_0)

We have fixed the centre of the rings in the tilted-ring model to the position derived in the continuum band 6 image of what we considered the AGN emission. This choice was made using the “2D fit tool” of the CASA-viewer, fitting a 2D Gaussian to a brightness distribution. We associate the emission peak with the AGN position. We obtained RA(J2000) +13:25:43.99 DEC(J2000) -29:50:00.02, slightly different from the coordinates of NGC 5135 found in the literature (e.g., Israel et al. [2015], Yang et al. [2015]), but consistent with the kinematic centre found by ^{3D}BAROLO and with the radio and X-ray AGN position.

- **The position angle:** (ϕ)

The position angle was fixed directly by looking at the position-velocity diagrams (*P-V diagrams*). This was done by using *kpvslice*, an extension of the *Karma* software (Gooch [1996]). We find $\phi \sim 10_{-10}^{+5}$ as the best approximation of the major (projected) axis orientation.

Later in this thesis, we will show and discuss the results obtained by assuming

The complex morphology and kinematics in the inner regions of NGC 5135: *Are we witnessing the AGN influence?*

different position angles for the galaxy disk; we will see how the angle set for the final models ($\phi = 10^\circ$) can be considered as the best choice to reproduce the average trends of the rotational curves, the radial velocity and the velocity dispersion profiles.

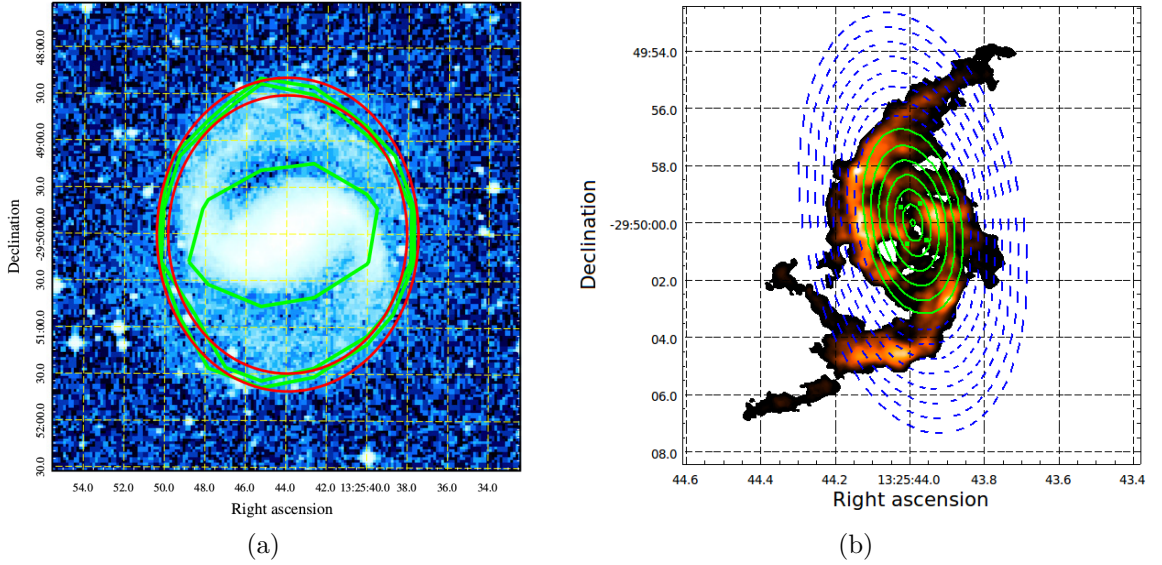


Figure 5.10: *left*: Optical DSS image of NGC 5135. Smoothed galaxy's contours are overlapped in green. The elliptical regions (in red) are built following the innermost and the outermost contours; *right*: Surface brightness distribution of the CO(2-1) data cube, produced by 3D BAROLO above a 3σ threshold. Elliptical regions are built on the size of the model rings. In green (solid lines) we show the rings within ~ 1 kpc from the AGN, while in blue (dashed lines) we show the rings from 1 to ~ 2.3 kpc.

- **The inclination of the galaxy disc: (i)**

The inclination (i) of the disk was set by using the DSS image of NGC 5135 (see Figure 5.10 (a)), to which we overlaid ellipses with different axis ratios to match the iso-surface brightness contours of the outer disks. The assumption is that the galaxy disk has circular symmetry, with radius equal to the major axis of the red elliptical regions. The angle between the galactic axis and the line of sight provides the apparent minor axis. The inner red ellipse corresponds to a angle of $i_{inner} = 59^\circ$, while the outer one corresponds to $i_{outer} = 55^\circ$. We decided to fix the inclination of the galaxy at the mean value, $i = 57^\circ \pm 2^\circ$, where the error is given by the difference between the angles of the inner and outer ellipses.

- **The thickness and the number of rings:**

Different choices have been made for these parameters, depending on the resolution of the analysed data cube.

5.2 Kinematic model

In case of low-resolution cube (whose results are shown in figures Figure 5.12 to Figure 5.15), the choice was to impose the same data resolution of the degraded cube ($\text{beamfwhm}=0.6$ arcsec).

For the high-resolution cube, in order to limit the presence of spikes in the model disk (with the **AZIM** normalization), we decided to exploit the convolution provided by $^3D\text{BAROLO}$ and set the resolution to 1/2 of the data resolution ($\text{beamfwhm}=0.13$ arcsec).

The number of rings has been set as to allow us to model the entire area within 1 kpc from the AGN (see Figure 5.10 (b)).

Several elements are found in the nuclear region of NGC 5135. Some of these are well reproduced by $^3D\text{BAROLO}$ software, a few are not in Figure 5.11 are shown the CO(2-1) moments obtained from data and from two $^3D\text{BAROLO}$ models with different normalization. Panels (a), (b) and (c) show the brightness distribution (0^{nd} moment), the velocity field (1^{nd} moment) and velocity dispersion field (2^{nd} moment) respectively, obtained from our CO(2-1) band 6 (concatenated) data-cube. Panels (d), (e) and (f) are the 0^{th} , 1^{st} and 2^{nd} moments obtained with the **LOCAL** normalization $^3D\text{BAROLO}$ model, while panels (g), (h) and (i) are the same moments for the **AZIM** normalization model. All moments are extracted at a threshold of 3σ and up to a maximum distance of 1.1 kpc from the AGN.

We clearly observe radial motions, with the gas streaming in from kpc scales to ~ 200 pc. The **AZIM** model in Figure 5.11 shows a concentration of material, corresponding to the point where the rotation curve has a clear change of shape, from very steep to relatively flat (see later discuss).

The 2^{nd} moment of both the **LOCAL** and **AZIM** models indicates that at larger galacto-centric radii the line-width is large, then it suddenly diminishes in the inner 200 – 300 pc. Along this ring we find region “B”, which can be one of the currently active star formation sites or the remnant of a past recent event.

Other SF regions are also observed at the outer edge of this “ring”, together with SNR and possibly “super-bubbles” (see later discussion). These features suggest that the region where the material is accumulated and becomes gravitationally unstable could be somewhat larger and that the minimum in panel (i) of Figure 5.11 could be generated by central parts of the bubbles.

We limited our analysis to 1 kpc since, as previously mentioned, the software finds the best kinematic parameters (V_{rot} , V_{rad} and σ) ring-by-ring, averaging the solutions in all the pixels within a ring. At distances longer than 1 kpc, while the gas distribution terminates along the minor axis, the gas emission continues to define the arm-like structure along the major axis. Such a complex and poorly sampled structure has the consequence that $^3D\text{BAROLO}$ may have trouble finding only one solution to associate with V_{rot} , V_{rad} and σ values.

The complex morphology and kinematics in the inner regions of
 NGC 5135: *Are we witnessing the AGN influence?*

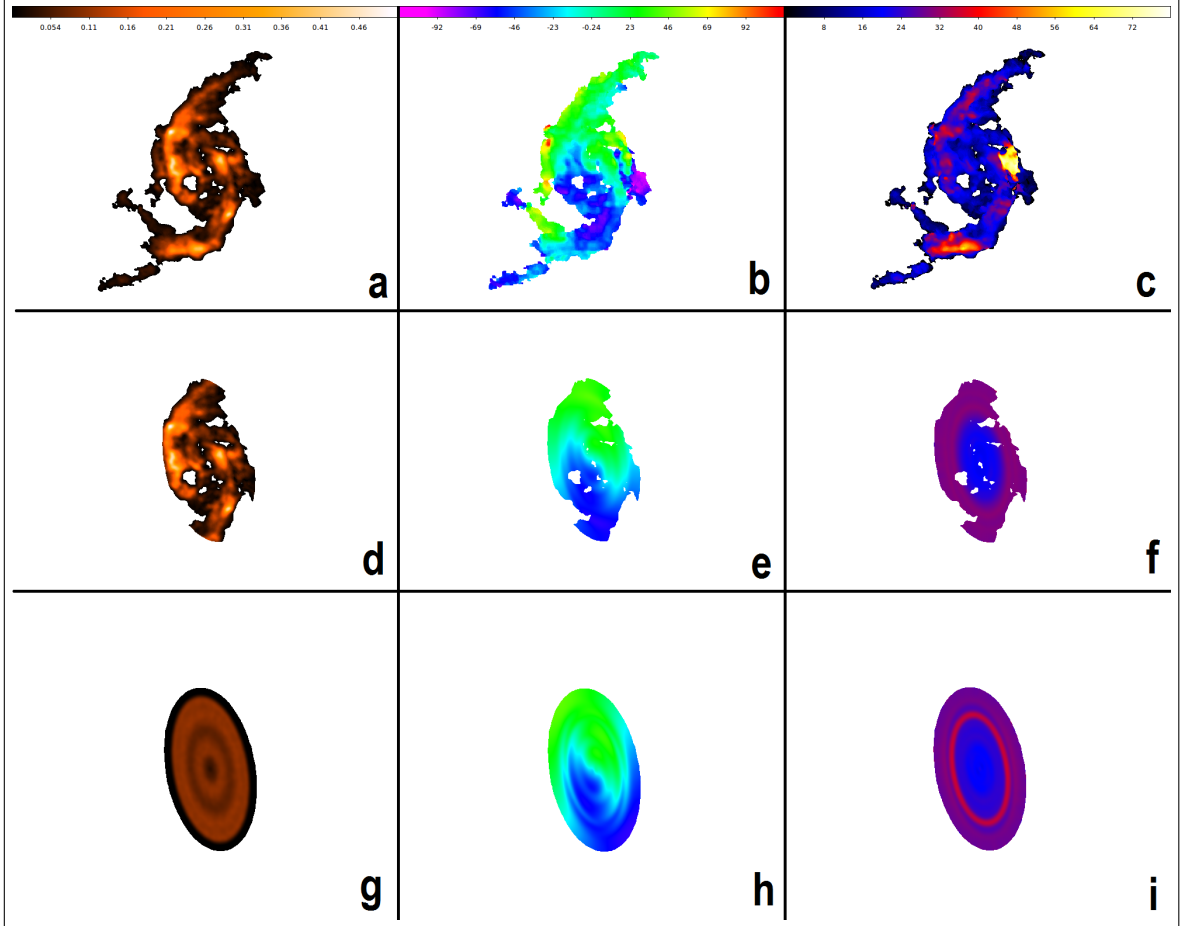


Figure 5.11: *Molecular gas distribution (i.e., CO(2-1)) in the centre of NGC 5135 and the relative models obtained with 3D BAROLO. Panels (a), (b) and (c) show the 0th (map), 1st (velocity field) and 2nd moments (velocity dispersion) respectively, obtained from our CO(2-1) B6-concatenated data cube. Panels (d), (e) and (f) are the 0th, the 1st and 2nd moments of the LOCAL normalization 3D BAROLO model, while panels (g), (h) and (i) are the same moments for the AZIM normalization model. All moments are extracted at a threshold of 3σ . Colour bars are expressed in unit of Jy beam^{-1} , km s^{-1} and km s^{-1} respectively from left to right.*

5.2.1 Results from the low resolution model

The low resolution model is shown in Figures from 5.12 to 5.15. In Figure 5.12 and 5.13 in same selected spectral scans our data-cube (in blue) are compared with the model (in red) in the two possible normalization modes respectively (`norm=AZIM` and `norm=LOCAL`). Note that the `LOCAL` model (Figure 5.13) can globally reproduce the global emission structure of our data. To obtain a similar result with the `AZIM` model is not possible for NGC 5135, due to the gas asymmetry in the data, which is hardly reproducible with a disk-like symmetry. Once fixed the position angle, `3D BAROLO` provides the velocity profiles along the major (defined by ϕ) and minor axis ($\phi + 90^\circ$). These profiles are shown in Figure 5.14 as contours overplotted to the data (in gray scale). The confidence contours overlapped to the data are: data-contours, labelled in blue, and model contours in red (at 4σ , 16σ and 32σ).

Both models succeed in reproducing the data, thus strengthening the two initial assumptions that the observed gas is described by a rotating-disk (tsee the P-V diagrams along the major axis) and that radial motions perturb the disk structure. In fact, the gas shows a real radial velocity component, indicating that it is slowly falling towards the AGN. It should be noticed that, although not reproducing the whole complexity of the observed data, the model is able to globally reconstruct the radial velocity of gas, along the major and minor axis. In the presence of a “standard” rotating disk, the P-V along the minor axis is expected to be flat, assuming an “S” shape if the rotation is perturbed by radial motion. The velocity profiles show instead several features, that allow us to directly investigate the structure of the high-velocity dispersion region, named “F” in the previous chapter. In fact, focusing on the left side of the profiles along the minor axis, we can notice the presence of a structure different to what we would expect for a rotating disk gas structure with superimposed radial motions. In fact, the gas forms two clouds at the same position (~ 1.8 arcsec from the center) moving in the opposite directions (one centred at the velocity of ~ 70 km/s and the other at ~ -70 km/s), separated by an empty semicircular region just where the model would expect to find emission (visible from the red contours of the model). This behaviour will be crucial to interpret what is happening to the gas in this galaxy, as we will discuss in detail in the next paragraph.

In Figure 5.15 we show the kinematic results of this model: the rotation curve (top row, in arcsec, panel (a), and in kpc, panel (b)) shows a slow rising from a value of ~ 20 km/s to ~ 60 km/s in the outer regions mapped by the model. Conversely, the radial velocity (middle row; in arcsec, panel (c), and in kpc, panel (d)) and velocity dispersion profiles (bottom row; in arcsec, panel (e), and in kpc, panel (f)) are somewhat constant (slightly increasing) from 0 to 1 kpc: the velocity ~ -30 km/s (infalling gas), with a dispersion of ~ 25 km/s.

Note that the results of the `LOCAL` normalization model are always included within the normalization of the azimuthal model error bars. This assures us that the built kinematic models correctly reproduce the global observed gas motion, since the observed gas distribution is clearly not axis-symmetric, thus it is not obvious that the solutions found by two different normalization models converge to the same values (if this is not the true value).

The complex morphology and kinematics in the inner regions of
NGC 5135: *Are we witnessing the AGN influence?*

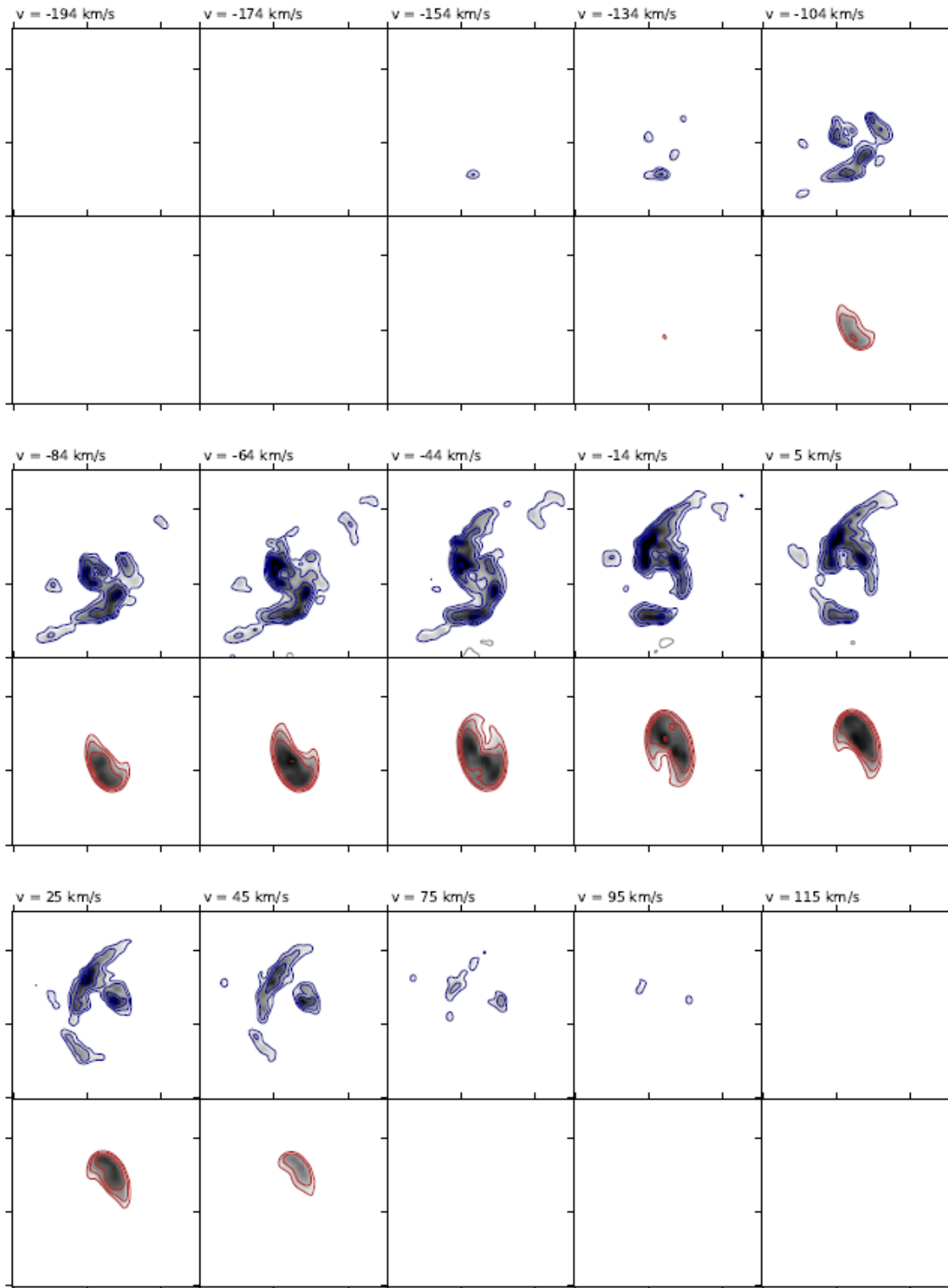


Figure 5.12: Selected velocity channels showing the comparison between data (in blue, top row) and the AZIM (in red, bottom row) model. This plot gives an idea of the goodness of the fit provided by ${}^3D\text{BAROLO}$. The cube is centred at $\nu_{\text{rest}} = 227.43$ GHz of the molecular transition of CO (2-1). Model and data are at $> 4\sigma$.

5.2 Kinematic model

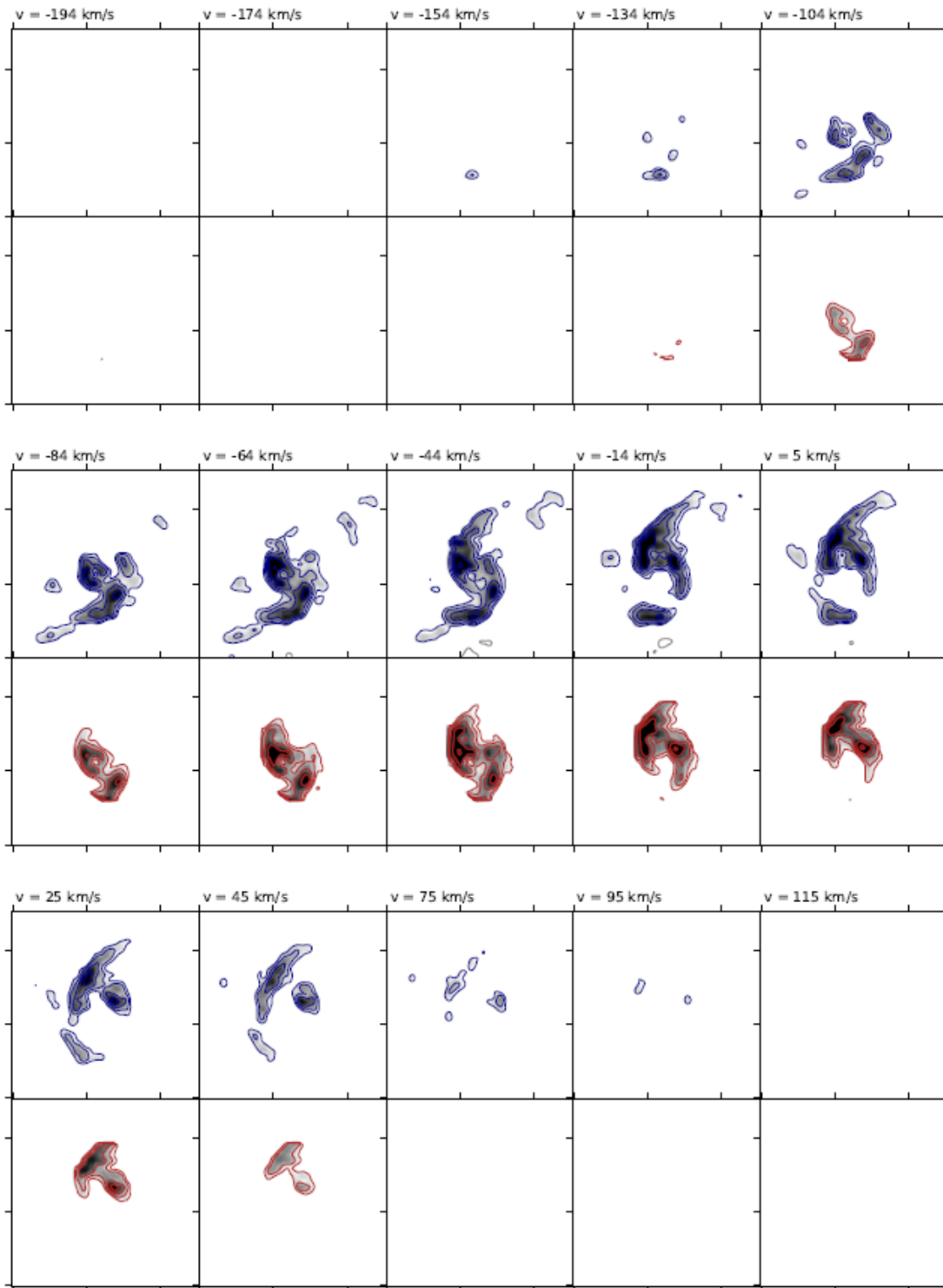


Figure 5.13: Same as in Figure 5.12, but with the LOCAL model (red, bottom row).

The complex morphology and kinematics in the inner regions of
NGC 5135: Are we witnessing the AGN influence?

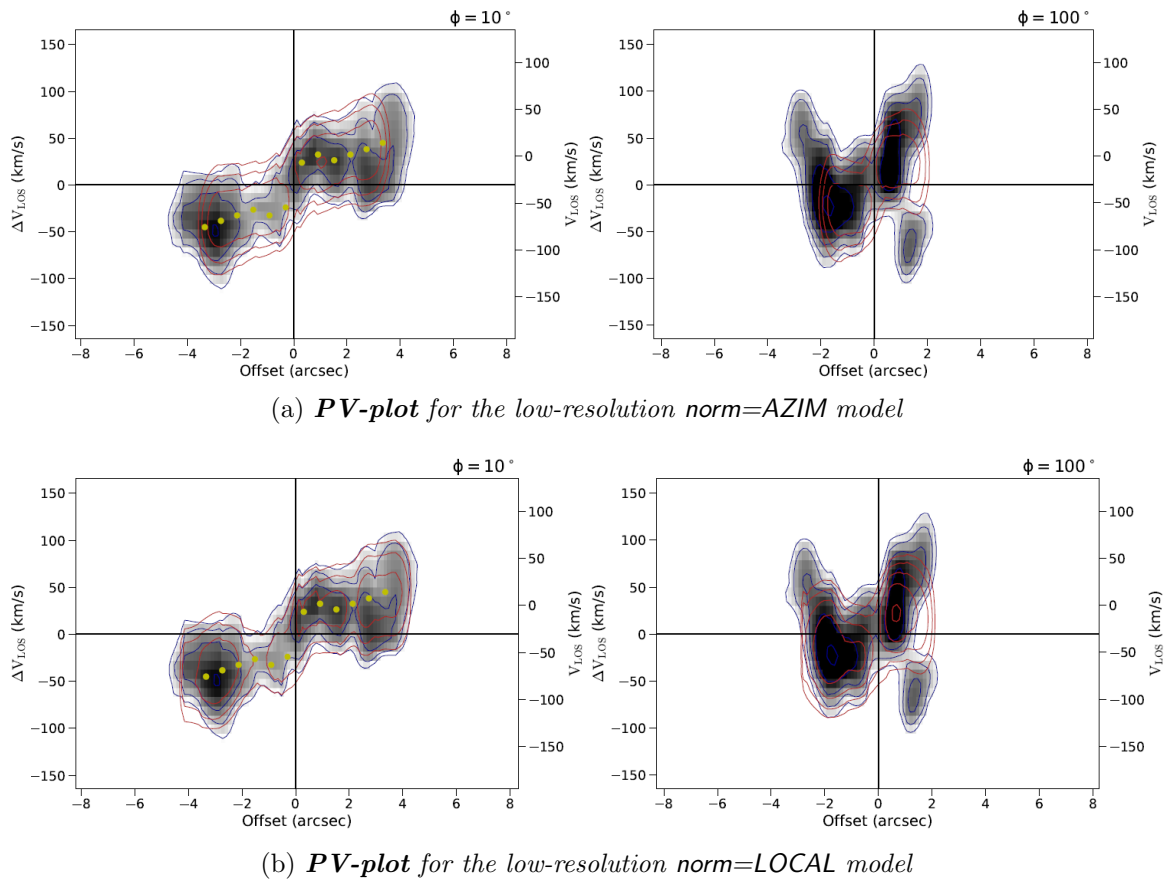


Figure 5.14: **Position-Velocity diagrams** along the major-axis (left) and the minor-axis (right) of the low-resolution data-cube. In the top panels we plot the *AZIM* model, in the bottom the *LOCAL* one, overimposed to the grey-scale density of data. The PA of the major axis is $\phi = 10^\circ$, while that of the minor axis is $\phi = 100^\circ$.

5.2 Kinematic model

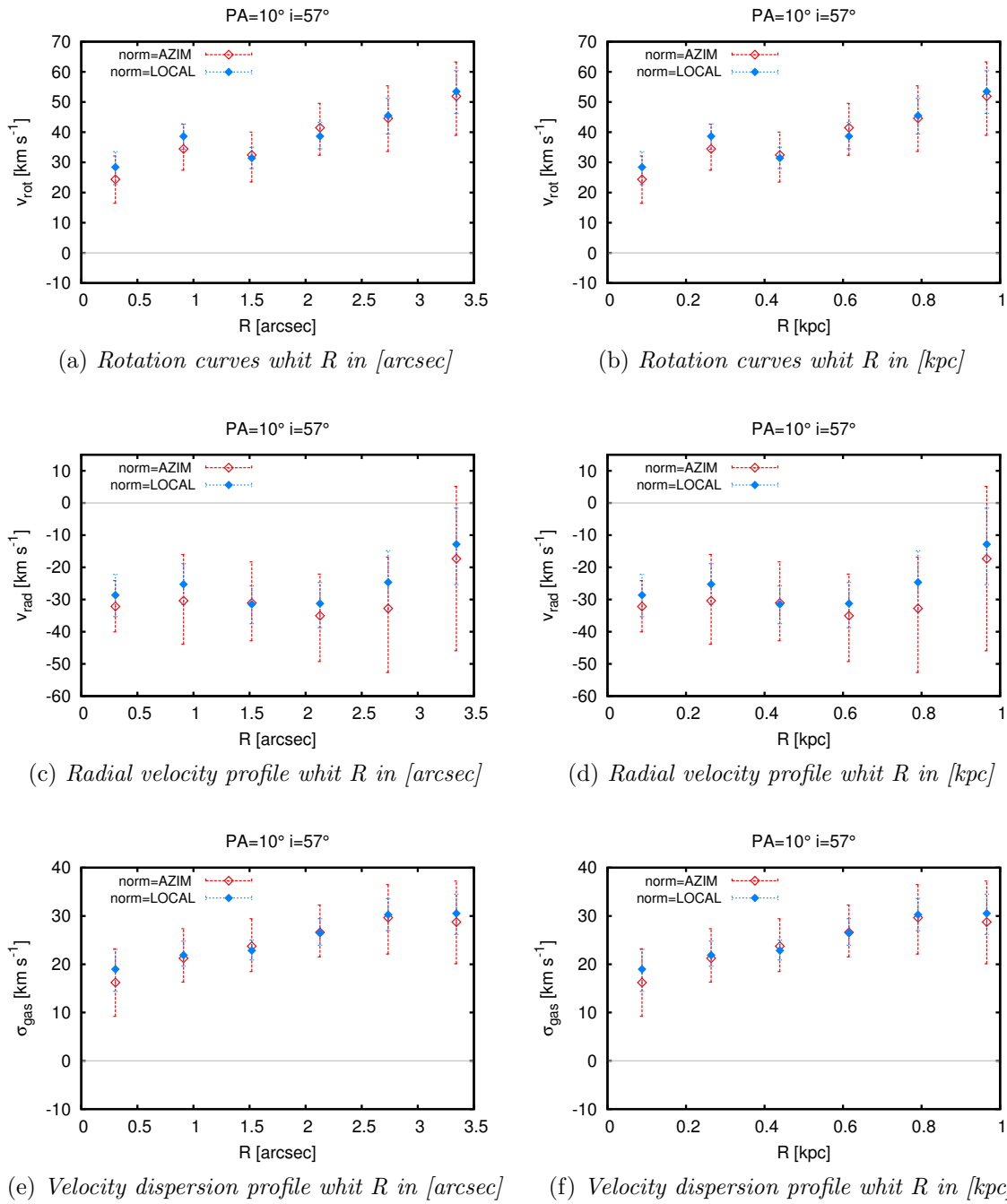


Figure 5.15: *Rotation curve, radial velocity and the velocity dispersion profiles within 1 kpc from the AGN, for the two models $norm=LOCAL$ (blue diamonds) and $norm=AZIM$ (red diamonds). The gray line represents the $''y'' = 0$ line.*

5.2.2 Result from the high-resolution model

To conclude, we show the results of the model at high resolution, with same parameter setting of the low resolution one. This has been done in order to verify in more details the trends derived by the low resolution model.

The comparison between the data-cube and the model, (at $> 3\sigma$) is shown in Figure 5.17 and 5.18. Also in this case, the models are able to reproduce the global gas distribution (channel by channel) of the gas.

Although the P-V diagrams (Figure 5.16) obtained with the high-resolution models show a less homogeneous distribution of the gas along both axes with respect to the low-resolution ones, both normalizations can well reproduce the gas density profile (and its rotation).

Figure 5.19 shows the rotation curve and velocity profiles, in analogy to Figure 5.15.

All plots show the V_{rot} , V_{rad} and σ trends as a function of distance from the BH.

However, with the high-resolution within each ring the variation can be emphasize by the larger inhomogeneities, which instead are averaged within larger rings. It can, therefore, happen (as it is in the case of the second point at ~ 0.1 kpc) that the model cannot find a solution consistent with the general trend.

Nevertheless, the slow velocity increasing followed by a rapid rise within 0.3 kpc and a nearly flat shape around ~ 55 km/s is best described in this case. The radial velocity and the velocity dispersion profiles, on the other hand, continue to show the same behaviour, keeping almost constant at -30 km/s and 25 km/s respectively.

In order to test the robustness of our solution, in particular its dependence on the position angle choice (which is the more uncertain parameter), we have varied ϕ , and re-fitted the the low resolution cube with models considering different values of ϕ (Figure 5.20). For all the ϕ values between 0° and 20° , the results obtained are nearly the same as those obtained by imposing $\phi = 10^\circ$. This allowed us to fix the position angle to the last value, as this was what we originally found from the analysis of the P-V diagrams by using `kpvslice`.

5.2 Kinematic model

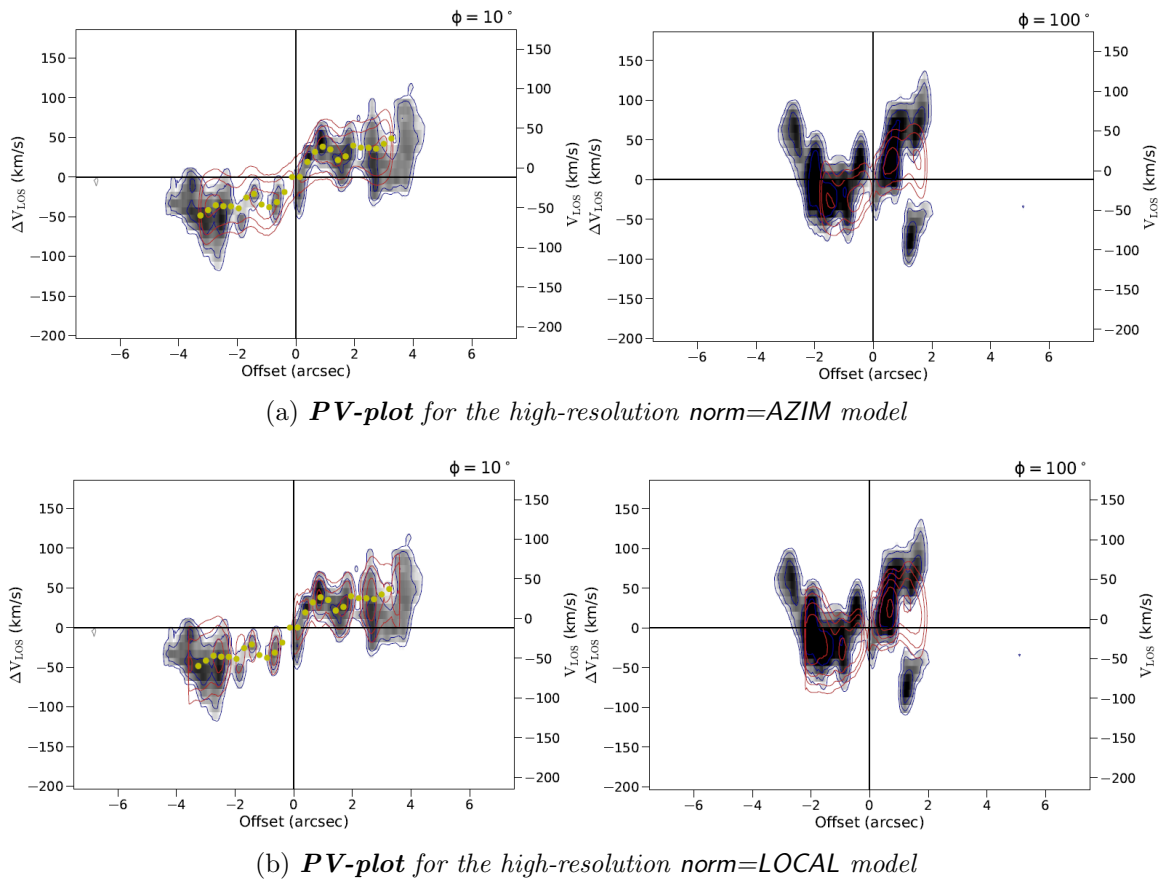


Figure 5.16: **Position-Velocity plots:** along the major axis (left) and along the minor-axis (right) for the high resolution data-cube. Top: PV-diagrams obtained from the model with *norm=AZIM*; bottom: PV-diagrams with the *norm=LOCAL* model. The major axis position angle is $\phi = 10^\circ$, while the minor axis is $\phi = 100^\circ$.

The complex morphology and kinematics in the inner regions of
NGC 5135: *Are we witnessing the AGN influence?*

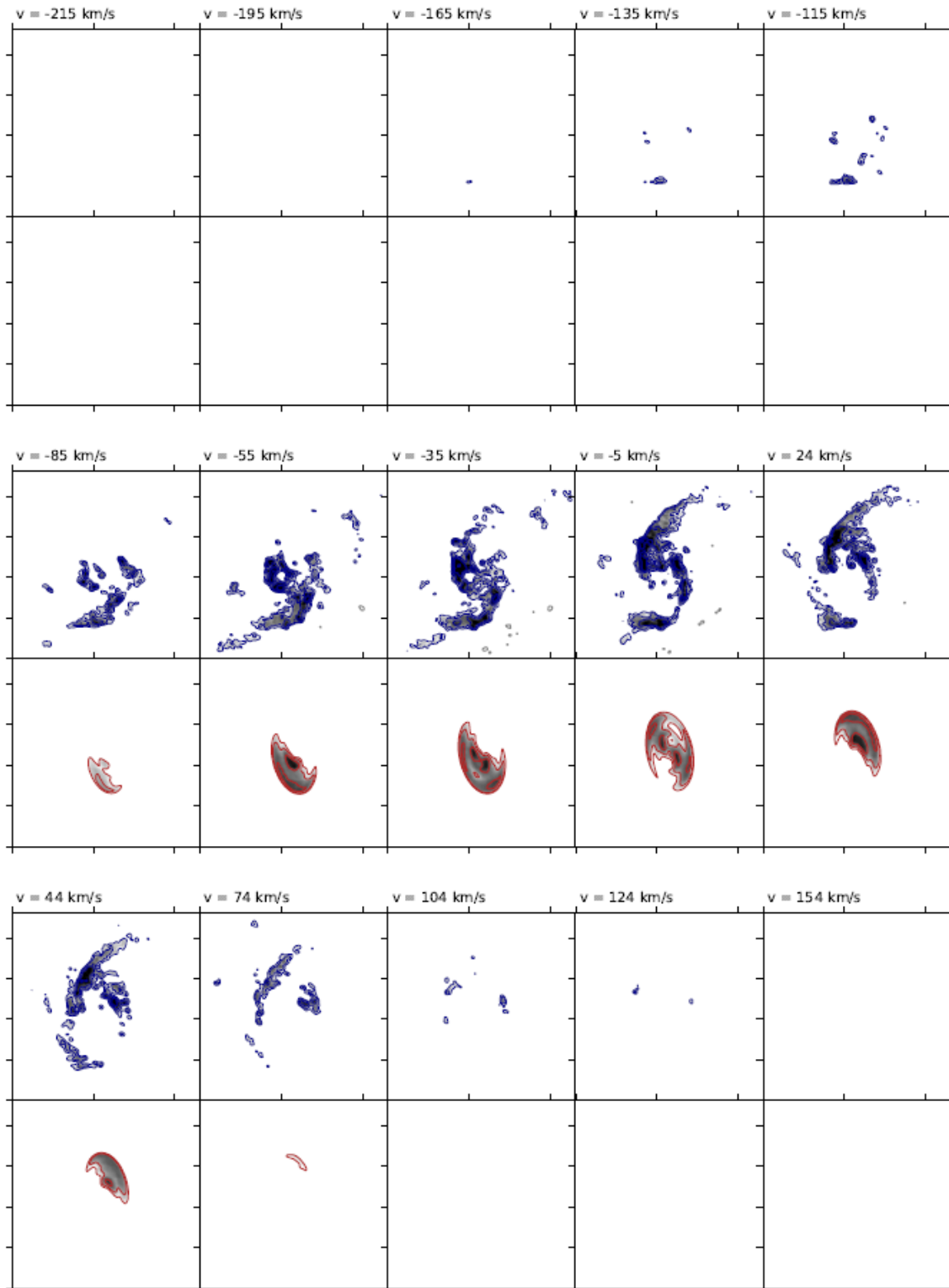


Figure 5.17: *Same as in Figure 5.12, but for the high resolution data cube and model.*

5.2 Kinematic model

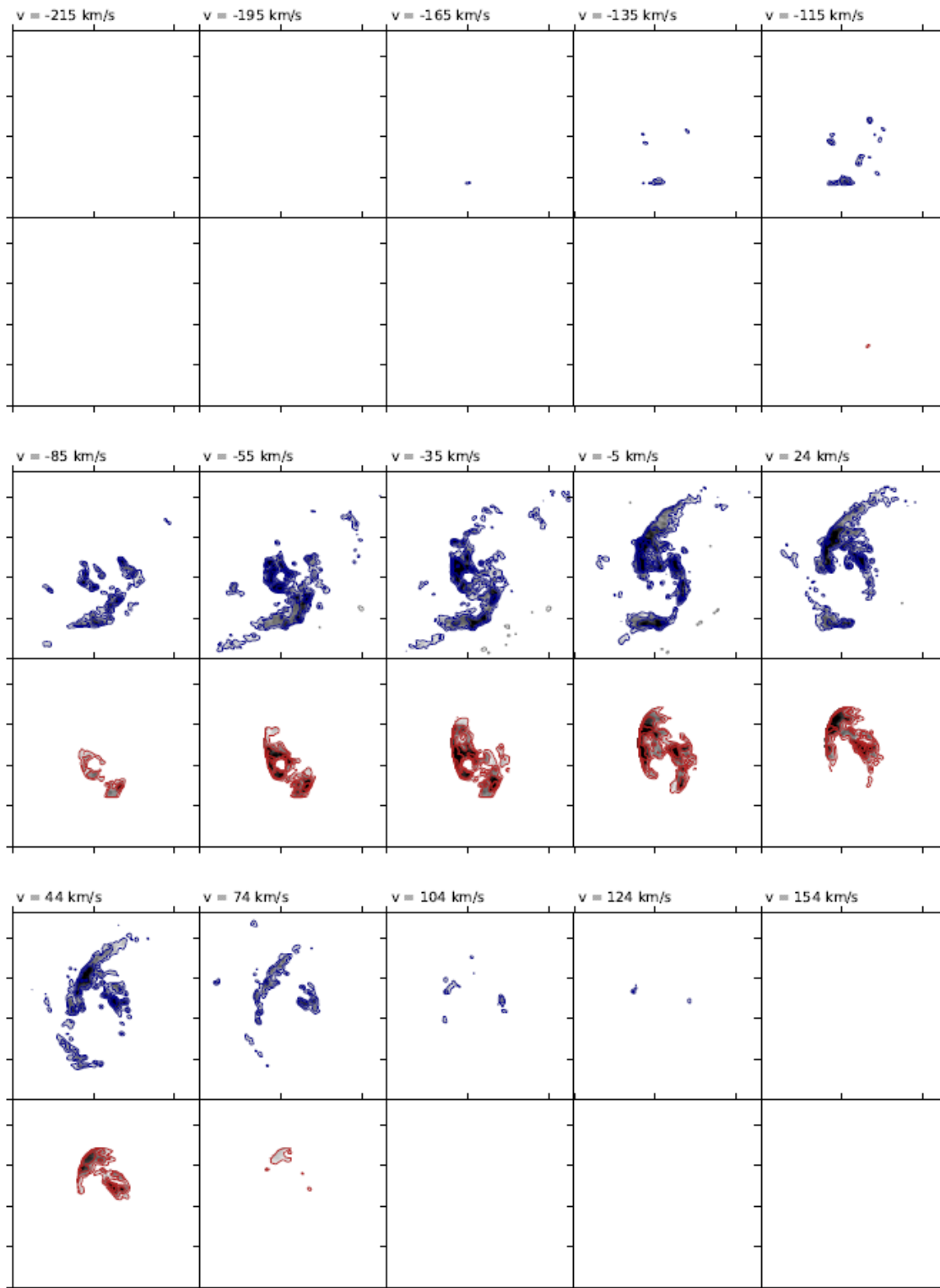


Figure 5.18: Same as in Figure 5.17, but for the high-resolution data cube and model.

The complex morphology and kinematics in the inner regions of
 NGC 5135: *Are we witnessing the AGN influence?*

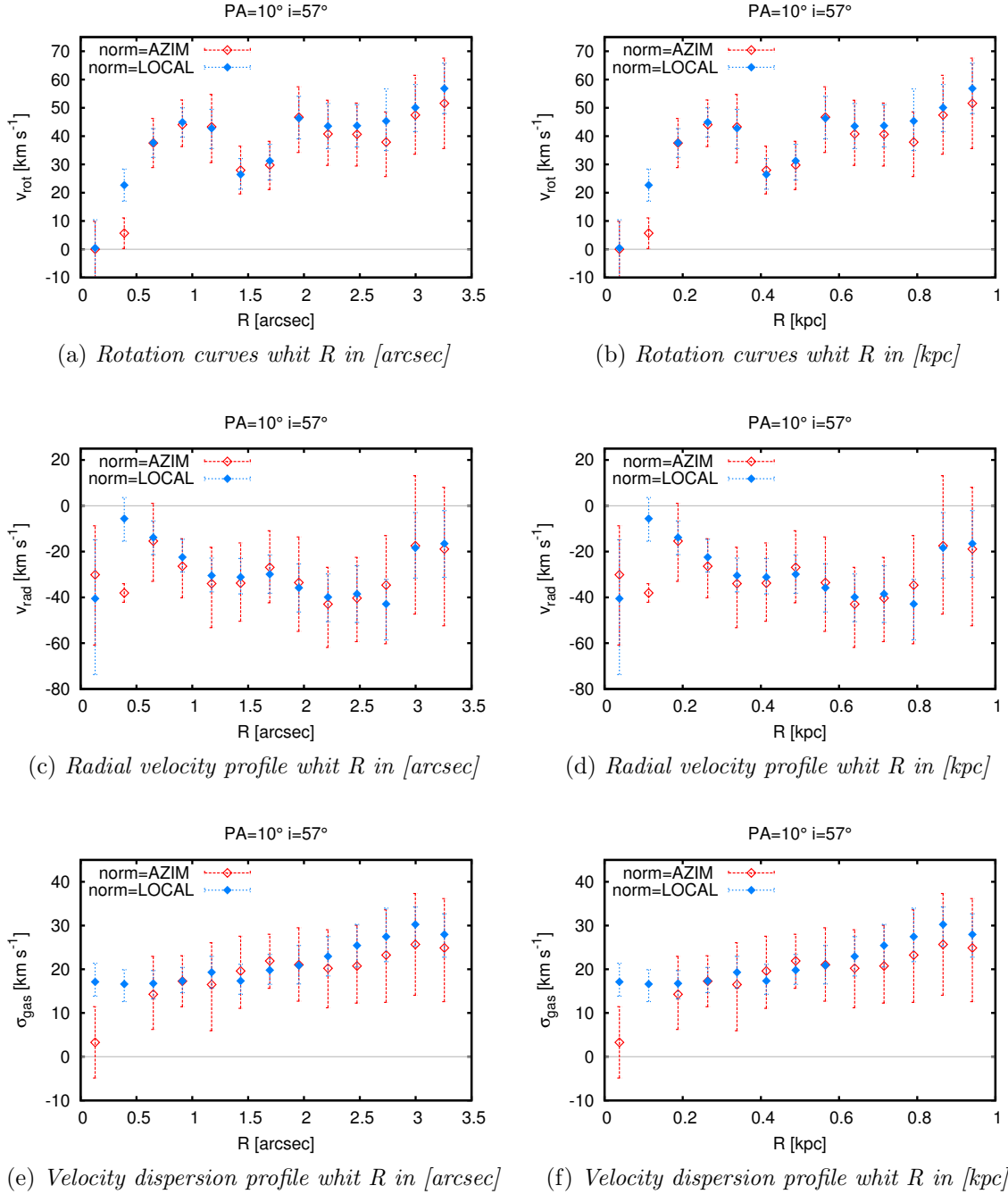


Figure 5.19: Same as in Figure 5.15, but for the high-resolution data cube and model.

5.2 Kinematic model

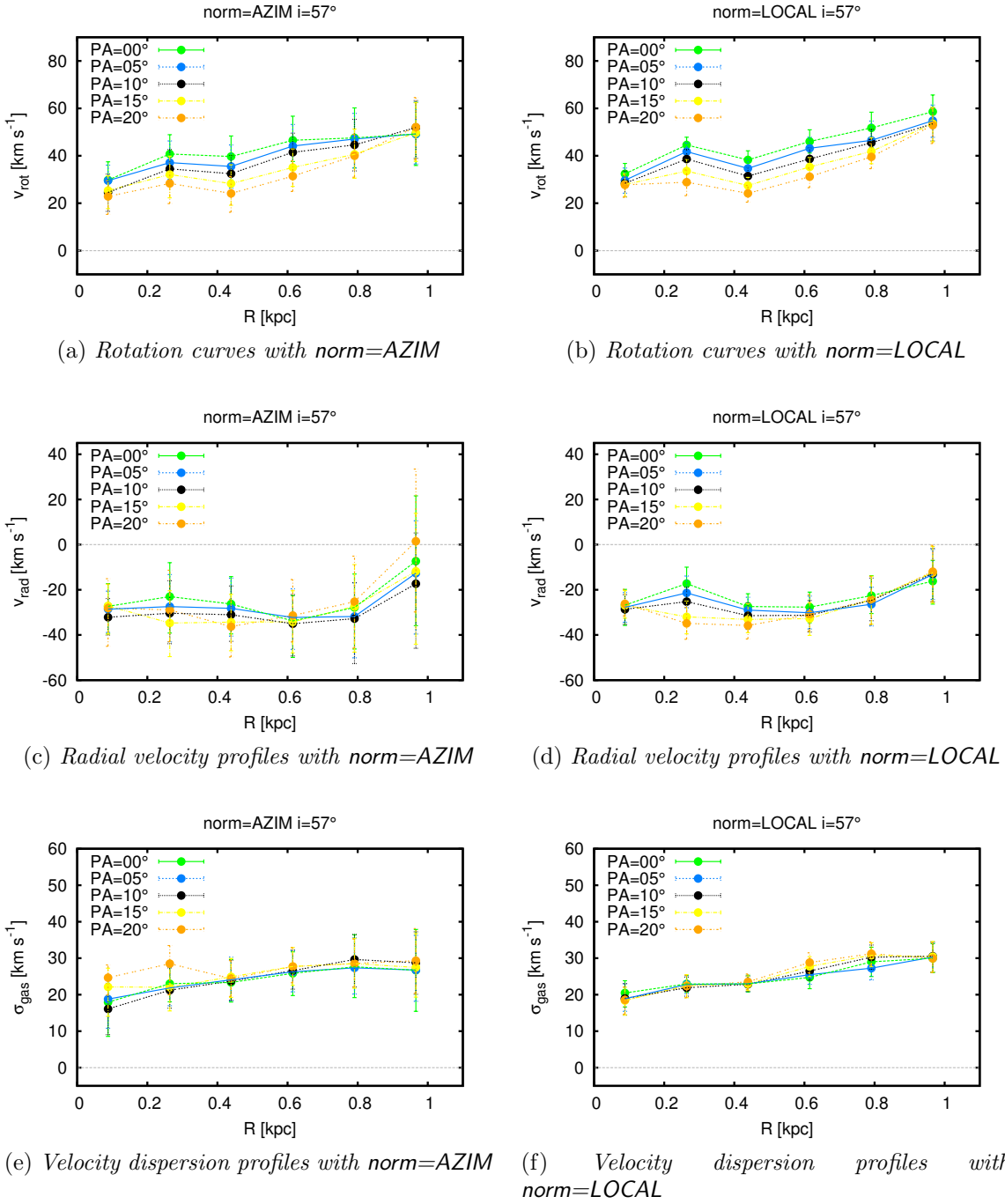


Figure 5.20: Rotation curves (panels (a) and (b)), radial velocity profiles (panels (c) and (d)) and velocity dispersion profiles (panels (e) and (f)), as functions of the distance from the kinematic center (in kpc) for the azimuthal (left column) and local models (right column). Both models have the disk inclination fixed at $i = 57^\circ$ and the position angles between $0^\circ < \phi < 20^\circ$ (with a separation of 5°). The black dotted line and filled circles correspond to $\phi = 10^\circ$, used in the final models.

5.3 Physical interpretations

As discussed in the previous section, the overall structure of the CO(2-1) molecular gas in NGC 5135, its density distribution and kinematic can be well explained by a model considering a rotating disk perturbed by radial motions. Based on the inclination of the disk and the spiral arms structure, we derive that the gas flows through the arms and the bar to the centre of the galaxy, i.e., we are facing a gas inflow towards the BH. Based on this general interpretation, we find several regions that fall outside the rotating disk + gas inflow model explanation.

In Figure 5.5 and 5.6 we have identified these regions, plus others that would deserve further explanation (marking them with letters and - if needed - encircling with ellipses), for a detailed discussion on the origin and nature of each of them.

Previous observations with different instruments (e.g., HST, VLT-SINFONI; e.g., Alonso-Herrero et al. [2006], Bedregal et al. [2009], Colina et al. [2012], González Delgado et al. [1998]) have identified the central AGN (marked with the “A” letter), few SF regions at the left edge of the inner bar (“C”, “D”, “E”), and a SNR in the Southern arm of the inner spiral gas structure (“G”).

The AGN region (“A”) is observable in continuum (both Bands 6 and 9), but not in CO line, in agreement with the finding that the BH is strongly obscured (i.e., Compton Thick, CT from X-ray data; Levenson et al. [2004]): the cold toroidal dust distribution has the size of the beam in ALMA Band 6, thus being unresolved at a galaxy scale of $\simeq 56$ pc.

The SF regions (“C”, “D”, “E”) are clearly identifiable in our data in continuum, CO (both (2-1) and (6-5)) and CS emission.

Regions “B” and “F” were not previously identified in any other bands, and seem to trace a shock front at the right edge of the bar, with an expanding super-bubble (see below) and gas likely thrown out of the galaxy at high velocity (in two opposite directions, thus showing a very large, double peaked width of the CO line). The alignment between zones “A”, “B” and “C” seems to indicate the presence of a bar, with enhanced star formation at its edges.

Zone “B” traces a shock front between the AGN and zone “F”, with the latter identifying the two opposite velocities region (clearly visible also in Figure 5.14 and 5.16, along the minor axes at ~ 1.8 arcsec from the center, with $\sim \pm 70$ km/s) at the edge of the bar.

Region “F” lies just outside the bar, close to the shock front and it is the more puzzling region observed in our data (a tentative explanation is given in the next paragraph). The high velocity dispersion observed in zone “H” is described and partially reproduced by our model (see Figure 5.18) as the superposition of matter associated with the two spiral arms, moving in two different directions and following the trend predicted by the kinematical models obtained in the previous paragraph (i.e. along the Southern arm path and along the Northern arm trajectory beyond the bar region) and overlapping in this region, plus material outflowing from the arm (in opposite direction to the spiral gas flow), not explained by the model and possibly associated to SN activity.

5.3 Physical interpretations

Both zones (“F” and “H”) were not identified by any previous observations in other bands.

A local emission from a SNR in the “F” region could be a simple explanation, but, differently from zone “G”, in “F” we do not observe significant emission either in continuum nor in spectral lines, but only a very large CO(2-1) line width (i.e., produced by the presence of the two opposite velocity peaks, from two gas clouds spatially overlapping). Hence the SNR origin hypothesis is likely to be discarded for no clear evidence of the presence of the remnant.

Another possibility is that in “F” we are facing a flow of material towards the AGN: an inflow of material along the bar connecting the SF region “C”, the AGN (“A”) and SF region “B” could justify the presence of the shock front (“B”), while the high velocity dispersion region (“F”) due to the overlapping components of opposite velocities outside the edge of the bar is of more intriguing interpretation. The gas, in-falling through the inner arms by spiralling towards the central BH, then suddenly changes its direction as approaching the nucleus and starts to follow the bar structure: such a flow is likely described by the velocity pattern observed in the CO(2-1) maps (see *left* panels of Figure 5.5 and Figure 5.6).

The possibility of an outflow from the AGN not lying along the bar (i.e., perpendicular to the galaxy plane and just projected in zone “F”) could be considered, but in this case the origin of the shock front in “B” will be unrelated to the outflow and unclear. Moreover, the outflow interpretation cannot explain the material expelled in two opposite velocities in “F”. In region “F”, the zone totally empty of gas between the two opposite velocity clouds, that the 3^D BAROLO model would instead predict to be filled, resembles an expanding super-bubble. Super-bubbles are known to be associated with very massive stars (OB-associations): strong stellar winds and subsequent SN explosions from those stars inject energy and mass into the ambient ISM, creating shock fronts that sweep-up the ISM (e.g., [Castor et al. \[1975\]](#)). As the SN explosions start occurring within the cavity formed by the stellar wind bubbles, super-bubbles are created (e.g., [McCray and Kafatos \[1987\]](#)) which may eventually reach sizes of kiloparsec.

These explosions never form a visible SNR, but instead, expend their energy in the hot interior as sound waves. Both stellar winds and stellar explosions thus power the expansion of the super-bubble in the ISM. The interstellar gas swept up by super-bubbles generally cools, forming a dense shell around the cavity (observed in HI and H α). The bubble interior contains hot ($>10^6$ K), rarefied material, usually associated with extended diffuse X-ray emission (thus appearing as an empty cavity in cold and molecular gas). In this interpretation, the two blobs of gas above and below the observed empty cavity in region “F” (at 1.8 arcsec offset, with velocities of 70 and -70 km/s, corresponding to the two peaks in Figure 5.9 (c)), can be easily explained as gas surrounding the “super-bubble” being thrown away in different directions by the expanding spherical volume.

In Figure 5.21 we show different CO(2-1) velocity channels, where the “super-bubble”, surrounded by material moving in opposite directions, shows up as an empty area (red circle in the plot), with a clear shock front at its left-hand side, peaking at

**The complex morphology and kinematics in the inner regions of
NGC 5135: *Are we witnessing the AGN influence?***

Zone	Characteristics	Possible nature
A	central, unresolved at <56 pc, continuum only	AGN dusty torus, also studied by Bedregal et al. [2009]
B	high moment 0 CO(2-1), at the edge of the bar	shock front, enhanced SF
C	high continuum and CO mom 0 (both B6 and B9)	SF region, also studied by Bedregal et al. [2009]
D	high continuum and CO mom 0 (both B6 and B9)	SF region, also studied by Bedregal et al. [2009]
E	high continuum and CO mom 0 (both B6 and B9), but also CS(5-4)	SF region, likely denser than C, D
F	high mom 1 and 2 of CO(2-1), two opposite velocity clouds + empty zone	expanding “super-bubble”
G	high continuum and CO mom 0 (both B6 and B9)	SNR also studied by Colina et al. [2012]
H	high mom 1 and 2 of CO(2-1), partially explained by ^{3D} BAROLO model	material flowing opposite to that of the arm: outflow?

Table 5.3: *Principal zones identified by ALMA in the nuclear region of NGC 5135.*

systemic velocities (~ 0 km/s). The complex kinematics observed in the central kpc of NGC 5135 is also intriguing when compared to the most recent models attempting to describe the dynamics and SF in the central molecular zone of the Milky Way. In particular, the models described by [Kruijssen et al. \[2014, 2015\]](#), [Krumholz and Burkhardt \[2016\]](#) predict that the gas is inflowing within the inner Lindblad resonance, where acoustic instabilities are stable to gravitational collapse and drive turbulence in the gas, maintaining large line-widths. As the gas streams in, the rotation curve passes from flat to the solid body. In this region a substantial quantity of gas is accumulated, the shear drops and the turbulence is dissipated, making the gas prone to gravitational instability.

In Table 5.3 we list the different zones identified by our data in the inner regions of NGC 5135 and summarise their characteristics.

5.3 Physical interpretations

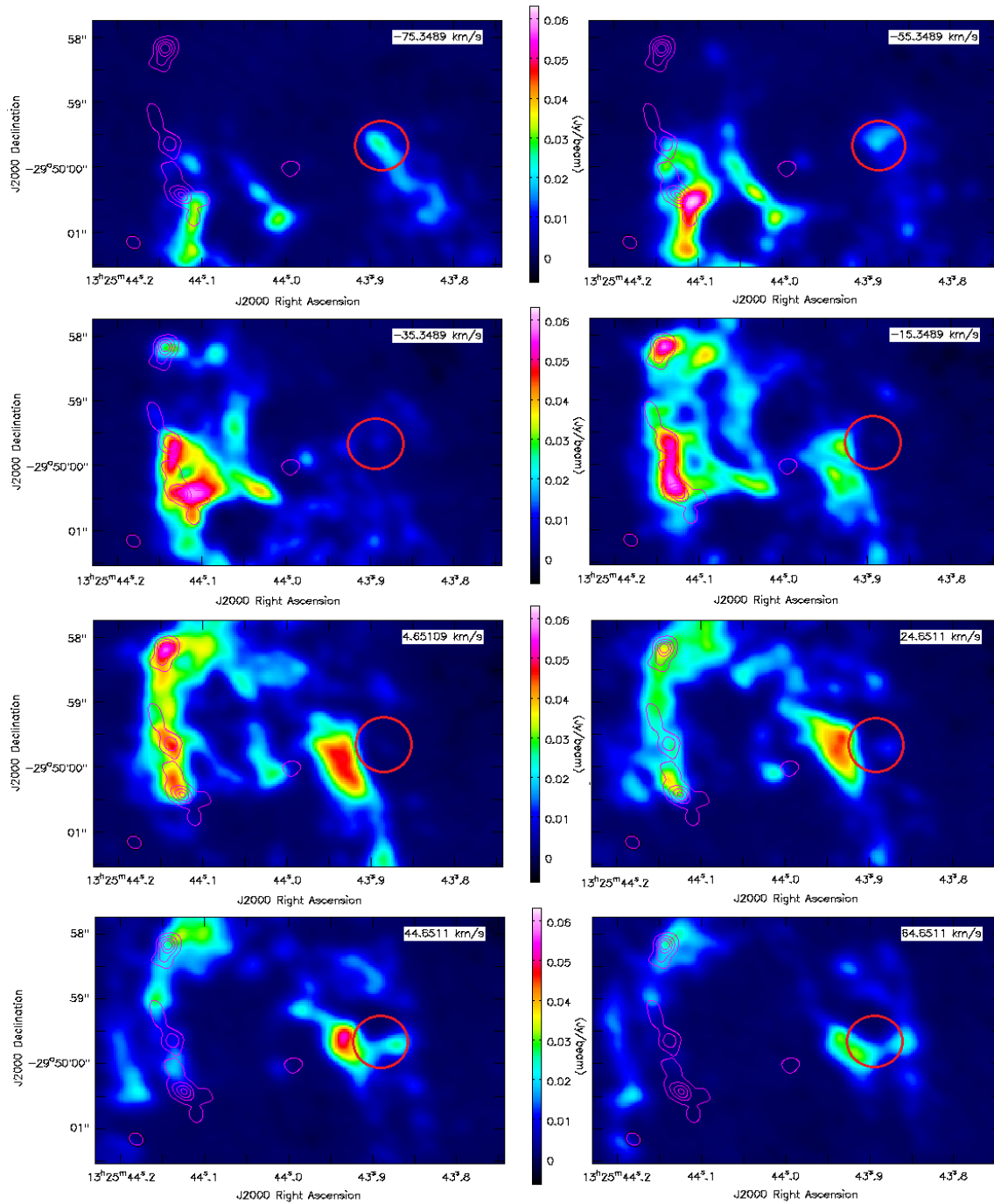


Figure 5.21: *Different CO(2-1) velocity channels showing in sequence the appearance – within the same region – of: a gas cloud moving at negative velocity, a shock front and an empty region (i.e., the “super-bubble”, encircled in red) peaking at 0 km/s, a gas cloud moving at positive velocity, almost opposite to the first one.*

Conclusions

In order to investigate the mutual interplay between AGN and SF activity within galaxies, their relative role in outflow or inflow phenomena, that can be related to either negative feedback towards SF or AGN fuelling with enhanced SF, we have analysed the ALMA archival data in band 6 and band 9 for the nearby Seyfert galaxy NGC 5135. Continuum and line maps have been obtained, showing a complex gas distribution and kinematic. We have then modelled our data with a code fitting the line data cubes of rotating galaxies with a 3D tilted-ring model (*^{3D}BAROLO*, Di Teodoro and Fraternali [2015]), in order to obtain a clearer picture of the phenomena occurring in the inner regions of our target.

Several possible explanations for the complex geometry and gas dynamics in this galaxy have been discussed, with the main result being the discovery of radial motions overlaid to the galaxy disk rotation, with clear evidence of them consisting of gas inflow towards the nucleus occurring through inner spiral arms and a bar.

Several regions of enhanced SF due to shocks, outflows or “super-bubbles” have been identified, clear signs of a turbulent activity near the galaxy centre and the AGN.

The main results of this work can be here summarised as follows:

- the ALMA band 6 and band 9 continuum and CO line data analysed show a complex morphology and gas kinematic in the inner regions of the nearby Seyfert galaxy NGC 5135;
- at the locus of the central AGN (previously observed with VLT-SINFONI and in X-ray) we detect unresolved flux at a galaxy scale of <59 pc in the band 6 continuum, while we do not detect anything in CO, in agreement with the AGN being heavily obscured (as from X-ray; Levenson et al. [2004]). The unresolved flux could contain a possible contribution from circum-nuclear SF: only higher resolution data will allow us to derive the AGN contribution only;
- the flux measured at ~ 0.5 and 1.2 mm in the central region, considered an upper limit to the AGN dusty torus emission due to the possible SF contamination, largely exceed the SED decomposition expectations for torus only (by about two orders of magnitude; see Figure 5.7). If the flux is dominated by the AGN (with negligible contribution from circum-nuclear SF), this result will imply a significantly higher contribution from cold dust heated by the AGN than predicted by torus models;

5.3 Physical interpretations

- the inner regions of the galaxy observed with ALMA show a barred spiral-like structure with two arms and a bar, connecting the central AGN with two enhanced SF regions at the edges of the bar itself;
- the analysis of the CO(2-1) transition moments (e.g., gas distribution, velocity field and velocity dispersion profiles) reveals a very complex structure and gas kinematic, globally explainable in terms of a rotating disk plus radial motions, but with several regions falling out of any model predictions;
- the regions not explainable by the kinematic model, identify potential gas outflows/inflows from/towards the AGN, associated to shock fronts and expanding “super-bubbles”.

Perspective for future works:

Given its complex structure and the multiple components shown by the ALMA observations of the innermost regions of NGC 5135, this galaxy constitutes a crucial benchmark for understanding the feeding and the feedback mechanisms associated to SMBHs.

Although extremely interesting and complex, the picture of the inner regions of NGC 5135 emerging from the current ALMA data is still incomplete: the dusty torus is unresolved in continuum and undetected in CO, and the CO velocity maps raise the issue of what generates the two (opposite) high velocity dispersion components at the nuclear bar edge and the possible “super-bubble”. This is a totally new result, needing further investigation.

1. To resolve the cold dust (at $<10\text{--}20$ pc, possibly at clump level) of the toroidal distribution surrounding and fuelling the AGN at the centre of the nearby Seyfert NGC 5135, measuring its Rayleigh-Jeans tail and testing the current models, could be obtained only with higher resolution observations (e.g., $\lesssim 0.03''\text{--}0.05''$ in continuum – $\sim 5\text{--}7\times$ better than current), both in continuum and line, allowing us to spatially resolve the torus and to trace its molecular structure with high density tracers.
2. Such high-resolution would also allow us to study in detail the complex kinematic of the high velocity dispersion region, in order to spatially resolve the zone with opposite velocities, investigating the nature of the material flowing in or out the nuclear region, and the possible presence of the “super-bubble”.
3. The detection of other CO molecular transitions would allow us to analyse in detail the physical properties of the different structures identified in this work, such as the mass flow rate and the energy associated with the gas inflow and outflow, investigating the role of these regions and of the related processes in the feedback, in enhancing the SF, and in feeding the BH (e.g., the rate of gas flow towards the AGN).

**The complex morphology and kinematics in the inner regions of
NGC 5135: *Are we witnessing the AGN influence?***

4. The work performed in this Thesis is a pilot study on a single object, to provide the guidelines for a future study to be applied to larger samples of local galaxies. This kind of investigation could help to highlight the mechanisms that guide the interconnection between SF and AGN-related phenomena exploring small scales around the local AGN and deriving average properties for the whole population. The sample selected by [Gruppioni et al. \[2016\]](#), can represent the most suitable AGN sample to start a statistical study with a large number of local galaxies.
5. ALMA data for a large sample of AGN could allow us to constrain the Rayleigh-Jeans tail of the dusty torus emission. This would provide the needed data to test the current AGN torus models.

Appendix A

Script for calibration: ALMA band 9

This part contains the integral calibration scrip, used for manual calibration of band 9 data.

The purpose of this appendix is to allow the reader to replicate the calibration of the data or apply personal changes.

A summary of the purposes of each code steps is provided at the beginning, as well as the observational intent of each source.

The step numbers and the our comments on the code are bolded in the text.

Finally, we highlighted with different colors, the various components of the code:

- **Blue:** the originally commented parts of the code in the QA2 script.
- **Pink:** task keyword values.
- **Green:** helpful comments to clarify the choice of some of the settings applied to the code. These include the personal choices on which basis, we have decided “to build” the calibration procedure to give the reader a quick explanation of our reasons.

ALMA Data Reduction Script for calibration

Calibration

```
thesteps = []
step_title = {0: 'Import of the ASDM',
              1: 'Fix of SYSCAL table times',
              2: 'listobs',
              3: 'A priori flagging',
              4: 'Generation and time averaging of the WVR cal table',
              5: 'Generation of the Tsys cal table',
              6: 'Generation of the antenna position cal table',
              7: 'Application of the WVR, Tsys and antpos cal tables',
              8: 'Split out science SPWs and time average',
              9: 'Listobs, clear pointing table, and save original flags',
              10: 'Initial flagging',
              11: 'Putting a model for the flux calibrator(s)',
              12: 'Save flags before bandpass cal',
              13: 'Bandpass calibration',
              14: 'Save flags before gain cal',
              15: 'Gain calibration',
              16: 'Save flags before applycal',
              17: 'Application of the bandpass and gain cal tables',
              18: 'Split out corrected column',
              19: 'Save flags after applycal'}
```

```
if 'applyonly' not in globals(): applyonly = False
```

```
try:
```

```
    print 'List of steps to be executed ...', mysteps
```

```
    thesteps = mysteps
```

```
except:
```

```
    print 'global variable mysteps not set.'
```

```
if (thesteps==[]):
```

```
    thesteps = range(0,len(step_title))
```

```
    print 'Executing all steps: ', thesteps
```

```
# The Python variable 'mysteps' will control which steps
```

```
# are executed when you start the script using
```

```
#   execfile('scriptForCalibration.py')
```

```
# e.g. setting
```

```
#   mysteps = [2,3,4]# before starting the script will make the script execute
```

```
# only steps 2, 3, and 4
```

```
# Setting mysteps = [] will make it execute all steps.
```

```
import re
```

```
import os
```

```
if applyonly != True: es = aU.stuffForScienceDataReduction()
```

```
##### This is a check that warns the operator if he is using the wrong CASA  
version or not
```

```
if re.search('^4.3.1', casadef.casa_version) == None:
```

```
    sys.exit('ERROR: PLEASE USE THE SAME VERSION OF CASA THAT YOU USED FOR  
GENERATING THE SCRIPT: 4.3.1')
```

```
##### INDICE #####
```

```
# CALIBRATE_AMPLI: J1337-129
```

```
# CALIBRATE_ATMOSPHERE: J1246-2547,J1256-0547,J1337-129,NGC5135
```

```
# CALIBRATE_BANDPASS: J1256-0547
```

```
# CALIBRATE_FLUX: J1337-129
```

```
# CALIBRATE_FOCUS:
```

```
# CALIBRATE_PHASE: J1316-3338
```

```

# CALIBRATE_POINTING: J1256-0547,J1316-3338
# OBSERVE_TARGET: NGC5135
# Using reference antenna = DV16

##### FINE INDICE #####

#####

# Import of the ASDM
mystep = 0
if(mystep in thesteps):
    casalog.post('Step '+str(mystep)+' '+step_title[mystep], 'INFO')
    print 'Step ', mystep, step_title[mystep]

    if os.path.exists('uid__A002_Xa216e2_Xcb0.ms') == False:
        importasdm('uid__A002_Xa216e2_Xcb0', asis='Antenna Station Receiver Source
CalAtmosphere CalWVR CorrelatorMode SBSummary', bdf flags=True, lazy=False)
        if applyonly != True: es.fixForCSV2555('uid__A002_Xa216e2_Xcb0.ms')
            #####

            #####
            # Fix of SYSCAL table times
mystep = 1
if(mystep in thesteps):
    casalog.post('Step '+str(mystep)+' '+step_title[mystep], 'INFO')
    print 'Step ', mystep, step_title[mystep]

    from recipes.almahelpers import fixsyscaltimes
    fixsyscaltimes(vis = 'uid__A002_Xa216e2_Xcb0.ms')

print "# A priori calibration"
#####

#####

# listobs
mystep = 2
if(mystep in thesteps):
    casalog.post('Step '+str(mystep)+' '+step_title[mystep], 'INFO')
    print 'Step ', mystep, step_title[mystep]

    os.system('rm -rf uid__A002_Xa216e2_Xcb0.ms.listobs')
    listobs(vis = 'uid__A002_Xa216e2_Xcb0.ms',
            listfile = 'uid__A002_Xa216e2_Xcb0.ms.listobs')
        #####

        #####
# A priori flagging
mystep = 3
if(mystep in thesteps):
    casalog.post('Step '+str(mystep)+' '+step_title[mystep], 'INFO')
    print 'Step ', mystep, step_title[mystep]

    flagdata(vis = 'uid__A002_Xa216e2_Xcb0.ms',
            mode = 'manual',
            spw = '1~24',
            autocorr = T,
            flagbackup = F)

    flagdata(vis = 'uid__A002_Xa216e2_Xcb0.ms',
            mode = 'manual',
            intent = '*POINTING*,*SIDEBAND_RATIO*,*ATMOSPHERE*',
            flagbackup = F)

    flagcmd(vis = 'uid__A002_Xa216e2_Xcb0.ms',
            inpmode = 'table',

```

```

    useapplied = True,
    action = 'plot',
    plotfile = 'uid___A002_Xa216e2_Xcb0.ms.flagcmd.png')

flagcmd(vis = 'uid___A002_Xa216e2_Xcb0.ms',
        inpmode = 'table',
        useapplied = True,
        action = 'apply')
#####

#####
# Generation and time averaging of the WVR cal table
mystep = 4
if(mystep in thesteps):
    casalog.post('Step '+str(mystep)+' '+step_title[mystep],'INFO')
    print 'Step ', mystep, step_title[mystep]

    os.system('rm -rf uid___A002_Xa216e2_Xcb0.ms.wvr')

    os.system('rm -rf uid___A002_Xa216e2_Xcb0.ms.wvrgcal')

    mylogfile = casalog.logfile()
    casalog.setlogfile('uid___A002_Xa216e2_Xcb0.ms.wvrgcal')

    wvrgcal(vis = 'uid___A002_Xa216e2_Xcb0.ms',
            caltable = 'uid___A002_Xa216e2_Xcb0.ms.wvr',
            spw = [17, 19, 21, 23],
            smooth = '2.016s',
            toffset = 0,
            tie = ['NGC5135,J1316-3338'],
            statsource = 'NGC5135')

    casalog.setlogfile(mylogfile)

    if applyonly != True:
    aU.plotWVRSolutions(caltable='uid___A002_Xa216e2_Xcb0.ms.wvr', spw='17',
    antenna='DV16',
        yrange=[-199,199],subplot=22, interactive=False,

figfile='uid___A002_Xa216e2_Xcb0.ms.wvr.plots/uid___A002_Xa216e2_Xcb0.ms.wvr')
#####

##### 'aU' stay for 'analysis utils' that are a small set of
Python tasks that provide a number of analysis and plotting utilities. The
utilities were developed for ALMA data reduction and are, in many cases, also
useful for EVLA data reduction.

#Note: If you see wraps in these plots, try changing yrange or unwrap=True
#Note: If all plots look strange, it may be a bad WVR on the refant.
#Note: To check, you can set antenna='' to show all baselines.

#####

# Generation of the Tsys cal table
mystep = 5
if(mystep in thesteps):
    casalog.post('Step '+str(mystep)+' '+step_title[mystep],'INFO')
    print 'Step ', mystep, step_title[mystep]

    os.system('rm -rf uid___A002_Xa216e2_Xcb0.ms.tsys')
    gencal(vis = 'uid___A002_Xa216e2_Xcb0.ms',
            caltable = 'uid___A002_Xa216e2_Xcb0.ms.tsys',
            caltype = 'tsys')

```

```

# Flagging edge channels

flagdata(vis = 'uid__A002_Xa216e2_Xcb0.ms.tsys',
mode = 'manual',
spw = '9:0~3;124~127,11:0~3;124~127,13:0~3;124~127,15:0~3;124~127',

#####here we are applying the flagging solutions to all spw

flagbackup = F)

if applyonly != True:
aU.plotbandpass(caltable='uid__A002_Xa216e2_Xcb0.ms.tsys', overlay='time',
xaxis='freq', yaxis='amp', subplot=22, buildpdf=False, interactive=False,
showatm=True,pwv='auto',chanrange='92.1875%',showfdm=True,
showBasebandNumber=True,
field='',
figfile='uid__A002_Xa216e2_Xcb0.ms.tsys.plots.overlayTime/uid__A002_Xa216e2_Xc
b0.ms.tsys')

if applyonly != True: es.checkCalTable('uid__A002_Xa216e2_Xcb0.ms.tsys',
msName='uid__A002_Xa216e2_Xcb0.ms', interactive=False)

#####

#####

# Generation of the antenna position cal table
mystep = 6
if(mystep in thesteps):
casalog.post('Step '+str(mystep)+' '+step_title[mystep],'INFO')
print 'Step ', mystep, step_title[mystep]

# Position for antenna DV12 is derived from baseline run made on 2015-06-01
09:18:48.
# Position for antenna DV18 is derived from baseline run made on 2015-06-01
09:18:48.
# Position for antenna DA64 is derived from baseline run made on 2015-06-01
09:18:48.
# Position for antenna DA49 is derived from baseline run made on 2015-06-01
09:18:48.
# Position for antenna DA62 is derived from baseline run made on 2015-06-01
09:18:48.
# Position for antenna DA61 is derived from baseline run made on 2015-06-01
09:18:48.
# Position for antenna DA60 is derived from baseline run made on 2015-06-01
09:18:48.
# Position for antenna DA45 is derived from baseline run made on 2015-06-01
09:18:48.
# Position for antenna DA44 is derived from baseline run made on 2015-06-01
09:18:48.
# Position for antenna DA47 is derived from baseline run made on 2015-06-01
09:18:48.
# Position for antenna DA46 is derived from baseline run made on 2015-06-01
09:18:48.
# Position for antenna DV15 is derived from baseline run made on 2015-06-01
09:18:48.
# Position for antenna DV14 is derived from baseline run made on 2015-06-01
09:18:48.
# Position for antenna DA43 is derived from baseline run made on 2015-06-01
09:18:48.
# Position for antenna DA42 is derived from baseline run made on 2015-06-01
09:18:48.
# Position for antenna DV23 is derived from baseline run made on 2015-06-01
09:18:48.

```



```

3.77528755057e-05,-0.000615584619017,-0.000226943378885,-4.14010567059e-05,-
0.000807458390078,-0.000326327903798,-2.18590721488e-05,-0.000689335167408,-
0.000251939054579,-0.000142673961818,-0.000911373645067,-0.000316276680678,-
6.0046557337e-05,-0.000716050155461,-0.000280926469713,-5.02578914165e-05,-
0.000705934129655,-0.000263813883066,-9.42028127611e-05,-0.000754212960601,-
0.000273138284683,-7.29830935597e-05,-0.000702889636159,-
0.000300982501358,2.8611626476e-05,-0.000542476773262,-0.000145872589201,-
0.000128336716443,-0.000892668962479,-0.000389360357076,-5.93103468418e-05,-
0.000742536969483,-0.000326462090015,-8.13896767795e-05,-0.000733030028641,-
0.000283647794276,-7.16696010634e-05,-0.000757206039978,-0.000288819115198,-
9.7189269853e-05,-0.000745017882945,-0.000325555832259,3.09403985739e-05,-
0.000587584450841,-7.96979293227e-05,-3.46824526787e-05,-0.000767325051129,-
0.000299644190818,-4.34912256178e-05,-0.000733670577825,-
0.000199449232959,4.71491366625e-05,-0.000481501221657,-0.000101380050182,-
6.39259815216e-06,-0.000707647763193,-0.000189945101738,2.79720545731e-05,-
0.00058340398718,-0.000143441109538,-7.6665702119e-05,-0.000726510927654,-
0.000270601629924,-4.65533297828e-05,-0.000723551013933,-0.000244940232958,-
5.16031868756e-05,-0.000685534439981,-0.000247301068157,-7.58674069447e-05,-
0.000770748992164,-0.000298871423258,4.73414547741e-05,-0.000494519248605,-
0.0001086643897,-1.34948639985e-05,-0.000556032749918,-
0.000181481320427,1.93920625165e-05,0.000264281516129,0.000219588770532,-
2.88505107164e-05,-0.000680461525917,-0.000212917104363,0.000368155262041,-
0.000762791454375,-0.000470939380561])

```

If the positions of the antennas have a big error, you must enter the correction above each antenna in the calibration script by replacing all the 0.

```
#####
```

```
#####
```

```
# Application of the WVR, Tsys and antpos cal tables
```

```
mystep = 7
```

```
if(mystep in thesteps):
```

```
    casalog.post('Step '+str(mystep)+' '+step_title[mystep],'INFO')
```

```
    print 'Step ', mystep, step_title[mystep]
```

```
    from recipes.almahelpers import tsysspwap
```

```
    tsysmap = tsysspwap(vis = 'uid__A002_Xa216e2_Xcb0.ms', tsystable =
```

```
'uid__A002_Xa216e2_Xcb0.ms.tsys', tsysChanTol = 1)
```

```
    applycal(vis = 'uid__A002_Xa216e2_Xcb0.ms',
```

```
        field = '0',
```

```
        spw = '17,19,21,23',
```

```
        gaintable = ['uid__A002_Xa216e2_Xcb0.ms.tsys',
```

```
'uid__A002_Xa216e2_Xcb0.ms.wvr', 'uid__A002_Xa216e2_Xcb0.ms.antpos'],
```

```
        gainfield = ['0', '', ''], #####field used in order to evaluate the gain
```

```
        interp = 'linear,linear',
```

```
        spwmap = [tsysmap, [], []],
```

```
        calwt = T,
```

```
        flagbackup = F)
```

```
    applycal(vis = 'uid__A002_Xa216e2_Xcb0.ms',
```

```
        field = '1',
```

```
        spw = '17,19,21,23',
```

```
        gaintable = ['uid__A002_Xa216e2_Xcb0.ms.tsys',
```

```
'uid__A002_Xa216e2_Xcb0.ms.wvr', 'uid__A002_Xa216e2_Xcb0.ms.antpos'],
```

```
        gainfield = ['1', '', ''],
```

```
        interp = 'linear,linear',
```

```
        spwmap = [tsysmap, [], []],
```

```
        calwt = T,
```

```
        flagbackup = F)
```

```
# Note: J1316-3338 didn't have any Tsys measurement, so I used the one made on
```

NGC5135. This is probably Ok.

```
applycal(vis = 'uid__A002_Xa216e2_Xcb0.ms',
         field = '2',
         spw = '17,19,21,23',
         gaintable = ['uid__A002_Xa216e2_Xcb0.ms.tsys',
'uid__A002_Xa216e2_Xcb0.ms.wvr', 'uid__A002_Xa216e2_Xcb0.ms.antpos'],
         gainfield = ['4', '', ''],
         interp = 'linear,linear',
         spwmap = [tsysmap, [], []],
         calwt = T,
         flagbackup = F)

applycal(vis = 'uid__A002_Xa216e2_Xcb0.ms',
         field = '3',
         spw = '17,19,21,23',
         gaintable = ['uid__A002_Xa216e2_Xcb0.ms.tsys',
'uid__A002_Xa216e2_Xcb0.ms.wvr', 'uid__A002_Xa216e2_Xcb0.ms.antpos'],
         gainfield = ['3', '', ''],
         interp = 'linear,linear',
         spwmap = [tsysmap, [], []],
         calwt = T,
         flagbackup = F)

applycal(vis = 'uid__A002_Xa216e2_Xcb0.ms',
         field = '4',
         spw = '17,19,21,23',
         gaintable = ['uid__A002_Xa216e2_Xcb0.ms.tsys',
'uid__A002_Xa216e2_Xcb0.ms.wvr', 'uid__A002_Xa216e2_Xcb0.ms.antpos'],
         gainfield = ['4', '', ''],
         interp = 'linear,linear',
         spwmap = [tsysmap, [], []],
         calwt = T,
         flagbackup = F)

if applyonly != True: es.getCalWeightStats('uid__A002_Xa216e2_Xcb0.ms')
#####

#####
# Split out science SPWs and time average
mystep = 8
if(mystep in thesteps):
    casalog.post('Step '+str(mystep)+' '+step_title[mystep],'INFO')
    print 'Step ', mystep, step_title[mystep]

    os.system('rm -rf uid__A002_Xa216e2_Xcb0.ms.split')
    os.system('rm -rf uid__A002_Xa216e2_Xcb0.ms.split.flagversions')
    split(vis = 'uid__A002_Xa216e2_Xcb0.ms',
          outputvis = 'uid__A002_Xa216e2_Xcb0.ms.split',
          datacolumn = 'corrected',
          spw = '17,19,21,23',
          keepflags = T)
    #####

print "# Calibration"

#####
# Listobs, clear pointing table, and save original flags
mystep = 9
if(mystep in thesteps):
    casalog.post('Step '+str(mystep)+' '+step_title[mystep],'INFO')
    print 'Step ', mystep, step_title[mystep]

    os.system('rm -rf uid__A002_Xa216e2_Xcb0.ms.split.listobs')
```

```

listobs(vis = 'uid__A002_Xa216e2_Xcb0.ms.split',
        listfile = 'uid__A002_Xa216e2_Xcb0.ms.split.listobs')

tb.open('uid__A002_Xa216e2_Xcb0.ms.split/POINTING', nomodify = False)
a = tb.rownumbers()
tb.removerows(a)
tb.close()

if not
os.path.exists('uid__A002_Xa216e2_Xcb0.ms.split.flagversions/Original.flags'):
    flagmanager(vis = 'uid__A002_Xa216e2_Xcb0.ms.split',
                mode = 'save',
                versionname = 'Original')
                #####

                #####
# Initial flagging:
mystep = 10
if(mystep in thesteps):
    casalog.post('Step '+str(mystep)+' '+step_title[mystep],'INFO')
    print 'Step ', mystep, step_title[mystep]

# Flagging shadowed data

flagdata(vis = 'uid__A002_Xa216e2_Xcb0.ms.split',
        mode = 'shadow',
        flagbackup = F)

# Flagging edge channels

flagdata(vis = 'uid__A002_Xa216e2_Xcb0.ms.split',
        mode = 'manual',
        spw = '0:0~7;120~127,1:0~7;120~127,2:0~7;120~127,3:0~7;120~127',
        flagbackup = F)

# flagging DV03 for erratic amplitudes and phases in certain bandpass
calibrator spws

flagdata(vis = 'uid__A002_Xa216e2_Xcb0.ms.split',
        mode = 'manual',
        spw = '0,2,3',
        antenna='DV03',
        field='J1256-0547',
        flagbackup = F)

# flagging DA54 for erratic phases in bandpass calibrator spw 1

flagdata(vis = 'uid__A002_Xa216e2_Xcb0.ms.split',
        mode = 'manual',
        spw = '1',
        antenna='DA54',
        field='J1256-0547',
        flagbackup = F)

# flag DV18 for erratic phases in bandpass calibrator
flagdata(vis = 'uid__A002_Xa216e2_Xcb0.ms.split',
        mode = 'manual',
        spw = '',
        antenna='DV18',
        field='J1256-0547',
        flagbackup = F)

# flag DV04 for erratic Tsys in scan9 (all spw)
flagdata(vis = 'uid__A002_Xa216e2_Xcb0.ms.split',

```

```

mode = 'manual',
spw = '',
scan = '9',
antenna='DV04',
field='J1256-0547',
flagbackup = F)
#####

#####

# Putting a model for the flux calibrator(s)
mystep = 11
if(mystep in thesteps):
    casalog.post('Step '+str(mystep)+' '+step_title[mystep],'INFO')
    print 'Step ', mystep, step_title[mystep]

    setjy(vis = 'uid__A002_Xa216e2_Xcb0.ms.split',
        standard = 'manual',
        field = 'J1337-129',
        fluxdensity = [1.39, 0, 0, 0], ####changed by cheking in the ALMA Calibrator
Source Catalogue
        spix = -0.568811142414,
        reffreq = '681.034799115GHz')
        #####

        #####

# Save flags before bandpass cal
mystep = 12
if(mystep in thesteps):
    casalog.post('Step '+str(mystep)+' '+step_title[mystep],'INFO')
    print 'Step ', mystep, step_title[mystep]

    flagmanager(vis = 'uid__A002_Xa216e2_Xcb0.ms.split',
        mode = 'save',
        versionname = 'BeforeBandpassCalibration')
        #####

        #####

# Bandpass calibration:
mystep = 13
if(mystep in thesteps):
    casalog.post('Step '+str(mystep)+' '+step_title[mystep],'INFO')
    print 'Step ', mystep, step_title[mystep]

    os.system('rm -rf uid__A002_Xa216e2_Xcb0.ms.split.ap_pre_bandpass')

    gaincal(vis = 'uid__A002_Xa216e2_Xcb0.ms.split',
        caltable = 'uid__A002_Xa216e2_Xcb0.ms.split.ap_pre_bandpass',
        field = '0', # J1256-0547
        spw = '0:2~126,1:2~126,2:2~126,3:2~126', #increased spw selection
        scan = '1,2,4',
        solint = '30s',#longer time to hopefully deal with cal source weakness,
usally ~6s
        refant = 'DV16',
        calmode = 'p')

    if applyonly != True:
    es.checkCalTable('uid__A002_Xa216e2_Xcb0.ms.split.ap_pre_bandpass',
    msName='uid__A002_Xa216e2_Xcb0.ms.split', interactive=False)

    os.system('rm -rf uid__A002_Xa216e2_Xcb0.ms.split.bandpass')
    bandpass(vis = 'uid__A002_Xa216e2_Xcb0.ms.split',
        caltable = 'uid__A002_Xa216e2_Xcb0.ms.split.bandpass',
        field = '0', # J1256-0547

```

```

scan = '1,2,4',
solint = 'inf',
combine = 'scan',
refant = 'DV16',
solnorm = True,
bandtype = 'B',
gaintable = 'uid__A002_Xa216e2_Xcb0.ms.split.ap_pre_bandpass')

if applyonly != True:
es.checkCalTable('uid__A002_Xa216e2_Xcb0.ms.split.bandpass',
msName='uid__A002_Xa216e2_Xcb0.ms.split', interactive=False)

# solve for the phase_offsets of all spws (calmode='p', gaintype='G') as in CAS-
7400
gaincal(vis = 'uid__A002_Xa216e2_Xcb0.ms.split',
caltable = 'uid__A002_Xa216e2_Xcb0.ms.split.phase_offsets',
field = '0', # J1256-0547
solint = 'inf',
refant = 'DV16',
gaintype = 'G',
calmode = 'p',
gaintable = 'uid__A002_Xa216e2_Xcb0.ms.split.bandpass')
#####

#####

# Save flags before gain cal
mystep = 14
if(mystep in thesteps):
casalog.post('Step '+str(mystep)+' '+step_title[mystep],'INFO')
print 'Step ', mystep, step_title[mystep]

flagmanager(vis = 'uid__A002_Xa216e2_Xcb0.ms.split',
mode = 'save',
versionname = 'BeforeGainCalibration')
#####

#####

# Gain calibration
mystep = 15
if(mystep in thesteps):
casalog.post('Step '+str(mystep)+' '+step_title[mystep],'INFO')
print 'Step ', mystep, step_title[mystep]

# if re-doing any steps with the tables, run this command first:
# flagmanager(vis = 'uid__A002_Xa216e2_Xcb0.ms.split',
# mode = 'restore',
# versionname = 'BeforeGainCalibration')

# from CAS-7400:

# 3) Everywhere the bandpass table is applied (or preapplied) subsequently,
apply this phase_offsets table right after it.
# 4) For all subsequent 'p' solutions, change to gaintype 'T', and set
combine='spw'.
# 5) For the phase_int solution, change from solint = 'int' to
solint=max([integrationTime, scanTime/4.0]).
# 6) When these spw-combined 'p' solutions are subsequently applied (or
preapplied), you will need to set spwmap for that solution to all zeros (e.g.
[0,0,0,0] for 4 spws).
# 7) The 'a' solves and applies should remain unchanged. Once valid 'p'
solutions are found, the subsequent 'a' solve generally proceeds more
successfully, even on a per-spw basis.

```

```

os.system('rm -rf uid__A002_Xa216e2_Xcb0.ms.split.phase_int')
gaincal(vis = 'uid__A002_Xa216e2_Xcb0.ms.split',
        caltable = 'uid__A002_Xa216e2_Xcb0.ms.split.phase_int',
        field = '0~3', # J1256-0547,J1337-129,J1316-3338,J1246-2547
        solint = '15.5s', #phase calibrator scan time ~ 62s => 15.5s > integration
time (~6s)
        refant = 'DV16',
        gaintype = 'T',
        calmode = 'p',
        combine = 'spw', # combine for better solution #####
        gaintable = ['uid__A002_Xa216e2_Xcb0.ms.split.bandpass',
'uid__A002_Xa216e2_Xcb0.ms.split.phase_offsets'])

if applyonly != True:
es.checkCalTable('uid__A002_Xa216e2_Xcb0.ms.split.phase_int',
msName='uid__A002_Xa216e2_Xcb0.ms.split', interactive=False)

minsnr = 3.0

os.system('rm -rf uid__A002_Xa216e2_Xcb0.ms.split.phase_inf')
gaincal(vis = 'uid__A002_Xa216e2_Xcb0.ms.split',
        caltable = 'uid__A002_Xa216e2_Xcb0.ms.split.phase_inf',
        field = '0~3', # J1256-0547,J1337-129,J1316-3338,J1246-2547
        solint = 'inf',
        refant = 'DV16',
        minsnr = minsnr,
        gaintype = 'T',
        calmode = 'p',
        spwmap = [[],[ ]],
        combine = 'spw', #combine for better solutions
        gaintable = ['uid__A002_Xa216e2_Xcb0.ms.split.bandpass',
'uid__A002_Xa216e2_Xcb0.ms.split.phase_offsets'])

os.system('rm -rf uid__A002_Xa216e2_Xcb0.ms.split.ampli_inf')
gaincal(vis = 'uid__A002_Xa216e2_Xcb0.ms.split',
        caltable = 'uid__A002_Xa216e2_Xcb0.ms.split.ampli_inf',
        field = '0~3', # J1256-0547,J1337-129,J1316-3338,J1246-2547
        solint = 'inf',
        refant = 'DV16',
        gaintype = 'T',
        minsnr = minsnr,
        calmode = 'a',
        spwmap = [[],[ ],[0,0,0,0]],
#because phase_inf only defined for one equivalent solution
        gaintable = ['uid__A002_Xa216e2_Xcb0.ms.split.bandpass',
'uid__A002_Xa216e2_Xcb0.ms.split.phase_offsets',
'uid__A002_Xa216e2_Xcb0.ms.split.phase_inf'])
#apply phase_inf because no phase_int

if applyonly != True:
es.checkCalTable('uid__A002_Xa216e2_Xcb0.ms.split.ampli_inf',
msName='uid__A002_Xa216e2_Xcb0.ms.split', interactive=False)

os.system('rm -rf uid__A002_Xa216e2_Xcb0.ms.split.flux_inf')
os.system('rm -rf uid__A002_Xa216e2_Xcb0.ms.split.fluxscale')
mylogfile = casalog.logfile()
casalog.setlogfile('uid__A002_Xa216e2_Xcb0.ms.split.fluxscale')

fluxscaleDict = fluxscale(vis = 'uid__A002_Xa216e2_Xcb0.ms.split',
        caltable = 'uid__A002_Xa216e2_Xcb0.ms.split.ampli_inf',
        fluxtable = 'uid__A002_Xa216e2_Xcb0.ms.split.flux_inf',
        reference = '1') # J1337-129

casalog.setlogfile(mylogfile)

```

```

if applyonly != True: es.fluxscale2(caltable =
'uid__A002_Xa216e2_Xcb0.ms.split.ampli_inf', removeOutliers=True,
msName='uid__A002_Xa216e2_Xcb0.ms', writeToFile=True, preavg=10000)
#####

#####
# Save flags before applycal
mystep = 16
if(mystep in thesteps):
    casalog.post('Step '+str(mystep)+' '+step_title[mystep],'INFO')
    print 'Step ', mystep, step_title[mystep]

    flagmanager(vis = 'uid__A002_Xa216e2_Xcb0.ms.split',
        mode = 'save',
        versionname = 'BeforeApplycal')
        #####

        #####
# Application of the bandpass and gain cal tables
mystep = 17
if(mystep in thesteps):
    casalog.post('Step '+str(mystep)+' '+step_title[mystep],'INFO')
    print 'Step ', mystep, step_title[mystep]

    for i in ['0', '1', '3']: # J1256-0547,J1337-129,J1246-2547
        applycal(vis = 'uid__A002_Xa216e2_Xcb0.ms.split',
            field = str(i),
            gaintable = ['uid__A002_Xa216e2_Xcb0.ms.split.bandpass',
'uid__A002_Xa216e2_Xcb0.ms.split.phase_offsets',
'uid__A002_Xa216e2_Xcb0.ms.split.phase_int',
'uid__A002_Xa216e2_Xcb0.ms.split.flux_inf'],
            gainfield = ['', '0', i, i],
            interp = 'linear,spline',
            spwmap = [[],[],[0,0,0,0],[[]],
#because phase_int and flux_inf only defined for one equivalent solution
            calwt = T,
            flagbackup = F)

        applycal(vis = 'uid__A002_Xa216e2_Xcb0.ms.split',
            field = '2,4', # NGC5135
            gaintable = ['uid__A002_Xa216e2_Xcb0.ms.split.bandpass',
'uid__A002_Xa216e2_Xcb0.ms.split.phase_offsets',
'uid__A002_Xa216e2_Xcb0.ms.split.phase_inf',
'uid__A002_Xa216e2_Xcb0.ms.split.flux_inf'],
            gainfield = ['', '0', '2', '2'], # J1316-3338
            interp = 'linear,spline',
            spwmap = [[],[],[0,0,0,0],[[]],
# because phase_int and flux_inf only defined for one equivalent solution
            calwt = T,
            flagbackup = F)
            #####

            #####
# Split out corrected column
mystep = 18
if(mystep in thesteps):
    casalog.post('Step '+str(mystep)+' '+step_title[mystep],'INFO')
    print 'Step ', mystep, step_title[mystep]
    #os.chdir('split')
    os.system('rm -rf uid__A002_Xa216e2_Xcb0.ms.split.cal')
    os.system('rm -rf uid__A002_Xa216e2_Xcb0.ms.split.cal.flagversions')
    split(vis = 'uid__A002_Xa216e2_Xcb0.ms.split',

```

```
outputvis = 'uid__A002_Xa216e2_Xcb0.ms.split.cal',
datacolumn = 'corrected',
keepflags = T)
#####

#####
# Save flags after applycal
mystep = 19
if(mystep in thesteps):
    casalog.post('Step '+str(mystep)+' '+step_title[mystep],'INFO')
    print 'Step ', mystep, step_title[mystep]

flagmanager(vis = 'uid__A002_Xa216e2_Xcb0.ms.split.cal',
mode = 'save',
versionname = 'AfterApplycal')
#####

##### END of Script for calibration #####
```


Bibliography

- Marek A. Abramowicz and P. Chris Fragile. Foundations of black hole accretion disk theory. *Living Reviews in Relativity*, 16(1):1, Jan 2013. ISSN 1433-8351. doi: 10.12942/lrr-2013-1. URL <https://doi.org/10.12942/lrr-2013-1>.
- J. Aird, K. Nandra, E. S. Laird, A. Georgakakis, M. L. N. Ashby, P. Barmby, A. L. Coil, J.-S. Huang, A. M. Koekemoer, C. C. Steidel, and C. N. A. Willmer. The evolution of the hard X-ray luminosity function of AGN. *MNRAS*, 401:2531–2551, February 2010. doi: 10.1111/j.1365-2966.2009.15829.x.
- A. Alonso-Herrero, G. H. Rieke, M. J. Rieke, L. Colina, P. G. Pérez-González, and S. D. Ryder. Near-Infrared and Star-forming Properties of Local Luminous Infrared Galaxies. *ApJ*, 650:835–849, October 2006. doi: 10.1086/506958.
- R. Antonucci. Unified models for active galactic nuclei and quasars. *ARA&A*, 31: 473–521, 1993. doi: 10.1146/annurev.aa.31.090193.002353.
- R. Antonucci. A panchromatic review of thermal and nonthermal active galactic nuclei. *Astronomical and Astrophysical Transactions*, 27:557–602, 2012.
- S. Asayama, A. Biggs, I. de Gregorio, B. Dent, J. Di Francesco, E. Fomalont, A. Hales, J. Hibbard, G. Marconi, S. Kameno, B. Vila Vilaro, E. Villard, and F. Stoehr. ALMA Partnership - ALMA Cycle 5 Technical Handbook. *ALMA Website*, 1: 1–218, March 2017. doi: ISBN978-3-923524-66-2.
- J. A. Baldwin, M. M. Phillips, and R. Terlevich. Classification parameters for the emission-line spectra of extragalactic objects. *PASP*, 93:5–19, February 1981. doi: 10.1086/130766.
- J. K. Banfield, O. I. Wong, K. W. Willett, R. P. Norris, L. Rudnick, S. S. Shabala, B. D. Simmons, C. Snyder, A. Garon, N. Seymour, E. Middelberg, H. Anderson, C. J. Lintott, K. Jacob, A. D. Kapińska, M. Y. Mao, K. L. Masters, M. J. Jarvis, K. Schawinski, E. Paget, R. Simpson, H.-R. Klöckner, S. Bamford, T. Burchell, K. E. Chow, G. Cotter, L. Fortson, I. Heywood, T. W. Jones, S. Kaviraj, Á. R. López-Sánchez, W. P. Maksym, K. Polsterer, K. Borden, R. P. Hollow, and L. Whyte. Radio galaxy zoo: host galaxies and radio morphologies derived from visual inspection. *Monthly Notices of the Royal Astronomical Society*, 453(3):2326–2340, 2015. doi: 10.1093/mnras/stv1688. URL [+http://dx.doi.org/10.1093/mnras/stv1688](http://dx.doi.org/10.1093/mnras/stv1688).

BIBLIOGRAPHY

- A. G. Bedregal, L. Colina, A. Alonso-Herrero, and S. Arribas. Near-IR Integral Field Spectroscopy Study of the Star Formation and AGN of the LIRG NGC 5135. *ApJ*, 698:1852–1871, June 2009. doi: 10.1088/0004-637X/698/2/1852.
- A. G. Bedregal, L. Colina, R. Azzollini, S. Arribas, and A. Alonso-Herrero. The Local LIRG NGC 5135: AGN and SN Activity Traced by NIR IFU Spectroscopy. In W. Wang, J. Lu, Z. Luo, Z. Yang, H. Hua, and Z. Chen, editors, *Galaxy Evolution: Infrared to Millimeter Wavelength Perspective*, volume 446 of *Astronomical Society of the Pacific Conference Series*, page 83, October 2011.
- S. Berta, D. Lutz, P. Santini, S. Wuyts, D. Rosario, D. Brisbin, A. Cooray, A. Franceschini, C. Gruppioni, E. Hatziminaoglou, H. S. Hwang, E. Le Floc’h, B. Magnelli, R. Nordon, S. Oliver, M. J. Page, P. Popesso, L. Pozzetti, F. Pozzi, L. Riguccini, G. Rodighiero, I. Roseboom, D. Scott, M. Symeonidis, I. Valtchanov, M. Viero, and L. Wang. Panchromatic spectral energy distributions of Herschel sources. *A&A*, 551:A100, March 2013. doi: 10.1051/0004-6361/201220859.
- J. C. Bischko, D. Steinhauser, and S. Schindler. The collaborative effect of ram pressure and merging on star formation and stripping fraction. *A&A*, 576:A76, April 2015. doi: 10.1051/0004-6361/201322741.
- A. Bosma. 21-cm line studies of spiral galaxies. II. The distribution and kinematics of neutral hydrogen in spiral galaxies of various morphological types. *AJ*, 86:1825–1846, December 1981a. doi: 10.1086/113063.
- A. Bosma. 21-cm line studies of spiral galaxies. I - Observations of the galaxies NGC 5033, 3198, 5055, 2841, and 7331. *AJ*, 86:1791–1824, December 1981b. doi: 10.1086/113062.
- R. J. Bouwens, G. D. Illingworth, P. A. Oesch, M. Franx, I. Labbé, M. Trenti, P. van Dokkum, C. M. Carollo, V. González, R. Smit, and D. Magee. UV-continuum Slopes at $z \sim 4-7$ from the HUDF09+ERS+CANDELS Observations: Discovery of a Well-defined UV Color-Magnitude Relationship for $z \geq 4$ Star-forming Galaxies. *ApJ*, 754:83, August 2012a. doi: 10.1088/0004-637X/754/2/83.
- R. J. Bouwens, G. D. Illingworth, P. A. Oesch, M. Trenti, I. Labbé, M. Franx, M. Stiavelli, C. M. Carollo, P. van Dokkum, and D. Magee. Lower-luminosity Galaxies Could Reionize the Universe: Very Steep Faint-end Slopes to the UV Luminosity Functions at $z \geq 5-8$ from the HUDF09 WFC3/IR Observations. *ApJ*, 752:L5, June 2012b. doi: 10.1088/2041-8205/752/1/L5.
- A. H. Bridle, E. B. Fomalont, G. G. Byrd, and M. J. Valtonen. The unusual radio galaxy 3C 288. *AJ*, 97:674–685, March 1989. doi: 10.1086/115013.
- D. S. Briggs. High Fidelity Interferometric Imaging: Robust Weighting Deconvolution. In *American Astronomical Society Meeting Abstracts*, volume 27 of *Bulletin of the American Astronomical Society*, page 1444, December 1995.

- P. M. Bryant and N. Z. Scoville. High-Resolution CO Observations of Luminous Infrared Galaxies. *AJ*, 117:2632–2655, June 1999. doi: 10.1086/300879.
- J. Castor, R. McCray, and R. Weaver. Interstellar bubbles. *ApJ*, 200:L107–L110, September 1975. doi: 10.1086/181908.
- C.-T. J. Chen, R. C. Hickox, S. Alberts, M. Brodwin, C. Jones, S. S. Murray, D. M. Alexander, R. J. Assef, M. J. I. Brown, A. Dey, W. R. Forman, V. Gorjian, A. D. Goulding, E. Le Floch, B. T. Jannuzi, J. R. Mullaney, and A. Pope. A Correlation between Star Formation Rate and Average Black Hole Accretion in Star-forming Galaxies. *ApJ*, 773:3, August 2013. doi: 10.1088/0004-637X/773/1/3.
- C. Cicone, R. Maiolino, E. Sturm, J. Graciá-Carpio, C. Feruglio, R. Neri, S. Aalto, R. Davies, F. Fiore, J. Fischer, S. García-Burillo, E. González-Alfonso, S. Hailey-Dunsheath, E. Piconcelli, and S. Veilleux. Massive molecular outflows and evidence for AGN feedback from CO observations. *A&A*, 562:A21, February 2014. doi: 10.1051/0004-6361/201322464.
- D. L. Clements, W. J. Sutherland, R. G. McMahon, and W. Saunders. Optical imaging of ultraluminous IRAS galaxies: how many are mergers? *MNRAS*, 279:477–497, March 1996. doi: 10.1093/mnras/279.2.477.
- L. Colina, M. Pereira-Santaella, A. Alonso-Herrero, A. G. Bedregal, and S. Arribas. Spatially Resolved [Fe II] 1.64 μm Emission in NGC 5135: Clues for Understanding the Origin of the Hard X-Rays in Luminous Infrared Galaxies. *ApJ*, 749:116, April 2012. doi: 10.1088/0004-637X/749/2/116.
- F. Combes, S. García-Burillo, V. Casasola, L. Hunt, M. Krips, A. J. Baker, F. Boone, A. Eckart, I. Marquez, R. Neri, E. Schinnerer, and L. J. Tacconi. ALMA observations of feeding and feedback in nearby Seyfert galaxies: an AGN-driven outflow in NGC 1433. *A&A*, 558:A124, October 2013. doi: 10.1051/0004-6361/201322288.
- James W. Cooley and John W. Tukey. An algorithm for the machine calculation of complex fourier series. *Mathematics of Computation*, 19(90):297–301, 1965. ISSN 00255718, 10886842. URL <http://www.jstor.org/stable/2003354>.
- O. Cucciati, L. Tresse, O. Ilbert, O. Le Fèvre, B. Garilli, V. Le Brun, P. Cassata, P. Franzetti, D. Maccagni, M. Scodreggio, E. Zucca, G. Zamorani, S. Bardelli, M. Bolzonella, R. M. Bielby, H. J. McCracken, A. Zanichelli, and D. Vergani. The star formation rate density and dust attenuation evolution over 12 Gyr with the VVDS surveys. *A&A*, 539:A31, March 2012. doi: 10.1051/0004-6361/201118010.
- R. M. Cutri, J. P. Huchra, F. J. Low, R. L. Brown, and P. A. Vanden Bout. IRAS F15307+3252: A hyperluminous infrared galaxy at $Z = 0.93$. *ApJ*, 424:L65–L68, April 1994. doi: 10.1086/187276.
- Bozena Czerny, Pu Du, Jian-Min Wang, and Vladimir Karas. A test of the formation mechanism of the broad line region in active galactic nuclei. *The Astrophysical*

BIBLIOGRAPHY

- Journal*, 832(1):15, 2016. URL <http://stacks.iop.org/0004-637X/832/i=1/a=15>.
- E. Daddi, F. Bournaud, F. Walter, H. Dannerbauer, C. L. Carilli, M. Dickinson, D. Elbaz, G. E. Morrison, D. Riechers, M. Onodera, F. Salmi, M. Krips, and D. Stern. Very High Gas Fractions and Extended Gas Reservoirs in $z = 1.5$ Disk Galaxies. *ApJ*, 713:686–707, April 2010. doi: 10.1088/0004-637X/713/1/686.
- T. Dahlen, B. Mobasher, M. Dickinson, H. C. Ferguson, M. Giavalisco, C. Kretchmer, and S. Ravindranath. Evolution of the Luminosity Function, Star Formation Rate, Morphology, and Size of Star-forming Galaxies Selected at Rest-Frame 1500 and 2800 Å. *ApJ*, 654:172–185, January 2007. doi: 10.1086/508854.
- W. J. G. de Blok, K. M. Keating, D. J. Pisano, F. Fraternali, F. Walter, T. Oosterloo, E. Brinks, F. Bigiel, and A. Leroy. A low H I column density filament in NGC 2403: signature of interaction or accretion. *A&A*, 569:A68, September 2014. doi: 10.1051/0004-6361/201423880.
- R. della Ceca, G. Lamorani, T. Maccacaro, A. Wolter, R. Griffiths, J. T. Stocke, and G. Setti. The properties of X-ray selected active galactic nuclei. 3: The radio-quiet versus radio-loud samples. *ApJ*, 430:533–544, August 1994. doi: 10.1086/174428.
- I. Delvecchio, C. Gruppioni, F. Pozzi, S. Berta, G. Zamorani, A. Cimatti, D. Lutz, D. Scott, C. Vignali, G. Cresci, A. Feltre, A. Cooray, M. Vaccari, J. Fritz, E. Le Floch, B. Magnelli, P. Popesso, S. Oliver, J. Bock, M. Carollo, T. Contini, O. Le Fèvre, S. Lilly, V. Mainieri, A. Renzini, and M. Scodreggio. Tracing the cosmic growth of supermassive black holes to $z \sim 3$ with Herschel. *MNRAS*, 439:2736–2754, April 2014. doi: 10.1093/mnras/stu130.
- E. M. Di Teodoro. *Kinematics of local and high- z galaxies through 3D modeling of emission-line datacubes*. PhD thesis, University of Bologna |EMAIL|enrico.diteodoro@unibo.it|EMAIL|, December 2015.
- E. M. Di Teodoro and F. Fraternali. ^{3D} BAROLO: a new 3D algorithm to derive rotation curves of galaxies. *MNRAS*, 451:3021–3033, August 2015. doi: 10.1093/mnras/stv1213.
- D. Downes and P. M. Solomon. Rotating Nuclear Rings and Extreme Starbursts in Ultraluminous Galaxies. *ApJ*, 507:615–654, November 1998. doi: 10.1086/306339.
- J. A. Eilek, J. O. Burns, C. P. O’Dea, and F. N. Owen. What bends 3C 465? *ApJ*, 278:37–50, March 1984. doi: 10.1086/161765.
- J. Einasto, E. Saar, A. Kaasik, and A. D. Chernin. Missing mass around galaxies - Morphological evidence. *Nature*, 252:111–113, November 1974. doi: 10.1038/252111a0.

- D. Elbaz, M. Dickinson, H. S. Hwang, T. Díaz-Santos, G. Magdis, B. Magnelli, D. Le Borgne, F. Galliano, M. Pannella, P. Chanial, L. Armus, V. Charmandaris, E. Daddi, H. Aussel, P. Popesso, J. Kartaltepe, B. Altieri, I. Valtchanov, D. Coia, H. Dannerbauer, K. Dasyra, R. Leiton, J. Mazzarella, D. M. Alexander, V. Buat, D. Burgarella, R.-R. Chary, R. Gilli, R. J. Ivison, S. Juneau, E. Le Floc'h, D. Lutz, G. E. Morrison, J. R. Mullaney, E. Murphy, A. Pope, D. Scott, M. Brodwin, D. Calzetti, C. Cesarsky, S. Charlot, H. Dole, P. Eisenhardt, H. C. Ferguson, N. Förster Schreiber, D. Frayer, M. Giavalisco, M. Huynh, A. M. Koekoer, C. Papovich, N. Reddy, C. Surace, H. Teplitz, M. S. Yun, and G. Wilson. GOODS-Herschel: an infrared main sequence for star-forming galaxies. *A&A*, 533:A119, September 2011. doi: 10.1051/0004-6361/201117239.
- H. I. Ewen and E. M. Purcell. Observation of a Line in the Galactic Radio Spectrum: Radiation from Galactic Hydrogen at 1,420 Mc./sec. *Nature*, 168:356, September 1951. doi: 10.1038/168356a0.
- A. C. Fabian. Observational Evidence of Active Galactic Nuclei Feedback. *ARA&A*, 50:455–489, September 2012. doi: 10.1146/annurev-astro-081811-125521.
- B. L. Fanaroff and J. M. Riley. The morphology of extragalactic radio sources of high and low luminosity. *MNRAS*, 167:31P–36P, May 1974. doi: 10.1093/mnras/167.1.31P.
- L. Ferrarese and D. Merritt. A Fundamental Relation between Supermassive Black Holes and Their Host Galaxies. *ApJ*, 539:L9–L12, August 2000. doi: 10.1086/312838.
- C. Feruglio, R. Maiolino, E. Piconcelli, N. Menci, H. Aussel, A. Lamastra, and F. Fiore. Quasar feedback revealed by giant molecular outflows. *A&A*, 518:L155, July 2010. doi: 10.1051/0004-6361/201015164.
- F. Fraternali, G. van Moorsel, R. Sancisi, and T. Oosterloo. Deep H I Survey of the Spiral Galaxy NGC 2403. *AJ*, 123:3124–3140, June 2002. doi: 10.1086/340358.
- J. Fritz, A. Franceschini, and E. Hatziminaoglou. Revisiting the infrared spectra of active galactic nuclei with a new torus emission model. *MNRAS*, 366:767–786, March 2006. doi: 10.1111/j.1365-2966.2006.09866.x.
- V. Gaibler, S. Khochfar, M. Krause, and J. Silk. Jet-induced star formation in gas-rich galaxies. *Monthly Notices of the Royal Astronomical Society*, 425(1):438–449, 2012. doi: 10.1111/j.1365-2966.2012.21479.x. URL [+http://dx.doi.org/10.1111/j.1365-2966.2012.21479.x](http://dx.doi.org/10.1111/j.1365-2966.2012.21479.x).
- Y. Gao and P. M. Solomon. The Star Formation Rate and Dense Molecular Gas in Galaxies. *ApJ*, 606:271–290, May 2004. doi: 10.1086/382999.
- S. García-Burillo, F. Combes, C. Ramos Almeida, A. Usero, M. Krips, A. Alonso-Herrero, S. Aalto, V. Casasola, L. K. Hunt, S. Martín, S. Viti, L. Colina,

BIBLIOGRAPHY

- F. Costagliola, A. Eckart, A. Fuente, C. Henkel, I. Márquez, R. Neri, E. Schinnerer, L. J. Tacconi, and P. P. van der Werf. ALMA Resolves the Torus of NGC 1068: Continuum and Molecular Line Emission. *ApJ*, 823:L12, May 2016. doi: 10.3847/2041-8205/823/1/L12.
- J. García-González, A. Alonso-Herrero, S. F. Hönic, A. Hernán-Caballero, C. Ramos Almeida, N. A. Levenson, P. F. Roche, O. González-Martín, C. Packham, and M. Kishimoto. A mid-infrared statistical investigation of clumpy torus model predictions. *Monthly Notices of the Royal Astronomical Society*, 470(3):2578–2598, 2017. doi: 10.1093/mnras/stx1361. URL [+http://dx.doi.org/10.1093/mnras/stx1361](http://dx.doi.org/10.1093/mnras/stx1361).
- R. M. González Delgado, T. Heckman, C. Leitherer, G. Meurer, J. Krolik, A. S. Wilson, A. Kinney, and A. Koratkar. Ultraviolet-Optical Observations of the Seyfert 2 Galaxies NGC 7130, NGC 5135, and IC 3639: Implications for the Starburst-Active Galactic Nucleus Connection. *ApJ*, 505:174–198, September 1998. doi: 10.1086/306154.
- R. Gooch. Karma: a Visualization Test-Bed. In G. H. Jacoby and J. Barnes, editors, *Astronomical Data Analysis Software and Systems V*, volume 101 of *Astronomical Society of the Pacific Conference Series*, page 80, 1996.
- C. Gruppioni, F. Pozzi, G. Rodighiero, I. Delvecchio, S. Berta, L. Pozzetti, G. Zamorani, P. Andreani, A. Cimatti, O. Ilbert, E. Le Floc’h, D. Lutz, B. Magnelli, L. Marchetti, P. Monaco, R. Nordon, S. Oliver, P. Popesso, L. Riguccini, I. Roseboom, D. J. Rosario, M. Sargent, M. Vaccari, B. Altieri, H. Aussel, A. Bongiovanni, J. Cepa, E. Daddi, H. Domínguez-Sánchez, D. Elbaz, N. Förster Schreiber, R. Genzel, A. Iribarrem, M. Magliocchetti, R. Maiolino, A. Poglitsch, A. Pérez García, M. Sanchez-Portal, E. Sturm, L. Tacconi, I. Valtchanov, A. Amblard, V. Arumugam, M. Bethermin, J. Bock, A. Boselli, V. Buat, D. Burgarella, N. Castro-Rodríguez, A. Cava, P. Chanial, D. L. Clements, A. Conley, A. Cooray, C. D. Dowell, E. Dwek, S. Eales, A. Franceschini, J. Glenn, M. Griffin, E. Hatziminaoglou, E. Ibar, K. Isaak, R. J. Ivison, G. Lagache, L. Levenson, N. Lu, S. Madden, B. Maffei, G. Mainetti, H. T. Nguyen, B. O’Halloran, M. J. Page, P. Panuzzo, A. Papageorgiou, C. P. Pearson, I. Pérez-Fournon, M. Pohlen, D. Rigopoulou, M. Rowan-Robinson, B. Schulz, D. Scott, N. Seymour, D. L. Shupe, A. J. Smith, J. A. Stevens, M. Symeonidis, M. Trichas, K. E. Tugwell, L. Vigroux, L. Wang, G. Wright, C. K. Xu, M. Zemcov, S. Bardelli, M. Carollo, T. Contini, O. Le Fèvre, S. Lilly, V. Mainieri, A. Renzini, M. Scodreggio, and E. Zucca. The Herschel PEP/HerMES luminosity function - I. Probing the evolution of PACS selected Galaxies to $z \sim 4$. *MNRAS*, 432:23–52, June 2013. doi: 10.1093/mnras/stt308.
- C. Gruppioni, S. Berta, L. Spinoglio, M. Pereira-Santaella, F. Pozzi, P. Andreani, M. Bonato, G. De Zotti, M. Malkan, M. Negrello, L. Vallini, and C. Vignali. Tracing black hole accretion with SED decomposition and IR lines: from local galaxies to the high- z Universe. *MNRAS*, 458:4297–4320, June 2016. doi: 10.1093/mnras/stw577.

- K. Gültekin, E. M. Cackett, J. M. Miller, T. Di Matteo, S. Markoff, and D. O. Richstone. The Fundamental Plane of Accretion onto Black Holes with Dynamical Masses. *ApJ*, 706:404–416, November 2009. doi: 10.1088/0004-637X/706/1/404.
- N. Häring and H.-W. Rix. On the Black Hole Mass-Bulge Mass Relation. *ApJ*, 604:L89–L92, April 2004. doi: 10.1086/383567.
- C. M. Harrison, D. M. Alexander, J. R. Mullaney, J. P. Stott, A. M. Swinbank, V. Arumugam, F. E. Bauer, R. G. Bower, A. J. Bunker, and R. M. Sharples. The KMOS AGN Survey at High redshift (KASHz): the prevalence and drivers of ionized outflows in the host galaxies of X-ray AGN. *MNRAS*, 456:1195–1220, February 2016. doi: 10.1093/mnras/stv2727.
- C. Hazard, M. B. Mackey, and A. J. Shimmins. Investigation of the Radio Source 3C 273 By The Method of Lunar Occultations. *Nature*, 197:1037–1039, March 1963. doi: 10.1038/1971037a0.
- T. M. Heckman and P. N. Best. The Coevolution of Galaxies and Supermassive Black Holes: Insights from Surveys of the Contemporary Universe. *ARA&A*, 52:589–660, August 2014. doi: 10.1146/annurev-astro-081913-035722.
- A. Hewitt and G. Burbidge. An optical catalog of extragalactic emission-line objects similar to quasi-stellar objects. *ApJS*, 75:297–356, February 1991. doi: 10.1086/191533.
- J. A. Högbom. Aperture Synthesis with a Non-Regular Distribution of Interferometer Baselines. *A&AS*, 15:417, June 1974.
- P. F. Hopkins, G. T. Richards, and L. Hernquist. An Observational Determination of the Bolometric Quasar Luminosity Function. *ApJ*, 654:731–753, January 2007. doi: 10.1086/509629.
- P. F. Hopkins, L. Hernquist, T. J. Cox, and D. Kereš. A Cosmological Framework for the Co-Evolution of Quasars, Supermassive Black Holes, and Elliptical Galaxies. I. Galaxy Mergers and Quasar Activity. *ApJS*, 175:356–389, April 2008. doi: 10.1086/524362.
- J. R. Houck, D. P. Schneider, G. E. Danielson, G. Neugebauer, B. T. Soifer, C. A. Beichman, and C. J. Lonsdale. Unidentified IRAS sources - Ultrahigh-luminosity galaxies. *ApJ*, 290:L5–L8, March 1985. doi: 10.1086/184431.
- F. P. Israel, M. J. F. Rosenberg, and P. van der Werf. Neutral carbon and CO in 76 (U)LIRGs and starburst galaxy centers. A method to determine molecular gas properties in luminous galaxies. *A&A*, 578:A95, June 2015. doi: 10.1051/0004-6361/201425175.
- G. Kauffmann and M. Haehnelt. A unified model for the evolution of galaxies and quasars. *MNRAS*, 311:576–588, January 2000. doi: 10.1046/j.1365-8711.2000.03077.x.

BIBLIOGRAPHY

- G. Kauffmann, T. M. Heckman, C. Tremonti, J. Brinchmann, S. Charlot, S. D. M. White, S. E. Ridgway, J. Brinkmann, M. Fukugita, P. B. Hall, Ž. Ivezić, G. T. Richards, and D. P. Schneider. The host galaxies of active galactic nuclei. *MNRAS*, 346:1055–1077, December 2003. doi: 10.1111/j.1365-2966.2003.07154.x.
- K. I. Kellermann, R. Sramek, M. Schmidt, D. B. Shaffer, and R. Green. VLA observations of objects in the Palomar Bright Quasar Survey. *AJ*, 98:1195–1207, October 1989. doi: 10.1086/115207.
- R. C. Kennicutt, Jr. The Global Schmidt Law in Star-forming Galaxies. *ApJ*, 498:541–552, May 1998a. doi: 10.1086/305588.
- R. C. Kennicutt, Jr. Star Formation in Galaxies Along the Hubble Sequence. *ARA&A*, 36:189–232, 1998b. doi: 10.1146/annurev.astro.36.1.189.
- L. J. Kewley, M. A. Dopita, R. S. Sutherland, C. A. Heisler, and J. Trevena. Theoretical Modeling of Starburst Galaxies. *ApJ*, 556:121–140, July 2001. doi: 10.1086/321545.
- L. J. Kewley, B. Groves, G. Kauffmann, and T. Heckman. The host galaxies and classification of active galactic nuclei. *MNRAS*, 372:961–976, November 2006. doi: 10.1111/j.1365-2966.2006.10859.x.
- E. Y. Khachikian and D. W. Weedman. An atlas of Seyfert galaxies. *ApJ*, 192:581–589, September 1974. doi: 10.1086/153093.
- J. Kormendy and R. C. Kennicutt, Jr. Secular Evolution and the Formation of Pseudobulges in Disk Galaxies. *ARA&A*, 42:603–683, September 2004. doi: 10.1146/annurev.astro.42.053102.134024.
- J. H. Krolik and M. C. Begelman. Molecular tori in Seyfert galaxies - Feeding the monster and hiding it. *ApJ*, 329:702–711, June 1988. doi: 10.1086/166414.
- J. M. D. Kruijssen, S. N. Longmore, B. G. Elmegreen, N. Murray, J. Bally, L. Testi, and R. C. Kennicutt. What controls star formation in the central 500 pc of the Galaxy? *MNRAS*, 440:3370–3391, June 2014. doi: 10.1093/mnras/stu494.
- J. M. D. Kruijssen, J. E. Dale, and S. N. Longmore. The dynamical evolution of molecular clouds near the Galactic Centre - I. Orbital structure and evolutionary timeline. *MNRAS*, 447:1059–1079, February 2015. doi: 10.1093/mnras/stu2526.
- M. R. Krumholz and B. Burkhardt. Is turbulence in the interstellar medium driven by feedback or gravity? An observational test. *MNRAS*, 458:1671–1677, May 2016. doi: 10.1093/mnras/stw434.
- F. La Franca, L. Gregorini, S. Cristiani, H. de Ruiter, and F. Owen. Deep VLA observations of an optically selected sample of intermediate redshift QSOs and the optical luminosity function of the radio loud QSOs. *AJ*, 108:1548–1556, November 1994. doi: 10.1086/117176.

- R. A. Laing. Brightness and Polarization Structure of Decelerating Relativistic Jets. In P. E. Hardee, A. H. Bridle, and J. A. Zensus, editors, *Energy Transport in Radio Galaxies and Quasars*, volume 100 of *Astronomical Society of the Pacific Conference Series*, page 241, 1996.
- L. Lanz, P. M. Ogle, D. Evans, P. N. Appleton, P. Guillard, and B. Emonts. Jet-ISM Interaction in the Radio Galaxy 3C 293: Jet-driven Shocks Heat ISM to Power X-Ray and Molecular H₂ Emission. *ApJ*, 801:17, March 2015. doi: 10.1088/0004-637X/801/1/17.
- G. Lanzuisi, I. Delvecchio, S. Berta, M. Brusa, A. Comastri, R. Gilli, C. Grupponi, S. Marchesi, M. Perna, F. Pozzi, M. Salvato, M. Symeonidis, C. Vignali, F. Vito, M. Volonteri, and G. Zamorani. Active galactic nuclei vs. host galaxy properties in the COSMOS field. *A&A*, 602:A123, June 2017. doi: 10.1051/0004-6361/201629955.
- A. Lapi, S. Raimundo, R. Aversa, Z.-Y. Cai, M. Negrello, A. Celotti, G. De Zotti, and L. Danese. The Coevolution of Supermassive Black Holes and Massive Galaxies at High Redshift. *ApJ*, 782:69, February 2014. doi: 10.1088/0004-637X/782/2/69.
- A. Lawrence, M. Rowan-Robinson, K. Leech, D. H. P. Jones, and J. V. Wall. High-luminosity IRAS galaxies. I - The proportion of IRAS galaxies in interacting systems. *MNRAS*, 240:329–348, September 1989. doi: 10.1093/mnras/240.2.329.
- N. A. Levenson, K. A. Weaver, T. M. Heckman, H. Awaki, and Y. Terashima. Accretion and Outflow in the Active Galactic Nucleus and Starburst of NGC 5135. *ApJ*, 602:135–147, February 2004. doi: 10.1086/380836.
- C. Li, G. Kauffmann, T. M. Heckman, Y. P. Jing, and S. D. M. White. Interaction-induced star formation in a complete sample of 10⁵ nearby star-forming galaxies. *MNRAS*, 385:1903–1914, April 2008a. doi: 10.1111/j.1365-2966.2008.13000.x.
- C. Li, G. Kauffmann, T. M. Heckman, S. D. M. White, and Y. P. Jing. Interactions, star formation and AGN activity. *MNRAS*, 385:1915–1922, April 2008b. doi: 10.1111/j.1365-2966.2008.13023.x.
- D. Lutz, S. Veilleux, and R. Genzel. Mid-infrared and optical spectroscopy of ultra-luminous infrared galaxies: A comparison. *The Astrophysical Journal Letters*, 517(1):L13, 1999. URL <http://stacks.iop.org/1538-4357/517/i=1/a=L13>.
- Dieter Lutz. Far-infrared surveys of galaxy evolution. *Annual Review of Astronomy and Astrophysics*, 52(1):373–414, 2014. doi: 10.1146/annurev-astro-081913-035953. URL <https://doi.org/10.1146/annurev-astro-081913-035953>.
- P. Madau and M. Dickinson. Cosmic Star-Formation History. *ARA&A*, 52:415–486, August 2014. doi: 10.1146/annurev-astro-081811-125615.
- P. Madau, L. Pozzetti, and M. Dickinson. The Star Formation History of Field Galaxies. *ApJ*, 498:106–116, May 1998. doi: 10.1086/305523.

BIBLIOGRAPHY

- B. Magnelli, D. Elbaz, R. R. Chary, M. Dickinson, D. Le Borgne, D. T. Frayer, and C. N. A. Willmer. Evolution of the dusty infrared luminosity function from $z = 0$ to $z = 2.3$ using observations from Spitzer. *A&A*, 528:A35, April 2011. doi: 10.1051/0004-6361/200913941.
- B. Magnelli, P. Popesso, S. Berta, F. Pozzi, D. Elbaz, D. Lutz, M. Dickinson, B. Altieri, P. Andreani, H. Aussel, M. Béthermin, A. Bongiovanni, J. Cepa, V. Charmandaris, R.-R. Chary, A. Cimatti, E. Daddi, N. M. Förster Schreiber, R. Genzel, C. Gruppioni, M. Harwit, H. S. Hwang, R. J. Ivison, G. Magdis, R. Maiolino, E. Murphy, R. Nordon, M. Pannella, A. Pérez García, A. Poglitsch, D. Rosario, M. Sanchez-Portal, P. Santini, D. Scott, E. Sturm, L. J. Tacconi, and I. Valtchanov. The deepest Herschel-PACS far-infrared survey: number counts and infrared luminosity functions from combined PEP/GOODS-H observations. *A&A*, 553:A132, May 2013. doi: 10.1051/0004-6361/201321371.
- R. McCray and M. Kafatos. Supershells and propagating star formation. *ApJ*, 317:190–196, June 1987. doi: 10.1086/165267.
- I. F. Mirabel. Neutral hydrogen in bright galaxies with strong radio sources. *ApJ*, 260:75–80, September 1982. doi: 10.1086/160235.
- J. S. Mulchaey and M. W. Regan. The Fueling of Nuclear Activity: The Bar Properties of Seyfert and Normal Galaxies. *ApJ*, 482:L135–L137, June 1997. doi: 10.1086/310710.
- J. R. Mullaney, D. M. Alexander, A. D. Goulding, and R. C. Hickox. Defining the intrinsic AGN infrared spectral energy distribution and measuring its contribution to the infrared output of composite galaxies. *MNRAS*, 414:1082–1110, June 2011. doi: 10.1111/j.1365-2966.2011.18448.x.
- J. R. Mullaney, E. Daddi, M. Béthermin, D. Elbaz, S. Juneau, M. Pannella, M. T. Sargent, D. M. Alexander, and R. C. Hickox. The Hidden “AGN Main Sequence”: Evidence for a Universal Black Hole Accretion to Star Formation Rate Ratio since $z \sim 2$ Producing an $M_{BH}-M_*$ Relation. *ApJ*, 753:L30, July 2012. doi: 10.1088/2041-8205/753/2/L30.
- G. Neugebauer, H. J. Habing, R. van Duinen, H. H. Aumann, B. Baud, C. A. Beichman, D. A. Beintema, N. Boggess, P. E. Clegg, T. de Jong, J. P. Emerson, T. N. Gautier, F. C. Gillett, S. Harris, M. G. Hauser, J. R. Houck, R. E. Jennings, F. J. Low, P. L. Marsden, G. Miley, F. M. Olmon, S. R. Pottasch, E. Raimond, M. Rowan-Robinson, B. T. Soifer, R. G. Walker, P. R. Wesselius, and E. Young. The Infrared Astronomical Satellite (IRAS) mission. *ApJ*, 278:L1–L6, March 1984. doi: 10.1086/184209.
- D. E. Osterbrock. Seyfert galaxies with weak broad H alpha emission lines. *ApJ*, 249:462–470, October 1981. doi: 10.1086/159306.

- J. P. Ostriker and P. J. E. Peebles. A Numerical Study of the Stability of Flattened Galaxies: or, can Cold Galaxies Survive? *ApJ*, 186:467–480, December 1973. doi: 10.1086/152513.
- J. P. Ostriker, P. J. E. Peebles, and A. Yahil. The size and mass of galaxies, and the mass of the universe. *ApJ*, 193:L1–L4, October 1974. doi: 10.1086/181617.
- P. Padovani. The Radio Loud Fraction of QSOS and its Dependence on Magnitude and Redshift. *MNRAS*, 263:461, July 1993. doi: 10.1093/mnras/263.2.461.
- F. G. Pease. The rotation and radial velocity of the central part of the andromeda nebula. *Proceedings of the National Academy of Sciences of the United States of America*, 4(1):21–24, 1918. ISSN 00278424. URL <http://www.jstor.org/stable/83925>.
- M. M. Phillips, P. A. Charles, and J. A. Baldwin. Nearby galaxies with Seyfert-like nuclei. *ApJ*, 266:485–501, March 1983. doi: 10.1086/160797.
- A. Pouw. The IRAS spacecraft. *Journal of the British Interplanetary Society*, 36: 17–20, January 1983.
- M. A. Prieto, O. Marco, and J. Gallimore. Morphology of the coronal-line region in active galactic nuclei*. *MNRAS*, 364:L28–L32, November 2005. doi: 10.1111/j.1745-3933.2005.00099.x.
- N. A. Reddy and C. C. Steidel. A Steep Faint-End Slope of the UV Luminosity Function at $z \sim 2-3$: Implications for the Global Stellar Mass Density and Star Formation in Low-Mass Halos. *ApJ*, 692:778–803, February 2009. doi: 10.1088/0004-637X/692/1/778.
- T. A. Reichard, T. M. Heckman, G. Rudnick, J. Brinchmann, G. Kauffmann, and V. Wild. The Lopsidedness of Present-Day Galaxies: Connections to the Formation of Stars, the Chemical Evolution of Galaxies, and the Growth of Black Holes. *ApJ*, 691:1005–1020, February 2009. doi: 10.1088/0004-637X/691/2/1005.
- F. Renaud, F. Bournaud, and P.-A. Duc. A parsec-resolution simulation of the Antennae galaxies: formation of star clusters during the merger. *MNRAS*, 446:2038–2054, January 2015. doi: 10.1093/mnras/stu2208.
- C. T. Richardson, J. T. Allen, J. A. Baldwin, P. C. Hewett, and G. J. Ferland. Interpreting the ionization sequence in AGN emission-line spectra. *MNRAS*, 437: 2376–2403, January 2014. doi: 10.1093/mnras/stt2056.
- G. H. Rieke and M. J. Lebofsky. The luminosity function for field galaxies in the infrared. *ApJ*, 304:326–333, May 1986. doi: 10.1086/164167.
- M. S. Roberts and A. H. Rots. Comparison of Rotation Curves of Different Galaxy Types. *A&A*, 26:483–485, August 1973.

BIBLIOGRAPHY

- A. S. G. Robotham and S. P. Driver. The GALEX-SDSS NUV and FUV flux density and local star formation rate. *MNRAS*, 413:2570–2582, June 2011. doi: 10.1111/j.1365-2966.2011.18327.x.
- A. Rodríguez-Ardila and X. Mazzalay. The near-infrared spectrum of Mrk 1239: direct evidence of the dusty torus? *MNRAS*, 367:L57–L61, March 2006. doi: 10.1111/j.1745-3933.2006.00139.x.
- P. R. Roelfsema and R. J. Allen. Radio observations of H I in UGC 2885, the largest identified SC galaxy. *A&A*, 146:213–222, May 1985.
- G. Roelofs. *Radial Motions in Spiral Galaxies*. PhD thesis, THE UNIVERSITY OF CHICAGO., January 1995.
- D. J. Rosario, P. Santini, D. Lutz, L. Shao, R. Maiolino, D. M. Alexander, B. Altieri, P. Andreani, H. Aussel, F. E. Bauer, S. Berta, A. Bongiovanni, W. N. Brandt, M. Brusa, J. Cepa, A. Cimatti, T. J. Cox, E. Daddi, D. Elbaz, A. Fontana, N. M. Förster Schreiber, R. Genzel, A. Grazian, E. Le Floch, B. Magnelli, V. Mainieri, H. Netzer, R. Nordon, I. Pérez Garcia, A. Poglitsch, P. Popesso, F. Pozzi, L. Riguccini, G. Rodighiero, M. Salvato, M. Sanchez-Portal, E. Sturm, L. J. Tacconi, I. Valtchanov, and S. Wuyts. The mean star formation rate of X-ray selected active galaxies and its evolution from $z \sim 2.5$: results from PEP-Herschel. *A&A*, 545:A45, September 2012. doi: 10.1051/0004-6361/201219258.
- B. Rush, M. A. Malkan, and L. Spinoglio. The extended 12 micron galaxy sample. *ApJS*, 89:1–33, November 1993. doi: 10.1086/191837.
- H. R. Russell, M. McDonald, B. R. McNamara, A. C. Fabian, P. E. J. Nulsen, M. B. Bayliss, B. A. Benson, M. Brodwin, J. E. Carlstrom, A. C. Edge, J. Hlavacek-Larrondo, D. P. Marrone, C. L. Reichardt, and J. D. Vieira. Alma Observations of Massive Molecular Gas Filaments Encasing Radio Bubbles in the Phoenix Cluster. *ApJ*, 836:130, February 2017. doi: 10.3847/1538-4357/836/1/130.
- S. Sakai, J. R. Mould, S. M. G. Hughes, J. P. Huchra, L. M. Macri, R. C. Kennicutt, Jr., B. K. Gibson, L. Ferrarese, W. L. Freedman, M. Han, H. C. Ford, J. A. Graham, G. D. Illingworth, D. D. Kelson, B. F. Madore, K. Sebo, N. A. Silbermann, and P. B. Stetson. The Hubble Space Telescope Key Project on the Extragalactic Distance Scale. XXIV. The Calibration of Tully-Fisher Relations and the Value of the Hubble Constant. *ApJ*, 529:698–722, February 2000. doi: 10.1086/308305.
- A. Sandage. Optical redshifts for 719 bright galaxies. *AJ*, 83:904–937, August 1978. doi: 10.1086/112271.
- D. Sanders and C. Ishida. Luminous Infrared Galaxies: Optical Morphology and Photometry, Molecular Gas Masses, and Starburst/AGN Activity versus Infrared Luminosity. In S. Aalto, S. Huttemeister, and A. Pedlar, editors, *The Neutral ISM in Starburst Galaxies*, volume 320 of *Astronomical Society of the Pacific Conference Series*, page 230, December 2004.

- D. B. Sanders, E. S. Phinney, G. Neugebauer, B. T. Soifer, and K. Matthews. Continuum energy distribution of quasars - Shapes and origins. *ApJ*, 347:29–51, December 1989. doi: 10.1086/168094.
- D. B. Sanders, J. M. Mazzarella, D.-C. Kim, J. A. Surace, and B. T. Soifer. The IRAS Revised Bright Galaxy Sample. *AJ*, 126:1607–1664, October 2003. doi: 10.1086/376841.
- M. A. Schenker, B. E. Robertson, R. S. Ellis, Y. Ono, R. J. McLure, J. S. Dunlop, A. Koekemoer, R. A. A. Bowler, M. Ouchi, E. Curtis-Lake, A. B. Rogers, E. Schneider, S. Charlot, D. P. Stark, S. R. Furlanetto, and M. Cirasuolo. The UV Luminosity Function of Star-forming Galaxies via Dropout Selection at Redshifts $z \sim 7$ and 8 from the 2012 Ultra Deep Field Campaign. *ApJ*, 768:196, May 2013. doi: 10.1088/0004-637X/768/2/196.
- D. Schiminovich, O. Ilbert, S. Arnouts, B. Milliard, L. Tresse, O. Le Fèvre, M. Treyer, T. K. Wyder, T. Budavári, E. Zucca, G. Zamorani, D. C. Martin, C. Adami, M. Arnaboldi, S. Bardelli, T. Barlow, L. Bianchi, M. Bolzonella, D. Bottini, Y.-I. Byun, A. Cappi, T. Contini, S. Charlot, J. Donas, K. Forster, S. Foucaud, P. Franzetti, P. G. Friedman, B. Garilli, I. Gavignaud, L. Guzzo, T. M. Heckman, C. Hoopes, A. Iovino, P. Jelinsky, V. Le Brun, Y.-W. Lee, D. Maccagni, B. F. Madore, R. Malina, B. Marano, C. Marinoni, H. J. McCracken, A. Mazure, B. Meneux, P. Morrissey, S. Neff, S. Paltani, R. Pellò, J. P. Picat, A. Pollo, L. Pozzetti, M. Radovich, R. M. Rich, R. Scaramella, M. Scodreggio, M. Seibert, O. Siegmund, T. Small, A. S. Szalay, G. Vettolani, B. Welsh, C. K. Xu, and A. Zanichelli. The GALEX-VVDS Measurement of the Evolution of the Far-Ultraviolet Luminosity Density and the Cosmic Star Formation Rate. *ApJ*, 619:L47–L50, January 2005. doi: 10.1086/427077.
- E. Schinnerer, A. Eckart, L. J. Tacconi, R. Genzel, and D. Downes. Bars and Warps Traced by the Molecular Gas in the Seyfert 2 Galaxy NGC 1068. *ApJ*, 533:850–868, April 2000. doi: 10.1086/308702.
- M. Schmidt. Observed properties of quasi-stellar objects. In *Contemporary Physics, Volume 1*, page 467, 1969.
- M. Schmidt and R. F. Green. Quasar evolution derived from the Palomar bright quasar survey and other complete quasar surveys. *ApJ*, 269:352–374, June 1983. doi: 10.1086/161048.
- Remco Hubertus Maria Schoenmakers. Asymmetries in spiral galaxies, 1999.
- K. Schwarzschild. Über das Gravitationsfeld einer Kugel aus inkompressibler Flüssigkeit nach der Einsteinschen Theorie. In *Sitzungsberichte der Königlich Preussischen Akademie der Wissenschaften zu Berlin, Phys.-Math. Klasse, 424-434 (1916)*, March 1916.

BIBLIOGRAPHY

- C. K. Seyfert. Nuclear Emission in Spiral Nebulae. *ApJ*, 97:28, January 1943. doi: 10.1086/144488.
- F. Shankar. The demography of supermassive black holes: Growing monsters at the heart of galaxies. *New A Rev.*, 53:57–77, April 2009. doi: 10.1016/j.newar.2009.07.006.
- I. Shlosman, M. C. Begelman, and J. Frank. The fuelling of active galactic nuclei. *Nature*, 345:679–686, June 1990. doi: 10.1038/345679a0.
- K. P. Singh. An Xray view of quasars. *Astroph*, December 2014. doi: arXiv:1310.0270.
- E. P. Smith, T. M. Heckman, G. D. Bothun, W. Romanishin, and B. Balick. On the nature of QSO host galaxies. *ApJ*, 306:64–89, July 1986. doi: 10.1086/164321.
- R. S. Somerville and R. Davé. Physical Models of Galaxy Formation in a Cosmological Framework. *ARA&A*, 53:51–113, August 2015. doi: 10.1146/annurev-astro-082812-140951.
- L. Spinoglio and M. A. Malkan. The 12 micron galaxy sample. I - Luminosity functions and a new complete active galaxy sample. *ApJ*, 342:83–99, July 1989. doi: 10.1086/167577.
- D. Steinhauser, S. Schindler, and V. Springel. Simulations of ram-pressure stripping in galaxy-cluster interactions. *A&A*, 591:A51, June 2016. doi: 10.1051/0004-6361/201527705.
- Mark R. Swain, Alan H. Bridle, and Stefi A. Baum. Internal structure of the jets in 3c 353. *The Astrophysical Journal Letters*, 507(1):L29, 1998. URL <http://stacks.iop.org/1538-4357/507/i=1/a=L29>.
- R. A. Swaters, R. H. M. Schoenmakers, R. Sancisi, and T. S. van Albada. Kinetically lopsided spiral galaxies. *MNRAS*, 304:330–334, April 1999. doi: 10.1046/j.1365-8711.1999.02332.x.
- T. T. Takeuchi, K. Yoshikawa, and T. T. Ishii. The Luminosity Function of IRAS Point Source Catalog Redshift Survey Galaxies. *ApJ*, 587:L89–L92, April 2003. doi: 10.1086/375181.
- S. Tommasin, L. Spinoglio, M. A. Malkan, H. Smith, E. González-Alfonso, and V. Charmandaris. Spitzer IRS High-Resolution Spectroscopy of the 12 μm Seyfert Galaxies. I. First Results. *ApJ*, 676:836–856, April 2008. doi: 10.1086/527290.
- S. Tommasin, L. Spinoglio, M. A. Malkan, and G. Fazio. Spitzer-IRS High-Resolution Spectroscopy of the 12 μm Seyfert Galaxies. II. Results for the Complete Data Set. *ApJ*, 709:1257–1283, February 2010. doi: 10.1088/0004-637X/709/2/1257.

- Chao-Wei Tsai, Peter R. M. Eisenhardt, Jingwen Wu, Daniel Stern, Roberto J. Assef, Andrew W. Blain, Carrie R. Bridge, Dominic J. Benford, Roc M. Cutri, Roger L. Griffith, Thomas H. Jarrett, Carol J. Lonsdale, Frank J. Masci, Leonidas A. Moustakas, Sara M. Petty, Jack Sayers, S. Adam Stanford, Edward L. Wright, Lin Yan, David T. Leisawitz, Fengchuan Liu, Amy K. Mainzer, Ian S. McLean, Deborah L. Padgett, Michael F. Skrutskie, Christopher R. Gelino, Charles A. Beichman, and Stéphanie Juneau. The most luminous galaxies discovered by wise. *The Astrophysical Journal*, 805(2):90, 2015. URL <http://stacks.iop.org/0004-637X/805/i=2/a=90>.
- R. B. Tully and J. R. Fisher. A new method of determining distances to galaxies. *A&A*, 54:661–673, February 1977.
- J. S. Ulvestad and A. S. Wilson. Radio structures of Seyfert galaxies. VII - Extension of a distance-limited sample. *ApJ*, 343:659–671, August 1989. doi: 10.1086/167737.
- C. M. Urry and P. Padovani. Unified Schemes for Radio-Loud Active Galactic Nuclei. *PASP*, 107:803, September 1995. doi: 10.1086/133630.
- H. C. van de Hulst, E. Raimond, and H. van Woerden. Rotation and density distribution of the Andromeda nebula derived from observations of the 21-cm line. *Bull. Astron. Inst. Netherlands*, 14:1, November 1957.
- S. Veilleux and D. E. Osterbrock. Spectral classification of emission-line galaxies. *ApJS*, 63:295–310, February 1987. doi: 10.1086/191166.
- S. Veilleux, D. B. Sanders, and D.-C. Kim. New Results from a Near-Infrared Search for Hidden Broad-Line Regions in Ultraluminous Infrared Galaxies. *ApJ*, 522:139–156, September 1999. doi: 10.1086/307635.
- S. Veilleux, D.-C. Kim, and D. B. Sanders. Optical and Near-Infrared Imaging of the IRAS 1 Jy Sample of Ultraluminous Infrared Galaxies. II. The Analysis. *ApJS*, 143: 315–376, December 2002. doi: 10.1086/343844.
- M.-P. Veron-Cetty and P. Veron. A catalogue of quasars and active nuclei. *European Southern Observatory Scientific Report*, 10:1–199, 1991.
- M.-P. Véron-Cetty and P. Véron. A catalogue of quasars and active nuclei: 12th edition. *A&A*, 455:773–777, August 2006. doi: 10.1051/0004-6361:20065177.
- A. S. Wilson and E. J. M. Colbert. The difference between radio-loud and radio-quiet active galaxies. *ApJ*, 438:62–71, January 1995. doi: 10.1086/175054.
- T. K. Wyder, M. A. Treyer, B. Milliard, D. Schiminovich, S. Arnouts, T. Budavári, T. A. Barlow, L. Bianchi, Y.-I. Byun, J. Donas, K. Forster, P. G. Friedman, T. M. Heckman, P. N. Jelinsky, Y.-W. Lee, B. F. Madore, R. F. Malina, D. C. Martin, P. Morrissey, S. G. Neff, R. M. Rich, O. H. W. Siegmund, T. Small, A. S. Szalay, and B. Y. Welsh. The Ultraviolet Galaxy Luminosity Function in the Local Universe from GALEX Data. *ApJ*, 619:L15–L18, January 2005. doi: 10.1086/424735.

BIBLIOGRAPHY

- H. Yang, J. Wang, and T. Liu. On the Anisotropy of Nuclei Mid-Infrared Radiation in Nearby Active Galactic Nuclei. *ApJ*, 799:91, January 2015. doi: 10.1088/0004-637X/799/1/91.
- F. Yuan and R. Narayan. Hot Accretion Flows Around Black Holes. *ARA&A*, 52: 529–588, August 2014. doi: 10.1146/annurev-astro-082812-141003.